On the role of well-defined co-precipitation and aging for the scalable preparation of high-quality Cu/ZnO based catalysts

Zur Erlangung des akademischen Grades eines
DOKTORS DER INGENIEURWISSENSCHAFTEN (DR.-ING.)

von der KIT-Fakultät für Chemieingenieurwesen und Verfahrenstechnik des
Karlsruher Instituts für Technologie (KIT)
genehmigte

DISSERTATION

von
M.Sc. David Geoffrey Guse
aus Karlsruhe

Tag der mündlichen Prüfung: 17.10.2025

Erstgutachter/-in: Prof. Dr.-Ing. Matthias Kind

Zweitgutachter/-in: TT-Prof. Dr. Moritz Wolf

Preface

The contents of this thesis originate from my time as a PhD student at the Institute of Thermal Process Engineering at Karlsruhe Institute of Technology from 2017 to 2024. These seven years were a formative period for me, both professionally and personally with my wedding and the birth of my son. My time in university research was characterized by great academic and personal freedom on the one side, which was granted and envisioned by Matthias Kind, my doctoral supervisor, and by fruitful, motivating and educational cooperations on the other side, whether with industrial or academic partners or dear colleagues.

With this in mind, my first thanks go to Matthias Kind, without whom this work would not exist and without whom my occupational development would look vastly different and most definitely would show a lack of Apfelschorle as an example for mixing and desert roses as an inspiration for research ideas. The joint syntheses and studies with my colleagues at IKFT had a similarly big impact on this work and I would especially like to thank Stephan Pitter, Lucas Warmuth, Sabrina Polierer, Moritz Herfet, Stefan Wild and Thomas Zevaco for the days together in the lab and at conferences. I also want to thank Moritz Wolf for kindly taking over the second review.

This work would lack in results if it hadn't been for the many students works which I had the honor to supervise. As is often the case in research, it has not always been a linear path forwards, so only some of the results from these works have been incorporated into this thesis. Yet, there was a lot to learn and enjoy in each single case. Thank you, Lingyue, Laura, Patrick, Ahmet, Lukas, Frederic, Kassian, Laurids, Sebastian, Florian, Xuelan, Alex, Thomas, Christiane, Mathias, Jiangyu, Jianyun, Enrique, Abraham, Katharina and Richard. I also want to thank Nicole Feger, Sebastian Schwarz, Vanessa Gamer, Max Renaud, Andreas Roth, Michael Wachter, Stefan Böttle, Stephan Fink, Annette Schucker and Sabrina Herberger for their support in administration, plant construction and in the lab.

While I enjoyed most of my PhD time, there were time and time again setbacks and challenging periods. The long days in the lab and at the desk were much easier to endure and overcome thanks to my dear colleagues and friends at TVT with whom I also enjoyed countless coffee breaks, lunch breaks, seminars, Hallenfeste and precious spare time. Thank you!

Finally, and above all, I want to thank my family for their endless support during my studies at KIT and my subsequent work on my dissertation. I want to thank my parents for enabling me to study and providing me with a home during that time and I want to thank my brother for being the ideal roommate. The most special thanks go to my wife, Katharina, who always had my back and supported me throughout my time in Karlsruhe with an incredible amount of understanding, patience and strength even though her own job is endlessly demanding. With Johannes, her workload certainly did not decrease. Thank you, Katharina. Johannes, thank you for making my life even brighter and for allowing me to write on the weekends and in the evenings. At least sometimes.

And for all those who are reading this thesis and are in the process of working on a doctor thesis themselves, I leave you with a German mantra that I took to heart during challenging

times: “tja”. Don’t take everything too seriously and leave behind what no longer can be changed. It is often more important to look ahead and look forward to what’s coming and those things you still can influence.

Kurzfassung

Die chemische Industrie steht vor einer außerordentlichen Herausforderung. Einerseits ist es notwendig, die Produktion in den kommenden Jahrzehnten hinsichtlich Nachhaltigkeit und CO_2-Neutralität grundsätzlich umzugestalten. Andererseits steigt die Nachfrage nach Grundchemikalien aus nicht erneuerbaren Rohstoffen weiter an. Beispielsweise wird prognostiziert, dass die jährliche Methanolproduktion bis 2050 von etwa 100 Mt auf 500 Mt anwachsen wird. Derzeit werden jedoch über 99 % des Methanols aus Synthesegas produziert, das durch Erdgasreformierung oder Kohlevergasung erzeugt wird. Ein vielversprechender Ansatz zur Bewältigung dieser Herausforderung ist die Produktion von grünem Methanol aus CO_2. Allerdings entsteht durch den Ersatz von CO durch CO_2 in der Katalyse eine große Menge an Wasser als Nebenprodukt, das den am häufigsten verwendeten $Cu/ZnO/Al_2O_3$-Katalysator vergiftet und deaktiviert. Alternative Zusammensetzungen, wie z.B. $Cu/ZnO/ZrO_2$, scheinen im Vergleich robuster gegenüber Wasser und somit besser für die Methanolproduktion aus CO_2 geeignet zu sein, sind aber hinsichtlich ihrer Performance noch nicht optimiert.

Aufgrund der Komplexität des mehrstufigen Katalysator-Herstellungsprozesses werden die Prozessparameter im Allgemeinen mittels weitgefasster Parameterstudien ausgewählt und optimiert. Der Prozess umfasst die folgenden fünf Hauptschritte: Ko-Fällung, bei der ein amorpher Feststoff aus den Eduktlösungen gebildet wird, Alterung, bei der sich dieser Feststoff in die angestrebte Feststoffphase Zinkmalachit ($Cu_{1.46}Zn_{0.54}CO_3(OH)_2$) umwandelt, Kalzinierung, bei der das Hydroxycarbonat zu den jeweiligen Metalloxiden zerfällt, Formgebung und abschließend Reduktion, bei der CuO zum katalytisch aktiven Cu reduziert wird. Die Gewinnung von Zinkmalachit als Zwischenprodukt erwies sich als essentiell für die Qualität des resultierenden Katalysators. Aufgrund der Kristallmorphologie und der definierten Anordnung von Cu- und Zn-Atomen im Kristallgitter wird durch die zwischenzeitliche Präsenz von Zinkmalachit die Cu-Oberfläche maximiert, was wiederum Produktivität und Stabilität in der Anwendung erhöht. Im Gegensatz zu diesem Detailwissen sind jedoch grundlegende Zusammenhänge zwischen den Prozessbedingungen der einzelnen Prozessschritte und den resultierenden Eigenschaften des Zwischenprodukts oder Katalysators, die sogenannten Prozessfunktionen, oft unbekannt. Da eben jene physikochemischen Eigenschaften die Qualität des resultierenden Katalysators maßgeblich bestimmen, ist ein grundlegendes Verständnis der Prozessfunktionen essentiell für eine schnellere und strukturierte Rezeptur- und Prozessentwicklung für jetzige und zukünftige Herausforderungen, wie eben den Wechsel von CO zu CO_2 im Synthesegas.

Daher war das Ziel dieser Arbeit, die Prozessfunktionen der einzelnen Prozessschritte bei der Herstellung von Cu/ZnO basierten Katalysatoren zu verstehen und zu quantifizieren. Dies sollte einerseits eine systematische und skalierbare Prozessentwicklung ermöglichen und andererseits die modellbasierte Optimierung von Raum-Zeit-Ausbeute und Produktqualität ermöglichen. Der Fokus lag hier auf den oft miteinander verflochtenen Prozessschritten Ko-Fällung und Alterung, da diese am Anfang der Prozesskette stehen und sie als entscheidend für die Qualität des resultierenden Katalysators identifiziert wurden.

Zunächst galt es eine neue Prozessvariante zu entwickeln, um Ko-Fällung und Alterung, im Gegensatz zum Standard, der Semi-batch Fahrweise im Rührkessel, zeitlich und räumlich strikt zu trennen. Auf diese Weise sollte dann jeweils eine isolierte Prozesscharakterisierung möglich sein. Zu diesem Zweck wurde eine kontinuierliche Ko-Fällung in einer Mischdüse mit einer sich anschließenden Batch-Alterung im Rührkessel kombiniert. Das energieintensive Mischen in der Mischdüse, das für einen Alterungs-Batch in weniger als 4 Minuten abgeschlossen war, ermöglichte Mikromischzeiten unter 10^{-4} s und somit das Entkoppeln der kinetisch kontrollierten initialen Feststoffbildung von Mischeinflüssen. Die entstehende Suspension, die in Partikelgröße und Feststoffzusammensetzung der einzelnen co-gefällten Partikeln homogen war, konnte dann verwendet werden, um Alterungsstudien unter definierten Bedingungen durchzuführen, ohne den Einfluss einer parallel stattfindende Ko-Fällung oder durch größere Variationen in der Alterungszeit zwischen einzelnen Partikeln.

Ein Vergleich der kontinuierlichen Mischung in einer Mischdüse mit einer Semi-batch Ko-Fällung in einem Rührkessel zeigte, dass die Mischmethode die Morphologie des Präzipitats und die Qualität des resultierenden Katalysators beeinflusst. Die neu entwickelte Fahrweise ermöglichte eine andere pH- und Übersättigungstrajektorie während der initialen Feststoffbildung, was zu kleineren Kristalliten nach der Alterung, einer zehnprozentigen Erhöhung der spezifischen Oberfläche und einer homogeneren Porengröße und Porenverteilung im Vergleich zum Semi-batch Material führte. Dies bestätigte, dass die Ko-Fällung kinetisch kontrolliert ist. Diese Unterschiede blieben über die Kalzinierung hinweg bestehen, was zu einem Katalysator mit einer bis zu dreimal größerer spezifischer Oberfläche und Kupferoberfläche sowie einer homogeneren nanoskaligen Cu- und Zn-Verteilung führte. Als Resultat verdreifachte sich auch die Methanolproduktivität. Die Variation des Gesamtvolumenstroms bei der kontinuierlichen Ko-Fällung zeigte, dass die Mikromischzeit die initiale Feststoffbildung beeinflusst. Zwei Regime wurden unterschieden: bei kleinen Volumenströmen unter 400 $ml \cdot min^{-1}$ bzw. Mikromischzeiten größer als $1.2 \cdot 10^{-4}$ s, ist die Anzahl an verfügbaren Gitterionen in der umgebenden Flüssigkeit durch die noch nicht abgeschlossene Vermischung limitiert. Das verringert die effektive Übersättigung, was wiederum zu einer Vergrößerung der mittleren Partikelgröße führt. Wenn der kritische Volumenstrom überschritten wurde, beeinflusste das Mischen die Partikelgröße nicht mehr. Die durch die unterschiedlichen Mischzeiten erzeugten Differenzen wurden in diesem Fall jedoch durch die Alterung ausgeglichen: das gealterte Zwischenprodukt zeigte keine Korrelation mit der Mischintensität und es ergaben sich Katalysatoren mit vergleichbarer katalytischer Aktivität. Dies war höchstwahrscheinlich das Ergebnis der Homogenität in Partikelgröße und Zusammensetzung der einzelnen Partikeln, die unter gleichbleibenden Bedingungen in der Mischdüse erzeugt wurden und darum auch ähnliche Alterungskinetiken besaßen. Ein idealer Herstellungsprozess sollte daher einen Ko-Fällungsschritt beinhalten, der im nicht-mischungslimitierten Regime, und idealerweise kontinuierlich, betrieben wird, um ein hinsichtlich Partikelgröße und -zusammensetzung homogenes Ko-Fällungsprodukt zu erhalten und so einen negativen Einfluss auf die Katalysatorqualität auszuschließen.

Aufgrund der Bedeutung von Zinkmalachit für die resultierende Katalysatorqualität war das Hauptziel bezüglich des Alterungsschritts die Entwicklung eines Modells, das die

Phasenzusammensetzung nach der Alterung auf Basis der wichtigsten Prozessparameter wie Eduktzusammensetzung, pH-Wert und Temperatur vorhersagt. Dieses Modell sollte zukünftig die Anzahl der erforderlichen Parameterstudien reduzieren und helfen, bisher unbekannte Prozessoptima zu identifizieren. Basierend auf der Hypothese, dass die Alterung ein Prozess hin zum thermodynamischen Gleichgewicht ist, wurde ein entsprechendes Gleichgewichts-Modell ohne Berücksichtigung der Kinetik entwickelt. Dieses besteht aus einem Aktivitätskoeffizientenmodell, das nicht-ideale Ionenwechselwirkungen berücksichtigt, und einer Stoffmengenbilanzierung basierend auf Löslichkeitsprodukten und Ionenassoziationsprodukten. Eine ergänzend entwickelte experimentelle Methode ermöglichte die Bestimmung fehlender Löslichkeitsdaten aus Titrationsexperimenten, wie z.B. die Temperaturabhängigkeit für synthetisches Zinkmalachit oder die Löslichkeit des Nebenprodukts $Na_2Zn_3(CO_3)_4 \cdot 3H_2O$. Diese Methodik bestätigte auch die Notwendigkeit separater Löslichkeitsprodukte für das metastabile Ko-Fällungsprodukt und das thermodynamisch stabilere gealterte Zwischenprodukt.

Das Modell wurde validiert, indem berechnete Phasenzusammensetzungen im thermodynamischen Gleichgewicht mit experimentell bestimmten Feststoffzusammensetzungen in Abhängigkeit von pH, Temperatur und Cu/Zn-Verhältnis im Feed verglichen wurden. Das Modell bildete die experimentell bestimmte Phasenzusammensetzung quantitativ korrekt ab und reproduzierte das Auftreten von Nebenprodukten, wie Rouait bei $pH \leq 5$ und Aurichalcit bei $T \geq 70$ °C. Abweichungen zwischen Modell und Messungen resultierten wahrscheinlich aus Ungenauigkeiten in der Rietveld-Verfeinerung. Weiterhin wurde das Modell angewandt, um Alterungsparameter zu bestimmen, die zu reinem Zinkmalachit mit möglichst kleinen Partikeln und somit großer spezifischer Oberfläche führen. Ein Vergleich mit experimentellen Daten bestätigte die Genauigkeit des Modells bei der Bestimmung dieser Optima und lieferte Erklärungen für experimentell bestimmte Temperatur- und pH-Optima aus der Literatur. Darüber hinaus ergaben die Berechnungen einen möglichen Ansatz zur Verwendung von CO_2 als Edukt in der Katalysatorherstellung. Mit diesen Ergebnissen wurde bestätigt, dass die Alterung als ein Prozess zum thermodynamischen Gleichgewicht hin betrachtet werden kann und dass die Zusammensetzung des gealterten Zwischenprodukts unter Verwendung der entsprechenden Fest-Flüssig-Gleichgewichte vorhergesagt werden kann. Daher ist die Entkopplung der kinetisch dominierten Ko-Fällung und der gleichgewichtsgetriebenen Alterung entscheidend, um beide Prozessschritte besser zu verstehen, vorherzusagen und zu optimieren und folglich die Performance des resultierenden Katalysators zu optimieren.

Das dritte Ziel dieser Arbeit war die Entwicklung einer Methode um die langsame Phasenumwandlung während der Alterung zu beschleunigen, um so die Raum-Zeit-Ausbeute zu erhöhen ohne dass dabei die Produktqualität negativ beeinflusst wird. Basierend auf vorherigen Ergebnissen und Literaturstudien wurden das Animpfen der Suspension mit Zinkmalachit-Kristallen und die Maximierung der massespezifischen Partikeloberfläche nach der Ko-Fällung als die vielversprechendsten Ansätze dafür identifiziert. Experimentelle Studien bestätigten, dass die Erhöhung der spezifischen Oberfläche des Ko-Fällungsprodukts die erforderliche Alterungszeit für die Phasenumwandlung halbierte. Der Effekt des Animpfens

war noch ausgeprägter: die erforderliche Alterungszeit wurde im Vergleich zu einer Alterung ohne Animpfen um 40 % bis 90 % reduziert, wenn zwischen 3 und 70 Gew.-% Impfkristalle zugegeben wurden. Bei höher konzentrierten Suspensionen (6 Gew.-% Feststoffe) und mehr als 30 Gew.-% Impfkristalle wurde eine instantane Phasenumwandlung nach der Zugabe erreicht. Auf diese Weise wurde die Raum-Zeit-Ausbeute von Co-Fällung und Alterung im Maximalfall um den Faktor 60 erhöht. Basierend auf den experimentellen Ergebnissen wurde die Hypothese aufgestellt, dass das Animpfen eine kontaktinduzierte Phasenumwandlung auslöst und auf diese Weise den Prozess beschleunigt. Der Vergleich von mit und ohne Animpfen hergestellter Katalysatoren bestätigte, dass das Animpfen erforderlich ist, um die angestrebte Phasenumwandlung in kristallines Zinkmalachit innerhalb einer verkürzten Alterungszeit von 60 Minuten abzuschließen. Ohne Animpfen wurden bezüglich Zusammensetzung und Größe inhomogene Partikel mit reduzierter Oberfläche gebildet, die eine verminderte Methanolproduktivität bei einem ersten Funktionstest aufwiesen. Im Gegensatz dazu zeigte das mittels geimpfter Alterung hergestellte Material eine Katalysatoraktivität, die vergleichbar war mit Katalysatoren mit langer Alterungszeit und einem kommerziellen CZZ-Katalysator. Daher wird das Animpfen für die Alterung uneingeschränkt empfohlen.

Grundsätzlich sind alle Erkenntnisse und Schlussfolgerungen dieser Arbeit auf ähnliche Katalysatorsysteme, die ebenfalls einen Alterungsschritt erfordern, und auf großskalige Prozesse für technische Anwendungen übertragbar. Zu diesem Zweck wurde ein Workflow entwickelt, der eine strukturierte Prozessentwicklung ermöglicht. In ihm werden zunächst systematisch Einflussgrößen identifiziert, um dann modellbasiert die optimalen Prozessparameter für die bestmögliche Katalysatorperformance zu bestimmen. Somit wurde das Hauptziel dieser Arbeit, die Prozessfunktionen der Ko-Fällung und Alterung zu quantifizieren, um eine systematische Prozessentwicklung zu ermöglichen, erfüllt. Für die komplementäre Optimierung der Raum-Zeit-Ausbeute sind das Animpfen und die Intensivierung der Vermischung während der Ko-Fällung probate Mittel. Dieser Ansatz macht die Katalysatorherstellung besser kontrollierbar und effizienter und trägt so zur nachhaltigen Entwicklung der chemischen Industrie bei.

Abstract

The chemical industry faces a major challenge. On one hand, it is indispensable to transition towards a sustainable production and focus on CO_2 neutrality in the immediate future. On the other hand, demand for commodity chemicals derived from non-renewable resources is steadily increasing. For instance, annual methanol production is expected to grow from approximately 100 Mt to 500 Mt by 2050. However, currently, over 99% of methanol is produced via low-pressure catalysis from syngas, which is generated through steam reforming or coal gasification. A promising approach to address this challenge is the production of green methanol from CO_2. However, substituting CO with CO_2 in the catalysis produces large quantities of water as a byproduct, which poisons and deactivates the most commonly used $Cu/ZnO/Al_2O_3$ catalyst. Alternative catalyst compositions, such as $Cu/ZnO/ZrO_2$, may be more suitable for CO_2 based methanol production, but are not yet optimized regarding their performance.

Due to the complexity of the multi-step production process of the catalyst, process parameters are in general chosen and optimized based on broad parameter studies. The process comprises the five key steps co-precipitation, where an initial, amorphous solid is formed from reactant solutions, aging, where this solid transforms into the targeted solid phase zincian malachite ($Cu_{1.46}Zn_{0.54}CO_3(OH)_2$), calcination, where the hydroxycarbonate decomposes into CuO and ZnO, shaping, and reduction, where CuO is reduced to the catalytically active Cu. Obtaining zincian malachite as an intermediate proved to be beneficial for the performance of the final catalyst. Due to its morphology and the defined ordering of Cu and Zn atoms in the crystal lattice, the Cu surface area is maximized which in turn increases productivity and stability. However, fundamental correlations between the process parameters of these individual process steps and the resulting physicochemical characteristics of the intermediate, which determine the later catalyst performance, the so-called process functions, are often unknown. Accordingly, a fundamental understanding of the respective process functions, would be essential for a faster and structured recipe and process adjustment for current and future challenges, such as the switch from CO to CO_2 in the syngas.

Therefore, this work aimed to understand and quantify the respective process functions of the individual process steps in the preparation of Cu/ZnO based catalysts. This should enable a systematic and scalable process design on the one hand and allow the model-based optimization of space-time yield and product quality on the other hand. The focus here was on the in general intertwined process steps co-precipitation and aging as they proved to be detrimental for the resulting catalyst performance.

First, a new preparation routine was to be developed to strictly separate co-precipitation and aging in time and space, allowing individual investigation in contrast to the state-of-the art semi-batch mode of operation. For this purpose, continuous co-precipitation in a mixing nozzle was followed by batch aging in a stirred tank reactor. The energy-intensive mixing in a mixing nozzle, that was in general completed in less than 4 min, enabled micro mixing times below 10^{-4} s and thus the decoupling of the kinetically controlled initial solids formation from mixing influences. The suspension, which was therefore homogeneous in particle size and solid composition between the individual co-precipitate particles, could then be used to conduct aging

studies under defined conditions without any influences by simultaneous co-precipitation or major variances in the aging time in between individual particles.

A comparison of continuous mixing in a mixing nozzle with a state-of-the-art semi-batch co-precipitation in a tank reactor revealed that the mixing method influences the co-precipitate morphology and the final catalyst quality. The newly developed experimental setup enabled a different pH and supersaturation trajectory during initial solids formation resulting in smaller crystallites after aging with a 10 % increase in specific surface area and more homogeneous pore sizes and pore distribution compared to the semi-batch material. This confirmed that co-precipitation is kinetically controlled. These differences persisted through calcination, resulting in a precatalyst with up to three times the specific surface and copper areas, and a more homogeneous Cu and Zn distribution at nanometer scale. Consequently, methanol productivity increased by a factor of three. Varying the total volume flow in the continuous co-precipitation showed that micro mixing time affects initial solids formation. Two regimes were differentiated: for small volume flow rates below 400 $ml \cdot min^{-1}$, respectively micro mixing times above $1.2 \cdot 10^{-4}$ s, mixing limits the available number of lattice ions in the surrounding liquid, decreasing the effective supersaturation which leads to an increase in the median particle size. When a critical volume flow rate was surpassed, mixing did no longer influence the co-precipitate morphology. However, these differences did not persist through aging, as aged intermediates showed no correlation with mixing intensity, resulting in catalysts with similar catalytic activities. This was most probably the result of the homogeneity in particle size and composition across the individual particles prepared in the mixing nozzle which in turn yielded the same aging kinetics for each particle. An ideal preparation process should therefore include a co-precipitation step conducted in the non-mixing influenced regime, ideally continuously, to obtain a homogeneous co-precipitate in terms of particle size and composition and rule out negative influences on the catalyst performance.

Given the significance of obtaining zincian malachite as an intermediate for high-performance catalysts, the main objective for the aging step was to develop a model that predicts phase composition after aging based on key process parameters such as educt composition, pH, and temperature. This model should reduce the number of required parameter studies and help to uncover hitherto unknown process optima. Based on the hypothesis that aging leads to thermodynamic equilibrium, the phase composition should be predictable using a thermodynamic model based on solid-liquid equilibria and hydrochemistry data without kinetic considerations. Accordingly, a model was developed that consists of an activity coefficient model accounting for ion interactions and a mass balance based on solubility products and ion association products. A complementarily developed experimental method made it possible to determine missing solubility data, such as the temperature dependency for synthetic zincian malachite and the solubility of the byproduct $Na_2Zn_3(CO_3)_4 \cdot 3H_2O$ from titration studies. It also confirmed the necessity of separate solubility products for the metastable co-precipitate and the more stable aged intermediate. The model was validated by comparing calculated phase compositions at thermodynamic equilibrium with experimentally determined solid compositions as a function of pH, temperature, and Cu/Zn ratio in the feed solution. The model accurately reproduced phase compositions, such as the presence of the byproducts

rouaite at $pH \leq 5$ and aurichalcite at $T \geq 70$ °C. Deviations between model and measurements likely resulted from uncertainties in the Rietveld refinement. The model was also applied in an optimization study to determine technically feasible process parameters that lead to a pure zincian malachite product with possibly small particles and thus large surface areas. A comparison with experimental data confirmed the accuracy of the model and provided explanations for temperature and pH optima previously found in the literature. Furthermore, it provided a possible approach for using CO_2 as a value-adding educt in future catalyst preparations. With these results it was confirmed, that aging can be considered a process towards thermodynamic equilibrium, and that the composition of the aged intermediate can be predicted using the corresponding solid-liquid equilibria. Thus, decoupling the kinetically dominated co-precipitation and the equilibrium-driven aging, is crucial to better understand, predict, and optimize both process steps and, consequently, the resulting catalyst.

The third objective was to develop a method to accelerate the slow phase transformation during aging without negatively affecting product quality, thus increasing the space-time yield of the aging step. Based on preliminary results and the literature, seeding the suspension with zincian malachite crystals and maximizing the mass-specific surface area of particles after co-precipitation were identified as the most promising approaches. Experimental studies confirmed that increasing the specific surface area of the co-precipitate through intense mixing halved the required aging time for phase transformation. The effect of seeding was even more profound as the required aging time was decreased between 40 % and 90 % compared to a preparation without seeding when 3 wt.% to 70 wt.% seeds were added. For higher concentrated suspensions (6 wt.% solids) and more than 30 wt.% seeds, an instantaneous phase transformation after mixing the co-precipitate suspension with the seeds was achieved. This way, seeding multiplied the space-time yield of aging and precipitation by up to a factor of 60. Based on these results, seeding is believed to promote the contact-mediated phase transformation. Comparing precatalysts from seeded and unseeded preparations confirmed that seeding is required to complete the targeted phase change to crystalline zincian malachite within a reduced aging time of 60 min. Without seeding, inhomogeneous particles in terms of particle size and composition at nanoscale with reduced surface area were formed that exhibited a diminished methanol productivity in a first functional test. In contrast, the material from seeded preparations exhibited a catalytic activity comparable to those of catalysts from unseeded preparations and a commercial CZZ catalyst. Thus, seeding is recommended without restrictions.

In principle, all findings and recommendations of this work are transferable to similar catalyst compositions requiring an aging step and to larger scales for technical application. A workflow that was developed based on the results shall enable a structured process development by systematically identifying influencing variables and providing optimal preparation parameters for the best catalyst performance. Thus, the main objective of this work, to quantify the process functions of co-precipitation and aging to enable a systematic process design, was fulfilled. For complementary space-time yield optimization, seeding or intensification of mixing during co-precipitation is recommended. This approach makes catalyst preparation more controllable and efficient, contributing to the sustainable transition of the chemical industry.

Contents

Acronyms and symbols

Acronyms

AGW	Institute of Applied Geosciences
AOC	Institute for Inorganic Chemistry
BET	Brunauer-Emmett-Teller theory
CHNS analysis	Element analysis of C, N, H and S
Cont	Continuous
CO_x	Entirety of CO and CO_2
CZ catalyst	Cu/ZnO based catalyst
CZA catalyst	$Cu/ZnO/Al_2O_3$ catalyst
CZZ catalyst	$Cu/ZnO/ZrO_2$ catalyst
DLS	Dynamic light scattering
DME	Dimethyl ether
EDXS	Energy dispersive X-ray spectroscopy
F-AES	Flame atomic emission spectrophotometry
FIB	Focused ion beam
FT-IR	Fourier transformed infrared spectroscopy
GHSV	Gas hourly space velocity
ICP-OES	Inductively coupled plasma optical emission spectroscopy
IKFT	Institute of Catalysis Research and Technology
LEM	Laboratory for Electron Microscopy
M	Motor
MeOH	Methanol
NRMSE	Normalized Root Mean Square Error
p.a.	Per analysis (degree of purity)
PDR	Differential pressure recording
PSD	Particle size distribution
PXRD	Powder X-ray diffraction
QR	pH recording
SB	Semi-batch
SEM	Scanning electron microscopy
SLS	Static light scattering

TCD	Thermal conductivity detector
TCR	Temperature control and recording
TEM	Transmission electron microscopy
TPR	Temperature-programmed reduction
XRD	X-ray diffraction
XRF	X-ray fluorescence

Dimensionless numbers and constants

$Re = u \cdot L_c \cdot (\nu_{fl})^{-1}$		Reynolds number
R	Universal gas constant	8.314 $\mathrm{J\ (mol\ K)^{-1}}$

Latin symbols

a	Molality based activity	$\mathrm{mol\ kg^{-1}}$
a	Lattice constant	Å
$b_{x,y}$	Molality of component x in y	$\mathrm{mol\ kg^{-1}}$
b	Lattice constant	Å
c	Lattice constant	Å
$c_{x,y}$	Concentration of component x in y	$\mathrm{g\ L^{-1}}$
$\tilde{c}_{x,y}$	Molar concentration of x in y	$\mathrm{mol\ L^{-1}}$
d	Diameter	m
$GHSV$	Gas hourly space velocity	$\mathrm{s^{-1}}$
h	Height	cm
I	Ionic strength	$\mathrm{mol\ (kg_{H_2O})^{-1}}$
K_{IA}	Ion association constant	$(\mathrm{mol\ L^{-1}})^{\sum_k \nu_{i,k}\ -1}$ *or* $\left(\mathrm{mol\ kg_{H_2O}}^{-1}\right)^{\sum_k \nu_{i,k}\ -1}$
K_{SP}	Solubility product	$(\mathrm{mol\ L^{-1}})^{\nu_\pm}$ *or* $\left(\mathrm{mol\ kg_{H_2O}}^{-1}\right)^{\nu_\pm}$
L_c	Characteristic length	m
$\widetilde{M}$	Molar mass	$\mathrm{g\ mol^{-1}}$
m	Mass	g
$\dot{m}$	Mass flow	$\mathrm{g\ min^{-1}}$
N	Amount (e.g. samples or experiments)	−
n	Stirrer speed	$\mathrm{min^{-1}}$

n	Amount of substance	mol
$\dot{n}_i$	Molar flux of component i	$\mathrm{mol\ s^{-1}}$
$NRMSE$	Normalized Root Mean Square Error	$-$
P_{MeOH}	Methanol productivity	$\mathrm{g_{MeOH}\ (kg_{cat}\ h)^{-1}}$
p	(Absolute) pressure	mbar
pH	pH value	$-$
S	Surface area	$\mathrm{m^2\ g^{-1}}$
S_j	Supersaturation of the phase j	$-$
S_{MeOH}	Selectivity towards methanol	$\mathrm{mol\%}$
T	Temperature	$\mathrm{°C}$
t	(Process) time	min
$t_{\mathrm{age,min}}$	Required aging time to complete phase transformation	min
u	Velocity	$\mathrm{m\ s^{-1}}$
V	Volume	L
$\dot{V}$	Volume flow	$\mathrm{ml\ min^{-1}}$
$X_{\mathrm{CO_x}}$	CO_x conversion	$\mathrm{mol\%}$
$X_{a,b}$	Loading of a in phase/stream b	$\mathrm{g\ kg^{-1}}$
x	Particle size	nm
$x_{50,3}$	Median particle size	nm
$x_{a,b}$	Mass fraction of component a in phase/stream b	$\mathrm{wt.\%}$
$\tilde{x}_{a,b}$	Molar fraction of component a in phase/stream b	$\mathrm{mol\%}$
$\tilde{x}_{\mathrm{Zn,zm}}$	Molar zinc fraction in relation to the total metal amount in zincian malachite	$\mathrm{mol\%}$
Y_{ST}	Space-time yield	$\mathrm{g\ (L\ h)^{-1}}$

Greek symbols

β	Lattice constant	°
$\Delta m_{\mathrm{age,dry}}$	Dry mass of formed solids	g
Δp_{Mix}	Pressure drop due to mixing	mbar

$\Delta_r\tilde{h}_{298\,K}$	Standard reaction enthalpy	$\mathrm{kJ\ mol^{-1}}$
$\bar{\varepsilon}$	Mean energy dissipation rate	$\mathrm{W\ kg^{-1}}$
η	Dynamic viscosity	$\mathrm{mPa\ s}$
θ	Diffraction angle	°
ρ	Density	$\mathrm{kg\ L^{-1}}$
σ	Electrical conductivity	$\mathrm{\mu S\ cm^{-1}}$
σ	Standard deviation	*miscellaneous*
τ_{micro}	Micromixing time	ms
ν	Kinematic viscosity	$\mathrm{m^2\ s^{-1}}$
ν	Stoichiometric coefficient	$-$
$\tilde{\nu}$	Wavenumber	$\mathrm{cm^{-1}}$
ξ	Pressure loss coefficient	$-$

Subscripts

$\pm$	Combined value (electrolyte)
0	Reference value/ standard conditions
age	Aging
aur	Aurichalcite
BET	According to the BET theory/ by physisorption
c	Characteristic
calc	Calculated
cat	Catalyst
cont	Continuous
CO_x	Sum of CO and CO_2
crit	Critical
Cu	Copper
eff	Effective
eq	Equilibrium
exp	Experimental
fl	Fluid
geo	Georgeite
hyd	Hydrozincite
i	Ion i

init	Initial
inlet	Inlet jet into the mixing chamber of the mixing nozzle
j	Solid phase *j*
k	Complex/ ion associate *k*
M	Metals
mal	Malachite
max	Maximum
meas	Measurement
min	Minimum
Mix	Mixing chamber
NaZn	$Na_2Zn_3(CO_3)_4 \cdot 3\ H_2O$ phase
prec	(Co-)precipitation
real	Actual value
ref	Reduction
ros	Rosasite
SB	Semi-batch
set	Set value
SLS	Determined by SLS
susp	Suspension
tank	Tank reactor
tot	Total
turb	Turbulent
XRD	Determined by XRD evaluation/ Rietveld refinement
zg	Zincian georgeite
zm	Zincian malachite

Superscripts

*	Saturated state
0	Reference state
aq	Dissolved (in the liquid phase)
l	Liquid (phase)
N	Normal conditions (298.15 K, 1.013 bar)
s	Solid (phase)

1 Application and preparation of Cu/ZnO based catalysts

1.1 Motivation and state of the art

The chemical industry is in a predicament. On the one hand, there is a push to become as sustainable and CO_2 neutral as feasible in the imminent future. On the other hand, the demand for commodity chemicals derived from non-renewable resources continues to rise: for instance, the annual methanol (MeOH) production is predicted to rise from currently around 100 Mt to 500 Mt in 2050[1,2]. One of the main drivers for this development is its use for the production of synthetic fuels in power-to-liquid processes via dimethyl ether (DME), cf. Eq. (1.4)[3–5]. Yet, as of now, more than 99% of MeOH is produced in a low-pressure catalysis from syngas synthesized either from steam reforming or coal gasification, cf. Eq. (1.1)[1,6–9].

$$\mathrm{CO} + 2\,\mathrm{H_2} \leftrightarrow \mathrm{CH_3OH} \qquad \Delta_\mathrm{r}\tilde{h}_{298\,\mathrm{K}} = -90.6\ \mathrm{kJ\ mol^{-1}} \tag{1.1}$$

$$\mathrm{CO_2} + 3\,\mathrm{H_2} \leftrightarrow \mathrm{CH_3OH} + \mathrm{H_2O} \qquad \Delta_\mathrm{r}\tilde{h}_{298\,\mathrm{K}} = -49.1\ \mathrm{kJ\ mol^{-1}} \tag{1.2}$$

$$\mathrm{CO_2} + \mathrm{H_2} \leftrightarrow \mathrm{CO} + \mathrm{H_2O} \qquad \Delta_\mathrm{r}\tilde{h}_{298\,\mathrm{K}} = 41.0\ \mathrm{kJ\ mol^{-1}} \tag{1.3}$$

$$2\,\mathrm{CH_3OH} \leftrightarrow \mathrm{C_2H_6O} + \mathrm{H_2O} \qquad \Delta_\mathrm{r}\tilde{h}_{298\,\mathrm{K}} = -23.4\ \mathrm{kJ\ mol^{-1}} \tag{1.4}$$

One promising approach to resolve the dilemma in this particular case is to manufacture green MeOH from CO_2 according to Eq. (1.2). Here, CO_2 originates from industrial point sources and H_2 is formed, for instance, by electrolysis powered by wind or solar energy[10–14]. However, by replacing CO with CO_2, large quantities of water are produced as a byproduct in the low-pressure catalysis at 230 to 300 °C and 50 to 100 bar, cf. Eqs. (1.2) and (1.3). H_2O then adsorbs at the catalyst surface which poisons and deactivates the $Cu/ZnO/Al_2O_3$ (CZA) catalyst that is typically used[8,10,15,16]. Additionally, the reaction is less exothermic compared to the reaction from CO which may facilitate the reactor design as less heat needs to be dissipated. Accordingly, the risk of hotspot formation is mitigated[17,18]. In their recent, fundamental review Beck et al. concluded that understanding the exact mechanisms of methanol synthesis and deactivation are two of the open key questions regarding CZA catalysts[8]. Alternative catalyst compositions, such as $Cu/ZnO/ZrO_2$ (CZZ), may be better suited for the production of methanol from CO_2 as ZrO_2 is less hydrophilic than Al_2O_3 and thus, poisoning of the catalyst is mitigated[10,19] and productivity is improved[10,19–23]. Another theory involves the concurrent adsorption of CO_2 on ZrO_2 and H_2 on adjacent Cu crystallites which facilitates the formation of formate species as intermediate towards MeOH[18,24–26], which is not evident for Al_2O_3[26]. In either case, a loss of productivity over time on stream[20] as well as reversible[27] and irreversible[28] deactivation processes also happen for CZZ catalysts. Looking at the decade long research on methanol synthesis, which is still ongoing, deactivation processes will remain a big challenge in the foreseeable future[8,29].

Thus, the catalyst has to be replaced regularly. It has to be replaced even more frequently, if methanol synthesis is conducted from CO_2[29,30]. Consequently, for a sustainable methanol economy in the future, the optimization of the catalysis regarding the catalyst performance and longevity alone is not sufficient. Instead, it has to go hand in hand with the development of efficient production processes for high-performance catalyst materials. These processes also need to be suited for scale-up, in order to be able to meet the expected demand in MeOH, and

be flexible enough to accommodate new insights in necessary properties for an optimized performance[31]. Still, the research of enhanced and industrially applicable preparation approaches for CZ catalysts is often neglected as is evident from the limited number of publications on this matter in the current decade[32–35]. Similarly, the focus of recent reviews is on the progress of understanding the mechanisms of catalysis and deactivation and mention the preparation only briefly[8,9].

In general, the most important catalyst properties to ensure a high methanol productivity[36–38], selectivity[39] and lifetime[40] are the specific surface area, the surface area of copper, which forms the catalytically active sites, and the periodic and finely distributed arrangement of Cu and ZnO crystallites[36,37,41], as also plotted schematically in Figure 1.1. ZnO prevents the sintering of single Cu crystallites at the high temperatures necessary for catalysis ($T > 200$ °C) and presumably enhances MeOH productivity and selectivity due to chemically bound interfaces of Cu and ZnO[37,38]. A fine dispersion of the promoter, here Al_2O_3 or ZrO_2, further improves the activity and stability[42,43]. In general, Cu and ZnO crystallites are targeted to be in the size range of 2 to 10 nm[10,43,44]. Accordingly, a homogeneous metal composition on the one- to two-digit nanoscale is key to obtain copper surface areas and interface areas as large as possible. Furthermore, the pore characteristics of the catalyst can be decisive since they influence gas diffusion to the active sites[45–47].

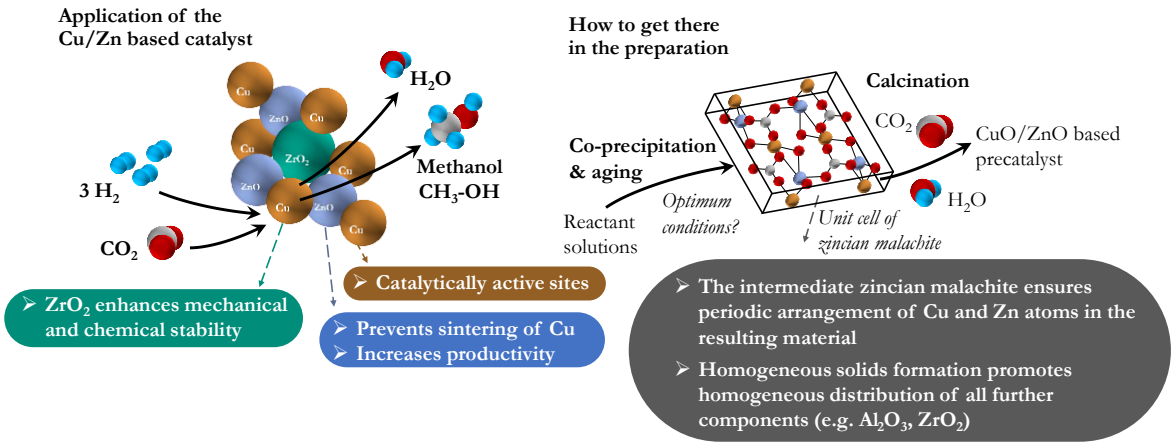

Figure 1.1: Schematic visualization of the roles of components in methanol synthesis and how the target properties can be obtained.

Thus, the primary goal of each preparation is to meet these requirements. Spray-pyrolysis is one approach to achieve small crystallites and large surface areas[48–50]. However, two major downsides are that particle formation is difficult to adapt as there is a limited number of process variables and that Cu and ZnO tend to form separate clusters leading to worse performance compared to a precipitation approach[51,52]. The preparation of Cu/ZnO catalysts was also realized via a sol-gel process[53,54] and impregnation[55–57], but only at lab scale.

Accordingly, the main approach considered scientifically and industrially is a multi-step preparation based on the simultaneous precipitation of all metals as oxides, hydroxides or hydroxycarbonates from an aqueous metal nitrate solution and a sodium carbonate solution [18,31,58–62]. This simultaneous precipitation of multiple metals and/or multiple solid phases is also referred to as co-precipitation and is depicted in Figure 1.2. Alternatively, one of the components, e.g. Al_2O_3 or ZrO_2, is provided as a carrier in a suspension and the remaining

metals are (co-)precipitated subsequently[56,63]. A variety of studies showed that by forming the mineral phase zincian malachite ($[Cu_{1-\tilde{x}_{Zn,zm}}Zn_{\tilde{x}_{Zn,zm}}]_2(CO_3)(OH)_2$) as a precursor during the preparation of the catalyst, all of the properties previously mentioned, and, thus, the catalyst performance in methanol synthesis, are improved[31,37,38,41,64]. This results from the periodic arrangement of Cu and Zn atoms in the crystal lattice of said phase[65]. Zn fractions as close to the thermodynamically limited maximum values as possible ($\tilde{x}_{Zn,zm} \leq 27$ mol%[66] or $\tilde{x}_{Zn,zm} \leq 31$ mol%[67]) proved to be particularly advantageous for large copper surface areas and copper/zinc interfaces that remain intact under the catalysis conditions and, thus, benefit the methanol productivity[67,68]. In addition, the needle-like morphology of the crystals, which aggregate to spherical entities, results in large surface areas and beneficial pore sizes[37,38,41,64].

However, direct co-precipitation of zincian malachite from the aqueous reactant solutions is not possible, probably due to kinetic constraints[67,69,70]. Instead, the mixing of the two educt solutions results in an amorphous precursor with a spherical morphology and separate Cu and Zn phases that co-precipitate within milliseconds to seconds[43,64,70–72]. The calcination of this precursor yields a catalyst with low specific surface area and Cu area and, consequently, a comparatively poor productivity[43,64,73,74].

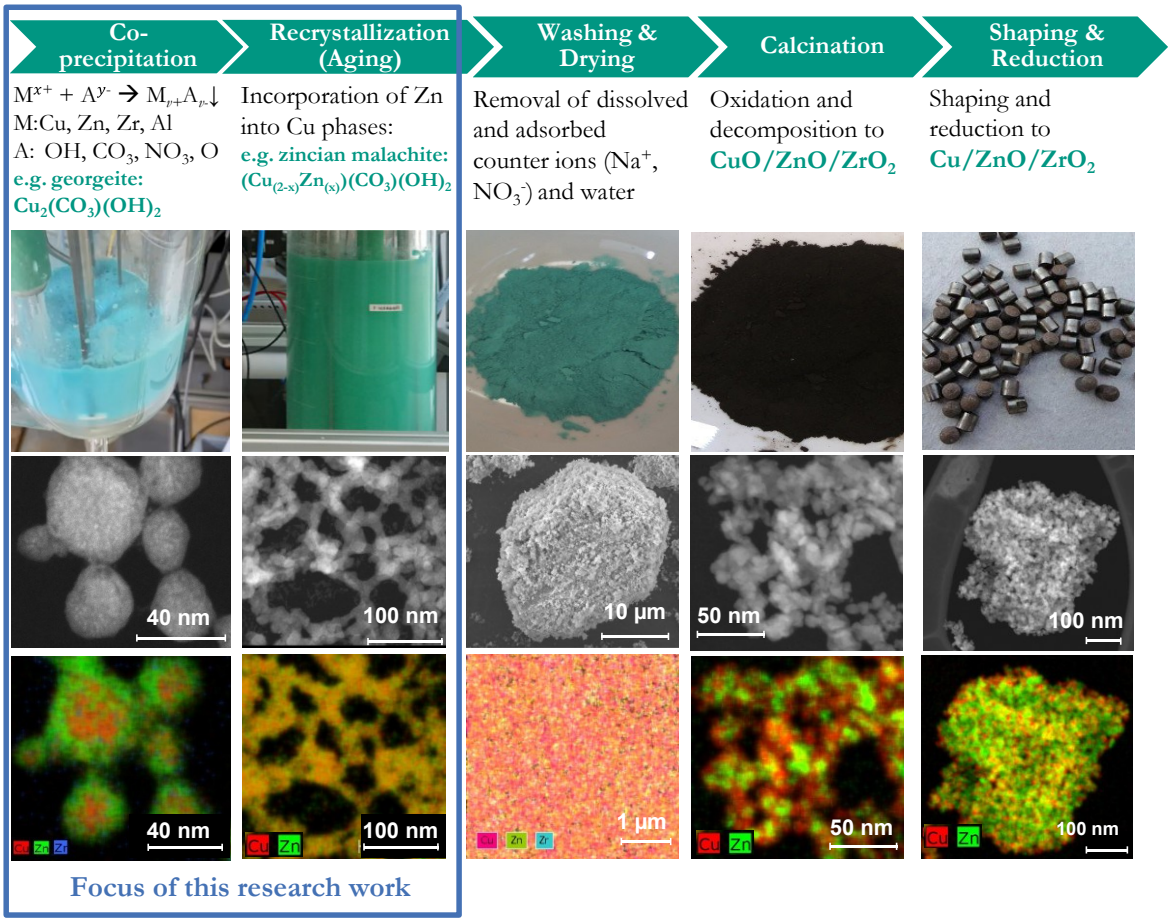

Figure 1.2: Key process steps in the preparation of Cu/Zn based catalysts showing photographs of the respective product (upper image), the respective particle morphology (center) and the metal distribution (bottom).

Therefore, an aging step is carried out so that the amorphous precursor turns into zincian malachite, most probably by incorporating Zn^{2+} ions from the solution[75,76] or by recrystallization[43,64,74,77,78]. For this purpose, the suspension is stirred at $30\,°C \leq T \leq 70\,°C$ and

$5 \leq pH \leq 9$[31,36,59,68,77,79] until the phase change is completed. Depending on composition, reactor design and solids concentration, the transformation can take between 15 minutes and several hours[36,61,64,72,74,75,78–81]. Deviating from the optimum conditions can result in the increased formation of byproducts that contain Na^+ and NO_3^- ions from the educt salts[36,43,78,82], lead to solids with different Cu/Zn ratios or separate Cu and Zn phases[64,72,78,82] or change the particle size[61,83]. This affects the catalyst negatively as it leads to a decrease of BET surface area, Cu surface area, stability and methanol productivity of the resulting catalyst[36,61]. Thus, for a high-quality catalyst, it is essential to meet the specifications and obtain zincian malachite as the main aging product[18,31,68].

Despite the importance of a defined aging product, the preceding co-precipitation also seems to affect the characteristics of the resulting catalyst. Studies by Jiang et al.[35,84,85] showed that different mixing geometries and mixing intensities in the co-precipitation affect the Cu/Zn distribution within the co-precipitate on the nanometer scale and, subsequently, the microstructure of the final catalyst. Furthermore, changing from a semi-batch to a continuous co-precipitation improved the physicochemical properties of CZA catalyst precursors and, in particular, the subsequent catalyst performance[73,86]. In contrast, Simson et al. and Hartig et al. found no significant differences in catalyst precursors prepared by batch co-precipitation in a stirred tank reactor and precursors from a continuous co-precipitation in a micromixer at different energy dissipation rates, respectively[59,71]. Accordingly, the role of mixing and local energy dissipation rates in co-precipitation in the preparation of catalysts is still disputed.

One main challenge for process optimization is that, in general, co-precipitation and aging of the catalyst precursor are conducted as a single semi-batch process in a stirred tank reactor[31,36,87]. In this case, co-precipitation and aging overlap in time and space because the supply of reactants requires several minutes. Thus, freshly precipitated particles and particles which have already aged for up to 20 to 60 min[44,88,89], coexist. This is the reason why influences of co-precipitation and, to some extent, aging on catalyst properties are often summarized under the term "chemical memory"[31,36,78,85,90]. The locally limited supply of both reactant solutions (metal nitrates and Na_2CO_3) and the inhomogeneous mixing conditions in stirred tank reactors also contribute to the spatial inhomogeneity of the co-precipitation and aging parameters. For these reasons, it is quite challenging, if not impossible, to fully control the co-precipitate homogeneity at nanoscale as well as in between individual particles and the repeatability of its preparation[89,91].

A second key challenge for process optimization is that the optimum conditions for aging depend very much on the reactants used[59,82] and the target catalyst composition[59,92,93] which, as described earlier, may change for the future use of syngas rich in CO_2. While validated models exist for the precipitation step[60,71], no such models which could predict the phase composition as a function of process parameters are available for the aging step. Thus, the optimization of process parameters for the preparation of CZA catalysts based on several decades of parameter studies would have to be repeated for CZZ catalysts as they function differently in methanol synthesis[94] and may require other particle properties for maximum activity.

The aforementioned long aging time of often several hours[36,61,64,72,74,78], that is necessary to complete the phase transformation, is the third principal challenge for an efficient catalyst preparation. Milliliter-scale experiments by Güldenpfennig et al. indicated that the phase transformation consists of an extended induction phase until first zincian malachite particles are present, and then a short transformation period until recrystallization is completed[75]. The data suggests that the induction phase may be accelerated by seeding or adjusting the metal composition. However, these approaches were not verified at larger scales or in the preparation of ready-to-use catalysts. In general, there is a noticeable pH minimum[31,72,78,79,81] and a shift in the color from blue to green[78,79] that go along with the phase transition from (zincian) georgeite to zincian malachite. This information, along with other techniques like XRD or FT-IR analysis[72,78], can be used to verify that aging is completed.

After aging is completed, the aged particles are filtered, washed to remove any Na^+ and NO_3^- residues that are adverse for catalyst performance and lifespan[72,95,96], and dried[31,97]. Upon the subsequent calcination, the aged precursor decomposes into CuO and ZnO, as well as ZrO_2 and/or Al_2O_3, forming the precatalyst while retaining the distinctive pore characteristics and an advantageous arrangement of Cu and Zn atoms on the nanoscale[64,98]. Finally, the material is formed, and CuO is reduced to Cu[31,99], yielding a catalytically active material with an enhanced surface area, nano-homogeneity, and nano-dispersity due to the intermediary phase, zincian malachite.

In summary, the efficient preparation of high-quality Cu/ZnO based catalysts is highly important for a sustainable methanol economy in the future. The preparation itself is a complex multi-step process with a manifold of individual parameters that influence not only the physicochemical properties of the respective intermediates, but also affect the resulting catalyst properties and performance. A step-by-step analysis of these multiple, partly overlapping process functions is time-consuming and resource-intensive. This is why parameter studies were and are the main approach in the literature to optimize preparation parameters instead of a fundamental, knowledge-based approach. This has two downsides: first, if the requirements for the catalyst change, as is the case now, detailed parameter studies will again be necessary in order to adapt the preparation to precisely these new specifications, in particular a composition that is more suitable for methanol production from CO_2. Second, a scale-up of the process steps to industrial scales, in particular those which are dominated by local effects, namely co-precipitation, is prone to failure without knowledge of the respective process function. Thus, a knowledge-based approach to understand, model and optimize the product quality-determining process steps will be key to brace the preparation of Cu/ZnO catalysts for a climate-neutral chemical industry and further future challenges.

1.2 Aim and scope of this work

In the state of the art discussed above, the importance of an optimized catalyst preparation for the future of a sustainable methanol economy was analyzed. Depending on the application and the composition of the feed gas used therein, the most suitable catalyst composition changes, e.g. CZA for syngas rich in CO or CZZ for syngas rich in CO_2. The greatest common denominator is the combination of Cu and ZnO (CZ) as the two main components, which is

used in approx. 60 % of all publications on methanol catalysts and in the absolute majority of industrial processes[9]. Since the results of this work are intended to be as widely applicable as possible and since the interaction of the Cu and ZnO precursors plays a key role in catalyst production, the focus is therefore on CZ catalysts as a model material system. In addition, the composition CZZ is considered, as it could assume a pivotal position in the conversion of MeOH synthesis to a CO_2 based industry[9,18,94]. By comparing the results for the simplified CZ system with the more complex CZZ composition, the transferability of the results can be evaluated. A transfer to further compositions, e.g. CZA, should then be possible with minor adjustments, as the process design of (co-)precipitation and aging is dominated by the interaction of the Cu and Zn precursors and zincian malachite as the key intermediate. Other metal precursors only play a subordinate role due to their lower mass fraction of typically $\leq$ 10 wt.%.

The available literature makes it clear that the catalyst performance results from an interconnected web of a multitude of parameters of the involved process steps. Three key challenges for the scalable preparation of high-quality Cu/ZnO based catalysts were identified. Accordingly, this work focusses on the following three topics.

I. How can the process steps co-precipitation and aging be separated in time and space to determine the role of co-precipitation in the preparation of defined catalysts?

The first step to enable a knowledge-based and scalable process optimization is to understand the correlation between the various process parameters and the resulting physicochemical properties for each individual process step considered. Here, co-precipitation and aging are investigated for these two process steps appear to have the highest impact on the resulting catalyst quality if conditions are varied[18,31,36,61]. For this purpose, the state-of-the-art process is to be modified as discussed in Section 2.3 with the ultimate goal to separate co-precipitation and aging, as well as their respective process functions, and to prevent any overlap.

Then, using the modified process, the roles of co-precipitation and local mixing effects during initial solids formation for the preparation of high-quality catalysts with defined properties will be investigated in Section 3 on the examples of a generalized CZ composition and CZZ catalysts. The evaluation of these results will show which key parameters of co-precipitation have to be considered for scale-up.

II. Is it possible to predict the solid phase composition after aging as a function of selected process parameters?

The separation of co-precipitation and aging will also make it possible to investigate aging separately from co-precipitation in Section 4. Due to the well-established importance of zincian malachite as the target phase for high-performance Cu/ZnO based catalysts[18,31,68], the focus will be to develop a model which enables the prediction of the phase composition after aging in dependence of key process parameters such as reactant composition, pH and temperature. Based on the vastly different times scales of solids formation in co-precipitation[43,64,70,72] and phase transformation during aging[36,61,64,72,74,78], it is hypothesized that aging leads to thermodynamic equilibrium and that, accordingly, the phase composition can be described with a corresponding model without kinetic consideration. The goal is to develop such a model,

validate it with the experimental setup described in Section 2.3 and evaluate this hypothesis. Ideally, this model approach may reduce the number of parameter studies needed for future process developments and reveal so far unknown process optima.

III. What are feasible methods for accelerating the aging step and, thus, for increasing the space-time-yield of catalyst preparation that simultaneously allow a process scale-up and maintain the product quality?

According to the literature, the aging step is essential to form zincian malachite[43,70,72], which ensures a homogeneous distribution of small Cu and ZnO crystallites in the calcined precatalyst on the one- to -two-digit nanometer scale, which, in turn, guarantees the production of a high-performance catalyst[18,31,68]. However, it comes with the economic and ecological downside that the aging suspension has to be stirred and heated for prolonged process times of more than 90 min until the phase transformation to zincian malachite is completed[36,61,64,72,74,78]. Thus, this work aims at developing a method to accelerate the phase transformation without negatively influencing the resulting product quality, cf. Section 5. One approach suggested in literature is an optimization of the preceding co-precipitation step to ensure a starting material for aging that is uniform in size, homogeneous regarding the composition at nano- and microscale and as fine as possible[85]. Other studies suggest to adjust the aging parameters (metal ratio, temperature, pH)[72,75,79,100] or to seed the freshly precipitated suspension with readily aged zincian malachite particles[75]. In the scope of this work these approaches are to be adapted, evaluated regarding their impact on aging kinetics and product quality, and optimized. This way, the space-time-yield of catalyst preparation should be increased which would help to meet the projected increase in demand for methanol catalysis from CO_2.

The overarching goal is to find answers to these three main questions. By doing so, this work will enable the scalable preparation of performant Cu/ZnO based catalysts with precisely defined properties. This way, it will hopefully contribute to preparing the methanol economy for the future challenges of a sustainable chemical industry and beyond.

2 Materials and methods

This chapter provides information on the materials used, the experimental setups applied and the analytical methods utilized. First, the various intermediates that are present in the multi-step preparation process are defined in Section 2.1 to establish a consistent terminology.

2.1 Definition of precursors, intermediates and products

Figure 2.1 provides an overview of the complete preparation process starting from the feed solutions and ending with the ready-to-use catalyst with a focus on the microstructure of the respective (intermediate) products. For a simplified visualization, a binary Cu/ZnO catalyst is represented since the interaction of these two components dominate the chemistry in co-precipitation and aging as well as the performance of the catalyst in methanol synthesis[31,68]. A third component, e.g. ZrO_2 or Al_2O_3 would precipitate concurrently or be added as a solid with the soda feed. The figure also includes the nomenclature of the intermediates chosen for this work.

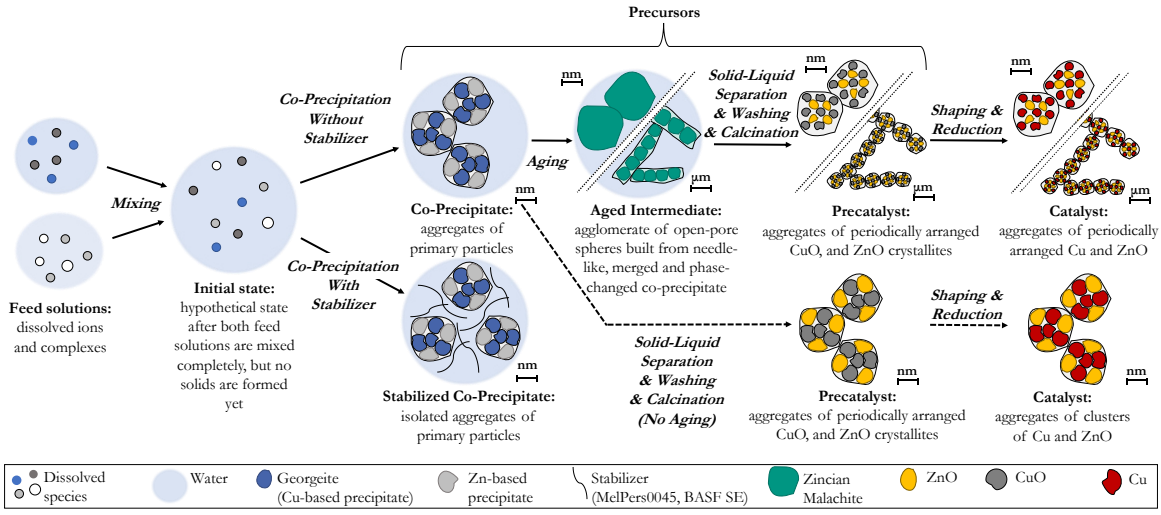

Figure 2.1: Evolution of microstructure and composition of the catalyst precursors during the multi-step preparation of Cu/ZnO based catalysts. The microstructure of the aged intermediate, precatalyst and catalyst are shown at two different size scales as indicated by the double dotted line. Based on Guse et al.[101].

In accordance with the emphasis of this work, the focus is on the precursors after initial solids formation by co-precipitation, the co-precipitate, and after the phase transformation by aging, the aged intermediate. In contrast, the processing steps solid-liquid-separation, washing and calcination as well the refinement steps shaping and reduction are combined. In the context of this work, the term '<u>precursor</u>' is used as a collective term. The following precursors and products are distinguished:

- The two <u>feed solutions</u> with the readily soluble metal nitrates respectively Na_2CO_3 or $NaHCO_3$ as the precipitant.
- The solutions are mixed to initiate solids formation. For the model-based determination of supersaturation, cf. Section 4, a hypothetical, <u>initial state</u> is assumed where both solutions are mixed completely, but no solids are formed yet. This state can be approached experimentally by minimizing the micromixing time, cf. Section 3.

- The metastable, initially present solids directly after co-precipitation consist of spherical aggregates of primary particles, cf. Section 3.3. They are defined as the co-precipitate. For the purpose of analyzing co-precipitation separately from aging, a stabilizer can optionally be added to better preserve the metastable co-precipitate and to prevent the formation of a net-like aggregate from the initially spherical particles, cf. Figure 2.4 and Figure 3.11. This results in the stabilized co-precipitate. For the purposes of this schematic diagram a homogeneous co-precipitate at nano- and micrometer scale is assumed.
- Afterwards, aging is conducted and it results in the aged intermediate: open-pore spheres at the micrometer scale which tend to agglomerate. They consist of intergrown needles that are built from merged and phase-changed nano-sized co-precipitate particles[36,64,88]. The schematic composition of the aged intermediate is illustrated at two scales which are divided by a double dotted line. This morphology is also evident in the SEM images in Figure 3.3 and Figure 3.12.
- Following the further processing steps, the precatalyst is obtained which is an aggregate of periodically arranged CuO and ZnO crystallites, cf. Figure 3.4 and Figure 5.10.
- By means of a reduction CuO is reduced to Cu to form the catalytically active product: the Cu/ZnO based catalyst.

Alternatively, if aging was skipped, e.g. by direct calcination after initial co-precipitation and solid-liquid separation[81], a catalyst with the same chemical composition, but with a much less homogeneous composition at nanoscale[43] and a smaller specific Cu surface area would result[64,73]. This is illustrated by the alternative process path (dashed line). By skipping aging, no zincian malachite is formed so that Cu and Zn tend to form separate phases. As a result, CuO and ZnO crystallites tend to increase in size compared to a process with an aging step[43,72].

2.2 Substances and material data

The intermediates and catalysts were prepared from nitrate salts, the most common educts in the preparation of Cu/ZnO based catalysts[102]. The key chemicals used for the studies, together with their purities and physicochemical properties, are listed in Table 2.1.

Table 2.1: List of key chemicals and their data used in this work.

Chemical	Molecular formula	$\tilde{M}$ (g·mol^{-1})	Purity (%)	Supplier	Verified composition*
Copper(II) nitrate trihydrate	$Cu(NO_3)_2{\cdot}3H_2O$	241.62	≥ 99.5	Merck	$Cu_{1.00}(NO_3)_{1.95}(CO_3)_{0.05}{\cdot}2.6\ H_2O$
MelPers0045 (polycarboxylate ether in water)	-	-	-	BASF SE	-
Sodium bicarbonate (sodium hydrogen carbonate)	$NaHCO_3$	84.01	≥ 99	Carl Roth GmbH	$NaHCO_3$
Nitric acid (65 %)	HNO_3 (in H_2O)	63.01	≥ 99.5	Carl Roth GmbH	64.8 wt.% HNO_3
Sodium carbonate	Na_2CO_3	105.99	≥ 99	Carl Roth GmbH	Na_2CO_3
Sodium hydroxide	NaOH	39.997	≥ 98	Carl Roth GmbH	$Na(OH)_{0.97}(CO_3)_{0.02}\cdot 0.08\ H_2O$
Zinc(II) nitrate hexahydrate	$Zn(NO_3)_2{\cdot}6H_2O$	297.47	≥ 99	Alfa Aeser	$Zn_{1.00}(NO_3)_{1.95}(CO_3)_{0.05}{\cdot}5.7\ H_2O$
Zirconium(IV) oxynitrate hydrate	$ZrO(NO_3)_2{\cdot}6H_2O$	339.32	≥ 99	Sigma-Aldrich	$ZrO_{1.00}(NO_3)_{1.95}(CO_3)_{0.05}{\cdot}6.5H_2O$

* The composition was analyzed by a combination of XRD, ICP-OES and CHNS.

The chemical composition was verified by combining XRD, ICP-OES and CHNS analysis. For this purpose, the measured weight fractions were converted into a hypothetical sum formula and compared with the manufacturer's specifications. The nitrate salts and sodium carbonate are prone to hygroscopy and tend to deliquesce or to form hydrates[103,104]. Thus, they were stored at defined conditions in desiccators. Their masses and compositions were controlled regularly and a deviation of less than 0.5 wt.% was found in each case over the course of eight weeks.

The key equations describing solids formation and their respective equilibria constants applied in this work are summarized in Table 2.2 for further reference.

Table 2.2: Selection of key solid phases, their reaction equations and solubility products.

Phase	Reaction equation	$\log\,(K_{SP}(298\ K)\ /\ (mol\ L^{-1})^{\nu_\pm})$	$\Delta_r\tilde{h}_{298\,K}$ / (kJ mol^{-1})
Aurichalcite	$Zn_{2.9}Cu_{2.1}(CO_3)_2(OH)_6^{(s)} \leftrightarrow 2.9\ Zn^{2+(aq)} + 2.1\ Cu^{2+(aq)} + 2\ CO_3^{2-(aq)} + 6\ OH^{-(aq)}$	-76.16*	-292.4*
Copper hydroxide	$Cu(OH)_2\ (s) \leftrightarrow Cu^{2+}(aq) + 2\ OH^-(aq)$	-19.32**	55.2**
Gerhardtite	$Cu_2NO_3(OH)_3\ (s) \leftrightarrow 2\ Cu^{2+}(aq) + NO_3^-(aq) + 3\ OH^-(aq)$	-32.74**	94.84**
Georgeite	$Cu_2CO_3(OH)_2 \cdot H_2O\ (s) \leftrightarrow 2\ Cu^{2+}(aq) + CO_3^{2-}(aq) + 2\ OH^-(aq) + H_2O$	-33.77*	60.2*
Hydrozincite	$Zn_5(CO_3)_2(OH)_6^{(s)} \leftrightarrow 5\ Zn^{2+(aq)} + 2\ CO_3^{2-(aq)} + 6\ OH^{-(aq)}$	-72.73*	-42.6*
Malachite	$Cu_2CO_3(OH)_2\ (s) \leftrightarrow 2\ Cu^{2+}(aq) + CO_3^{2-}(aq) + 2\ OH^-(aq)$	-35.02*	49.5*
Rosasite	$Cu_{1.16}Zn_{0.84}CO_3(OH)_2\ (s) \leftrightarrow 1.16\ Cu^{2+}(aq) + 0.84\ Zn^{2+}(aq) + CO_3^{2-}(aq) + 2\ OH^-(aq)$	-36.4§	n.a.
Rouaite	$Cu_2NO_3(OH)_3\ (s) \leftrightarrow 2\ Cu^{2+}(aq) + NO_3^-(aq) + 3\ OH^-(aq)$	-32.74#	n.a.
Tenorite	$CuO\ (s) + H^+(aq) \leftrightarrow Cu^{2+}(aq) + OH^-(aq)$	-6.36**	-9.06**
Unnamed Zinc-sodium intermediate	$Na_2Zn_3(CO_3)_4 \cdot 3H_2O\ (s) \leftrightarrow 2\ Na^+(aq) + 3\ Zn^{2+}(aq) + 4\ CO_3^{2-}(aq) + 3\ H_2O$	-33.89+	-197.6+
Zinc hydroxide (amorphous)	$Zn(OH)_2\ (s) \leftrightarrow Zn^{2+}(aq) + 2\ OH^-(aq)$	-15.52#	31#
Zincian georgeite	$Cu_{1.46}Zn_{0.54}CO_3(OH)_2 \cdot H_2O\ (s) \leftrightarrow \ldots\ldots 1.46\ Cu^{2+}(aq) + 0.54\ Zn^{2+}(aq) + CO_3^{2-}(aq) + 2\ OH^-(aq) + H_2O$	-32.97*	-103.7*
Zincian malachite	$Cu_{1.46}Zn_{0.54}CO_3(OH)_2\ (s) \leftrightarrow 1.46\ Cu^{2+}(aq) + 0.54\ Zn^{2+}(aq) + CO_3^{2-}(aq) + 2\ OH^-(aq)$	-34.78*	-60.2*
Zincite	$ZnO\ (s) + H^+(aq) \leftrightarrow Zn^{2+}(aq) + OH^-(aq)$	-2.67**	-33.81**
Zirconia oxide	$ZrO_2\ (s) + 2\ H^+(aq) \leftrightarrow Zr^{4+}(aq) + 2\ OH^-(aq)$	-35~	32.06~

* from Guse et al.[105]; ** from minteq.v4 database[106]; § from Alwan et al.[107]; # from NIST database[108]; ~ from Giffaut et al.[109]; + cf. Section A.4; n.a.: not available

The complete list of solid phases considered and their respective solubility products is embedded into the database file, cf. Guse et al.[101,110]. The listed solubility products K_{SP} describe

the solubility of salts in water, cf. Eq. (4.1), and are key in the determination of supersaturation as the driving force for solids formation, cf. Section 4.2.1. The respective reaction enthalpies $\Delta_r\tilde{h}$ are applied to account for the temperature-dependency of the solubilities, cf. Eq. (4.6).

2.3 Experimental setup

One main focus of this work is to investigate the process steps co-precipitation and aging separately from each other, cf. Sections 3 and 4. For this purpose, continuous co-precipitation and batch aging were strictly separated according to Figure 2.2 (a).

In the continuous co-precipitation, a micro mixing nozzle was applied to ensure reproducible and spatially homogeneous mixing conditions at high energy dissipation rates. Further details on the process, the mixing nozzle and mixing are discussed in Section 2.3.1. In selected cases, aging was then conducted consecutively in a stirred tank reactor either to investigate aging or to prepare catalyst material, cf. Section 2.3.2. Complementary, the state-of-the-art semi-batch process depicted in Figure 2.2 (b) was used to prepare reference material for catalyst testing, cf. Section 2.5.

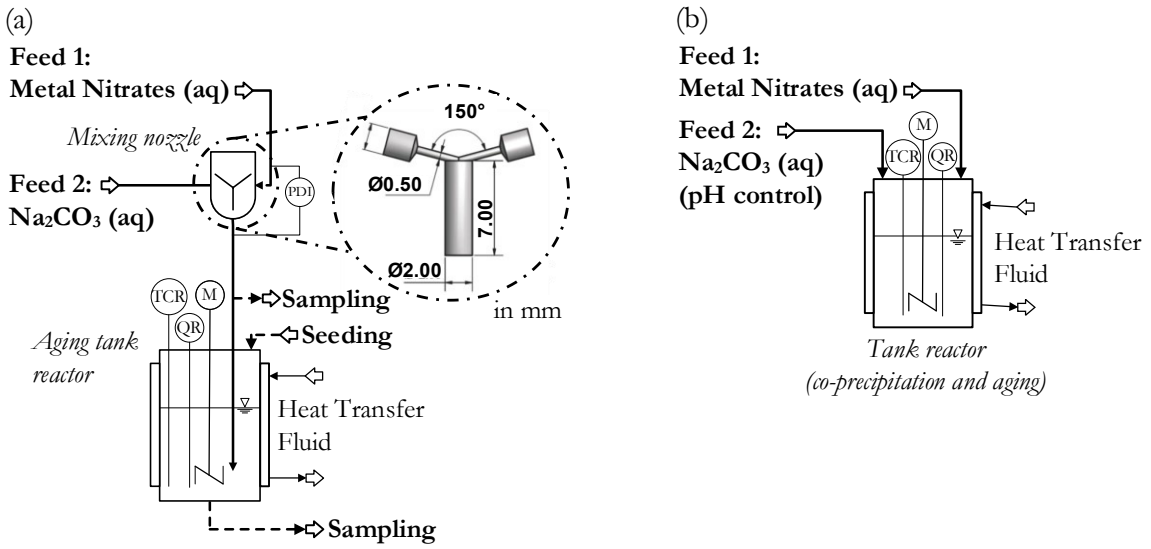

Figure 2.2: Experimental setups for **(a)** a continuous co-precipitation followed by batch aging and **(b)** a semi-batch co-precipitation and aging. M: motor, TCR: temperature control and recording, QR: pH recording, PDR: differential pressure recording. Based on Guse et al.[101].

2.3.1 Continuous (co-)precipitation

The setup depicted in Figure 2.2 (a) is used for all studies where co-precipitation is investigated isolated from the other process steps. The micro mixing nozzle, also referred to as an impinging micro jet mixer in the literature[111–113], enables a continuous precipitation. This way, each particle that is formed experiences the same formation history, so that e.g. the influence of mixing on the particle size can be investigated, cf. Section 3.1. Detail information on the two nozzles used in this work are available in the appendix, cf. Section A.1.

An aqueous metal nitrate solution (feed 1) and a basic Na_2CO_3 or $NaHCO_3$ solution (feed 2) with equal volume flows were continuously mixed in the nozzle where co-precipitation then takes places in a millisecond to second scale[60,71,112,114]. For the co-precipitation studies in Section

3, where precisely defined volume flows are essential to investigate the influence of mixing, a modified testing machine (Z010, Zwick Roell GmbH&Co. KG) with incorporated syringe pumps is used, cf. Figure A.2. The setup allowed total volume flows of up to 1800 ml·min^{-1}, which corresponds to 76 m·s^{-1} in the inlet jets, at a precision of $\dot{V}_{\mathrm{Feed,real}} = \dot{V}_{\mathrm{Feed,set}} \pm 1\ \mathrm{ml/min^{-1}}$, cf. Figure 2.3, and pressure differences of up to 32 bar and is described elsewhere in detail[111]. The pump capacity is sufficient to prevent plugging due to solids formation at the walls. The differential pressure measurement (Deltabar PMD75, Endress+Hauser) is used to determine energy dissipation rates from the set volume flows and correlate them with the resulting particle sizes, cf. Section 3.3.

However, the syringe pump setup only allows a total batch volume of approx. 300 ml. Thus, two gear pumps (GB-P23-DEELE, Micropump) in combination with magnetic-inductive flow meters (IFC90, Krohne) were used if larger suspension volumes were needed, e.g. for the experiments with a succeeding aging step. Here, total volume flows of up to 800 mL·min^{-1} [105], which corresponds to 34 m·s^{-1} in the jets, with a precision of at least ±5 % were achieved, cf. Figure 2.3. In both setups, the stirred reactant tanks, piping and jet mixer were temperature-controlled (± 1 K). Due to the higher precision, all co-precipitation experiments without aging in Section 3.3 regarding the influence of mixing on the co-precipitate were conducted in the syringe pump setup. The higher deviations for the gear pump setup are not expected to affect the results for the aging studies as deviations only occur sporadically over the dosing time. These assumptions are confirmed by the small deviation in suspension pH directly after co-precipitation is completed, cf. Figure 5.3 (a) that is discussed later. In seven independent experiments, pH only deviates by ± 0.05 from the target value of 6.7.

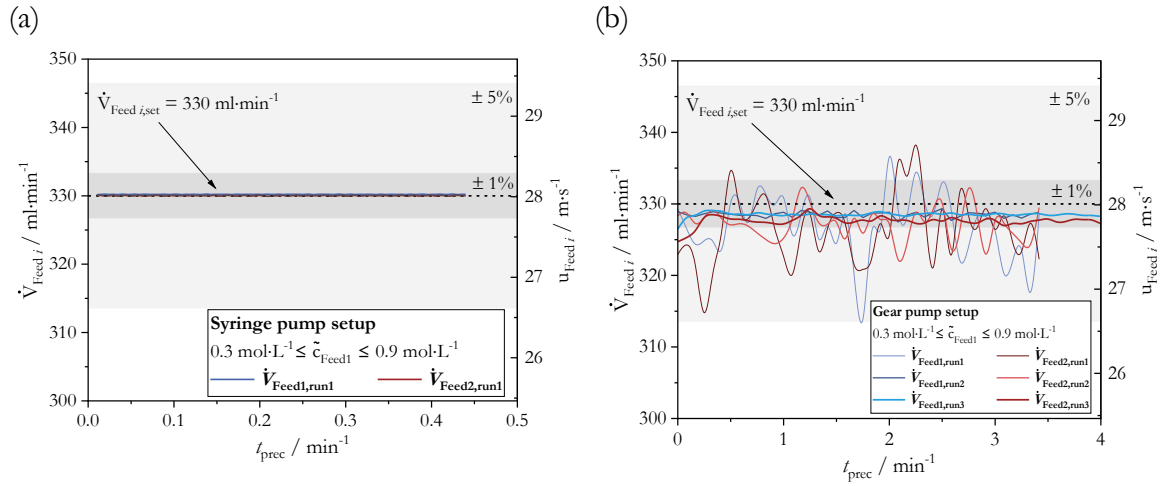

Figure 2.3: Fluctuation of the feed volume flows over the precipitation time for different reactant concentrations and at a representative set volume flow (330 ml·min^{-1}) for (a) the syringe pump setup and (b) the gear pump setup.

For all experiments on the binary co-precipitate in Section 3.3 $b_{\mathrm{Cu(NO_3)_2,Feed1}} = 0.18\ \mathrm{mol \cdot (kg\ H_2O)^{-1}}$, $b_{\mathrm{Zn(NO_3)_2,Feed1}} = 0.09\ \mathrm{mol \cdot (kg\ H_2O)^{-1}}$, $b_{\mathrm{NaHCO_3,Feed2}} = 1.01\ \mathrm{mol \cdot (kg\ H_2O)^{-1}}$ and $T = 50\ °\mathrm{C}$ were used which corresponds to a solids concentration in the suspension of approx. 2 wt.%. The total metal concentration in the suspension with the volume V_{susp} is given by Eq. (2.1):

$$c_{\mathrm{M,susp}} = \frac{n_{\mathrm{Cu(NO_3)_2}} + n_{\mathrm{Zn(NO_3)_2}} + n_{\mathrm{ZrO(NO_3)_2}}}{V_{\mathrm{susp}}} \tag{2.1}$$

The studies on the ternary co-precipitate in Section 3.3 were conducted with $b_{\mathrm{Cu(NO_3)_2,„Feed1}} = 0.06\ \mathrm{mol} \cdot (\mathrm{kg\ H_2O})^{-1}$, $b_{\mathrm{Zn(NO_3)_2,„Feed1}} = 0.03\ \mathrm{mol} \cdot (\mathrm{kg\ H_2O})^{-1}$, $b_{\mathrm{ZrO(NO_3)_2,„Feed1}} = 0.01\ \mathrm{mol} \cdot (\mathrm{kg\ H_2O})^{-1}$, $b_{\mathrm{NaHCO_3,Feed2}} = 0.38\ \mathrm{mol} \cdot (\mathrm{kg\ H_2O})^{-1}$ and $T = 30\ °\mathrm{C}$ which also corresponds to approx. 2 wt.% solids. There were no issues of plugging for these molalities.

2.3.2 Aging and semi-batch processes

In this work, three different process designs are used for aging: first, the newly developed batch aging after continuous co-precipitation in a mixing nozzle as depicted in Figure 2.2 (a). This approach is applied for the studies in Section 4, where aging is investigated isolated, and for preparing the catalysts investigated in Sections 3.2, 3.3 and 5. Second, batch aging after continuous co-precipitation with seeding at $t_{\mathrm{age}} = 0\ \mathrm{min}$ which is applied in Section 5.3 to possibly increase the space-time-yield of aging. Third, a state-of-the-art semi-batch preparation where co-precipitation and aging overlap. This approach is used in Section 3.2 for the preparation of reference material.

Continuous co-precipitation & batch aging

In this approach, co-precipitation was conducted continuously in a mixing nozzle as described above. The resulting co-precipitate suspension was then fed directly into one of two identical double-jacketed glass tank reactors ($V_{\mathrm{tank}} = 4000\ \mathrm{ml}$; $d_{\mathrm{tank}} = 120\ \mathrm{mm}$) with four baffles according to DIN 28131. Co-precipitation was completed when the target volume in the tank reactor was reached. This took, depending on the volume and volume flows chosen, a maximum of 4 min. Thus, co-precipitation time is, generally, small compared to the aging time necessary to induce a complete phase transformation ($t_{\mathrm{age}} > 80\ \mathrm{min}$).

Aging took place under stirring with a two-staged three-blade propeller agitator ($d_{\mathrm{stirrer}} = 50\ \mathrm{mm}$, 30° pitch) at 950 rpm. This corresponds to a mean energy input of 0.41 W·kg^{-1} and a stirrer tip speed of 2.5 m·s^{-1}. The temperature was controlled with ± 1 K accuracy and pH was measured with ± 0.05 accuracy (HI1090T, Hanna Instruments). For this purpose, the pH electrode was calibrated daily using a two-point calibration with two of following three references (pH buffer solution 4.01, pH buffer solution 7.00, pH buffer solution 10.01, all by Carl Roth GmbH). Samples at specified aging times were obtained by withdrawing suspension (30 – 50 ml) in the proximity of the stirrer via the bottom drain valve. These samples were processed identically to the co-precipitate suspension, as described in Section 2.4.1. In general, aging was terminated 30 min after a pH minimum had been reached to ensure that the phase transformation was completed[115].

The continuously prepared catalyst investigated in Section 3 was prepared with $b_{\mathrm{Cu(NO_3)_2,„Feed1}} = 0.16\ \mathrm{mol} \cdot (\mathrm{kg\ H_2O})^{-1}$, $b_{\mathrm{Zn(NO_3)_2,„Feed1}} = 0.08\ \mathrm{mol} \cdot (\mathrm{kg\ H_2O})^{-1}$, $b_{\mathrm{ZrO(NO_3)_2,„Feed1}} = 0.03\ \mathrm{mol} \cdot (\mathrm{kg\ H_2O})^{-1}$ and $b_{\mathrm{NaHCO_3,Feed2}} = 1.018\ \mathrm{mol} \cdot (\mathrm{kg\ H_2O})^{-1}$ at 40 °C resulting in a $\mathrm{pH} = 6.9$ after co-precipitation and a solids fraction in the suspension of approx. 2 wt.%. For the phase studies and model validation in Section 4, the mass fractions of Cu, Zn and Zr in feed 1 and the temperature were varied, but the total molality of metal salts in feed 1

was kept at $b_{\mathrm{tot,Feed1}} = 0.27\ \mathrm{mol \cdot (kg\ H_2O)^{-1}}$. For the reference material in Section 5, the initial pH after co-precipitation at $t_{\mathrm{age}} = 0\ \mathrm{min}$ was adjusted to 6.7 by addition of HNO_3 to feed 1 ($X_{65\%\ \mathrm{HNO_3,Feed2}} = 22\ \mathrm{mL \cdot kg_{H_2O}^{-1}}$) and temperature was increased to $T = 55\ °\mathrm{C}$ as optimization studies showed an improved methanol productivity for these conditions, cf. Section 4.5. For these optimization studies, temperature and pH were varied by addition of NaOH and HNO_3, while all further reactant molalities were kept constant. Additionally, scale-up studies with an increased solids fraction of 6 wt.% in the suspension were conducted by increasing the feed molalities to $b_{\mathrm{Cu(NO_3)_2,Feed1}} = 0.516\ \mathrm{mol \cdot kg_{H_2O}^{-1}}$, $b_{\mathrm{Zn(NO_3)_2,Feed1}} = 0.258\ \mathrm{mol \cdot kg_{H_2O}^{-1}}$, $b_{\mathrm{ZrO(NO_3)_2,Feed1}} = 0.086\ \mathrm{mol \cdot kg_{H_2O}^{-1}}$ and $b_{\mathrm{Na_2CO_3,Feed2}} = 0.889\ \mathrm{mol \cdot kg_{H_2O}^{-1}}$.

Seeding

For the seeding studies in Section 5.3, the same setup and general procedure were applied as for continuous co-precipitation and batch aging approach. The key difference is that, additionally, seed crystals composed of zincian malachite were added to the suspension to accelerate phase transformation during aging. For this purpose, two methods were used: using a suspension of freshly prepared seeds as a direct approach and, alternatively, adding previously dried seeds which allow a more precisely defined storage.

Suspensions of freshly prepared seed crystals were obtained by conducting a separate preparation without seeding but otherwise at the same process conditions beforehand. This way, a suspension of aged intermediate consisting of zincian malachite was formed and prefilled into the aging tank reactor (± 0.01 g). Then, co-precipitation via the mixing nozzle was started anew and the resulting co-precipitate suspension was added directly to the seed suspension in the aging tank reactor as described previously in Section 2.3.1.

In order to produce dried seeding material, an unseeded aging was carried out under identical conditions as the planned seeding experiment. The solids were then filtered, washed, dried, and mortared as described in Section 2.4.1 in order to analyze and store them. Additionally, the seed crystals were fractionated ($x < 40\ \mu\mathrm{m}$) using a sieve shaver (AS 200, Retsch). They were then resuspended in 30 mL of demineralized water for 5 min at $n = 9800\ \mathrm{min^{-1}}$ using a disperser (T 25 Ultra Turrax, IKA). After co-precipitation was completed ($t_{\mathrm{age}} = 0\ \mathrm{min}$), the seeding material was inserted into the aging tank reactor from the top of the reactor using a syringe, cf. Figure 2.2 (a). The seeding process took a maximum of two minutes to finish.

Reference semi-batch process

Two different setups, which both follow the same key approach, were used for the semi-batch preparation of reference material, cf. Figure 2.2 (b). Here, co-precipitation and aging overlap in time and space as it is generally done in literature and industrial production[5,10,31,87,99] These reference catalysts are used in the precatalyst characterization and performance tests in Section 3.2.

The first variant is based on a procedure suggested by Arena et al.[10]. Allahyari et al.[116] and Frusteri et al.[5] and was initially chosen due to its positive effects on product homogeneity at nanoscale and surface area by using ultrasound: an amount of 1000 ml of 0.2 mol·L^{-1} $NaHCO_3$ was placed in a 2000 ml stirred vessel which was submerged into an ultrasonic bath (Sonorex

RK 510 H, Bandelin) at 40 °C and stirred with a two-blade anchor impeller at 520 rpm. Then, 100 mL of a 0.8 mol·L^{-1} metal nitrate solution with $n_{Cu(NO_3)_2} / n_{Zn(NO_3)_2} / n_{ZrO(NO_3)_2} = 6/3/1$ was fed into the reactor at a flow rate of $\dot{V}_{Feed1} = 1.6\ ml \cdot min^{-1}$. pH was kept between 7.0 and 7.2 by adding a 1 mol·L^{-1} $NaHCO_3$ solution (feed 2). Subsequently, the suspension was aged for 2 h without further pH control[44].

For the second semi-batch setup the same stirred tank reactor as for the "continuous co-precipitation and batch aging" approach is used. In this case, approx. 1500 mL Na_2CO_3 solution is provided in the tank reactor and the metal nitrate solution is slowly added via a submerged dosing line in the proximity of the lowest stirrer stage with $\dot{V}_{Feed1} = 20\ ml \cdot min^{-1}$. Additional Na_2CO_3 solution was added to maintain the target pH of 6.9 during precipitation. When addition of the metal solution was completed, aging without pH control was carried out for 2 h.

2.4 Product characterization

In accordance with the aim of this thesis, the precursors, intermediates and products investigated in this work are mainly characterized regarding their morphology and composition.

Depending on particle size, the particle morphology is analyzed by either SEM or TEM imagining. Additionally, the particle size distribution (PSD) is evaluated by dynamic and static light scattering and the surface characteristics by BET studies and N_2O chemisorption. The phase composition is evaluated by XRD evaluation or, for amorphous samples, by FT-IR. The elemental composition is resolved by a combination of XRF and ICP-OES for the metal components and combustion analysis for C, H and N. Complementary, the spatial distribution of components was investigated by TEM-EDXS studies.

These analytical methods are all well established. This is why they are only briefly summarized in the following sections with a focus on the chosen measurement parameters and customized evaluation routines.

2.4.1 Sample preparation

For the analysis of solids, the sample suspensions of the (co-)precipitate, the time samples taken during aging and the aged intermediate were collected without dilution. They were filtered directly after sampling (< 5 min) using a water aspirator or a vacuum pump ($p \leq 100\ mbar$) and a Büchner funnel with filter paper (MN85/70, Macherey-Nagel). The filter cake was then washed by displacement washing with demineralized water at room temperature until an electrical conductivity of $\sigma < 100\ \mu S \cdot cm^{-1}$ (Profiline LF 197, WTW) was achieved and until no nitrate could be detected by nitrate test strips ($c_{NO_3^-} < 10\ mg \cdot L^{-1}$, VWR Chemicals). The conductometer was calibrated weekly with two references (Conductivity standard 1413 µS·cm^{-1} and conductivity standard 84 µS·cm^{-1}, Carl Roth GmbH).

For the semi-batch prepared samples, a centrifuge was used to sediment the solution. Washing was then conducted by resuspending the solids in demineralized water und repeating the centrifugation until the nitrate concentration fell below $c_{NO_3^-} < 10\ mg \cdot L^{-1}$.

The moist sample was then either dried at ambient pressure and at the aging temperature, or at $p \leq 10^{-4}$ mbar and 35 °C, for at least 16 h (Vacutherm VT6130 M-BL, Heraeus with Trivac D16B/DS, Leybold). No influence of the washing and drying method on the phase composition or morphology was evident as long as washing was conducted until a residual conductivity of $\sigma < 100\ \mu S \cdot cm^{-1}$ in the filtrate was reached, cf. Section A.2 in the appendix. Thus, methods were chosen according to their availability and throughput. Selected samples were then calcined in air with a heating ramp of 3 K min^{-1} and a maximum temperature of 350 °C, which was held for 4 h, and manually ground in a mortar until no more lumps were visually detected[44,101].

2.4.2 SEM and TEM(-EDXS) measurements

The particle morphology of the nanosized (co-)precipitate and precatalysts were analyzed by transmission electron microscopy (TEM) with a FEI Osiris ChemiStem (200 kV) at the Laboratory for Electron Microscopy (LEM) at KIT, Karlsruhe, by Heike Störmer. For this purpose, the dried sample was suspended in demineralized water by means of an ultrasound bath and then spread on a TEM gold grid using an ultrasonic fogger. Energy-dispersive X-ray spectroscopy (EDXS) was conducted at LEM by Heike Störmer by using an equipped Bruker Quantax system (XFlash detector) and used to examine the spatially resolved elemental distribution of metals inside the particles of the co-precipitate and the precatalyst on the nanometer scale.

TEM imaging was also applied to validate the PSD determined by dynamic light scattering. For this, a sufficient number of binarized TEM images to evaluate a total of at least 1000 particles was processed with the public domain software ImageJ. Only the cross-sectional areas of complete particles in the images were considered for the determination of the mean particle size and the span.

The particle morphology of the aged intermediate as well as of the seed crystals was analyzed by scanning electron microscopy (SEM) by Volker Zibat, using a Zeiss Gemini SEM 500 with a Schottky field emission cathode at LEM, KIT, Karlsruhe. The particles of the dried sample were fixated on adhesive carbon pads. By combining SEM with a focused Ga^+ ion beam (FIB), the preparation and examination of cross-sections of chosen samples was possible with the FEI Strata 400 STEM and the help of Erich Müller (LEM, KIT, Karlsruhe). For this purpose, the samples were coated with Pt beforehand to prevent sample deterioration during FIB preparation.

2.4.3 Dynamic and static light scattering

Particle size distributions (PSD) of co-precipitate samples were measured by means of dynamic light scattering (DLS) with a Zetasizer Nano ZS (Malvern Panalytical). The suspension was diluted with demineralized water to suppress any aging processes on the one hand and to minimize measurement errors by agglomeration and light scattering at multiple particles on the other hand. However, only the addition of an electro-steric stabilizer (polycarboxylate ether in water; MelPers0045, BASF SE) to the metal nitrate feed ($c_{\mathrm{MelPers0045,Feed1}} = 20\ g \cdot L^{-1}$) in combination with a dilution prevented agglomeration completely, cf. Figure 2.4. Accordingly, a

sample of 5 mL of the co-precipitate suspension was directly fed as a free jet into a 1000 mL beaker ($d_{\mathrm{beaker}} = 95\ \mathrm{mm}$) (about 10 cm travel distance). The beaker was equipped with a magnetic stirring bar ($d_{\mathrm{stirrer}} = 40\ \mathrm{mm}$) operating at 300 rpm, baffles and 500 mL of demineralized water. For the measurements, a refractive index of 1.813, a mean value for malachite[117], and an absorption index of 0.3 [118] were applied. Due to the partly high concentrations of MelPers0045, viscosity measurements as a function of the stabilizer concentration were conducted resulting in the following correlation (Eq. (2.2)) which was used to determine the viscosity:

$$\eta = (0.0156 \cdot c_{\mathrm{MelPers0045}} \cdot \mathrm{g} \cdot \mathrm{L}^{-1} + 0.8937)\mathrm{mPa} \cdot \mathrm{s} \tag{2.2}$$

Figure 2.4 (a) shows the co-precipitate without any stabilizer after a process time of approx. 0.5 s based on the volume flow of $\dot{V}_{\mathrm{total}} = 10\ \mathrm{mL} \cdot \mathrm{min}^{-1}$ and the aforementioned travel distance. It is evident that the initially spherical co-precipitate particles, that are discussed in more detail in Section 3.3, are already aggregated to an intergrown net-like entity. A kinetic description of co-precipitation in terms of nucleation and growth rates, along with a pragmatic determination of particle sizes via DLS, is not achievable in this way. In contrast, aggregation of the spherical co-precipitate particles is effectively inhibited by the addition of MelPers0045 to the metal nitrate feed, as is evident in Figure 2.4 (b). The individual aggregates are clearly segregated and stabilized as spherical particles, which is essential for DLS measurements. This method possibly also decelerates the aging process by inhibiting particle collisions, cf. Section 5 on the effect of seeding[101].

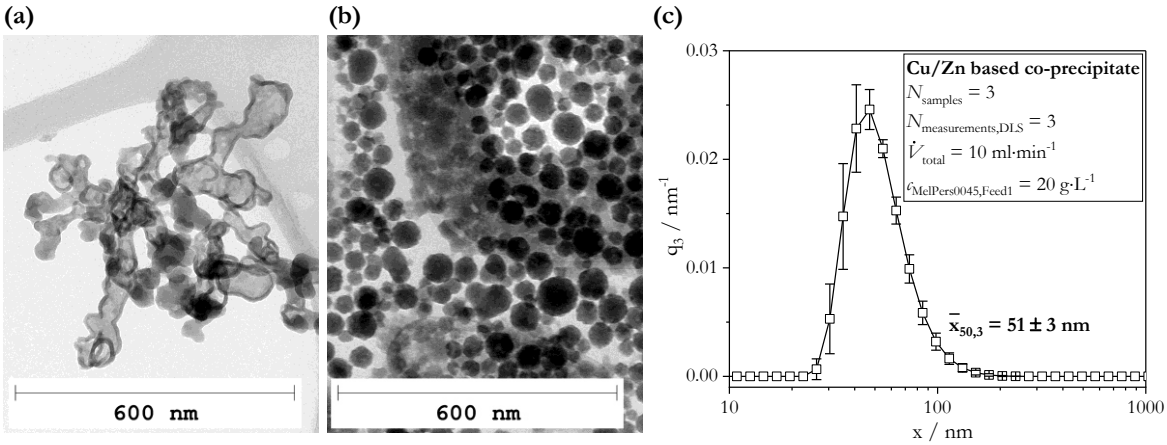

Figure 2.4: TEM images and particle size distribution of a Cu/Zn based co-precipitate for $\dot{V}_{\mathrm{total}} = 10\ \mathrm{mL} \cdot \mathrm{min}^{-1}$. Comparison of **(a)** the co-precipitation without stabilizer and **(b)** with $c_{\mathrm{MelPers0045,Feed1}} = 20\ \mathrm{g} \cdot \mathrm{L}^{-1}$. **(c)** shows stable and reproducible DLS measurements after the successful stabilization of the spherical aggregates. Adapted from Guse et al.[101].

Figure 2.4 (c) shows the volumetric density distribution q_3 determined by DLS upon the addition of the stabilizer to the metal nitrate feed. The mean values from three independent samples, each measured three times in a row, are plotted. Minor deviations suggest excellent reproducibility and adequate suppression of secondary processes during measurement, including agglomeration and aging. The volume-based median particle size $\bar{x}_{50,3,\mathrm{DLS}} = 51 \pm 3\ \mathrm{nm}$ matches the value from the graphical analysis of more than 1000 particles in TEM images ($\bar{x}_{50,3,\mathrm{TEM}} = 53\ \mathrm{nm}$) where the same stabilizer was added ($c_{\mathrm{MelPers0045,Feed1}} = 20\ \mathrm{g} \cdot \mathrm{L}^{-1}$). Consequently, DLS combined with MelPers0045 as a stabilizer is a valid procedure for

characterizing the spherical aggregates identified as the co-precipitate. Each sample was measured three times in a row (approx. 5 min) to ensure that no secondary processes occur during measurement that may influence the particle size[101].

The particle size distribution of the seeds in the suspension, which are coarser than the initial co-precipitate by around three orders of magnitude, was determined by static light scattering (SLS). The Mastersizer 3000 with Hydro EV (Malvern Panalytical), which was used for this purpose, allows size measurements in the range of $10\ \text{nm} \leq x \leq 3.5\ \text{mm}$[118,119]. The suspension was analyzed directly after sampling ($\Delta t < 5\ \text{min}$) and diluted with demineralized water (approx. 1:100)[120].

2.4.4 Surface analyses

For the analysis of the specific particle surface areas (S_{BET}), the dried samples were first fractionated to $250\ \mu\text{m} \leq x \leq 500\ \mu\text{m}$ and degassed for 20 h at 130 °C. Then, N_2 physisorption measurements were conducted in a Quantachrome NOVA 2000e device (Anton Paar) at 77.35 K by Thomas Otto at the Institute of Catalysis Research and Technology (IKFT), KIT, Eggenstein-Leopoldshafen. The isotherms were analyzed using the Brunauer–Emmett–Teller model (BET) in the 0.08 – 0.3 p/p_0 range.

The analysis of the copper surface area S_{Cu} by N_2O pulse chemisorption was combined with a preceding temperature-programmed reduction (TPR) and carried out by Thomas Zevaco (IKFT, KIT). For this purpose, an Altamira AMI-300 device equipped with a thermal conductivity detector (TCD) was used. For the TPR measurement, approx. 100 mg of the precatalyst sample was placed in a quartz reactor, dried and then cooled under argon. Then, the samples were heated from 50 °C to 250 °C at a rate of 1 K/min (250 °C, holding for 45 min) in a gas mixture containing 5 vol% H_2/Ar. The active Cu surface of the thus reduced catalyst sample S_{Cu} can then be determined according to the following reaction:

$$2\ \text{Cu} + \text{N}_2\text{O} \rightarrow \text{N}_2 + \text{Cu} - \text{O} - \text{Cu} \tag{2.3}$$

The controlled oxidation of the Cu surface is conducted by sending N_2O pulses of a definite volume (518 mL, 10 vol% N_2O/He Air Liquide CRYSTAL gas Mixture). The released N_2 is quantified with the cumulated data of the TCD and the oxidized surface of the catalysts can thus be calculated. Further details on the TPR and N_2O pulse chemisorption procedure are given elsewhere[120].

2.4.5 FT-IR, XRD and Rietveld refinement

The phase composition of the dried and ground solid samples was determined using a combination of X-ray diffraction (XRD) for the crystalline fractions and Fourier transform infrared spectroscopy (FT-IR) for the amorphous fractions and samples. The FT-IR spectra in the range of $4000\ \text{cm}^{-1} < \tilde{\nu} < 230\ \text{cm}^{-1}$ were obtained using a Varian 660-IR spectrometer (Agilent) with a resolution of $2\ \text{cm}^{-1}$ with the support of Thomas Zevaco (IKFT, KIT). For this purpose, approx. 3 mg sample is added to an agate mortar together with 300 mg KBr (≥ 99.5 % purity, VWR Chemicals). The mixture is ground for one minute and pressed into a disc ($h_{\text{KBr disc}} = 1\ \text{mm}$) with a hydraulic press (10 tons, 1 min). This way, the FT-IR spectra can be

compared quantitatively. Before each measurement, the chamber was purged for 5 min with N_2 to remove any CO_2 from the measuring chamber.

The XRD diffractograms in the range of $5° < 2\theta < 80°$ were recorded over a period of 120 min using a Panalytical X'Pert Pro (Malvern Panalytical) with Bragg–Brentano geometry and a Cu K-α light source (1.54 Å wavelength) with a Ni filter with the support of Diana Deutsch (IKFT, KIT). The mass fractions of the solid phases were determined using Rietveld refinement with Profex software, version 5.1[121]. The data of the reference phases used are given in the appendix, cf. Table A.1. For zincian malachite, Behrens et al. found a correlation between the amount of Zinc incorporated into the lattice $\tilde{x}_{\mathrm{Zn,zm}}$ according to Eq. (2.4) and the lattice constants a, b, c and γ, cf. Eqs. (2.5) to (2.8)[66], each with a coefficient of determination of $R^2 > 0.99$. These four correlations can then be used in a Rietveld refinement to determine a mean Zn fraction in zincian malachite $\tilde{x}_{\mathrm{Zn,zM}} \pm \sigma$ from the XRD diffractogram up to a maximum Zn fraction of 27 mol%. Zwiener et al. found similar correlations up to 31 mol% Zn[67]. However, these functions led to higher deviations than Eqs. (2.5) to (2.8). Furthermore, aurichalcite was detected as an additional phase in samples with total Zn fractions of 30 to 35 mol%[115]. Thus, the correlations by Behrens et al. and an assumed upper boundary of $\tilde{x}_{\mathrm{Zn,zm}} = 27\ \mathrm{mol\%}$[66] are applied here.

$$\tilde{x}_{\mathrm{Zn,zm}} = \frac{n_{\mathrm{Zn^{2+},zm}}}{n_{\mathrm{Zn^{2+},zm}} + n_{\mathrm{Cu^{2+},zm}}} \tag{2.4}$$

$$a_{\mathrm{zm}} \cdot \mathrm{Å}^{-1} = -0.0045\, \tilde{x}_{\mathrm{Zn,zm}} + 9.4938 \tag{2.5}$$

$$b_{zm} \cdot \mathrm{Å}^{-1} = 0.0056\, \tilde{x}_{\mathrm{Zn,zm}} + 11.9131 \tag{2.6}$$

$$c_{\mathrm{zm}} \cdot \mathrm{Å}^{-1} = -0.0024\, \tilde{x}_{\mathrm{Zn,zm}} + 3.2451 \tag{2.7}$$

$$\beta_{\mathrm{zm}} \cdot (°)^{-1} = -0.0924\, \tilde{x}_{\mathrm{Zn,zm}} + 98.7179 \tag{2.8}$$

A corresponding correlation was developed for aurichalcite, cf. Section A.3.2 and Eq. (A.1).

2.4.6 Elemental composition

The elemental composition of the samples was analyzed using two complementary methods: 1) inductively coupled plasma optical emission spectrometry (ICP-OES) for the total mass fractions of metals (Al, Cu, Na, Zn, Zr) and 2) flame atomic emission spectrophotometry (F-AES) to determine the total mass fractions of the light elements (C, H, N, S). Additionally, the metal fractions of chosen samples were determined by X-ray fluorescence (XRF) with a Pioneer S4 (Bruker) by the IKFT, KIT to validate the ICP-OES analysis. For each method, the dried samples were manually ground in a mortar until no more lumps were visually detected[120].

For the ICP-OES measurement, 50 to 100 mg of the samples were first digested by adding 6 ml of 65 % HNO_3 (subboiled) and 2 ml of 30 % HCl (p.A.). The mixture was then heated to 250°C for 45 min using a microwave system (Multiwave 5000, Anton Paar). Subsequently, the digests were diluted to a volume of 50 ml with ultrapure water (≤ 0.75 µS·cm^{-1}) and analyzed with an iCAP 7000 (Thermo Scientific) by Chantalle Kotschenreuther and Elisabeth Eiche at the Institute of Applied Geosciences (AGW), KIT, Karlsruhe. The ICP multielement standard

IV (Carl Roth GmbH) was applied for calibration and the ICP-OES reference solution VHG-MISA6-500 (VHG Labs) was used for quality assurance[120].

F-AES analysis was conducted in a Vario Micro Cube (Elementar Analysensysteme GmbH) by Nicole Klaassen at the Institute of Inorganic Chemistry (AOC), KIT, Karlsruhe. Each sample was measured twice to rule out major variances. The mass fraction of nitrogen $x_{\mathrm{N,total}}$ determined by F-AES analysis was applied to calculate the mass fraction of the phase rouaite ($Cu(NO_3)(OH)_3$) $x_{\mathrm{rouaite,solids}}$ according to Eq. (2.9) under the assumption that all N atoms are present as NO_3 in the rouaite lattice with $x_{\mathrm{N,rouaite}} = 7.93\ \mathrm{wt.\%}$ as the stoichiometric mass fraction of N in the rouaite lattice[105].

$$x_{\mathrm{rouaite,solids}} = \frac{x_{\mathrm{N,total}}}{x_{\mathrm{N,rouaite}}} \tag{2.9}$$

The oxygen mass fraction $x_{\mathrm{O,total}}$ was calculated from all other mass fractions measured by ICP-OES, XRF and F-AES assuming that no significant amount of other elements is present in the respective sample.

2.5 Catalyst testing

A six-fold parallel reactor system with continuous-flow fixed bed reactors at IKFT, KIT was used for evaluating the catalyst performance in methanol and direct DME synthesis from syngas of varying composition (45 vol% H_2; 35 vol% N_2; 20% CO_x). The volume fraction of CO_2 in relation to the total volume fraction of CO and CO_2 ($\dot{V}_{\mathrm{CO_2}}/\dot{V}_{\mathrm{CO_x}}$) in the syngas was varied between $\dot{V}_{\mathrm{CO_2}}/\dot{V}_{\mathrm{CO_x}} = 0$ and $\dot{V}_{\mathrm{CO_2}}/\dot{V}_{\mathrm{CO_x}} = 1.0$. The feed gases carbon monoxide (CO, 99.97 vol%), nitrogen (N_2, 99.9999 vol%), hydrogen (H_2, 99.9999 vol%) and a mixture of CO_2 and N_2 (50: 50 ± 1.0 vol%) were supplied by Air Liquid Germany GmbH. Wild et al. gave a detailed description of the process[122]. Each reactor contained one precatalyst sample and was run at the same volume flow rate, pressure and temperature[120,122].

For the studies on the influence of mixing during co-precipitation on the resulting catalyst properties in Section 3.2, the catalysts were applied by Stefan Wild (IKFT, KIT) in a direct DME synthesis with methanol as an intermediate with $T = 230\ °\mathrm{C}$ and $p = 50\ \mathrm{bar}$. For this purpose, the catalysts under investigation were mixed in a mass ratio of 1:1 with the zeolite H-FER 20 (Zeolyst International CP914C, Si/Al ratio of 20) which acts as a dehydration catalyst and enables the further reaction from methanol to DME. This mixture was then mixed with silicon carbide (SiC, Hausen Mineraliengroßhandel GmbH) in a mass ratio of 1:5 to prevent the formation of hotspots in the reactor. The beds were filled with a total of 12 ± 0.001 g of mixed material in fivefold stacks with additional SiC layers at the top and bottom of the beds to ensure the uniform grain distribution of all components and a homogeneous temperature in the reaction zone. The modified gas hourly space velocity (GHSV) was maintained at $GHSV = 8.8\ \mathrm{s^{-1}}$ for all feed gas compositions, cf. Eq. (2.10), to ensure that conversion took place in the kinetic region. FT-IR spectroscopy and gas chromatography were used for analysis. More details on the procedure can be found elsewhere[20,44].

$$GHSV = \frac{\dot{V}^{\mathrm{N}}_{\mathrm{feed\ gas}}}{V_{\mathrm{cat}}} = \frac{\dot{V}^{\mathrm{N}}_{\mathrm{feed\ gas}} \cdot \rho_{\mathrm{bulk}}}{m_{\mathrm{cat}}} \tag{2.10}$$

For the experiments on the influence of seeding on the catalyst performance in methanol synthesis in Section 5.3, the precatalysts (2 ± 0.0005 g) were sieved into a size fraction of 250 to 500 µm and mixed with 8.2715 ± 0.0002 g SiC of the same grain. This setup was also applied for the activity tests as a function of mixing intensity in Section 3.3 and an additional comparison of semi-batch and continuous precipitation in Section 3.2. The catalyst beds were 30 ± 2 mm in length, with a bulk density of $\rho_{\mathrm{cat,bulk}} = 0.8825\ \mathrm{g \cdot ml^{-1}}$ [120,122]. The experiments were conducted by Moritz Herfet (IKFT, KIT) at $p = 30\ \mathrm{bar}$ and $GHSV = 4.41\ \mathrm{s^{-1}}$, cf. Eq. (2.10), for a total process time of 176 h. First, the reactor system was run with $\mathrm{CO_2/CO_x} = 0.5$ at $T = 230\ \mathrm{°C}$ for approx. 120 h. The first approx. 70 h were used for initialization and the following 50 h were used to evaluate the methanol productivity P_{MeOH} according to Eq. (2.11), the CO_x conversion (Eq. (5.4)) and methanol selectivity (Eq. (5.5)) of the different catalysts.

$$P_{\mathrm{MeOH}} = \frac{\dot{m}_{\mathrm{MeOH,out}}}{m_{\mathrm{cat}}} \tag{2.11}$$

Then, the syngas composition was changed to $\mathrm{CO_2/CO_x} = 1.0$ and the temperature was increased to $T = 250\ \mathrm{°C}$. Productivity, selectivity and conversion were then evaluated over an additional time on stream of approx. 45 h. Based on these test conditions, i.e. the relatively small GHSV and the short overall testing time, all results from methanol synthesis are solely assessed as a functional test of the differently prepared catalysts without any in-depth analysis and interpretation of potential differences in performance.

3 Co-precipitation and its role in the preparation of defined Cu/ZnO based catalysts

In general, Cu/ZnO based catalysts are prepared in a complex multi-step process. Most research on process development focusses on reactant variation[21,72,81,93,123,124] to accommodate new insights on the optimum metal composition and on aging conditions[31,36,43,61,80,125] to enhance the resulting surface characteristics of the final catalyst. Studies on the influence of the initial solids formation by co-precipitation is sparser and ambiguous[35,59,71,73,84,86,126], also due to the common overlap of co-precipitation and aging in stirred tank reactors used both in technical application and research[5,10,31,87,99]. The goal of this section is to analyze if co-precipitation itself does influence the resulting catalyst characteristics and, if so, how. For this purpose, a suitable process to separate co-precipitation from aging must be established, cf. Section 2.3. The aforementioned ambiguous state of the art will be dissected critically first.

3.1 State of the art and research hypotheses

When the $Cu(NO_3)_2$ containing reactant solution is mixed with an alkaline Na_2CO_3 or $NaHCO_3$ solution, an amorphous precipitate is formed first[64,70,75]. Due to the metastable and amorphous nature of the precipitate, the relevant phases as well as their structure are still under ongoing discussion. The two most likely Cu phases, depending on pH and T, are georgeite ($Cu_2CO_3(OH)_2$)[69,70,127] and copper hydroxide ($Cu(OH)_2$)[71,128,129]. Similarly, amorphous phases for the other metals, such as $Zn(OH)_2$, $ZrO(OH)_{2-y}(CO_3)_{0.5y}$ and $Al(OH)_3$, are present depending on the reactant composition[64,70,93,106,109]. In contrast to their crystalline counterparts, e.g. malachite with the same sum formula ($Cu_2CO_3(OH)_2$), amorphous solids are characterized by their lack of long-range order resulting in a lack of X-ray diffraction peaks. Similar to quartz glass (SiO_2), they have the rheological properties of solids, but the molecular properties of liquids and their sum formula describes the mean composition of the randomly ordered individual molecules[130,131]. Secondary processes lead to the formation of firmly intergrown aggregates of these single-phase primary particles[64,72].

When both Cu and Zn are present, Zn may be incorporated into the amorphous georgeite phase similar to the formation of zincian malachite during aging[70,95,132], cf. Section 4.1. The key difference is that, due to the amorphous structure of zincian georgeite, no strictly defined distribution of both metals on the one- to two-digit nanometer scale is achieved. Furthermore, the co-precipitate tends to form spherical particles that result in a low surface area compared to the aged material[43,64,70–73]. For these reasons, the general conclusion is that aging is essential to obtain a high-performance catalyst[18,43,68,74,89]. One study by Rua Gonzalez deviates from this consensus and suggests that aging impacts catalyst properties and performance negatively and that a process without an aging step is recommended when co-precipitation is conducted continuously[133]. However, co-precipitation in that case was carried out over 7 h in a microfluidic setup and the precipitation product was stored unwashed after filtration over this period, which is detrimental for the nanoscale homogeneity and purity of the sample. In addition, an aging time of 17 h was chosen. Other studies show that excessively long aging times of more than 3 h can lead to the formation of CuO or ZnO as byproducts, reduce the surface area and

performance[64,79], and should therefore be avoided. Accordingly, the conclusion by Rua Gonzalez is to be evaluated critically.

If dissolved Al^{3+} ions are present in the preparation of CZA catalysts, hydrotalcite-like phases such as $(Cu,Zn)_{1-x}Al_x(OH)_2(CO_3)_{0.5x}\cdot y\ H_2O$), also known as layered double-hydroxides, that incorporate Al, Cu and Zn, can form[134]. The single crystal lattice for all three metals results in a homogeneous distribution of all metals on the one-digit nanoscale and small CuO crystallites after calcination. However, due to the stronger embedment of Cu in the $ZnAl_2O_4$ matrix compared to zincian malachite, the resulting specific surface areas are smaller. Additionally, Al fractions of the best-performing catalysts are typically below 20 wt.% so that hydrotalcite-like phases do not play the major role during solids formation[31]. For these reasons, and since the main focus of this work is on CZZ catalysts, hydrotalcite phases are not further considered. Yet, the model discussed in Section 4, could be easily expanded with the respective solubility products for future application.

Independent from the exact metal composition and whether an aging step is conducted or not, co-precipitation and the morphology of the resulting co-precipitate can influence the properties and performance of the resulting catalyst material significantly[58,85,135]. This correlation between co-precipitation and the performance of the final catalyst is often summarized; together with influences by aging, under the term "chemical memory"[31,72,78,136]. Hereby, influences of co-precipitation on the resulting catalyst are so profound that they are evident despite the aging step and despite the further solids formulation in the succeeding drying, calcination and shaping steps.

Studies by Jiang et al. showed that different mixer geometries and parameters in the co-precipitation affect the homogeneity of Cu/Zn distribution in the co-precipitate at nanoscale[84,85]. For this purpose, they investigated an Y mixer with an inner diameter of 0.6 mm and a Caterpillar mixer at relatively low total flow rates below 100 ml·min^{-1}. This corresponds to maximum velocities of approx. 3 m·s^{-1} in the inlets and a transient flow regime in the outlet between laminar and turbulent[137] ($Re_{\mathrm{mix}} \approx 1170$) when values for a co-precipitate suspension are assumed, cf. Table A.2. The chosen co-precipitation setup also affected the microstructure of the final catalyst. They subsequently investigated the impact of flow rate ($60 \leq Re_{\mathrm{mix}} \leq 1170$) and mixing times (400 ms to 20 ms) on the nanoscale homogeneity and activity of the resulting catalyst and found a positive impact of mixing intensity on both without an upper limit in the range considered[35]. On a similar note, Zhang et al. determined improvements in the physicochemical properties of CZA catalyst precursors and the subsequent catalyst performance for a continuous co-precipitation compared to a semi-batch process[73]. Kaluza et al. and Schur et al. also found that the activity of a continuously precipitated and aged catalyst was 50 % respectively 26 % higher compared to a semi-batch material, presumably due to changes in the morphology due to "a change in the kinetic boundary conditions"[58,135]. The same trend was found by Angelo et al. and Tofighi et al. in a microfluidic setup[86,138], where continuous co-precipitation led to a more homogeneous at nanoscale and more performant material, even more so after further process optimization[126]. However, all five studies did not provide details on why the physicochemical properties were improved by switching from a semi-batch to a continuous co-precipitation process.

In summary, these studies all show that co-precipitation, and especially mixing during initial solids formation, can significantly influence the properties of the resulting intermediates and catalysts. However, most of the studies are exploratory and provide no indication of why faster mixing leads to a better product. Furthermore, they are limited to volume flows significantly below 100 ml·min^{-1} ($Re_{\mathrm{mix}} \approx 1170$) making an industrial application difficult despite the seemingly beneficial impact on catalyst performance.

In contrast to these studies, there is also a series of publications concluding that the method and mixing characteristics of co-precipitation are insignificant for the properties of the resulting catalyst: Simson et al. prepared precatalysts by batch co-precipitation in a stirred tank reactor and by continuous co-precipitation in a micromixer, respectively. They found no significant differences in the morphology, composition and surface area[59]. Hartig et al. conducted precipitation simulations and experimental studies with a focus on the influences by mixing and pH for simplified Cu and Cu/Zn systems[60,71]. They concluded that the energy dissipation rate, which correlates with the volume flow according to Eq. (3.2), does not influence pH, solids mass or the median particle size in co-precipitation in the range investigated. However, their simulations did show that an increase of the energy dissipation rate from 10 W·kg^{-1} to 10^5 W·kg^{-1} accelerated the built-up of supersaturation in a mixing nozzle from more than 10^{-2} s to approx. 10^{-4} s without influencing the maximum supersaturation or the resulting particle size. This suggests that the calculations were exclusively conducted in a range where mixing is completed before solids formation starts, i.e. where solids formation is unaffected by mixing effects. The existence of such a non-mixing limited regime next to a regime where mixing does influence solids formation was verified for other precipitation processes[139,140].

In general, mixing in a micro jet mixer is limited by the micromixing time τ_{micro}[141] and can, therefore, be described using τ_{micro}. In the turbulent regime, where technical processes generally are conducted to ensure sufficient mixing, $\tau_{\mathrm{micro,turb}}$ is quantified with Eq. (6) as a function of the kinematic viscosity ν and the mean energy dissipation $\bar{\varepsilon}$ according to the engulfment model[142,143].

$$\tau_{\mathrm{micro,turb}} = \frac{12}{ln\,(2)} \cdot \left(\frac{\nu}{\bar{\varepsilon}}\right)^{\frac{1}{2}} \tag{3.1}$$

$\bar{\varepsilon}$ can be calculated based on the pressure drop induced by mixing Δp_{Mix}, the density ρ of the mixed fluid, the volume of the mixing zone V_{Mix}, the total volume flow $\dot{V}_{\mathrm{total}} = \dot{V}_{\mathrm{Feed1}} + \dot{V}_{\mathrm{Feed2}}$ and the mass flows $\dot{m}_i$ and mean velocities $\bar{u}_i$ of the feeds and in the outlet, cf. Eq. (3.2). Alternatively, all $\dot{m}_i$ and mean velocities $\bar{u}_i$ can be expressed as $\dot{V}_{\mathrm{total}}$ [144].

$$\bar{\varepsilon} = \frac{\Delta p_{\mathrm{Mix}} \cdot \dot{V}_{\mathrm{total}} + (\frac{1}{2} \cdot \dot{m}_{\mathrm{Feed1}} \cdot \bar{u}^2_{\mathrm{Feed1}} + \frac{1}{2} \cdot \dot{m}_{\mathrm{Feed2}} \cdot \bar{u}^2_{\mathrm{Feed2}} - \frac{1}{2} \cdot \dot{m}_{\mathrm{Mix}} \cdot \bar{u}^2_{\mathrm{Mix}})}{\rho \cdot V_{\mathrm{Mix}}} \tag{3.2}$$

Using $\bar{\varepsilon}$, a comparison between different mixer geometries that are limited by micromixing is possible. In this work, the same experimental setup is used for all investigations on continuous co-precipitation. Therefore, $\dot{V}_{\mathrm{total}}$ as the directly adjustable parameter is used to display and discuss the results instead.

In summary, the role of mixing in co-precipitation for the preparation of catalysts is still disputed. Most of the studies reported a correlation between mode of co-precipitation and catalyst performance, while some found no impact. One plausible explanation for the ambiguous results is that some studies conducted experiments in the mixing-influenced regime while others varied parameters, but still remained in the range where mixing is completed before solids formation begins[139,140]. Additionally, the influence of mixing was mostly investigated only on the surface. In general, solely the impact of different precipitation setups or the impact of different flow rates in a limited range on the nanoscale homogeneity and performance of the resulting catalyst were considered. Thus, structured data on the direct impact of mixing intensity on the co-precipitate as an intermediate is missing. Focusing on how mixing influences ion concentrations, pH and supersaturation spatially and temporally could help to understand co-precipitation and why it may impact the nanoscale homogeneity and morphology of the resulting catalyst as several studies suggest. Another challenge in previous studies might have been the occurrence of aging effects and secondary processes of the highly metastable co-precipitate which might explain the lack of experimental data on the co-precipitate[138].

Accordingly, the goal of this section is to apply the fundamentals of mixing theory to clarify if co-precipitation affects the quality of the resulting catalyst and if these fundamentals provide an explanation for the ambiguous conclusions in the literature. For this purpose, co-precipitation has to be separated from the aging step in order to rule out any influences by secondary processes and phase transformation. The process modified for this purpose is described in Section 2.3. First, this modified process is applied in Section 3.2 to verify if any influence of co-precipitation on the final catalyst quality is evident as suggested in the literature. Then, in Section 3.3, the roles of co-precipitation and local mixing effects during initial solids formation for the preparation of high-quality catalysts with defined properties are investigated in detail. Based on the available studies, the following two-parted working hypothesis is used:

Mixing can influence the morphology of the resulting co-precipitate if mixing and solids formation overlap temporally. Then, a change in the pH trajectory or in the amount of locally available lattice ions, e.g. by a modified precipitation approach, affects precipitation. The thus altered morphology withstands the subsequent process steps and can then, in turn, influence the morphology of the final catalyst and its performance.

The physicochemical and fluid-dynamic mechanisms and their interplay which explain why the co-precipitate properties are maintained throughout the further process chain and then influence the catalyst performance will be discussed as far as necessary for the scope of this work. However, a detailed analysis of this complicated topic would require a work of its own. Instead, the main focus of this section will be on how mixing influences the co-precipitate and if this effect also affects the resulting catalyst performance.

3.2 Semi-batch or continuous – how the operation mode influences product and productivity

The basic idea of this chapter is to validate if the strict separation of co-precipitation and aging by conducting co-precipitation as a continuous process in a micro jet mixer under strictly defined conditions does affect the morphology and nanoscale and interparticular homogeneity

of the precursor and, ultimately, also the catalyst performance. In this context, the sub hypothesis that the co-precipitate morphology is preserved throughout the further process chain and influences the later microstructure of the catalyst is to be discussed.

For this purpose, a CZZ catalyst is prepared, on the one hand, by a state-of-the-art semi-batch process with low volume flows where co-precipitation and aging overlap in time and space, cf. Section 2.3.2. On the other hand, a continuous co-precipitation and separated batch aging is conducted, cf. Section 2.3.1. The CZZ composition was chosen so that the impact of the precipitation method on the methanol synthesis from syngas rich in CO_2 can be evaluated in comparison to a state-of-the-art commercial catalyst. There are four main differences between both operation modes:

- For the continuous co-precipitation in the mixing nozzle, a large volume flow of $\dot{V}_{\mathrm{total}} = 600\ \mathrm{mL \cdot min^{-1}}$ is chosen. This ensures that mixing is conducted in the turbulent regime ($Re_{\mathrm{mix}} = 2109$), cf. Section A.3.3, and that mixing is completed before solids formation begins, cf. Section 3.3.
- Independent from the mean energy input, initial solids formation and depletion of supersaturation regarding zincian georgeite is completed in less than 1 s as determined by Hartig et al.[71] and confirmed by TEM imagining after 0.5 s, cf. Figure 2.4. Thus, using the continuous mode of operation, co-precipitation is completed before the co-precipitate suspension reaches the aging tank reactor after approx. 1.3 s.
- None of the co-precipitate particles that are formed in the continuous co-precipitation process experiences any relevant aging time and all particles will have the same aging time at the end of the process since $t_{\mathrm{prec}} \ll t_{\mathrm{age}}$ is valid for the Cu/ZnO based catalyst precursors.
- The pH and supersaturation trajectories that the respective particles traverse during solids formation differ, both temporally and spatially, as it is evident from Figure 3.1 and Figure 3.2, which are discussed below, as well as from Figure A.21 and Figure A.22 in the appendix,

Supersaturation, ionic strength and pH were calculated as a function of reactant composition using the thermodynamic model discussed in Section 4.2. In accordance with the experimental procedure, bulk pH for the semi-batch approach was adjusted to 6.7 by adding $NaHCO_3$. In Figure 3.1 and Figure 3.2, the initial supersaturation S_{init} is considered assuming complete mixing without solids formation, cf. Section 4.2 for further details. It represents a hypothetical boundary case where mixing is completed before solids formation begins and corresponds to the thermodynamically maximum supersaturation at set educt concentrations. In reality, this is not the case for the semi-batch process, where feed addition and initial solids formation overlap, but it helps to understand the underlying mechanisms of co-precipitation. For the semi-batch process, the intermixing of the metal nitrate feed solution into the bulk is considered. For time-resolved modeling, it is assumed that the added metals (Cu, Zn, Zr) completely convert to the respective solids (zincian georgeite, ZrO_2) within one time step ($\Delta t = 1\ \mathrm{s}$). Consequently, the time-resolved supersaturations depicted result from the additional amount of metal nitrate solution added within each subsequent time step. For the continuous

co-precipitation in the mixing nozzle, the equivoluminar blending of the metal nitrate solution with the $NaHCO_3$ solution is modeled.

In Figure 3.1, the development of the initial supersaturations of the target phases zincian georgeite ($S_{zg,init}$) and ZrO_2 ($S_{ZrO_2,init}$) over the duration of co-precipitation are plotted for both process variants. Additionally, the supersaturations of the undesired by-products rouaite ($S_{rou,init}$) and $Na_2Zn_3(CO_3)_4 \cdot 3\ H_2O$ ($S_{NaZn,init}$) are plotted, as well as the ionic strength I as an indicator for the amount of ions present in the surrounding solution. The co-precipitation in the mixing nozzle is conducted continuously at steady-state. Thus, each Cu^{2+} atom and each particle formed experiences the same conditions regardless if it is formed directly after start-up of the precipitation ($t_{prec} = 0$ min) or near the end when the aging tank is almost filled ($t_{prec} = 3$ min).

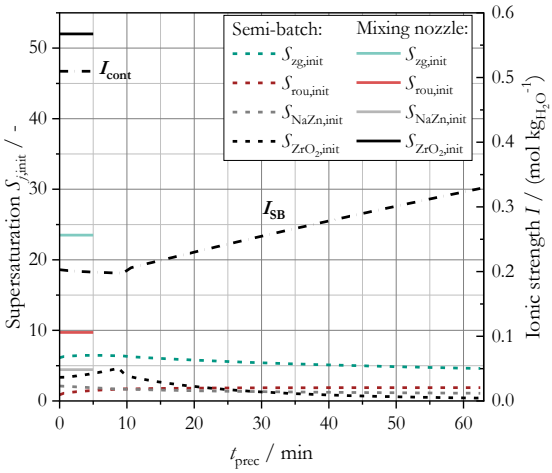

Figure 3.1: Time-dependent development of phase-specific initial supersaturations and ionic strength assuming ideal mixing without solids formation at each timestep for the semi-batch (SB) and the continuous (cont) co-precipitation.

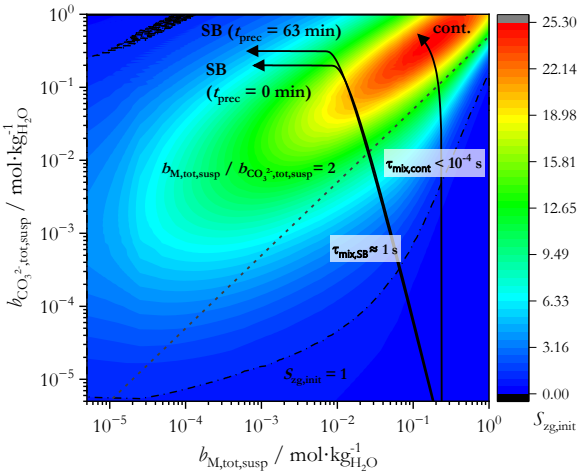

Figure 3.2: Maximum supersaturation of zincian georgeite as a function of reactant concentrations. The respective trajectories for a continuous co-precipitation (cont) and a semi-batch process (SB) show the development of supersaturation for a single Cu^{2+} ion travelling through the process. For the semi-batch process, two process time points are visualized (t_{prec} = 0 min and 63 min).

In contrast, the conditions for the semi-batch process, i.e. supersaturations and ionic strength, change with process time. The first drop of metal nitrate feed added to the reactor at $t_{prec} = 0$ min mixes and reacts with a pure $NaHCO_3$ solution (pH =7.9) with a low ionic strength $I = 0.20\ \text{mol} \cdot \text{L}^{-1}$. While pH is above the target value of 7.1 due to the initial surplus of $NaHCO_3$, I_{SB} is stable. As soon as additional $NaHCO_3$ needs to be added to maintain pH at 7.1 ($t_{prec} > 10$ min), I_{SB} increases. Thus, the last drop of the metal nitrate solution is mixed into a suspension with the predefined bulk pH of 7.1, but with a higher ionic strength ($I = 0.33\ \text{mol} \cdot \text{L}^{-1}$) due to the presence of additional counter ions (Na^+ and NO_3^-), as well as zincian georgeite particles. Due to the small volume flow of the metal nitrate solution and its dilution in the $NaHCO_3$ reservoir, $S_{zg,init}$ is lower compared to the continuous process in the mixing nozzle, although pH after solids formation is the same in both cases, cf. Figure A.22. Therefore, the supersaturation of zincian georgeite is much closer to the supersaturations of the by-products for the semi-batch process which may promote formation of these byproducts.

In addition to the temporal development of supersaturation during the semi-batch process, spatial inhomogeneities due to mixing times in the range of the solids formation time affect particle formation. This is evident from the trajectories plotted in the supersaturation map in Figure 3.2. The trajectories show the development in molalities and the resulting $S_{\mathrm{zg,init}}$ that the metal nitrate feed experiences during mixing with the bulk suspension, respectively with the $NaHCO_3$ feed. Again, the initial supersaturation without any solids formation in the respective time step is calculated. Additionally, the solubility curve for zincian georgeite ($S_{\mathrm{zg,init}} = 1$) and the stoichiometric ion ratio ($b_{M,\mathrm{tot,susp}} \,/\, b_{\mathrm{CO_3^{2-}},\mathrm{tot,susp}} = 2$), which in general leads to the maximum supersaturation[145–147], are highlighted. Due to the complex formation discussed in Section 4.5, the area of maximum supersaturation is shifted towards a nominal surplus of carbonate ions. For the semi-batch process two trajectories are given for two chosen process time points ($t_{\mathrm{prec}} = 0\ \mathrm{min}$ and $t_{\mathrm{prec}} = 63\ \mathrm{min}$), which differ in composition and ionic strength due to the presence of additional counter ions, to visualize the change in the trajectory over process time although the bulk pH is constant, cf. Figure A.21 and Figure A.22. The intermixing of the feed into the bulk at the chosen feed rate in the semi-batch approach ($\dot{V}_{\mathrm{Feed1}} = 1.6\ \mathrm{ml \cdot min^{-1}}$) takes, in general, at least 1 s at micro scale[148]. Thus, precipitation takes place over a wide range of pH, lattice ion concentrations and supersaturation ($1 \leq S_{\mathrm{zg,init}} \leq 20$). In contrast, the high-intensity mixing in the mixing nozzle is completed in less than 10^{-4} s and does not affect solids formation, cf. Figure 3.7. As a result, the end point of the trajectory is reached before solids formation begins and precipitation proceeds with a defined $S_{\mathrm{zg,init}} \approx 24$.

According to classical nucleation theory and literature on the influence of the mode of operation, the change from semi-batch to continuous and the associated change in the supersaturation profile should affect crystal shape and particle size of the CZZ co-precipitate significantly[149]:

- By aligning the precipitation conditions for each individual particle formed, the co-precipitate should become more uniform in size, composition and the spatial homogeneity at nanometer scale[149].
- By achieving higher supersaturations, the mean particle size should decrease as nucleation becomes increasingly dominant over crystal growth for increasing supersaturations[139,149–151].

The actual effect on the morphology of the aged intermediate is evident from Figure 3.3 and Figure 3.4 where SEM and TEM-EDX images for both approaches are compared.

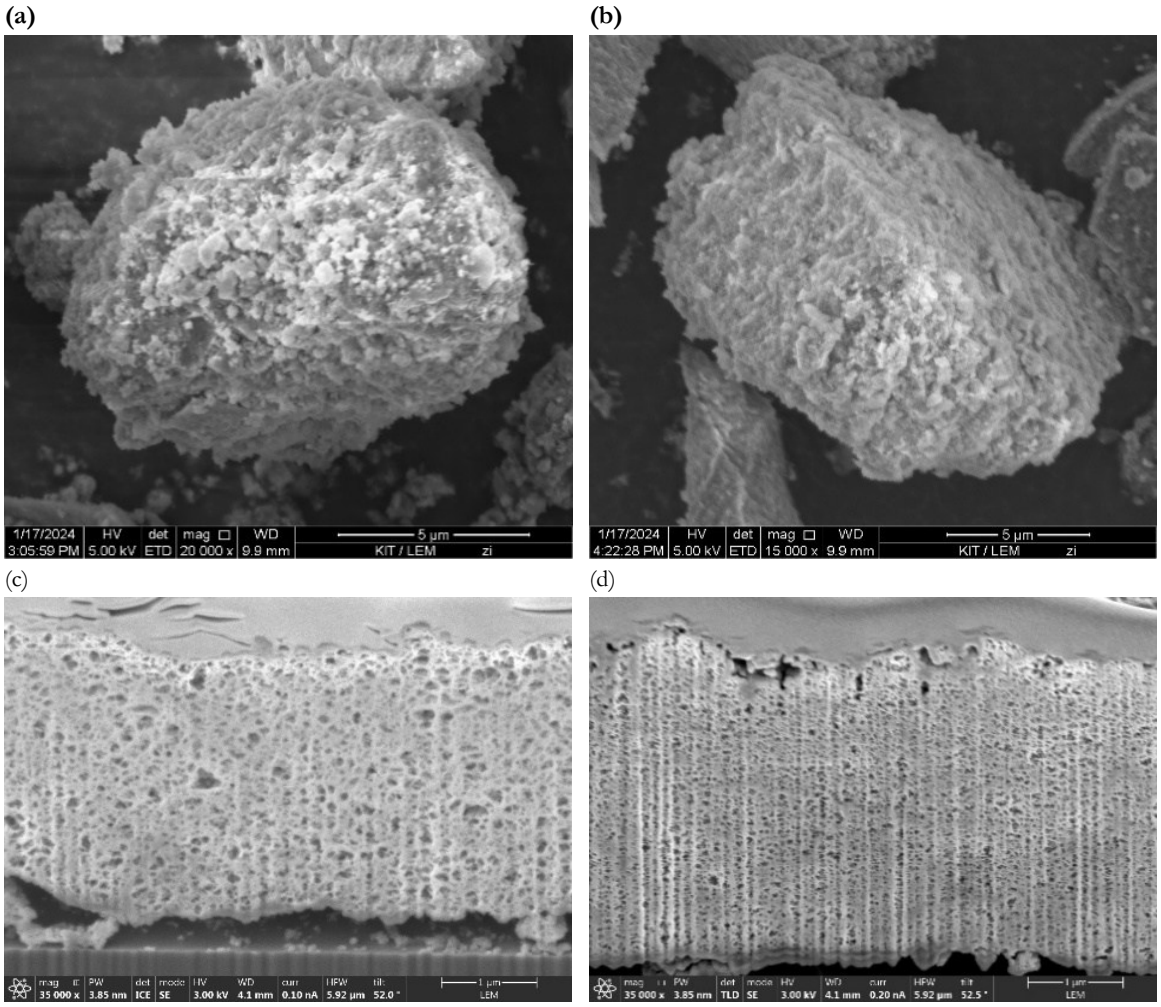

Figure 3.3: SEM images of the CZZ aged intermediate prepared by **(a)** semi-batch and **(b)** continuous precipitation and SEM images of the cross-sections of the respective samples prepared by FIB with **(c)** the semi-batch material and **(d)** the continuously precipitated material.

The SEM images of the CZZ aged intermediates in Figure 3.3 (a) and (b) show particles, respectively prepared by semi-batch (SB) and continuous (cont) co-precipitation, that look similar regarding morphology, surface texture and size. Also, XRD analyses confirmed zincian malachite as the main phase in both cases (Figure A.13) and a total Cu fraction in the metals of respectively 64 mol% despite the different concentration and pH pathways, cf. Table 3.1. For the semi-batch material, the aurichalcite fraction is increased by approx. 10 percentage points which probably results from the transient pH and supersaturation profile during intermixing and the changing solution composition and supersaturation over the process time despite keeping the bulk pH constant. More importantly, the respective cross-sections in Figure 3.3 (c) and (d) differ with the semi-batch material showing larger and more uneven pores. These observations are confirmed quantitatively by the evaluation of the crystallite sizes via XRD, which were determined to $d_{\mathrm{SB}} = 11.8 \pm 1.2\ \mathrm{nm}$ and $d_{\mathrm{cont}} = 7.0 \pm 0.4\ \mathrm{nm}$, and by the BET surface areas: $S_{\mathrm{BET,SB}} = 142 \pm 2\ \mathrm{m^2 \cdot g^{-1}}$ and $S_{\mathrm{BET,cont}} = 156 \pm 5\ \mathrm{m^2 \cdot g^{-1}}$. These characteristics may be a result of smaller and more uniform co-precipitate particles for the continuous precipitation under higher energy input, which is investigated in more detail in the subsequent chapter 3.3. Fast mixing leads to spatially defined and temporal constant lattice ion molalities and thus to effective supersaturations close to the maximum supersaturation

calculated in Figure 3.2[149,152]. This effect was also evident in the temporally resolved model calculations by Hartig et al.[71]. In general, increasing supersaturations typically result in smaller and increasingly homogeneous initial particles[139,150]. This was also the case here as evident from the crystallite sizes, pore characteristics and SEM images discussed above that show the co-precipitate particles that aggregated during aging and formed the intergrown aggregate depicted in Figure 3.3. Accordingly, bulk pH alone, despite its prominent role in the literature, is insufficient for the definition of constant precipitation conditions as it only contains immediate information on the activity of OH^- ions, but does not directly describe the availability of e.g. Cu^{2+}, Zn^{2+} and CO_3^{2-} ions. This is evident from the inhomogeneity of the semi-batch material in the two- to three-digit nanometer scale.

These effects are also evident in the precatalyst after calcination as illustrated by the data in Table 3.1. In two independent studies, the material from the continuous co-precipitation shows an increase of BET surface area and copper surface area by approx. 50 % to more than 100 % as well as smaller pores and CuO crystallites compared to materials from a semi-batch preparation and a commercial CZA catalyst. The copper fraction is comparable for all samples and corresponds to the target value of $x_{\mathrm{Cu,metals}} = 60\ \mathrm{wt.\%}$. Impurities in the form of Na^+ and NO_3^- ions are not present in any of the cases. The difference between $S_{\mathrm{Cu,meas1}}$ and $S_{\mathrm{Cu,meas2}}$ results from different sample preparation regarding fractionation and differences in the analytical methods, which are described in detail in Section 2.4.4 and by Polierer et al.[44]. Thus, the absolute values are only comparable to values from the same measurement routine, but both datasets show the same trend.

Table 3.1: Selected physicochemical properties of the precatalysts considered for performance tests.

Catalyst	$x_{\mathrm{Cu,metals}}$ (wt.%)	$x_{\mathrm{Na,total}}$ (wt.%)	$x_{\mathrm{N,total}}$ (wt.%)	S_{BET} ($m^2 \cdot g^{-1}$)	$S_{\mathrm{Cu,meas1}}$ ($m^2 \cdot g^{-1}$)	$S_{\mathrm{Cu,meas2}}$ ($m^2 \cdot g^{-1}$)	$d_{\mathrm{CuO,XRD}}$ (nm)	$\bar{d}_{\mathrm{pores}}$ (nm)
Continuous co-precipitation	61.6 61*	0 0	0 0	128 125*	68 -	- 27*	2.6 ± 0.1 4*	11 14*
Semi-batch co-precipitation	61.2 57*	0 0	0 0	107 65*	44 -	- 10*	3.6 ± 0.3 8*	14 18.5*
Commercial CZA catalyst	64*	0	0	91 98*	63	13*	4*	11*

*Data from Polierer et al.[44].

The effects of changing from a semi-batch co-precipitation to a continuous mode are also evident in the TEM(-EDX) images in Figure 3.4, which depict the precatalysts for both preparation methods. Additional images from a separate study, where the Zr is also visualized, are available in the appendix, cf. Figure A.9. For the semi-batch material, large areas of pure copper, respectively, zinc enrichments exist. These clusters are not present in the precatalyst prepared continuously. Here, Cu and Zn are finely and homogeneously dissipated as small CuO and ZnO crystallites on the one- to two-digit nanometer scale. Furthermore, spherical particles with a diameter of $x > 100\ \mathrm{nm}$ are present in the semi-batch material complementary to a dominant number of particles with $x \ll 100\ \mathrm{nm}$ aggregated to a net-like structure. In contrast, the continuously precipitated material consists exclusively of intergrown particles with $x \ll 100\ \mathrm{nm}$. This difference in the microstructure explains the diverting values for S_{BET} and S_{Cu}. The clusters may be a result of local pH extrema resulting from insufficient mixing during co-

precipitation. Since the pH regimes for the precipitation of copper and zinc salts differ[82,105], the amount of Zn incorporated into zincian georgeite varies depending on the local pH Thus, low fractions of hydrozincite form additionally to zincian georgeite and outlast aging as confirmed by Rietveld refinement, cf. Figure A.13. These differences in the microstructure of the precatalyst confirm that influences by co-precipitation are maintained throughout the subsequent process steps.

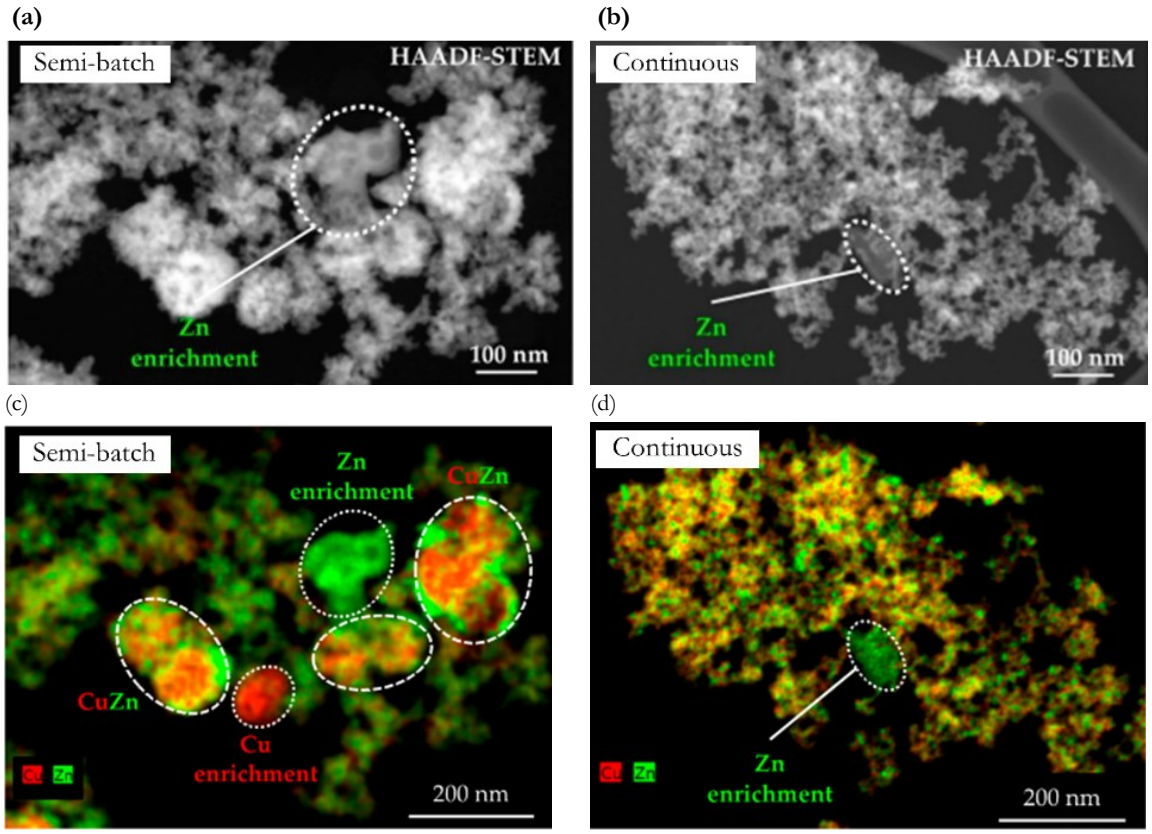

Figure 3.4: TEM images of the precatalysts prepared by (a) semi-batch and (b) continuous co-precipitation with $\dot{V}_{\text{total}} = 300\ \text{mL} \cdot \text{min}^{-1}$ as well as TEM-EDX images of the same materials: (c) semi-batch and (d) continuous with red: Cu, green: Zn. From Polierer et al. and Guse et al.[44,101].

In general, an increase of the BET and specific Cu surface areas correlates with a vastly improved catalyst performance[36,37,41] with minor beneficial effects by reduced mean pore size and crystallite size[46,47]. Accordingly, the three catalysts from the two independent studies were investigated in two separate syntheses to verify if this effect is also evident for the adapted precipitation method. For this purpose, the materials from the first study were applied in a methanol synthesis, cf. Eq. (1.1) and Figure 3.5, and the materials from the second study were tested in a direct dimethyl ether (DME) synthesis, cf. Eq. (1.4) and Figure 3.6. In both cases, the productivity was evaluated as a function of the volumetric ratio of CO_2 to CO_2 and CO in the syngas at a constant H_2 fraction.

For the methanol synthesis in Figure 3.5, a relatively low pressure $p = 30\ \text{bar}$[9,18], a small GHSV of 4.41 s^{-1}, cf. Eq. (2.10), and a relatively short time-on-stream, cf. Section 2.5, were applied, which may have put the conversion outside the kinetic region where the individual performance of the respective catalyst is most significant[20,44,122,153]. Therefore, this performance test is used solely as a functional test of the manufactured materials without any in-depth

interpretation of potential differences. Following this principle, all manufactured catalysts can be confirmed as active, regardless of whether they are operated with a CO/CO_2 mixture or pure CO_2 as the feed gas.

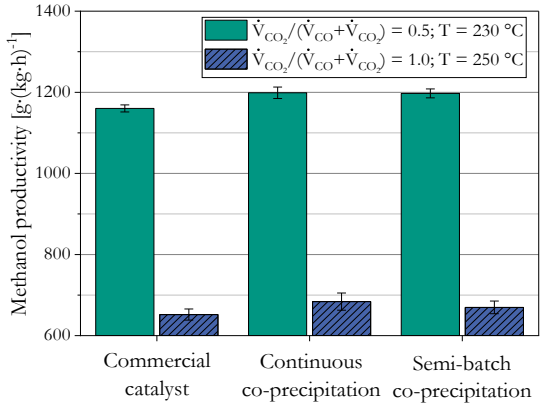

Figure 3.5: Functional test of the manufactured CZZ catalysts and a commercial CZA catalyst. The methanol synthesis was conducted at $p = 30$ bar and a GHSV of 4.41 s^{-1}.

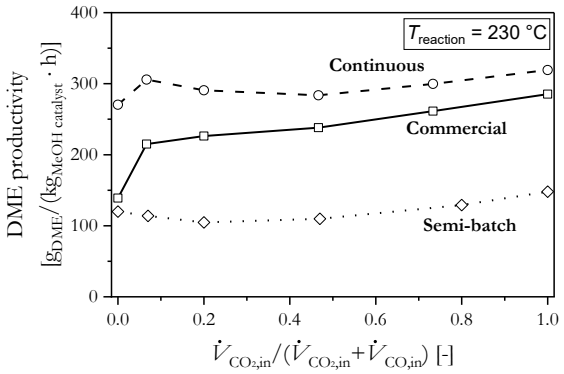

Figure 3.6: DME productivity as a function of syngas composition for three different CZ catalysts in combination with a H-FER 20 zeolite for dehydration. Synthesis parameters: $p = 50$ bar, GHSV = 8.8 s^{-1}. Based on data from Polierer et al., Guse et al. and Wild et al.[20,44,101].

In contrast, the direct DME synthesis in Figure 3.6 was conducted at a doubled GHSV of 8.8 s^{-1} and strictly in the "strongly kinetically controlled" regime regarding the conversion of CO and CO_2 to MeOH, cf. Wild et al.[20] and Polierer et al.[44]. Here, the performance results do confirm the expectations from the precatalyst characterization. Over the complete range of syngas composition investigated, the continuously prepared CZZ catalyst outperforms the semi-batch catalyst by a factor of two to three. The commercial CZA benchmark catalyst consistently has a higher DME productivity than the semi-batch material, but shows productivities that are 10 to over 50 % lower than those of the catalyst precipitated in the jet mixer. The same tendencies are evident for a reaction temperature of 250 °C as discussed in the literature[44,101].

In summary, how co-precipitation is carried out impacts the subsequent particle properties, i.e. the microstructure of the precatalyst, significantly. The spatially and temporal homogeneous conditions during initial solids formation in a jet mixer improve the homogeneity of the precatalyst and aged intermediate at nanoscale and improve their BET and Cu surface areas compared to a material prepared with a state-of-the-art semi-batch process. The improved properties are most probably the result of clearly defined and spatially homogeneous pH, ionic concentrations and supersaturation during solids formation and higher effective supersaturations due to intense mixing. The influence of mixing is further investigated in the following section. This also confirms that influences by co-precipitation are maintained throughout the subsequent process steps. S_{BET} and S_{Cu} are known key characteristics determining the performance of the catalyst in MeOH and DME synthesis. Accordingly, the continuously prepared material outperformed the semi-batch material by a factor of at least two in DME synthesis with MeOH as an intermediate and, furthermore, showed better productivities than a commercial CZA catalyst for all process conditions investigated. Based on these results, conducting the co-precipitation continuously in a micro jet mixer is recommended

to guarantee the formation of a highly performant catalyst with large surface areas and a homogeneous nano- and microstructure.

3.3 Influence of mixing on the co-precipitate and the catalyst

The comparison of a continuous co-precipitation in a jet mixer with the state-of-the-art semi-batch co-precipitation in a stirred tank reactor in the previous section confirmed that how mixing is carried out during co-precipitation can, in general, affect the final catalyst and its performance in MeOH synthesis significantly. Based on these findings, this chapter aims at understanding how exactly mixing during co-precipitation can affect the performance of the final catalyst despite the multi-step character of the preparation. For this purpose, first it is quantified how changing the mixing intensity in the impinging micro jet mixer influences the morphology and composition of the co-precipitate quantitatively. In a second step, it will be investigated how these alterations in the morphology are maintained throughout the further process steps and whether the catalyst performance can be optimized by achieving certain mixing intensities during initial solids formation.

The morphology of the co-precipitate can be quantified by its PSD, its specific surface area and the material homogeneity at nanoscale and in between individual particles. The volume-based median particle size $x_{50,3}$, as the representative for a monomodal PSD, is plotted as a function of the total volume flow $\dot{V}_{\mathrm{total}}$ and the micro mixing time τ_{micro} in Figure 3.7. τ_{micro} was calculated based on pressure drop measurements and semi-empirically determined energy dissipation rates as described in Section A.3.3 in the appendix. Here, a simplified binary Cu/Zn based catalyst precursor is investigated first. The rationale behind this approach is that the interaction between Cu and Zn ions and Cu/Zn based salts dominate solids formation and the phase composition of the co-precipitate and aged precursor[18,78]. Meanwhile, the third and possibly fourth metal component with mass fractions of generally $x \leq 10\ \mathrm{wt.\%}$ precipitates separately, as is the case for ZrO_2 [93], or is added to the process already as a solid[56,63]. Furthermore, the study is to be representative for a large variation of Cu/Zn based catalyst recipes regardless of which metal oxides are added as the third and/or fourth component. Complementary to the PSD, the influence of mixing intensity on the specific surface area was investigated, cf. Figure 3.8.

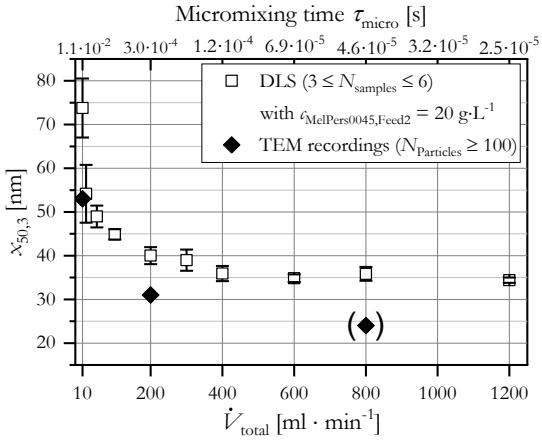

Figure 3.7: Median particle size $x_{50,3}$ as a function of the total volume flow for a Cu/Zn based co-precipitate. Comparison of dynamic light scattering (DLS) measurements from at least three independent precipitations with TEM imaging. Adapted from Guse et al.[101].

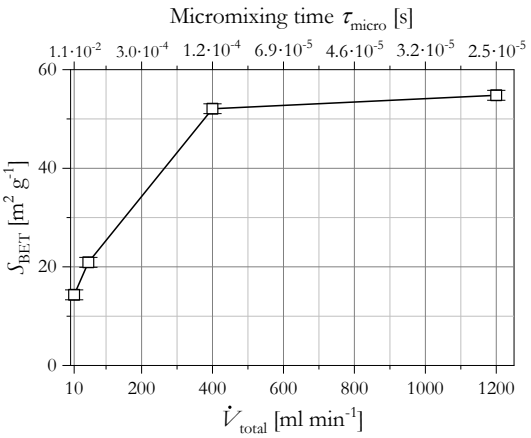

Figure 3.8: Mass-specific surface area S_{BET} of the Cu/Zn based co-precipitate as a function of total volume flow. Adapted from Guse et al.[101].

The data determined by DLS can be separated into two regimes. For small volume flows $\dot{V}_{\mathrm{total}} < 400\ \mathrm{mL \cdot min^{-1}}$ ($u_{\mathrm{Feed1}} = u_{\mathrm{Feed2}} = 17\ \mathrm{m \cdot s^{-1}}$) in the laminar and transition regime, the median particle size $x_{50,3}$ decreases with increasing $\dot{V}_{\mathrm{total}}$ until a minimum of $x_{50,3} \approx 35\ \mathrm{nm}$ is reached for $\dot{V}_{\mathrm{total}} \approx 400\ \mathrm{mL \cdot min^{-1}}$, which corresponds to the beginning of the turbulent regime. Above this threshold, a further increase of the mixing intensity, by further increasing $\dot{V}_{\mathrm{total}}$, does not affect the median particle size anymore. The increased particle size in the mixing-influenced regime results from a decreased effective supersaturation of zincian georgeite compared to the thermodynamically maximum value for an ideal mixing of both reactant solutions as plotted in Figure 3.2. For micro mixing times above $1.2 \cdot 10^{-4}$ s, solids formation and intermixing of the reactants happen simultaneously which reduces the local carbonate concentration and supersaturation. Thus, particle growth becomes more relevant and PSD shifts towards bigger particle sizes[149,154]. Spatial and temporal inhomogeneities for $\tau_{\mathrm{micro}} > 1.2 \cdot 10^{-4}\ \mathrm{s}$ also explain the increased span of the PSD. For $\dot{V}_{\mathrm{total}} \geq 400\ \mathrm{mL \cdot min^{-1}}$, mixing is quasi-instantaneous and completed before solids formation sets in. Thus, the theoretical maximum supersaturation is reached initially and is then gradually depleted by solids formation. In general, higher supersaturations result in more, but finer particles due to the domination of homogeneous nucleation in this range[149,154].

TEM imaging shows the presence of spherical particles independent from volume flow, cf. Figure 2.4 and Figure A.7 in the appendix. Partly, a strong tendency towards agglomeration is evident despite the use of MelPers0045 as an electro-steric stabilizer. Furthermore, samples were only stable to a limited extent in the TEM setup and showed a reduction in size with prolonged exposure, possibly due to the evaporation of CO_2 and/or H_2O from the amorphous solid, cf. Figure A.5 in the appendix. This also affected the accuracy of the semi-automated size analysis from the TEM images. In principle, the trend from DLS evaluation is confirmed. However, the absolute sizes are up to 30 % smaller in the non-mixing limited regime. In accordance with the size analysis, the specific surface area S_{BET} of the co-precipitate in Figure 3.8 shows the same trend as a function of volume flow: as long as solids formation is influenced by mixing, S_{BET}

increases with $\dot{V}_{\mathrm{tot}}$. As soon as the particle size is unaffected by mixing, the same applies for the surface area as is to be expected in theory.

In contrast, the composition of the co-precipitate is, at a first glance, unaffected by changing the mixing intensity as is evident from the FT-IR analyses in Figure 3.9. PXRD analysis confirmed that all co-precipitate samples are amorphous, cf. Figure A.14.

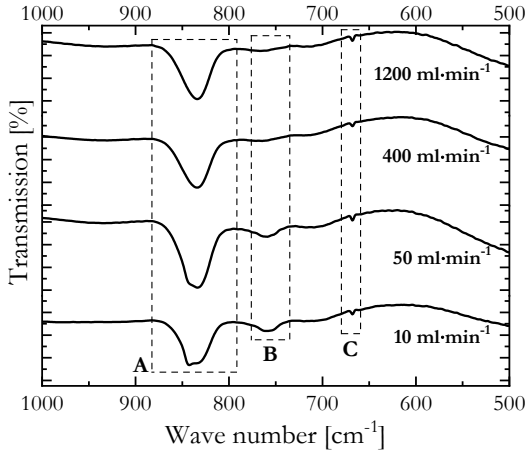

Figure 3.9: Excerpts of the FT-IR spectra for various total volume flows $\dot{V}_{\mathrm{total}}$ for the Cu/Zn based co-precipitate. Areas marked with A, B and C correspond to bands of (zincian) georgeite, asymmetric O-C-O bending mode of CO_3^{2-} ions and metal-O interactions, respectively. Adapted from Guse et al.[101].

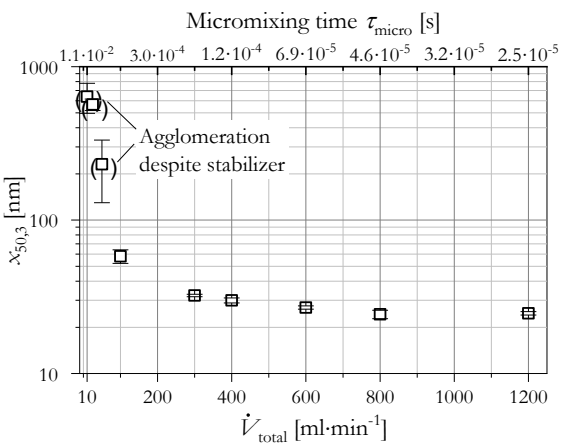

Figure 3.10: Median particle size $x_{50,3}$ by DLS measurements from at least three independent precipitations as a function of the total volume flow for a Cu/Zn/Zr based co-precipitate. Adapted from Guse et al.[101].

For $\dot{V}_{\mathrm{total}} = 1200\ \mathrm{mL \cdot min^{-1}}$ ($u_{\mathrm{Feed1}} = u_{\mathrm{Feed2}} = 51\ \mathrm{m \cdot s^{-1}}$) and $\dot{V}_{\mathrm{total}} = 400\ \mathrm{mL \cdot min^{-1}}$ ($u_{\mathrm{Feed1}} = u_{\mathrm{Feed2}} = 17\ \mathrm{m \cdot s^{-1}}$), there are no detectable differences in the relative intensities and band locations, indicating the same phase composition. The most prominent band in area A corresponds to the anticipated main phase georgeite[70,88]. For the two lower volume flows this band flattens and instead a small band in area B becomes apparent. Bands in the region 760 cm^{-1} to 700 cm^{-1} correspond to the asymmetric O-C-O bending mode of CO_3^{2-} ions and their "intensity […] decreases when copper ions are replaced by zinc ions"[155]. This indicates that less Zn is incorporated into zincian georgeite for volume flows in the mixing-influenced regime. Yet, the total zinc fraction in the metals remains unchanged between 27 ± 3 mol% and 31 ± 3 mol% for all volume flows indicating that Zn possibly enriches in the solid at low volume flows as a separate phase. This is affirmed by the TEM-EDXS images in Figure 3.11 where no stabilizer was applied.

For $\dot{V}_{\mathrm{total}} = 50\ \mathrm{mL \cdot min^{-1}}$ ($u_{\mathrm{Feed1}} = u_{\mathrm{Feed2}} = 2\ \mathrm{m \cdot s^{-1}}$), i.e. mixing in the laminar regime, isolated spherical particles are present that show a distinctive core-shell structure with a copper-rich core and a zinc-rich shell. Based on the total volume flow and the travel distance between jet mixer and dilution vessel, about 0.5 s have passed between the first contact of reactants and the dilution of the co-precipitate suspension in water[101]. The distinct spatial separation of Cu and Zn atoms indicates that the metals are not bound in a common crystal lattice, but exist as separate solid phases which precipitated one after the other forming a common aggregate. The aforementioned XRD and FT-IR analyses confirm that independent from volume flow no zincian malachite, aurichalcite or hydrozincite is present. Thus, the definition of the co-

precipitate in Section 2.1 is justified. A further investigation of the respective Cu and Zn based primary particles as preceding intermediates in solids formation may be possible using a Cryo-TEM setup[156]. However, this is beyond the scope of this work which is geared towards application. Thus, the Cu/Zn based aggregates are considered as the relevant intermediate after co-precipitation.

$\dot{V}_{\mathrm{total}} = 50\ \mathrm{ml} \cdot \mathrm{min}^{-1}$

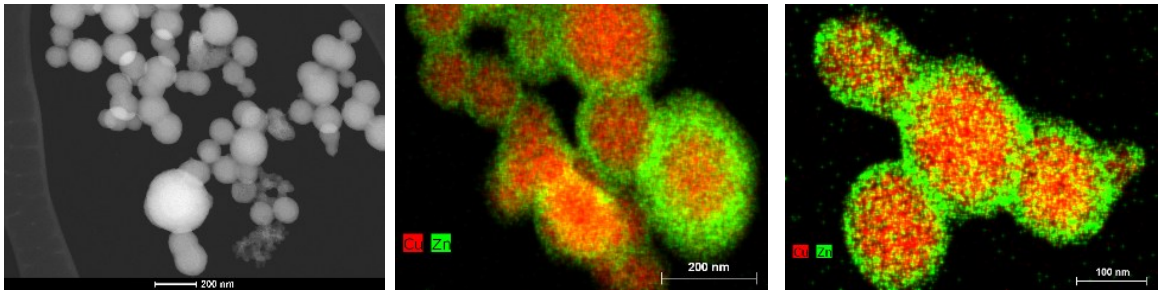

$\dot{V}_{\mathrm{total}} = 900\ \mathrm{ml} \cdot \mathrm{min}^{-1}$

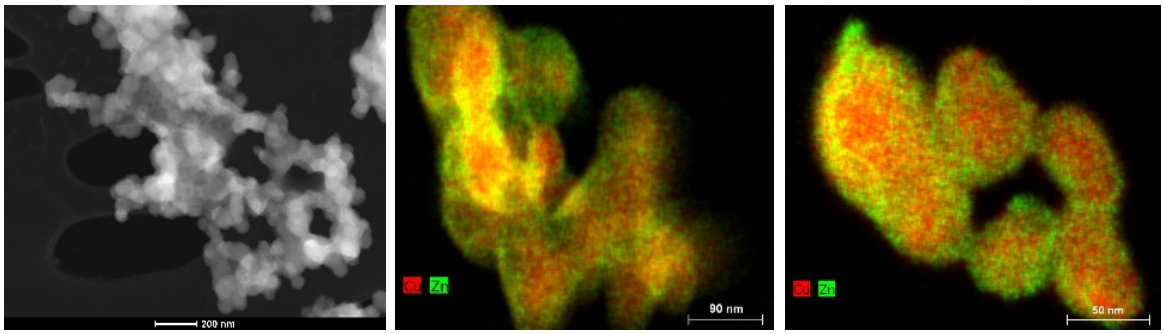

Figure 3.11: TEM(-EDXS) images showing the morphology and, respectively, the Cu (red) and Zn (green) distribution of Cu/Zn based co-precipitate in dependence of the total volume flow in three different areas without addition of a stabilizer.

For $\dot{V}_{\mathrm{total}} = 900\ \mathrm{mL} \cdot \mathrm{min}^{-1}$ ($u_{\mathrm{Feed1}} = u_{\mathrm{Feed2}} = 38\ \mathrm{m} \cdot \mathrm{s}^{-1}$), a sufficiently large volume flow in the turbulent mixing regime to exclude any influences by mixing, the particles are halved in size, much more aggregated and more homogeneous on the one-digit nanometer scale. Yet, there are still areas where Zn accumulates. This most probably results from the fact that the total Zn fraction in the co-precipitate ($29\ \mathrm{mol\%} \leq \tilde{x}_{\mathrm{Zn,M}} \leq 32\ \mathrm{mol\%}$) exceeds the maximum possible Zn fraction in zincian georgeite ($\tilde{x}_{\mathrm{Zn,zg}} = 27\ \mathrm{mol\%}$)[66]. The excess Zn^{2+} ions then precipitate separately as e.g. amorphous $ZnCO_3$ or $Zn(OH)_2$ at a slower rate due to a different dependency of supersaturation with pH[82] and attach to the surface of the zincian georgeite particles already present. For small volume flows in the mixing-limited regime, solids formation is possibly controlled by a shortage of CO_3^{2-} ions. Thus, due to faster kinetics, first a Cu-rich solid forms. Then, Zn^{2+} precipitate as soon as additional carbonate ions are available by further mixing of the two feed solutions resulting in the shell rich in Zn.

Fast aggregation occurs due to the metastable nature of zincian georgeite and the underlying supersaturation towards zincian malachite, cf. Figure A.33. Aggregation happens faster for $\dot{V}_{\mathrm{total}} = 900\ \mathrm{mL} \cdot \mathrm{min}^{-1}$ due to the smaller particle size and the correspondingly higher specific surface area. The weight fraction of the impurities Na^+ and NO_3^- was below 0.5 wt.% in each case and negligible considering the measurement accuracy.

The same mixing study was repeated in Figure 3.10 for a CZZ catalyst precursor to validate whether the results are reproducible for the more complex ternary catalyst. Compared to the CZ based co-precipitate, $x_{50,3}$ is increased in the laminar mixing regime ($\dot{V}_{\mathrm{total}} \leq 50\ \mathrm{mL \cdot min^{-1}}$) by up to a factor of 10. TEM-EDXS images indicate that agglomeration and aggregation are not prevented completely at low volume flows, cf. Figure A.6. This possibly correlates with the presence of ZrO_2 as a third component which precipitates independently from the Cu and Zn phases as initially small particles[93] and may promote agglomeration this way, cf. Figure A.8. Due to the low amount of Zr in the reactant solution, only a few of the aggregates at the bottom left in Figure A.6 show measurable, but negligibly small quantities of Zr (5 mol%). For this reason and due to the independence between Cu/Zn based phases and Zr phases during precipitation and aging, cf. Sections 3.1 and 4.1, the neglection of Zr ions and the focus on the interaction of Cu and Zn ions during co-precipitation and aging is deemed adequate. Similar to the binary co-precipitate, the median particles size $x_{50,3}$ decreases with increasing volume flow until a minimum of $x_{50,3} \approx 25\ \mathrm{nm}$ is reached for $\dot{V}_{\mathrm{total}} = 400\ \mathrm{mL \cdot min^{-1}}$ ($u_{\mathrm{Feed1}} = u_{\mathrm{Feed2}} = 17\ \mathrm{m \cdot s^{-1}}$), i.e. and particle size no longer is affected by more intense mixing.

Thus, in both cases, a mixing-influenced regime and a non-mixing influenced regime exist and in which regime mixing is carried out influences the co-precipitate morphology significantly. This is a plausible explanation for the contradictory statements in the literature regarding the influence of mixing in co-precipitation, cf. Section 3.1. Studies, where no influence was evident[59,60,71], may have been conducted in the non-mixing limited regime. For the setup and concentrations considered here, a minimum volume flow of $\dot{V}_{\mathrm{total,crit}} \approx 400\ \mathrm{mL \cdot min^{-1}}$ must be chosen to rule out mixing influences in the co-precipitation and obtain the highest effective supersaturation possible, cf. Eq. (3.3). If this condition is met, primary particles and, accordingly, the aggregates, decrease in size down to a threshold only limited by solids formation kinetics. According to a vast number of studies and the results of the previous section, these changes in morphology should persist throughout aging, drying and calcination and predetermine the microstructure of the resulting catalyst, i.e. the pore structure, specific surface area and copper surface area[58,84–86,135,138].

$$\lim_{\dot{V}_{\mathrm{total}} \to \dot{V}_{\mathrm{total,crit}}} S_{\mathrm{eff}} = S_{\mathrm{max}} \tag{3.3}$$

However, this is not the case here as is evident from Table 3.2, where the key quantities for the CZZ aged intermediate prepared with varying volume flows during co-precipitation but otherwise identical precipitation and aging conditions are compared. The aging time was adjusted according to the required transformation time in each case, cf. Section 5.2.

Table 3.2: Selected physicochemical properties of the CZZ aged intermediate for different mixing intensities during co-precipitation.

$\dot{V}_{\mathrm{total,prec}}$ (ml·min^{-1})	$\tilde{x}_{\mathrm{Cu,metals}}$ (mol%)	$\tilde{x}_{\mathrm{Zn,metals}}$ (mol%)	$\tilde{x}_{\mathrm{Zr,metals}}$ (mol%)	$x_{\mathrm{Na,total}}$ (wt.%)	$x_{\mathrm{N,total}}$ (wt.%)	$x_{\mathrm{zm,XRD}}$ (wt.%)	$\tilde{x}_{\mathrm{Zn,zm}}$ (mol%)	$d_{\mathrm{zm,XRD}}$ (nm)	S_{BET} (m^2·g^{-1})
25	63.7 63.5	27.5 27.5	8.8 9.0	0 0	0 0	98.6 ± 5.2	26.9 ± 0.1	8.5 ± 0.5	150
50	67.9 63.9	25.5 27.0	6.5 9.1	0 0	0 0.02	97.1 ± 0.2	26.9 ± 0.2	8.5 ± 0.5	170
100	63.7	28.6	7.7	0	0	90.5 ± 5.0	26.9 ± 0.1	7.2 ± 0.8	n.a.
600	63.6 ± 0.6*	28.1 ± 0.6*	8.2 ± 0.9*	0	0.04 ± 0.06*	96.9 ± 2.1*	26.9 ± 0.5	5.8 ± 0.6*	156 ± 5

*Mean value based on four independent preparations; n.a.: not available.

All samples, regardless of the mixing intensity during co-precipitation, show the same metal composition and phase composition as far as reproducibility and measuring accuracy allow. In each case, zincian malachite is present as the main phase ($x_{\mathrm{zm,XRD}} \gg 90\ \mathrm{wt.\%}$) with maximum Zn fractions of $\tilde{x}_{\mathrm{Zn,zm}} \approx 27\ \mathrm{mol\%}$ according to Rietveld refinement. Small amounts of surplus Zn are present as hydrozincite. There are also no apparent deviations between the samples in terms of the specific surface area, the incorporation of impurities or the morphology and pore structure, cf. Figure A.10 in the appendix. Only the crystallite size $d_{\mathrm{zm,XRD}}$ shows a weak tendency, which correlates with the development of the particle size of the co-precipitate.

Based on these results, aging seems to annihilate any differences in morphology and composition which were present for the co-precipitate samples. This is in contrast to the results of the previous chapter where the disparities for a semi-batch and continuous co-precipitation were maintained throughout aging and calcination. The main difference between both cases is that even for low volume flows in the mixing-influenced regime, each particle experiences similar conditions during initial solids formation in the continuous preparation whereas the speciation, ionic strength and amount of solids change with time for the semi-batch process. This can lead to a much more inhomogeneous solid during aging regarding particle size and the phase and metal composition in between individual particles and at nanometer scale. This assumption is confirmed by the SEM images in Figure 3.12. For the semi-batch preparation, spherical non-aged particles and crystalline particles in the μm range are present simultaneously. In contrast, for the continuous preparation in the mixing-influenced regime, only one type of particles is evident after 15 min of aging: an aggregate composed of individual nanoscale particles.

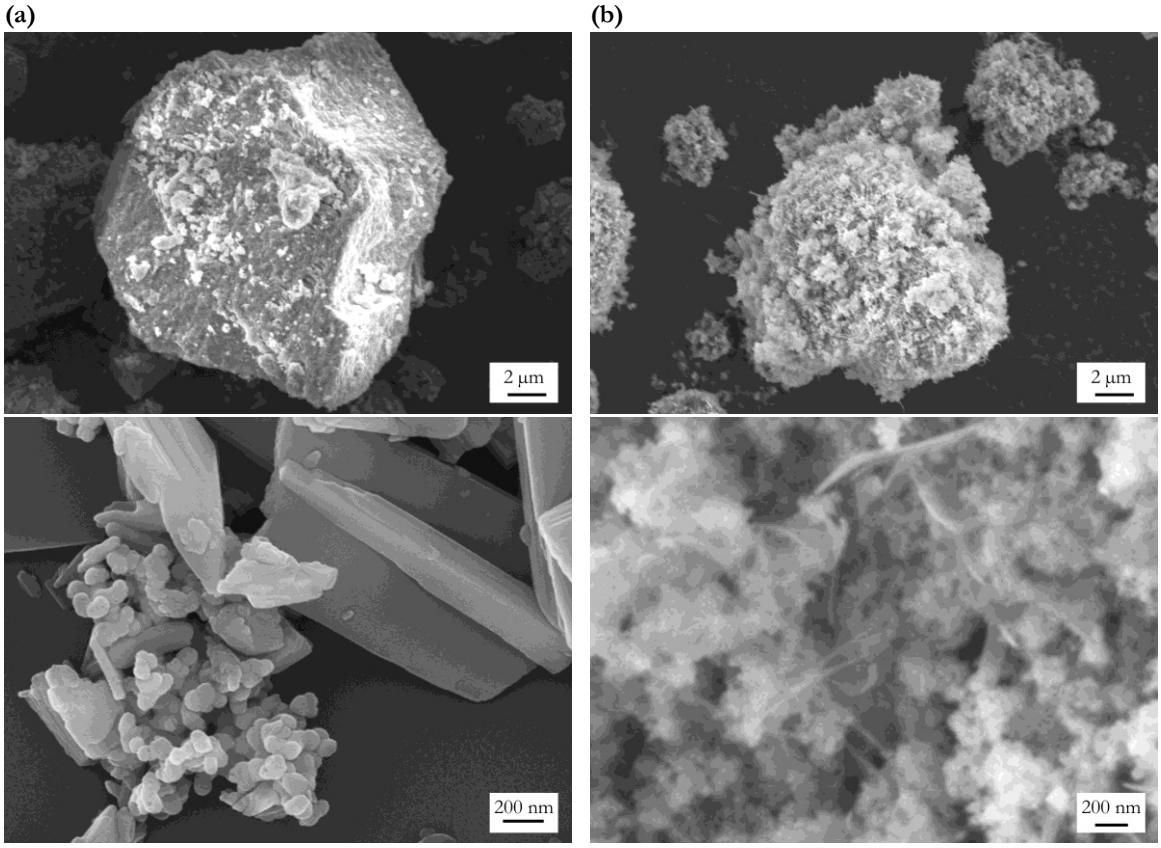

Figure 3.12: SEM images of a (a) CZZ semi-batch sample and (b) a continuously precipitated CZZ sample ($\dot{V}_{\mathrm{total}} = 50\ \mathrm{ml \cdot min^{-1}}$) for $t_{\mathrm{age}} \approx 15$ min.

Jiang et al. suggested a similar explanation for the importance of a high degree of homogeneity between individual co-precipitate particles and that aging will not completely annihilate these inhomogeneities[35]. Due to the variation in crystal size and composition, the chosen aging time may be insufficient to mitigate all inhomogeneities of the semi-batch samples, e.g. via a dissolution step as proclaimed in literature[75,78]. This is affirmed by the previously discussed residual amounts of aurichalcite in the solids, cf. Figure A.13, and the inhomogeneous particle composition on the one- to two-digit nanometer scale, cf. Figure 3.4. In contrast, the inhomogeneity of particles that were precipitated continuously, but in the mixing-influenced regime ($\dot{V}_{\mathrm{total}} \leq 400\ \mathrm{ml \cdot min^{-1}}$), is limited to within the individual particles, cf. Figure 3.11. In this case, the gradient in the metal composition at nanoscale can be completely eliminated by sufficiently long aging, as all particles require an identical time for phase transformation[35].

As to be expected from the analysis of the aged intermediate, the precatalyst properties also do not differ when comparing material precipitated in the mixing-influenced regime with material precipitated in the non-mixing limited range, cf. Table 3.3.

Table 3.3: Selected physicochemical properties of the CZZ precatalysts for different mixing intensities during co-precipitation.

$\dot{V}_{\mathrm{total,prec}}$ (ml·min^{-1})	$\tilde{x}_{\mathrm{Cu,metals}}$ (mol%)	$\tilde{x}_{\mathrm{Zn,metals}}$ (mol%)	$\tilde{x}_{\mathrm{Zr,metals}}$ (mol%)	S_{BET} ($m^2 \cdot g^{-1}$)	S_{Cu} ($m^2 \cdot g^{-1}$)	$d_{\mathrm{CuO,XRD}}$ (nm)	$\bar{d}_{\mathrm{pores}}$ (nm)
25	63.7	27.5	8.8	126	46	2.9 ± 0.3	11
600	64.3 ± 0.2*	27.7 ± 0.2*	8.0 ± 0.0*	127 ± 2*	68	3.3 ± 0.7*	13 ± 2*

*Mean value based on three independent preparations.

The only exception is the specific copper surface area S_{Cu}, which is reduced by 50 % for the reduced volume flow of $25\ \mathrm{ml \cdot min^{-1}}$ which corresponds to laminar mixing ($Re_{mix} = 88$) in the mixing-influenced regime. S_{BET} is equal for both preparation approaches. Thus, the inhomogeneous metal distribution within the individual particles at nanoscale, that is visualized in Figure 3.11, may be the reason for this apparent reduction. This would suggest that the chosen aging time has been too short to completely eliminate the gradients that are apparent in the co-precipitate samples. Based on the overall small differences in their properties, the productivities of both catalysts should be similar. The respective MeOH productivities in a MeOH synthesis are plotted in Figure 3.13 for two different CO/CO_2 ratios. They serve solely as a functional test of the differently prepared catalysts, cf. Section 2.5 and Section 3.2.

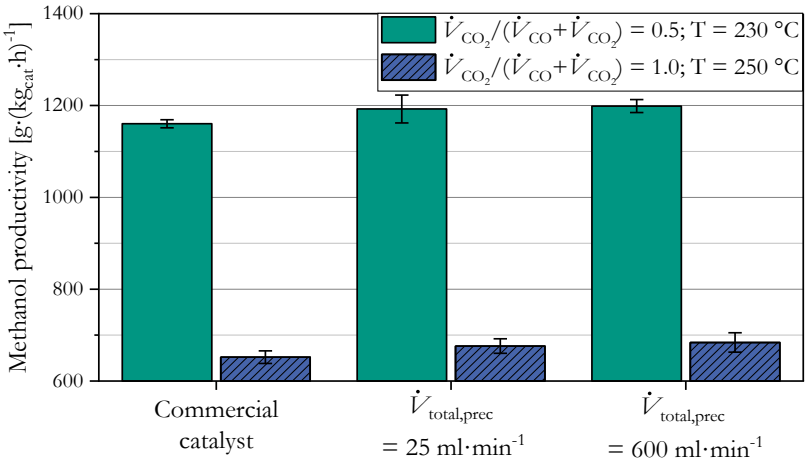

Figure 3.13: Functional test of CZZ catalysts prepared with different volume flows during co-precipitation and a commercial CZA catalyst. Methanol synthesis with $p = 30$ bar and GHSV of 4.41 s^{-1}.

Both prepared catalysts are confirmed to be active regardless of volume flow during co-precipitation and regardless of feed gas composition. Their activity is also verified when compared to a commercial CZA catalyst. Accordingly, neither a coherent influence of the mixing intensity during continuous co-precipitation on the precatalyst properties nor a definitive correlation between the co-precipitate morphology and the performance of the resulting catalyst exists in this case.

In summary, a clear correlation between the mixing intensity during co-precipitation and the particle size as well as metal distribution of the co-precipitate on the nanometer scale was found. For lower volume flows, here for total volume flows in the micro-mixing nozzle of less than $\dot{V}_{total,prec} \approx 400\ \mathrm{ml \cdot min^{-1}}$, initial solids formation is limited by mixing. This results in an increase in particle size and a separation of Cu and Zn ions in the individual particles. For sufficiently large volume flows, here $\dot{V}_{total,prec} > 400\ \mathrm{ml \cdot min^{-1}}$, solids formation is no longer affected by mixing and small particles that are homogeneous on the one-digit nanometer scale are formed. However, aging until a phase transformation is detectable seems to annihilate the differences in particle morphology of the individually inhomogeneous, yet mutually similar particles as the aged intermediates shows no dependency on the volume flow during co-precipitation. Accordingly, the properties of the resulting precatalysts are nearly identical. The activity in methanol synthesis was confirmed independent of $\dot{V}_{total,prec}$ during co-precipitation.

To what extent the co-precipitate properties influence the necessary aging time is evaluated separately in Section 5.2.

3.4 Conclusions

The goal of this chapter was to determine if and under which circumstances mixing during co-precipitation does influence the properties of the formed co-precipitate and to which extent possible changes affect the performance of the resulting catalyst as previous studies on this subject were inconclusive[59], contradictory[60,71,84,85] or addressed the topic only on the surface[58,135].

A comparison of materials from a state-of-the-art semi-batch co-precipitation with samples from a continuous co-precipitation proved that the method by which the two feeds are mixed can influence the pH pathway during solids formation as well as the speciation in the surrounding liquid and thus the composition and morphology of the resulting material. A more detailed study on the influence of energy input, respectively mixing time, in the continuous co-precipitation in a mixing nozzle confirmed that the initial solids formation in the preparation of Cu/Zn base catalysts can be limited by mixing. This led to an increase in the median particle size of the co-precipitate as well as the separation of Cu and Zn within the individual particles due to the limited availability of precipitant, i.e. CO_3^{2-} ions, when the mixing intensity is decreased. For the setup here, this was the case for a total volume flow of $\dot{V}_{\mathrm{total,prec}} \leq 400\ \mathrm{ml} \cdot \mathrm{min}^{-1}$. As soon as the mixing intensity is high enough so that mixing is completed before solids formation begins, a further increase of the mixing intensity, or here the volume flows, does not affect co-precipitation anymore and the particle size is constant. The existence of these two regimes is one possible explanation for the somewhat contradictory results in the literature with some authors proclaiming an impact of mixing on the co-precipitate and catalyst properties[58,85,86,135,138] and some studies showing no correlation between mixing and particle properties[59,60,71].

However, contrary to the second part of the hypothesis and previous assumptions[85,101], the change in morphology and composition as a function of mixing intensity during co-precipitation did not withstand aging as the aged intermediate showed no correlation with the total volume flow set during co-precipitation. This can be explained with the fact that while the individual particles are built inhomogeneously at nanoscale, all particles are similar in size, shape and structure. Thus, if a sufficiently long aging time is chosen, all particles behave similarly and the completion of phase transformation, e.g. via the liquid phase, can be guaranteed. Accordingly, catalyst activity in methanol synthesis was confirmed independent of mixing intensity during co-precipitation.

In contrast, the impact of changing from a semi-batch to a continuous co-precipitation was reproducibly evident in the aged precursors and the precatalyst, cf. Figure 3.4 and Table 3.1. S_{BET} and S_{Cu} were increased by a factor of up to three and the distribution of Cu and Zn within the precatalyst was more homogeneous on the nanometer scale. The co-precipitate particles from the semi-batch preparation are more inhomogeneous in relation to each other than the co-precipitate particles from a continuous co-precipitation even with mixing in the mixing-influenced regime, cf. Figure 3.12. Thus, an aging time based on the well-described

methodologies (pH drop, color change, change in PXRD/ FT-IR signal) seems to be insufficient to mitigate the impacts from co-precipitation for the semi-batch material. As to be expected from the characterization of the aged intermediate and precatalyst, the methanol productivity of the less homogeneous semi-batch material is decreased by a factor of two to three across the entire feed gas composition compared to the continuously prepared material.

In conclusion, the initial hypothesis is adapted as follows:

Mixing does influence the morphology of the resulting co-precipitate if mixing and solids formation overlap temporally. Then, a change in the pH trajectory or in the amount of locally available lattice ions, e.g. by a modified precipitation approach, affects precipitation. The thus altered morphology withstands the subsequent process steps only if the particles are diverse in size, composition and morphology or if aging time is insufficiently short to mitigate all these differences. Only then, the morphology of the final catalyst and its performance are influenced by mixing. In particular, this is the case for material produced in semi-batch operated stirred vessels.

For future syntheses, the key focus of co-precipitation should be to obtain a material as homogeneous as possible regarding composition on the one- to two-digit nanometer scale, particle size and morphology, e.g. by conducting co-precipitation in a mixing nozzle in the non-mixing influenced regime. The formation of particles as small as possible that are composed of zincian georgeite is preferable since they proved to result in faster aging kinetics, cf. Section 5.2. This way, the homogeneity of the resulting intermediate after aging can be much better predicted and controlled, which, in turn, leads to a defined high-performance catalyst.

4 Aging of the co-precipitate – a process towards the thermodynamic equilibrium?

The majority of recipes for Cu/ZnO based catalysts include an aging step, where the (co-)precipitate transforms into the target phase, most commonly zincian malachite. The key process conditions, i.e. temperature, pH, process time and reactant concentrations, are generally based on semi-empiric studies and decades of technical know-how. In this section, an alternative approach is evaluated: is it feasible to describe the aging process as a thermodynamic equilibrium process and model it accordingly? This way, efficient model-based adjustments of process conditions to accommodate new target specifications regarding catalyst composition, e.g. for catalysts for the green transformation, should be possible. First, the current state of the art on understanding the mechanisms behind aging and the structure of the thermodynamic model developed here are discussed. Then, the model validity regarding the aforementioned key parameters is analyzed. Finally, the model approach is applied to understand why certain process conditions proved to be ideal to achieve performant catalysts and find process conditions that may result in even more performant material.

4.1 State of the art and research hypotheses

Cu/ZnO based catalysts show a high stability[40], activity[36–38,79] and MeOH selectivity[39] if the Cu and Zn atoms are finely and homogeneously distributed on the one- to two-digit nanometer scale. Thus, the goal of aging is to produce such a material, e.g. by forming the aforementioned zincian malachite as the predominant phase[31]. The higher the targeted Zn fraction in the material is, the longer the aging takes to complete the phase transformation from the amorphous precipitate to zincian malachite[72,75]. The necessary aging time may further increase to more than six hours[80] depending on the reactor design, pH, temperature and reactant concentrations[36,72,75,78–81].

The crystalline structure of zincian malachite is based on the mineral malachite ($Cu_2(OH)_2CO_3$). In the presence of Zn^{2+} ions, Cu^{2+} ions at certain lattice positions can be substituted, thus creating zincian malachite[68,157]. According to various studies, up to 27 mol %[66] or 31 mol %[67] of Cu ions can be substituted. For the naturally occurring variant, called rosasite, Zn fractions of up to 42 mol% were reported by Perchiazzi et al.[157,158]. However, the applied methodology is vague und no similarly high values were reported in the last two decades. Rosasite shows small differences to its synthetic counterpart zincian malachite in the space group symmetry operators. Yet, according to Behrens et al., a differentiation between both forms is nearly impossible[66], which is why zincian malachite is used as the general denotation in the following. Additionally, Parádsasvárite, another mineral in the malachite-rosasite group with the chemical formula $(Zn_{1.91}Cu_{0.06}Mg_{0.02})(CO_3)(OH)_2$ was discovered in 2008[158–160]. However, it was not yet found in any synthetic material[120] and is therefore not considered in this work.

The general consensus is that the resulting catalyst improves its activity and stability if zincian malachite is the predominant phase and the Zn fraction of zincian malachite is as close as possible to the maximum of approx. 30 mol%[18,31,37,38,41,43,64,67,68,74]. The reason for this is the previously discussed importance of a homogeneous and periodic arrangement of Cu, the main

active center of the catalyst, and ZnO as a stabilizer on the nanometer scale. The uniform composition is ensured by the crystal lattice of zincian malachite and is maintained throughout the subsequent process steps and product formulation[78,90]. This way, large Cu surface areas are achieved in the final catalyst that are stabilized against sintering by the ZnO crystallites and thus stable under the process temperatures necessary for catalysis[9]. Additionally, recent studies concluded that the Cu/ZnO interfaces directly enhance activity, either by the stabilization of Cu^+ species for the binding of CO_2[161], as a second kind of active centers where the hydrogenization of CO and CO_2 is enabled[162], by forming Cu-Zn alloys for the activation of CO_2[6,163,164], or by forming highly-active ZnO nanostructures or films on the Cu particles[165–167].

Accordingly, a vast number of experimental studies focused on determining aging conditions for which zincian malachite with $\tilde{x}_{\mathrm{Zn,zM}}$ close to maximum forms as the predominant phase. For $Cu/ZnO/Al_2O_3$ catalysts, the most commonly used variant, 60 to 70 °C and $6 \leq pH \leq 7$ result in the highest amounts of zincian malachite[31]. When pH is further increased, CuO forms instead of zincian malachite. This causes a spatial separation of Cu and Zn atoms in the resulting material[82]. For pH < 6, gerhardtite or rouaite (both $Cu_2NO_3(OH)_3$) is formed which leads to the performance-reducing incorporation of NO_3^- anions[36,82]. The two polymorphs are crystallographically similar and challenging to distinguish by XRD at small amounts. Gerhardtite is the energetically more favorable form at room temperature, but rouaite is metastable once it is formed[168]. Nitrate can be removed in the subsequent calcination step by choosing $T_{\mathrm{calc}} > 300\,°\mathrm{C}$[169,170]. However, this would increase energy consumption and require additional investment in a flue gas cleaning process. Additionally, the homogeneity of Cu and Zn at nanoscale is nevertheless compromised due to the prior formation of these separate Cu phases[72,82]. Temperatures above 70 °C result in the by-products aurichalcite ($[Zn, Cu]_5(CO_3)_2(OH)_6$) and hydrozincite ($Zn_5(CO_3)_2(OH)_6$). Although aurichalcite also consists of Cu and Zn, it results in a worse catalyst, probably due to locally too high Zn fractions of at least 60 mol% which decrease the available Cu surface area[68]. In addition to pH and temperature, the ratio of Cu and Zn ions in the liquid phase is a dominant factor for the resulting phase composition of the aged intermediate. If too few Zn^{2+} ions are available or too few are incorporated, the resulting Zn fraction in zincian malachite is decreased which results in a decreased Cu surface area, a thus reduced activity and an increased sintering tendency of the Cu crystallites during catalysis[88,123]. If more than 27 % Zn^{2+} ions are present in the solids, the aforementioned by-products aurichalcite and hydrozincite form[68,123]. Additionally, metastable Na/Zn phases such as $Na_2Zn_3(CO_3)_4(H_2O)_3$ may form, especially at $pH \geq 7$ where a large number of Na^+ ions from Na_2CO_3 are present[76,78,171,172]. Similarly to nitrate, sodium poisons the catalyst by promoting sintering of Cu crystallites[43]. However, in contrast to nitrate, Na^+ ions cannot be separated by calcination. Thus, sufficient aging and washing are required to rule out the presence of sodium phases in the aged intermediate. Yet, even the temporary existence of Na/Zn phases during aging proved to be detrimental for the resulting catalyst properties, due to remaining residues in the solids phase or by segregation of Cu and Zn due to the formation of these separate Zn phases[78,97]. As a result, deviating from the optimum conditions specified above generally results in a decrease of BET surface area, Cu surface area and, thus, methanol productivity of the resulting catalyst[31,36,61,68,123].

In general, these parameter specifications, that result in a high zincian malachite fraction in the aged intermediate and a performant catalyst material, remain similar when switching from a $Cu/ZnO/Al_2O_3$ recipe to e.g. a $Cu/ZnO/ZrO_2$ catalyst[44,173,174]. However, reactant concentrations must be adjusted in order to obtain the same pH, as the dissociation equilibria differ for different metals[106,108,110]. Also, the optimum pH and temperature for maximum activity deviate from the optimum conditions determined for CZA catalysts[44,175,176]. The differences are even greater for Cu based catalysts without Zn, as the aging mechanisms and kinetics change fundamentally, e.g. for MgO[177]. The same applies for categorically different catalysts prepared by precipitation, such as Co_3O_4 for the total oxidation of toluene and propane[178], Au/MgO for benzaldehyde synthesis[179] or Pt/CeO_2 for H_2 production[180]. This is why there is a large number of experimental parameter studies required for each new catalyst composition, e.g. as for CZZ catalysts targeted at the current effort to produce MeOH from CO_2 instead of CO[44,48,181–183].

Despite the importance of phase control during aging[18,31,68] and the time and cost associated with experimental parameter studies, there is surprisingly little research on the modeling and prediction of optimum aging conditions in the preparation of Cu/Zn based catalysts. The only model known to the author focusses on the time-resolved description of the transformation from zincian georgeite to zincian malachite[75] and is discussed in detail in Section 5. The two main reasons for the lack of models are the often and diffuse overlap with co-precipitation[44,88,89] and the complexity of the aging step itself whose effect on product quality is encapsulated in the generic term 'chemical memory'[31,72,78,136]. A drop in pH[79,81,88], a change in color[73,79], the change in crystallinity trackable by XRD[78,88,171,184] and the change in structure trackable by FT-IR[75,76,184] are established methods to monitor the phase transformation during aging. However, the mechanism behind the phase transformation is still being investigated. There is majority consensus that during initial precipitation, georgeite and/or zincian georgeite form first, probably due to kinetic reasons[70,95,132], cf. Section 3. When surrounded by mother liquid, the co-precipitate eventually crystallizes to (zincian) malachite, most probably by interacting with the liquid phase as the drop in pH indicates. This transformation is strongly non-linear as typical pH profiles suggest. First, pH increases only slowly and slightly for 15 minutes to more than two hours or even more than six hours[80], depending on temperature, initial pH, composition, and reactor design[36,72,75,78–81]. Then, pH suddenly dips and the up to then amorphous material becomes crystalline in the span of less than 5 minutes[75,78,88,171,184].

Güldenpfennig et al. applied in-situ ATR/FT-IR analysis to observe the aging step in microliter scale[75]. They evaluated the most prominent vibrational bands between 1026 and 1120 cm^{-1}, which are attributed to the δ-MeO−H mode of OH^- ions bonded to metal in the zincian malachite lattice[70,185,186]. From their measurements, they concluded that the aging process is composed of a long induction period of up to 30 minutes with no measurable change in the solids and a brief transformation period of generally less than 5 minutes where the solids transform into crystalline zincian malachite. The length of the induction period was subject to statistical variation. Both the length of the induction period and of the transformation period are reduced by increasing temperature and the concentration of metal reactants in the system. By comparing their experimental data with a model based on the kinetics of solvent-mediated phase transformations[187–189], Güldenpfennig et al. concluded that the aging process does happen

via the liquid phase. Similar conclusions were made for transient Na-Zn phases which were observable with in-situ analysis, but are not apparent in the aged intermediate[78]. Based on the Ostwald theory, (zincian) georgeite is assumed as a metastable, but energetically unfavorable solid phase while (zincian) malachite is assumed to be the most stable form with the lowest free energy, cf. Behrens et al.[66]. Through dissolution of (zincian) georgeite, the supersaturation of (zincian) malachite increases. This accelerates the formation of (zincian) malachite with the progression of (zincian) georgeite dissolution. However, they emphasize the difficulty of observing the metastable phase and provide no explanation for the characteristic pH course. Due to the nature of the model, a model-based process design to prevent the formation of detrimental phases as by-products is also not possible.

Complementary to this model approach and the vast amounts of parameter studies available in the literature, another model approach with a focus on the final phase composition in the aged intermediate is developed in this work. The goal is to enable a knowledge-based choice of process conditions to obtain the targeted phase composition, e.g. zincian malachite as the single phase. This way, a more versatile and flexible process design and optimization should be possible when new requirements to the catalyst composition arise. One key question for this purpose is how detailed the complex aging step needs to be described and what a suitable model must be capable of. They key idea here is to focus on the idea of zincian malachite, as well as the other phases present in the final aged intermediate, as the thermodynamically stable phases with the least amount of free energy as proposed by Behrens and Girgsdies[66] and applied by Güldenpfennig et al.[75]. Accordingly, possible kinetic influences are neglected and assumed as irrelevant for the resulting phase composition. This idea is summarized as the following working hypothesis:

Aging is a process towards the thermodynamic equilibrium. Therefore, an entirely thermodynamic model without consideration of kinetics is sufficient to predict the influence of aging parameters on the resulting phase composition of the final aged intermediate.

In contrast, co-precipitation is believed to be dominated by kinetics and so is the phase composition of the co-precipitate. Accordingly, the role of mixing in the solids formation is discussed separately in Section 3 using (zincian) georgeite as the presumably matching phase. Using this strict separation of co-precipitation and aging, as also described in Section 2.3, the following sections focus on the structure, validation and application of the developed aging model as well as the research hypothesis without any cross influences from co-precipitation.

4.2 Thermodynamic model

The modeling in the scope of this work focuses on the correlation between fundamental aging parameters, such as reactant concentrations, temperature and pH, and the resulting phase composition in the solids. Additionally, the same model is applied to understand the mechanisms behind the initial solids formation and the formation of the metastable co-precipitate. There are readily available software solutions for this purpose, e.g. PhreeqC[106] or OLI Studio (OLI Systems), which proved their applicability for a broad range of precipitation processes[190–192], and are also applied in the model developed here. They solve the system of

equations which results from the equilibria between solids, liquid and complexes described below. However, they rely on the accuracy and completeness of the underlying databases regarding these equilibria reactions for the substances under investigation. The following sections give an overview over the fundamentals applied in the adapted model, its structure and an evaluation of the model and database quality for the purposes of this work.

4.2.1 Fundamentals

For sparingly soluble salts, such as zincian malachite, aurichalcite or hydrozincite, the solubility product $K_{\mathrm{SP},j}$ according to Eq. (4.1) describes the equilibrium between the solids-forming ions i in the liquid phase and each solid phase j[193].

$$K_{\mathrm{SP},j} = \prod {a_{i,j}^*}^{\nu_{i,j}} \tag{4.1}$$

$K_{\mathrm{SP},j}$ is a function of the individual activities of each ion i of the solid j at thermodynamic equilibrium $a_{i,j}^*$ and its stoichiometric coefficient $\nu_{i,j}$.

Due to the very limited solubility of sparingly soluble salts in water of generally less than $1\ \mathrm{g \cdot L^{-1}}$, the determination of their solubility products requires particularly time-consuming sample preparation as well as complex and accurate analytical methods[107,168,194,195]. The sensitive methodology results in vastly deviating values, e.g. for hydrozincite where values between $K_{\mathrm{SP,hyd}} = 3 \cdot 10^{-75}\ \mathrm{mol^5 \cdot L^{-5}}$ and $K_{\mathrm{SP,hyd}} = 5 \cdot 10^{-76}\ \mathrm{mol^5 \cdot L^{-5}}$ are reported for 25 °C[196–198]. For other relevant solid phases such as georgeite or zincian malachite, no data is available at all due to the demanding procedure. Instead, authors rely on the solubility products of similar phases, here, the naturally occurring minerals malachite and rosasite[71,115]. However, applying such different K_{SP} to kinetic solids formation modeling results in supersaturations which differ by several orders of magnitude as well as nucleation rates and particle sizes that differ by several orders of magnitude[151]. Furthermore, the incorporation of ions and temperature effects cannot be modeled accurately due to impurities[71], different stoichiometries[115] and data that is limited to 25 °C[105,115]. Thus, a careful evaluation and validation of available data is required, cf. Section 4.2.3. Recent studies by Cornu et al., Güldenpfennig et al. and Guse et al. discuss the determination of solubility products from titration curves as a new, faster alternative[105,151,199]. Data from the latter work is integrated in the database used in this work to allow temperature effects and variable Zn contents in zincian malachite to be depicted, cf. Table 2.2 and Guse et al.[110]

The driving force for solids formation during co-precipitation and aging is the difference in the chemical potential for each possible solid j between the solid and liquid phase. Here, it is expressed as the phase-specific supersaturation S_j as a function of the actual activities of solids-forming ions a_i in the solution, the solubility product $K_{\mathrm{SP},j}(T)$ of the solid phase j and the stoichiometric coefficients ν_i and $\nu_\pm$ according to Eq. (4.2).

$$S_j = \left(\frac{\prod a_{i,j}^{\nu_{i,j}}}{K_{\mathrm{SP},j}(T)} \right)^{1/\nu_\pm} \tag{4.2}$$

In a system, in which only a single solid phase is possible, three cases have to be distinguished: first, for $S_j = 1$, thermodynamic equilibrium prevails between the liquid phase and the solid j; the system is in a stable state regarding j. Second, if $S_j > 1$ is valid, the solution is supersaturated with respect to j. In this case, the supersaturation can be depleted by formation of the solid j until $S_j = 1$ is achieved. Finally, $S_j < 1$ corresponds to an undersaturated solution regarding the solid phase j. If any solid j is present, it will dissolve until $S_j = 1$ is reached or the solid is completely dissolved. In a system with several possible solid phases, certain ions may be incorporated into various solid phases and the ions of one solid interact with ions from another solids. As a result, the phase-specific supersaturation progression can deviate from the behavior in the single-phase system above, e.g. if two solid phases are supersaturated but only one is formed. Ultimately, however, $S_j \leq 1$ has to be valid for each solid phase j. Otherwise, thermodynamic equilibrium is not reached yet.

The activity a_i of an ion i can be calculated from its molality b_i and its activity coefficient γ_i according to Eq. (4.3). This way, non-ideal ion interactions are considered. Details on the chosen activity coefficient model are discussed in Section 4.2.3.

$$a_i = \gamma_i \cdot b_i \tag{4.3}$$

According to Eq. (4.4), the total amount of ions in the system $b_{i,\mathrm{total}}$ which are available for the formation of solids, is reduced by speciation reactions and the formation of complexes k. Here, $\nu_{i,k}$ is the stoichiometric coefficient for i in k and b_k is the molality of the complex k. Additionally, some ions may already be incorporated in the solid phase j with the molality b_j. The remainder of ions available for solid formation is also referred to as free ions or dissociated ions.

$$b_i = b_{i,\mathrm{total}} - \sum_k \nu_{i,k} \cdot b_k - \sum_j \nu_{i,j} \cdot b_j \tag{4.4}$$

The respective speciation equilibrium is described with the ion association constant $K_{\mathrm{IA},k}$ according to Eq. (4.5).

$$K_{\mathrm{IA},k} = \frac{a_k^*}{\prod {a^*}_{i,k}^{\nu_{i,k}}} \tag{4.5}$$

The determination of K_{IA} in the liquid phase follows a similar procedure as the aforementioned determination of K_{SP}. The validity of the applied and expanded database as a whole is evaluated in Section 4.2.3.

4.2.2 Structure and assumptions

The two main goals of the process modeling in the scope of this work are, for one, to calculate supersaturations to better understand initial solids formation during co-precipitation and, for another, to predict the resulting phase composition at thermodynamic equilibrium. The required model structure is fundamentally the same in both cases and is outlined below with Figure 4.1.

In accordance with the two objectives, the key output quantities are the molalities $b_{s,j}$ of each solid phase j, the phase-specific supersaturation S_j, as well as pH and the activity a_i of all species i for characterization of the liquid phase. The required input parameters are derived from Eqs. (4.1) to (4.5) and are divided into the process parameters and the database which contains the material properties, i.e. $K_{\mathrm{SP},j}(T)$ and $K_{\mathrm{IA},k}(T)$ with the corresponding reaction equations, and the selected activity coefficient model with its respective parameters.

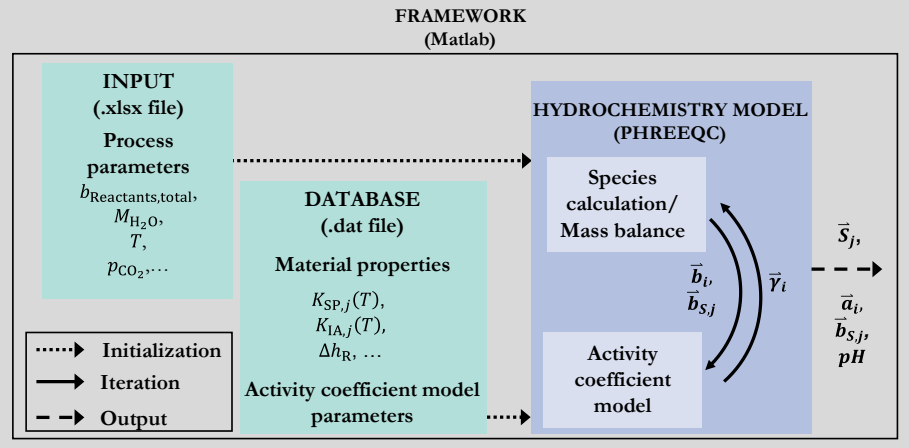

Figure 4.1: Overview of the thermodynamic model.

The temperature dependency for $K_{\mathrm{SP},k}(T)$ and $K_{\mathrm{IA},k}(T)$ is either specified by analytical expressions or given by the respective value at $T^0 = 298.15$ K and a standard reaction enthalpy $\Delta\tilde{h}^0_{\mathrm{r},k}$. $K_{\mathrm{SP},k}(T)$ and, accordingly, $K_{\mathrm{IA},k}(T)$ can then be calculated using the van't Hoff equation given in Eq. (4.6)[105].

$$\ln\left(\frac{K_{\mathrm{SP},k}(T)}{K_{\mathrm{SP},k}(T^0)}\right) = \frac{\Delta\tilde{h}^0_{\mathrm{r}}}{R}\left(\frac{1}{T^0} - \frac{1}{T}\right) \tag{4.6}$$

The database used is based upon the database 'pitzer.dat' included in the PHREEQC software package (iphreeqc version 3.7.1)[200]. The original version was expanded by previously missing Pitzer coefficients[201–205], speciation equilibria for the Cu, Zn, Zr, Na, nitrate and carbonate species[108,129,197,206,207], the solubility data listed in Table 2.2 as well as specifically determined, temperature-dependent solubility products for all relevant phases that were missing data[105]. The accuracy and completeness of the underlying database regarding these equilibria reactions determine the accuracy of the model calculations and are discussed in the following chapter. The database is archived separately[110].

The hydrochemistry software PHREEQC is used to calculate the thermodynamic state of equilibrium by solving the system of equations that results from the solids-liquid equilibria, speciation as well as mass and substance balance equations, cf. Section 4.2.1. For this purpose, the model also calculates the activity of species in the liquid phase by using appropriate activity coefficient models like the Pitzer or the SIT model which are discussed in the following section. By iteration, these calculations are repeated until all solid phases considered are saturated or undersaturated. For communication, import of the database and the process parameters as well as output of the target quantities, Matlab (R2021a) is used.

For all calculations, an ideally mixed and isotherm system is assumed and no kinetics are considered. The isothermal boundary condition results from the experimental setup, cf. Section 2.3, and corresponds to the state-of-the-art approach[18,31,97]. For both cases considered, kinetics and mixing are neglected:

- $\boldsymbol{t = t_{\mathrm{init}}}$**:** a hypothetical initial state after mixing of the reactant solutions is completed, but no solids were formed yet. This way, the initial supersaturations $S_{j,\mathrm{init}}$, which is presumed as the main driving forces for solids formation in co-precipitation, are calculated. Experimentally, the independence of solids formation from mixing is ensured by the mixing studies in Section 3.3.
- $\boldsymbol{t = t_{\mathrm{eq}}}$**:** the state of equilibrium where all considered solid phases are saturated or undersaturated. This state is applied to calculate the phase composition of the aged intermediate for $t_{\mathrm{age}} \rightarrow \infty$ and to verify the working hypothesis regarding the thermodynamic nature of the aging process.

Both cases also differentiate regarding the gas phase interaction. For the initial state of co-precipitation, which happens at a time scale of 10^{-5} to 10^{-2} s according to the mixing studies in Section 3.3, no gas-phase interaction is assumed. Additionally, zincian georgeite instead if zincian malachite is considered for the metastable state of equilibrium after initial co-precipitation. The database is modified accordingly to exclude (zincian) malachite. In contrast, for the phase equilibrium at the end of aging, the liquid-gas interaction is modeled for $CO_2^{(g)}$ either using the Peng-Robinson equation of state[106] and assuming an infinitely large reservoir of ambient air for $t_{\mathrm{age}} \rightarrow \infty$ or by applying a temperature-dependent fitted value for the equilibrium reaction between $CO_2^{(g)}$ and $HCO_3^{-(aq)}$, cf. Eq. (4.8)[105]. The correct representation of the interplay between $CO_2^{(g)}$ solubility, carbonate balance and pH[208] is key for the correct calculation of supersaturations and phase composition as the carbonate activity directly affects the supersaturation of e.g. zincian malachite. A comparison of calculated and experimentally determined pH for $t = t_{\mathrm{init}}$ and $t = t_{\mathrm{age}}$ proved that these assumptions and calculation approaches are justified, respectively[105]. The further process parameters needed are the same in each case: the total reactant molalities $b_{\mathrm{reactants,total}}$, the water mass $M_{\mathrm{H_2O}}$ and the process temperature T.

4.2.3 Validation and parameterization

The accuracy and completeness of the solubility products, speciation equilibria and activity coefficient model in the database primarily determine the accuracy of the model calculations. Thus, the database and model applied for all modeling in this work are validated in three steps: first, the speciation and activity coefficient model are verified by looking at the reactant solutions without any solids formation. Next, individual solubility products are validated and, if necessary, determined with titration studies in which only a singular solid phase precipitates[105]. Finally, the model is compared to experimental aging studies and applied in the subsequent section for process optimization regarding the phase composition of the aged intermediate.

In Figure 4.2 and Figure 4.3, four activity coefficient models with varying degree of complexity are compared regarding their applicability in modeling the co-precipitation and aging

of Cu/ZnO based catalyst precursors. In general, the more complex a model, the higher its validity range. However, this comes with the drawback that more, in part ion-specific parameters are required, especially for a complex material system, as is the case here. The following models are considered:

- The Davies extended Debye-Hückel model without any ion-specific parameters and a validity range of typically up to $I_{\mathrm{Davies}} \leq 0.5\ \mathrm{mol} \cdot (\mathrm{kg\ H_2O})^{-1}$ [71,209]. For this approach, the software CHEAQS Next (64 bits, Version 0.2.1.3) was used.
- The WATEQ model with ion-specific parameters based on the database 'WATEQ_minteq.v4' and a validity range of approx. $I_{\mathrm{WATEQ}} \leq 1.0\ \mathrm{mol} \cdot (\mathrm{kg\ H_2O})^{-1}$ [210].
- The Pitzer model with multiple ion-pair specific parameters which, in general, allow modeling ranges of up to $I_{\mathrm{Pitzer}} \leq 6.0\ \mathrm{mol} \cdot (\mathrm{kg\ H_2O})^{-1}$ [101,203]. Details on the numerous equations and correlations can be found elsewhere[204]. Ion association reactions are considered if the respective interaction parameters for this ion pairing are unavailable, cf. Guse et al.[115]
- A modified hybrid Pitzer model where both Pitzer parameters and $K_{\mathrm{IA},k}$ are considered for the same ion pairing if the formation of a complex is described in the literature, cf. Guse et al.[101,115]

According to Eqs. (4.7) to (4.12), pH correlates with a multitude of ion association reactions both for dissolved Na_2CO_3 as well as dissolved metal nitrates. Accordingly, based on the definition of $K_{\mathrm{IA}}(t)$ in Eq. (4.5), the calculated pH also depends on the validity of the ion activity a_i. Thus, pH can be applied to simultaneously validate the ion association constants and the respective activity coefficient model.

$$\mathrm{CO_3^{2-} + H_3O^+ \leftrightarrow HCO_3^- + H_2O} \tag{4.7}$$

$$\mathrm{HCO_3^- + H_3O^+ \leftrightarrow H_2CO_3^{(aq)} + H_2O} \tag{4.8}$$

$$\mathrm{Cu^{2+} + OH^- \leftrightarrow Cu(OH)^+} \tag{4.9}$$

$$\mathrm{Cu^{2+} + 2\ OH^- \leftrightarrow Cu(OH)_2^{(aq)}} \tag{4.10}$$

$$\mathrm{H_3O^+ + OH^- \leftrightarrow 2\ H_2O} \tag{4.11}$$

$$\mathrm{pH} = -\log\left(a_{\mathrm{H_3O^+}}\right) \tag{4.12}$$

In Figure 4.2, the calculated pH of Na_2CO_3 solutions with varying molalities between 10^{-5} mol·(kg H_2O)$^{-1}$ and 2 mol·(kg H_2O)$^{-1}$ at 298.15 K is plotted against the experimentally determined pH. All four activity coefficient models deviate less than 5 % from the measured data across the entire concentration range up to $I = 6\ \mathrm{mol} \cdot (\mathrm{kg\ H_2O})^{-1}$.

In Figure 4.3, the same procedure is repeated for an aqueous, equimolar solution of $Cu(NO_3)_2$ and $Zn(NO_3)_2$ with $10^{-4}\ \mathrm{mol} \cdot (\mathrm{kg\ H_2O})^{-1} < b_{\mathrm{metal\ nitrates}} < 4\ \mathrm{mol} \cdot (\mathrm{kg\ H_2O})^{-1}$. In this case, the four models only show small deviations of less than 6 % for $pH_{\mathrm{exp}} > 3.9$, which corresponds to $I \leq 0.6\ \mathrm{mol} \cdot (\mathrm{kg\ H_2O})^{-1} \approx I_{\mathrm{Davies}}$. However, for higher molalities of up to $I = 12\ \mathrm{mol} \cdot (\mathrm{kg\ H_2O})^{-1}$, the Davies and WATEQ models show high deviations between 18 % and more than 300 % and are unable to reproduce the pH trend towards $pH_{\mathrm{exp}} < 1$. The hybrid

Pitzer model does depict the pH curve. However, it also shows deviations of more than 15 % for $I \geq 6\ \mathrm{mol} \cdot (\mathrm{kg\ H_2O})^{-1}$. In contrast, deviations for the Pitzer model remain below 15 %. Yet, in the range of $2.8 < pH < 3.9$, i.e. $0.6\ \mathrm{mol} \cdot (\mathrm{kg\ H_2O})^{-1} < I < 3\ \mathrm{mol} \cdot (\mathrm{kg\ H_2O})^{-1}$, the hybrid variant is more accurate which has been predicted by Pitzer et al. as "maxima of association" in certain concentration ranges[211].

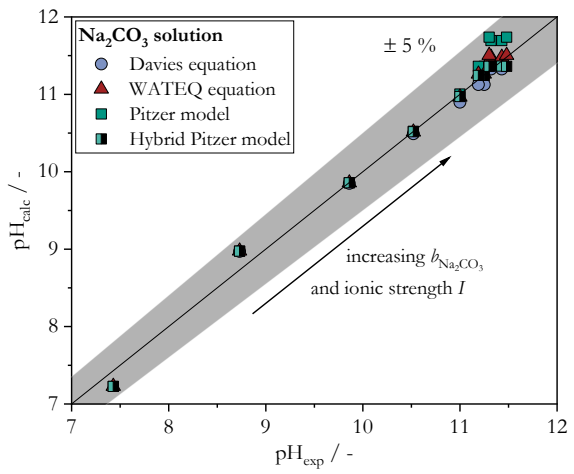

Figure 4.2: Parity plots for calculated and experimentally determined pH for four different activity coefficient models for an aqueous Na_2CO_3 solution with $b_{Na_2CO_3}$ between $10^{-5}\ \mathrm{mol} \cdot \mathrm{kg}_{H_2O}^{-1}$ and $2\ \mathrm{mol} \cdot \mathrm{kg}_{H_2O}^{-1}$ at 298.15 K. Adapted from Guse et al.[115]

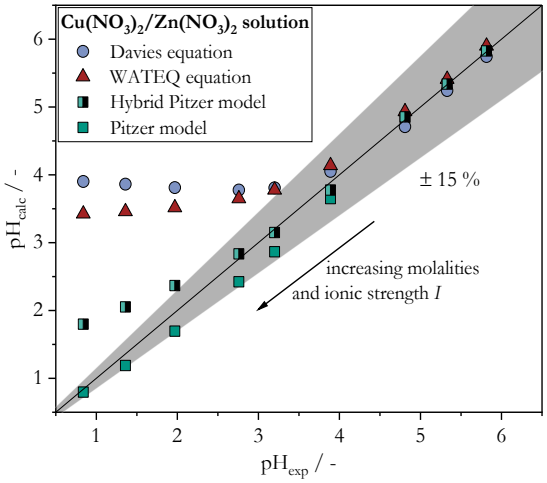

Figure 4.3: Parity plots for calculated and experimentally determined pH for four different activity coefficient models for an aqueous $Cu(NO_3)_2/Zn(NO_3)_2$ solution at 298.15 K with $n_{Cu(NO_3)_2}/n_{Zn(NO_3)_2} = 1$ and $b_{\mathrm{metal\ nitrate}}$ between $10^{-4}\ \mathrm{mol} \cdot \mathrm{kg}_{H_2O}^{-1}$ and $4\ \mathrm{mol} \cdot \mathrm{kg}_{H_2O}^{-1}$. Adapted from Guse et al.[115]

In conclusion, each activity coefficient model considered here is suited to described the behavior of Na^+ and CO_3^{2} ions in the solution, even at ionic strengths as high as 2 mol (kg H_2O)$^{-1}$. However, the more complex speciation of $Cu(NO_3)_2$ and $Zn(NO_3)_2$ solutions can only be described with a reasonable deviation of less than 15 % if the Pitzer model is applied. The differences between the hybrid approach and the Pitzer approach suggest that ion association reactions should only be considered when applying the Pitzer model if proven necessary as suggested by Lassin et al. in their general evaluation[212]. For these reasons, the Pitzer model variant is used for all further calculations.

Next, the validity of readily-available solubility products, that are required for the model, are verified and, if necessary, supplemented by specifically determined $K_{SP,j}$. For this purpose, Guse et al. used titration studies which are discussed exemplarily for the temperature-dependent solubility of aurichalcite in Figure 4.4 and the difference in solubility between zincian georgeite and zincian malachite in Figure 4.5. In general, a Na_2CO_3 solution was provided as an analyte in which the respective metal nitrate solution was then added dropwise while pH was monitored. Depending on the amount of solids formed and the amount of ions incorporated into said solids, pH is reduced. Analogue to the approach for the activity coefficient model, pH was then used to evaluate the accuracy of the solubility products for hydrozincite and zincian malachite, cf. Table 2.2.

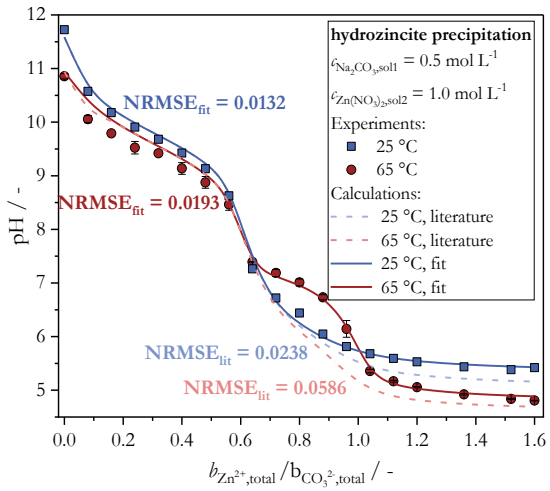

Figure 4.4: Influence of temperature on the titration curve for the precipitation of hydrozincite ($Zn_5(CO_3)_2(OH)_6$) and comparison of literature data[196] with fitted data. Adapted from Guse et al.[105]

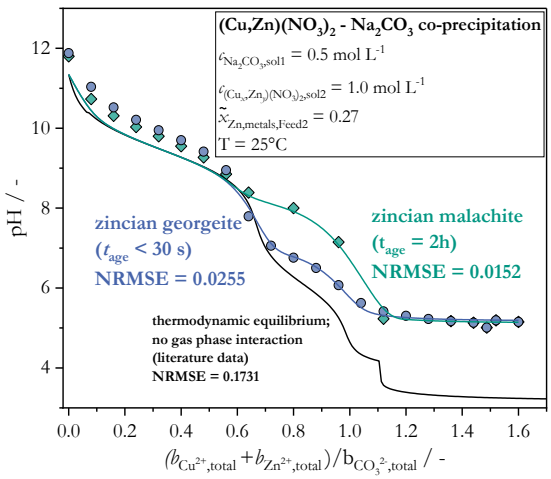

Figure 4.5: Difference between the titration curves for the precipitation of zincian georgeite and zincian malachite (both $Cu_{1.46}Zn_{0.54}CO_3(OH)_2$) and comparison with literature data[107,128]. Adapted from Guse et al.[105]

By comparing experimental pH trends with model calculations, the normalized root mean square error (NRMSE) was calculated according to Eqs. (4.13) and (4.14) and, if necessary, minimized to determine missing solubility products or correct deviating K_{SP} from the literature. Additionally, the solids were analyzed regarding their phase composition using XRD and element analysis[105].

$$NRMSE = \frac{\sqrt{\frac{\sum_{i=1}^{N}\left(pH_{\mathrm{calc},i} - pH_{\mathrm{exp},i}\right)^2}{N}}}{\overline{pH}_{\mathrm{exp}}} \tag{4.13}$$

$$\overline{pH}_{\mathrm{exp}} = \frac{\sum_{i=1}^{N} pH_{\mathrm{exp},i}}{N} \tag{4.14}$$

For hydrozincite, the experimental titration curve changes with process temperature. The model calculations based on literature data[196] cannot reproduce the temperature influence correctly and show increasing deviations from the experimental curve for increasing $Zn(NO_3)_2$ amounts. In contrast, a fit of the calculated pH curve to the experimental data[105] results in solubility products of $K_{SP}(25\,°C) = 1.86 \cdot 10^{-73}\ mol^{13}L^{-13}$, respectively $K_{SP}(65\,°C) = 2.40 \cdot 10^{-74}\ mol^{13}L^{-13}$, which accurately depict the respective solid-liquid equilibrium.

For zincian malachite, the deviation between the model calculations with literature data[107,128] and the experimental pH curve is even larger. Again, the pH trend, and thus, the solid-liquid-equilibrium can be reproduced correctly, if the fitting routine is applied. Furthermore, the difference in the titration curves for zincian malachite and zincian georgeite, which were obtained by varying the process time t_{age} between each sample point, confirm the need for two distinctive solubility products for the co-precipitate and the aged intermediate: $K_{SP,zg}(25\,°C) = 1.07 \cdot 10^{-33}\ mol^5 \cdot L^{-5}$ and $K_{SP,zm}(25\,°C) = 1.66 \cdot 10^{-35}\ mol^5 \cdot L^{-5}$. XRD and FT-IR analyses confirmed that amorphous zincian georgeite is formed for $t_{age} = 30\ s$ while, due to the lower solubility, crystalline zincian malachite is formed for $t_{age} \geq 2\ h$ as the more stable phase, cf.

Guse et al.[105]. The approach was furthermore applied for the unnamed by-product $Na_2Zn_3(CO_3)_4(H_2O)_3$[76,171], the occurrence of which leads to the detrimental presence of Na in the final catalyst[43,78,97], but has not yet been described thermodynamically, cf. Section A.4. These results confirm the need for critical evaluation of available $K_{SP,j}$ and the necessity to apply the newly determined $K_{SP,j}$, cf. Guse et al.[105] and Table 2.2, in the following model calculations.

Lastly, the impact of the newly determined solubility product for zincian georgeite on the model quality compared to the use of literature data for rosasite is evaluated in Figure 4.6 and Figure 4.7. Here, the solid mass of the co-precipitate as a function of the reactant concentration and the pH of the suspension are considered.

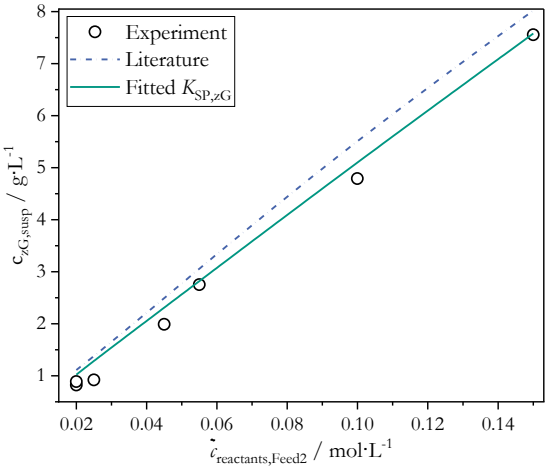

Figure 4.6: Comparison of the calculated and experimentally determined solid mass concentration of zincian georgeite as a function of the reactant concentration at 55 °C. Adapted from Guse et al.[105]

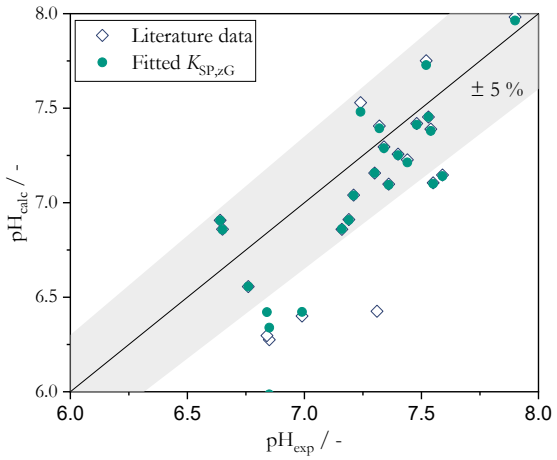

Figure 4.7: Comparison of the calculated and experimentally determined pH under variation of reactant concentrations at 55 °C. Adapted from Guse et al.[105]

The concentration of zincian georgeite in the suspension $c_{zg,susp}$ rises linearly with the concentration of Cu and Zn in the feed solution $\tilde{c}_{reactants,Feed2}$ in both the experiment and in the model calculations, as would be anticipated for maximum yield. Both model variants provide numbers that are comparable for low concentrations. Due to the lack of alternatives, the literature variant assumes the supposedly smaller solubility product of rosasite for zincian georgeite: $K_{SP,ZG} \approx K_{SP,rosasite}(25\,°C) = 3.98 \cdot 10^{-37}$ [107,128]. This causes $c_{zg,susp}$ to be increasingly overestimated for higher feed concentrations in comparison to the experimental findings. In contrast, if the corrected solubility product ($K_{SP,ZG}(55\,°C) = 2.34 \cdot 10^{-35}$) is used, the model coincides with the experimental results for large $\tilde{c}_{reactants,Feed2}$.

For the pH variation in Figure 4.7, the reactant ratio of metal nitrates and sodium carbonate was varied. In some cases, HNO_3 and NaOH were added to the reactant solutions to further adjust pH while maintaining the total lattice ion ratio of e.g. Cu^{2+} and CO_3^{2-}. The pH range was limited to obtain zincian georgeite as the only solid phase in each case. Both model variations perform similarly and mostly exhibit deviations of less than 5 % compared to the experimental data. The remaining uncertainties are a result of the limitations of the activity coefficient model as well as the speciation equilibria applied, cf. Figure 4.2 and Figure 4.3. However, when large

amounts of HNO_3 were added ($\tilde{c}_{HNO_3,Feed2} > 0.1\ mol \cdot L^{-1}$), the deviation of the literature model is increased compared to the model variant with the adjusted $K_{SP,ZG}$.

In conclusion, the validity of the Pitzer model as the chosen activity coefficient model as well as the speciation equilibria included in the model database were confirmed. For several solid phases relevant in the preparation of Cu/ZnO based catalysts, additional solubility products were required due to the lack of data for synthetic phases in the literature. By determining and including these $K_{SP,j}$ in the model, precipitation and pH tendencies in titration studies as well as the solid mass of zincian georgeite in the co-precipitation were predicted accurately. Thus, the model is deemed suitable for the assessment of whether aging can be assumed as a process towards the thermodynamic equilibrium.

4.3 Influence of reactants

The reactant composition is, next to temperature and aging time, one of three key parameters to control the phase composition of the aged intermediate, cf. Section 4.1. Accordingly, the target of this section is to evaluate if the correlation between reactant composition and phase composition can be reproduced and predicted by the thermodynamic equilibrium model approach. For this purpose, the total molar ratio between Cu and Zn ions and the pH resulting from the ratio between metal nitrate and Na_2CO_3 solution, are varied separately. Since the focus is on the interplay of Cu and Zn based phases, no third component, e.g. ZrO_2, is added since it does not form a common phase with Cu or Zn[93].

In Figure 4.8 and Figure 4.9, the solid phase composition after aging and the Zinc fraction in zincian malachite $\tilde{x}_{Zn,zm}$ are plotted as a function of the molar Zn metal fraction in the feed $\tilde{x}_{Zn,Feed1}$ as defined in Eq. (4.15):

$$\tilde{x}_{Zn,Feed1} = \frac{b_{Zn^{2+},Feed1}}{b_{Cu^{2+},Feed1} + b_{Zn^{2+},Feed1} + b_{Zr^{4+},Feed1}} \tag{4.15}$$

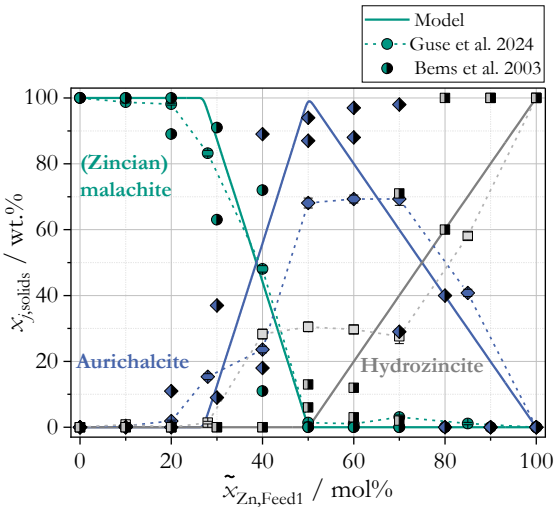

Figure 4.8: Solid phase composition as a function of the molar Zn fraction in the feed for $T = 65$ °C. Data from Guse et al. (●) and Bems et al. (◑)[72,105]

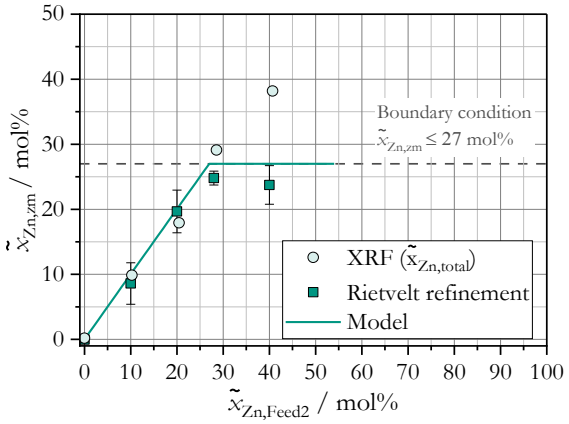

Figure 4.9: Zinc fraction in zincian malachite $\tilde{x}_{Zn,zm}$ as a function of the molar Zn fraction in the feed for $T = 65$ °C. Data from Guse et al.[105]

The experimental phase composition, as well as the Zinc fraction of zincian malachite, were determined by a Rietveld refinement of the dried aged intermediate, cf. Section 2.4.5. For $\tilde{x}_{\mathrm{Zn,Feed1}} = 0\ \mathrm{mol\%}$, copper is present as the only metallic reactant. Accordingly, pure malachite (equal to zincian malachite with $\tilde{x}_{\mathrm{Zn,zm}} = 0$) is formed as it is evident by the thermodynamic model and confirmed experimentally in Figure 4.8 and Figure 4.9. For zinc fractions of $\tilde{x}_{\mathrm{Zn,Feed1}} \leq 27\ \mathrm{mol\%}$, zincian malachite is then formed exclusively. It is evident from Figure 4.9 that all additional Zn in this range is incorporated into the malachite lattice. Only for zinc fractions in the metal nitrate feed of $\tilde{x}_{\mathrm{Zn,Feed1}} > 27\ \mathrm{mol\%}$, an increasing amount of Zn is present in the solids that is not bound in the zincian malachite lattice as the comparison of XRF data and the Rietveld refinement confirms. Instead, an increasing amount of aurichalcite is formed and, for zinc fraction of more than 40 mol%, hydrozincite. These trends are also apparent in the data of two experimental parameter studies conducted by Bems et al.[72] Minor differences between the experimental results, especially for Zn fractions beyond 50 mol%, either result from similarities in the crystal lattices of hydrozincite and aurichalcite[72,105,115] and the corresponding uncertainties in Rietveld refinement, cf. Figure A.11, or from the deviations in the experimental pH profile[72]. Further experimental studies at similar temperatures and pH confirm the predominance of zincian malachite for Zn fractions of less than approx. 30 mol% as well as the increasing amounts of aurichalcite and hydrozincite for higher Zn fractions[68,123].

The phase composition and zinc fractions calculated with the thermodynamic model match the experimental data quantitatively. Only in the range of $0.3 < \tilde{x}_{\mathrm{Zn,Feed1}} < 0.7$, there are deviations between the experimental and calculated mass fractions of aurichalcite and hydrozincite. These are the result of the similar crystal lattices of aurichalcite and hydrozincite which prevent a reliable quantification in the Rietveld refinement[72,105,115]. Furthermore, both in the thermodynamic model as well as the Rietveld refinement aurichalcite with $\tilde{x}_{\mathrm{Cu,aur}} = 50\ \mathrm{mol\%}$ and hydrozincite with $\tilde{x}_{\mathrm{Cu,hyd}} = 0\ \mathrm{mol\%}$ are considered as the two boundary cases and may form simultaneously. In reality, $\tilde{x}_{\mathrm{Cu,hyd}}$ decreases gradually with increasing $\tilde{x}_{\mathrm{Zn,Feed1}}$ and a single aurichalcite phase with $0\ \mathrm{mol\%} \leq \tilde{x}_{\mathrm{Cu,aur}} \leq 50\ \mathrm{mol\%}$ forms for $0.3 < \tilde{x}_{\mathrm{Zn,Feed1}} < 1.0$ granted that the material is completely homogeneous at nanoscale and in between all particles. This can be represented in the model by the summation of x_{hyd} and x_{aur}. Then, $\tilde{x}_{\mathrm{Cu,aur}}$ results from Eq. (4.16).

$$\tilde{x}_{\mathrm{Cu,aur}} = \frac{\tilde{x}_{\mathrm{Cu,aur,max}} \cdot x_{\mathrm{aur}} + \tilde{x}_{\mathrm{Cu,hyd}} \cdot x_{\mathrm{hyd}}}{x_{\mathrm{aur}} + x_{\mathrm{hyd}}} = \frac{0.5 \cdot x_{\mathrm{aur}}}{x_{\mathrm{aur}} + x_{\mathrm{hyd}}} \tag{4.16}$$

In summary, both the model and the experimental results indicate that if the amount of available Zn in the solution exceeds the amount of Zn that can be incorporated into zincian malachite, cf. Section 4.1, aurichalcite forms instead of hydrozincite. Accordingly, the surplus of Zn ions does not form an isolated phase but incorporate some Cu ions that would otherwise precipitate as (zincian) malachite reducing the absolute amount of zincian malachite compared to lower Zn fractions. This effect was also observed by Behrens and Girgsdies. who hypothesized that aurichalcite may be the thermodynamically favored phase for these conditions due to a lower Gibbs energy[66]. The model results here confirm their theory.

In Figure 4.10 and Figure 4.11, the phase composition of the aged intermediate, the zinc fraction in zincian malachite and the copper fraction in aurichalcite are plotted as a function of $pH_0 = pH(t_{age} = 0\ \text{min})$ for $\tilde{x}_{Zn,Feed1} = 0.3$ for the more complex CZZ composition. In general, the longer the aging time, the higher the amount of gassed out CO_2 which affects pH at the end of aging. Thus, pH_0 was chosen as a fixed reference. The model calculations are compared to experimental data and literature data. It is evident from the experimental data of both studies that for $6 \leq pH_0 \leq 8$, zincian malachite is the dominant phase at the end of aging with mass fractions of 90 to 100 wt.%. Small fractions of aurichalcite result from the limited amount of Zn that can be incorporated into zincian malachite (27 mol%[66]). Vice versa, the amount of Cu incorporated into aurichalcite fluctuates much more according to Rietveld refinement and the evaluation method described in the appendix, cf. Section A.3.2. This is caused by the uncertainty of the evaluation method in combination with the small amounts of aurichalcite detectable. ZrO_2 is barely found by XRD due to its limited amount, small crystallites, cf. Section 3.3, and possibly amorphous nature[93]. This confirms its subordinate role in the modeling of aging.

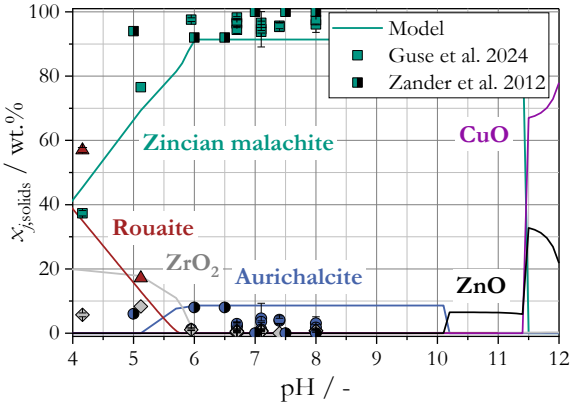

Figure 4.10: Solid phase composition as a function of pH_0 for $T = 55\ °C$ (Guse et al.[115]), respectively $T = 65\ °C$ (Zander et al.[78]), with $\tilde{x}_{Zn,Feed1} = 0.3$ and $\tilde{x}_{Zr,Feed1} = 0.1$ (Guse et al.).

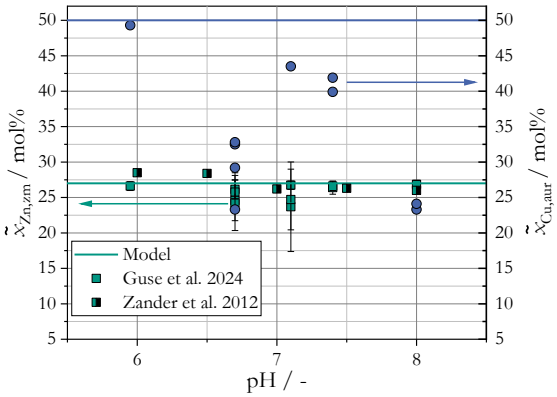

Figure 4.11: Zinc fraction in zincian malachite $\tilde{x}_{Zn,zm}$ as a function of pH_0 for $T = 55\ °C$ (Guse et al.[115]), respectively $T = 65\ °C$ (Zander et al.[78]), with $\tilde{x}_{Zn,Feed1} = 0.3$ and $\tilde{x}_{Zr,Feed1} = 0.1$ (Guse et al.).

The evaluation of $\tilde{x}_{Zn,zM} = f(pH_0)$ confirms that the maximum possible amount of Zn is incorporated into zincian malachite over the complete pH range investigated. For pH < 6, the amount of aurichalcite and zincian malachite is reduced and increasing amounts of rouaite form which is the reason why precipitation and aging are, in general, conducted at pH ≥ 6[31,36,82]. Higher values in the range pH ≥ 9 were not tested experimentally since they are confirmed to result in the separated, and thus not wanted, oxides CuO and ZnO[82]. These trends regarding Zn incorporation into zincian malachite and the phase composition as a function of pH are also evident in the model calculations. They provide a thermodynamic explanation for the formation of the undesired by-products at extreme pH and enable a faster model-based limitation of possible pH windows for future studies.

In summary, the thermodynamic equilibrium model with the newly determined solubility products of (zincian) malachite, aurichalcite and hydrozincite was able to predict the phase composition as a function of the metal nitrate feed composition and pH not only qualitatively, but also, for the most part, quantitatively. The deviations between model and experiment are

most probably the result of uncertainties in the Rietveld refinement due to the similar lattices of aurichalcite and hydrozincite. Altogether, these results affirm the hypothesis that aging can be understood as a process towards the thermodynamic equilibrium.

4.4 Temperature influence

The aging temperature is the second key parameter known to influence the phase composition of the aged intermediate[36,61,79]. Accordingly, its influence on the phase composition as well as the model's capability to reproduce the phase composition as a function of temperature are evaluated in Figure 4.12. Additionally, the influence of temperature on the composition of zincian malachite is analyzed in Figure 4.13.

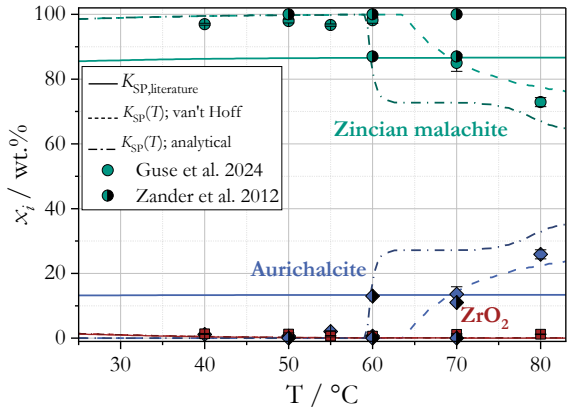

Figure 4.12: Comparison of the calculated and experimentally determined phase composition of the aged intermediate for a Cu/Zn ratio of $n_{Cu,tot} = 2\,n_{Zn,total}$ as a function of the temperature. Data from Guse et al. and Zander et al.[78,105].

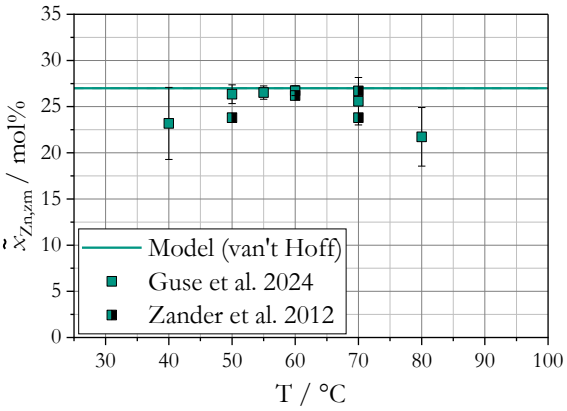

Figure 4.13: Experimental data and calculations for the zinc fraction in zincian malachite $\tilde{x}_{Zn,zM}$ as a function of temperature for $\tilde{x}_{Zn,Feed1} = 0.3$. Data from Guse et al. and Zander et al.[78,115]

In both experimental studies, the experimental phase composition was determined by Rietveld refinement. The data from Guse et al. for a ternary CZZ catalyst precursor indicates that for a metal ratio of $n_{Cu,total} = 2\,n_{Zn,total} = 6\,n_{Zr,total}$ and $pH(t_{age} = 0\ min) = 6.9$, zincian malachite and ZrO_2 with a mass ratio of approx. 9:1 are formed up to $T = 60\ °C$[105]. For higher temperatures, the mass fraction of aurichalcite increases up to $x_{aurichalcite} \approx 26\ w\%$ at 80 °C. This confirms studies for Cu/ZnO catalysts at similar conditions where the same trend was observed qualitatively[79] and quantitatively[78]. Since temperature-dependent solubility products are not available for all relevant phases in the literature, cf. Table 2.2 and Guse et al.[105], this effect cannot be described when applying a readily available database. In contrast, by applying the solubility products determined by the titration studies, cf. Section 4.2.3, the formation of aurichalcite for $T > 60\ °C$ is correctly predicted regardless of which temperature dependency was applied for $K_{SP,aur}$. The increasing mass fraction of aurichalcite with increasing temperature can now be explained using the solubility products: while the solubility of zincian malachite shows a small temperature dependency ($K_{SP,zm}(65\ °C) = 6.0 \cdot 10^{-35}\ mol^5 \cdot L^{-5}$), the solubility of aurichalcite drops significantly at increasing process temperatures: $K_{SP,aur}(65\ °C) = 6.5 \cdot 10^{-83}\ mol^{13} \cdot L^{-13}$, cf. Table 2.2 and Eq. (4.6)[105].Simultaneously, the zinc fraction in zincian malachite begins to drop when aurichalcite is present.

In summary, the influence of temperature on the phase composition of the aged intermediate can be reproduced quantitatively by the model. Due to the lack of temperature-dependent solubility products available in the literature, determining and applying solubility products in easy-to-implement titration studies was necessary for this approach to succeed.

4.5 Parameter optimization

As highlighted in Section 4.1, zincian malachite is the primary target phase of the aging process as its composition proved beneficial for the performance of the resulting catalyst[31,37,38,41,64]. Experimental studies to determine parameter ranges for which zincian malachite forms exclusively are time-consuming in execution and analysis and intrinsically at risk of overlooking optima. Thus, the thermodynamic equilibrium model is applied to evaluate its potential for process optimization regarding the optimum parameter ranges to obtain zincian malachite. Since the focus is on the interplay of Cu and Zn based phases, no third component, e.g. ZrO_2, is considered as it does not form a common phase with Cu or Zn[93] and its weight fraction is negligible compared to the hydroxycarbonate phases of Cu and Zn, cf. Section 4.3 and 4.4. In Figure 4.14, the prevailing phases at thermodynamic equilibrium are plotted as a function of the total reactant molalities $b_{CO_3^{2-},tot}$ and $b_{M,tot}$ in the mixed suspension for a binary $Cu(NO_3)_2/Zn(NO_3)_2$ feed with $\tilde{x}_{Zn,Feed1} = 27\ \%$ and $T = 55\ °C$.

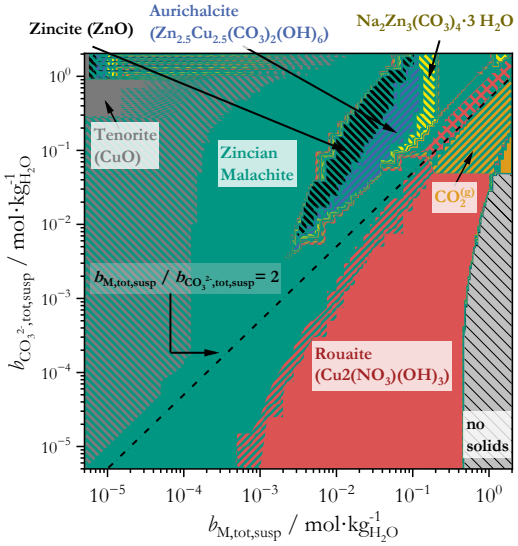

Figure 4.14: Prevailing solid phases at thermodynamic equilibrium as a function of the two total reactant molalities of Na_2CO_3 and $Cu(NO_3)_2/Zn(NO_3)_2$ in the mixed suspension for $T = 55\ °C$.

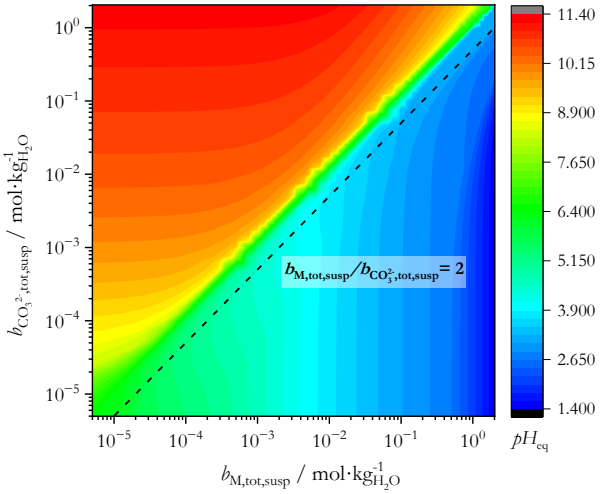

Figure 4.15: pH at thermodynamic equilibrium as a function of the two total reactant molalities of Na_2CO_3 and $Cu(NO_3)_2/Zn(NO_3)_2$ in the mixed suspension for $T = 55\ °C$.

In the proximity of a stoichiometric reactant ratio ($b_{M,tot,susp}/b_{CO_3^{2-},tot,susp} = 2$), zincian malachite is formed exclusively according to the model. At higher molalities, a nominal surplus of carbonate is required due to increased complex formation of Cu^{2+} ions, cf. Figure A.25 and Figure A.26. The shift towards these complexes also reduces the effective supersaturation for increasing reactant molalities, cf. Figure A.27 and Figure A.28. This is contrary to typical supersaturation trends, where supersaturation steadily increases with increasing reactant concentrations[145–147], and accordingly decreases the resulting mean particle size due to an

increasing dominance of nucleation compared to crystal growth[139,149–151]. This may also affect pore structure and surface area of the resulting catalyst as previously reported[35,58], or the aging kinetics as discussed further below in Section 5.2, and is therefore of pivotal importance for process and product optimization.

If there is a shortage of carbonate ions, rouaite forms as a second phase or exclusively. For $b_{\mathrm{M,tot,susp}} > 0.4\ \mathrm{mol \cdot kg_{H_2O}^{-1}}$ and $b_{\mathrm{CO_3^{2-},tot,susp}} < 0.1\ \mathrm{mol \cdot kg_{H_2O}^{-1}}$, no solids will form due to $pH \leq 4$, cf. Figure 4.15. In contrast, a surplus of carbonate ions results in an increased pH of 8 and more. Consequently, tenorite and zincite form additionally to zincian malachite. For $b_{\mathrm{M,tot,susp}} \approx 0.01 - 0.2\ \mathrm{mol \cdot kg_{H_2O}^{-1}}$ and a surplus of Na_2CO_3, the model indicates that aurichalcite and $Na_2Zn_3(CO_3)_4 \cdot 3H_2O$ form as additional by-products due to the increased amount of CO_3^{2-} and Na^+ ions in the system and the less pronounced complexation of Zn^{2+} ions with hydroxide ions compared to the aforementioned Cu^{2+} complexation at these conditions. This explains the repeatedly described presence of $Na_2Zn_3(CO_3)_4 \cdot 3H_2O$ [43,76,78,97,171] and aurichalcite[78,79] in various studies independent from the Cu/Zn ratio. All trends previously mentioned are similar when substituting Na_2CO_3 with $NaHCO_3$ albeit with shifted predominance ranges due to lower pH, cf. Figure A.23 and Figure A.24. Thus, the carbonate concentrations in future preparations should be at least double the stoichiometrically required quantity to avoid the formation of by-products and the incorporation of NO_3^- into the solids.

Alternatively, pH of the suspension can be adjusted independently from the two reactant molalities by adding nitric acid and sodium hydroxide for better phase control. Exemplary, the phase composition of solids as a function of the reactant molalities is plotted for $pH_{\mathrm{eq}} = 6.0$, $pH_{\mathrm{eq}} = 6.7$ and $pH_{\mathrm{eq}} = 8.0$ in Figure 4.16, Figure 4.17 and Figure A.32 in the appendix, which represent the typical range of pH chosen in the literature[31,36].

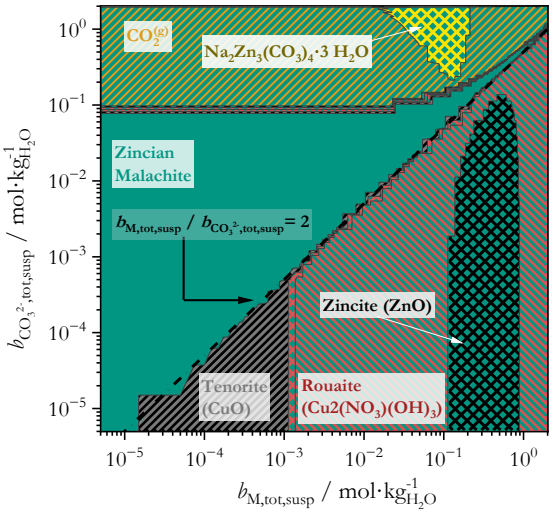

Figure 4.16: Prevailing solid phases at thermodynamic equilibrium as a function of the two total reactant molalities of Na_2CO_3 and $Cu(NO_3)_2/Zn(NO_3)_2$ in the mixed suspension for $pH_{\mathrm{eq}} = 6.0$ and $T = 55$ °C.

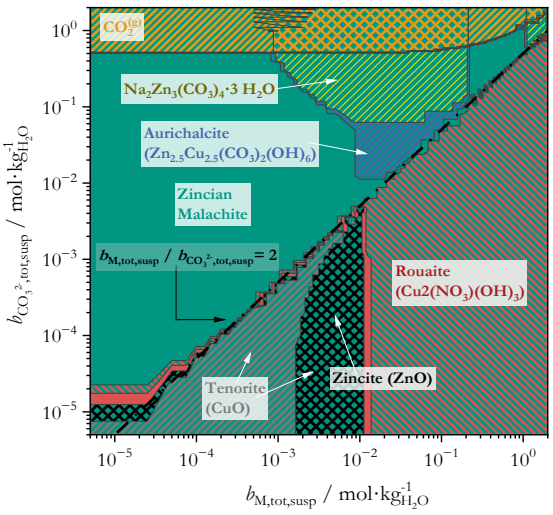

Figure 4.17: Prevailing solid phases at thermodynamic equilibrium as a function of the two total reactant molalities of Na_2CO_3 and $Cu(NO_3)_2/Zn(NO_3)_2$ in the mixed suspension for $pH_{\mathrm{eq}} = 6.7$ and $T = 55$ °C.

It is evident that in each of these cases the formation of zincite and tenorite is prevented when pH is kept constant and a surplus of carbonate ions is ensured. The biggest effect is

evident for $pH_{eq} = 6.0$ where $Na_2Zn_3(CO_3)_4 \cdot 3H_2O$ is formed as the only by-product next to zincian malachite. However, due to the state of the CO_3^{2-}/CO_2 equilibrium at this pH, $CO_2^{(g)}$ formation is prevalent for technically relevant carbonate molalities of $b_{CO_3^{2-},tot} \geq 0.1\ mol \cdot kg_{H_2O}^{-1}$ and supersaturation is reduced significantly, cf. Figure A.29 ff. This effect is less pronounced for $pH_{eq} = 6.7$ and not evident for $pH_{eq} = 8.0$. For $pH_{eq} = 8.0$ however, aurichalcite and $Na_2Zn_3(CO_3)_4 \cdot 3H_2O$ form for a broader reactant range. Thus, out of the three pH considered, $pH_{eq} = 6.7$ is the recommended pH based on model calculations.

If pH or the reactant molalities are not constant during aging, the process may follow a trajectory across different areas of predominance, cf. Figure 3.2 and Figure A.23, resulting in an aged intermediate that consists of multiple solid phases. This can also be true for inhomogeneous conditions in a stirred tank reactor, especially if reactants are intermixed at low energy dissipation rates, e.g. at the surface. This way, undesired by-products may form unnoticed and Na^+ or NO_3^- may be incorporated into the material. If the thus formed solid phases are sufficiently stable under the aging conditions applied, this will result in an inhomogeneous metal distribution within particles at the nanoscale and in between particles at micrometer scale. These inhomogeneities in the aged intermediate will then also be present in the resulting catalyst. In Figure 4.18, the influence of pH on the specific surface area of the resulting CZZ precatalyst is investigated experimentally for $b_{M,tot,susp} = 0.12\ mol \cdot kg_{H_2O}^{-1}$ and $b_{CO_3^{2-},tot,susp} = 0.51\ mol \cdot kg_{H_2O}^{-1}$ at 55°C. The maximum specific surface area S_{BET} is achieved for $pH = 6.7$ which is in agreement with the previous discussion on the pH dependence of phase composition after aging and literature data for the CZA catalyst[36]. It furthermore coincides with the maximum initial supersaturation of zincian malachite confirming the hypothesis that, in general, higher supersaturations result in smaller primary particles and thus larger specific surface areas. Increase and decrease of the pH both lead to decreasing supersaturations and surface areas. Accordingly, the model-based recommendation is confirmed.

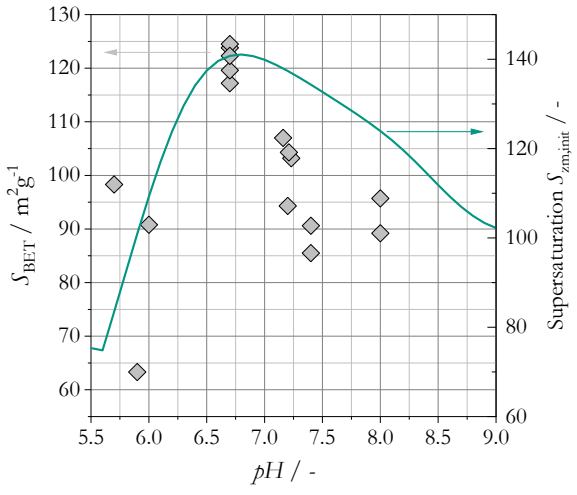

Figure 4.18: Influence of pH during aging on the supersaturation of zincian malachite $S_{zm,init}$ and the specific surface area of the resulting CZZ precatalyst.

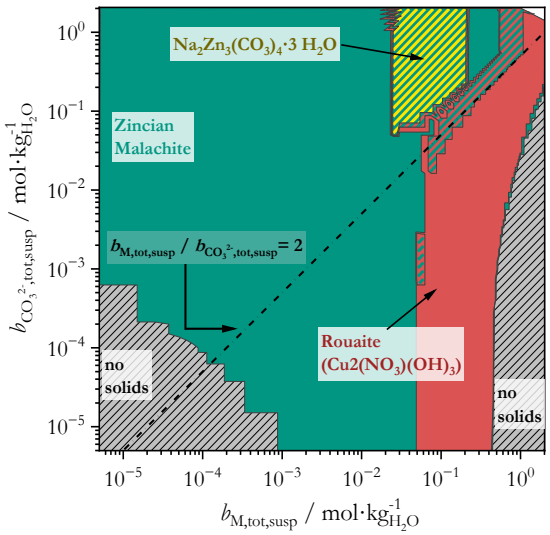

Figure 4.19: Phases at thermodynamic equilibrium as a function of the total reactant molalities of Na_2CO_3 and $Cu(NO_3)_2/Zn(NO_3)_2$ in the mixed suspension for a set pressure of $p_{CO_2} = 10\ bar$ and $T = 55\ °C$.

One possible approach to mitigate the release of CO_2 in future preparations is to condition the aging tank reactor with a CO_2 overpressure. The effect of the partial pressure of CO_2 on the solid-liquid equilibrium in a Cu^{2+}-H_2O-CO_2 system was previously discussed in the literature[213]. The authors concluded that, in theory, an increase of p_{CO_2} enables the formation of zincian malachite and azurite at reduced pH. The exemplary calculation results for $p_{CO_2} = 10\ \text{bar}$ in Figure 4.19 reaffirm these assumptions. Thanks to the overlay with CO_2, zincian malachite already forms at lower carbonate concentrations, thus lower pH. Furthermore, the formation of rouaite, aurichalcite, tenorite and zincite is seemingly suppressed due to the surplus of CO_2 and the corresponding shift in the carbonate speciation. This may be the way forward for a more sustainable, yet economic, catalyst production with a reduction of Na_2CO_3 usage, value-adding CO_2 utilization and the associated decline in CO_2 emissions. However, studies on the effect of a CO_2 atmosphere on the resulting catalyst properties are contradictory. The results by Taylor et al. indicate the formation of Cu/ZnO catalysts with reduced specific surface areas and thus reduced performances when applying a CO_2 atmosphere[214], while Wang et al. found a positive impact on the surface area and activity of a Cu/ZnO/Al2O3 catalyst[215]. The preparation by Taylor et al. was conducted at a slightly lower starting pH before CO_2 was added (7 instead of 8). The addition of CO_2 thus resulted in pH values below 7 which, in combination with aging times of up to five hours, might have promoted the formation of detrimental by-phases such as rouaite or gerhardtite. Further model-based studies will help to understand the contradictory results in detail and help to optimize catalyst preparation via CO_2.

Finally, the aging temperature as an established parameter to influence the phase composition of the aged precursor[78,79,82] and the characteristics of the (pre)catalyst[36,78], is considered in Figure 4.20 and Figure 4.21.

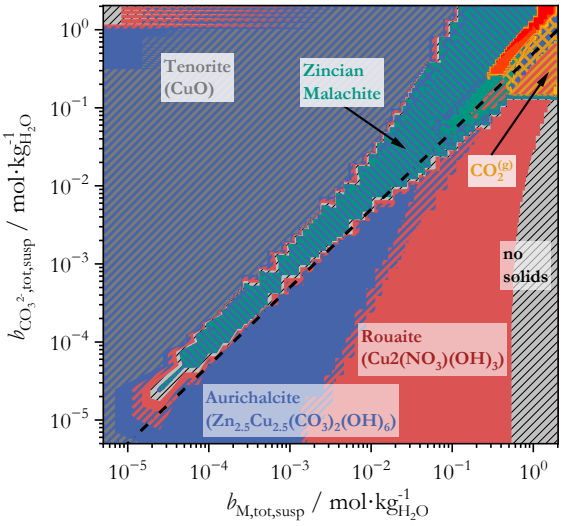

Figure 4.20: Prevailing phases at thermodynamic equilibrium as a function of the two total reactant molalities of Na_2CO_3 and $Cu(NO_3)_2/Zn(NO_3)_2$ in the mixed suspension for $T = 70\ °C$.

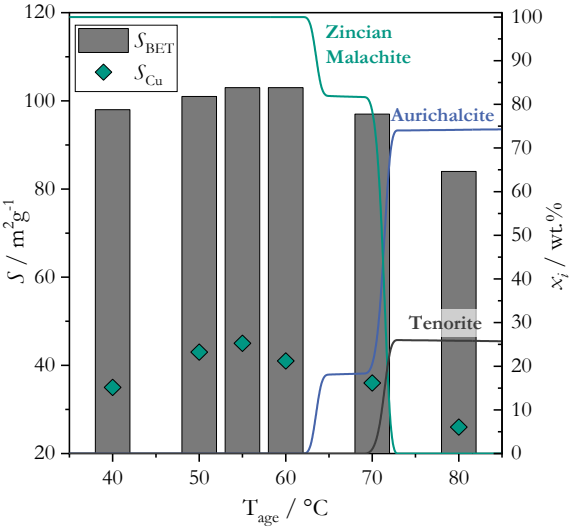

Figure 4.21: Influence of temperature during aging on the specific surface area S_{BET} and the specific copper surface area S_{Cu} of the resulting precatalyst as well as on the phase composition after aging. Experimental data from Pitter et al.[175,176]

Due to the negative reaction enthalpy of zincian malachite, cf. Table 2.2, higher temperatures should result in a reduced solubility product $K_{SP,zm}$ and, thus, smaller particles

with larger surface areas as well as a stronger tendency towards zincian malachite. This is true when comparing the solid phase plot for 40 °C, cf. Figure A.31, and 55 °C, cf. Figure 4.14. However, for 70 °C the solid phase composition plotted in Figure 4.20 is shifted towards aurichalcite across the entire concentration range considered. This can be explained by the more negative reaction enthalpy of aurichalcite, cf. Table 2.2. This also affects the surface area of the CZZ precatalyst plotted in Figure 4.21. Initially, both S_{Cu} and S_{BET} increase with increasing aging temperature up to 55 °C due to the increasing supersaturation of zincian malachite from $S_{\mathrm{zm,init}} = 92$ at 40 °C to $S_{\mathrm{zm,init}} = 127$ at 60 °C resulting in smaller PSD which seemingly are maintained throughout the subsequent drying and calcination. However, higher temperatures lead to the formation of aurichalcite, cf. Section 4.4, and thus a reduction of both surface areas. Consequently, the catalyst prepared at 55 °C also showed the highest methanol productivity[175,176].

In summary, the thermodynamic model proved to be suited for finding parameter ranges that result in the targeted solid phases. Experimental data confirmed that by doing so, S_{Cu} and S_{BET} of the precatalyst and the catalyst performance can be improved. In general, the following suggestions should be complied, if (zincian) malachite is the target phase:

- The ratio between carbonate ions and metal ions in the suspension should exceed the stoichiometric ratio: $b_{\mathrm{CO_3^{2-},tot,susp}}/b_{\mathrm{M,tot,susp}} > 2$ to compensate for the formation of complexes.
- For better phase control, pH should be kept constant, either by defined mixing in a mixing nozzle or pH control in a stirred tank reactor. Local inhomogeneities in the tank reactor are to be avoided.
- A preferrable pH to mitigate the formation of by-products is $pH \approx 6.7$. The exact value depends on the chosen reactant concentrations and can be determined via the model.
- If Zn ions are present, the ideal temperature is around $T_{\mathrm{age}} \approx 55 \pm 5$ °C. Otherwise, the optimum temperature may be higher.

By usage of thermodynamic equilibrium calculations, the number of necessary experiments for optimizing process parameters can be reduced to a minimum necessary for model validation and process development becomes more sustainable. An overall workflow for the transfer to technical application is discussed in Section 6.

4.6 Conclusions

The notion of this section was to evaluate if aging can be understood as a process towards the thermodynamic equilibrium and if it can be modeled accordingly. This would also clearly separate aging from the initial (co-)precipitation step, where the solids composition is assumed to be kinetically dominated. For this purpose, a thermodynamic solid-liquid equilibrium model was developed on basis of readily-available software solutions with a focus on the Cu/Zn based intermediates involved. The model consists of two parts: an activity coefficient model, which considers ion interaction, and a compilation of solubility products and ion association products

to represent speciation in the liquid phase and the equilibrium between solids and liquid phase. Based on pH measurements, the Pitzer model was deemed the most suitable activity coefficient model with deviations of a maximum of 15 % even at ionic strengths above 6 mol·L^{-1}. Certain solubility data was unavailable, e.g. the temperature-dependency for synthetic zincian malachite, or the solubility of the by-product $Na_2Zn_3(CO_3)_4 \cdot 3H_2O$. For these cases, an experimental method to determine missing K_{SP} from titration studies was developed and applied. Furthermore, the titration studies also confirmed that separate solubility products are necessary for the description of the co-precipitate and the aged intermediate.

Accordingly, two boundary cases were considered in the model. On the one hand, the initial state before solids formation sets in was regarded assuming complete and ideal mixing. It was successfully applied for the theoretical interpretation of the co-precipitation studies in Section 3. On the other hand, the thermodynamic state of equilibrium was calculated which, according to the hypothesis, should correspond to the final state after aging. For validation, the calculated phase compositions at thermodynamic equilibrium were compared to experimentally determined solid compositions as a function of pH, temperature and Cu/Zn ratio in the feed solution. In each case considered, the experimentally determined phase composition was reproduced quantitatively by the thermodynamic model, e.g. the presence of rouaite at $pH \leq 5$ additionally to zincian malachite or the emergence of aurichalcite as a by-product for $T \geq 70\ °C$ and $n_{Cu}/n_{Zn} = 2$ or $T = 65\ °C$ and $\tilde{x}_{Zn,Feed1} \geq 27\ mol\%$. The model results as well as the Rietveld refinement of experimental data confirmed that the mass fractions of ZrO_2 as a third catalyst component is negligibly small compared to the Cu and Zn based hydroxycarbonate phases. Thus, a simplification of the system to exclusively Cu, Zn and Na phases is valid if the focus is on finding optimum conditions to obtain zincian malachite. Deviations between model and measurement in the transition area between zincian malachite predominance and aurichalcite predominance are most probably a result of uncertainties in the Rietveld refinement. In conclusion, aging can be considered as a process towards the thermodynamic equilibrium and the composition of the aged intermediate can be described with the corresponding solid-liquid equilibrium.

Thus, the hypothesis from Section 4.1 is affirmed.

Additionally, the validated model was applied to determine technical feasible process parameters (reactant ratio, pH, temperature, p_{CO_2}) that lead to a product that is as pure as possible in zincian malachite and result in small particles, ergo large surface areas S_{BET}. A comparison of the thus determined parameter regimes with experimental S_{BET} confirmed that this approach yields accurate results for parameter optimization. It also provides explanations for temperature and pH optima that have long been promoted in the literature and a concept on how CO_2 could be used as a value-adding educt in the catalyst synthesis of the near future.

In summary, the strict separation of (co-)precipitation as a kinetically dominated step and aging as a separate step that is governed by the thermodynamic equilibrium is a key concept to better understand, predict and optimize co-precipitation and aging and, consequently, the resulting catalyst.

5 How to increase the space-time-yield of co-precipitation and aging for technical application

Next to the ability to prepare high-performance catalysts with a precisely defined composition, the economic efficiency of the preparation is essential to transfer a catalyst recipe to technical application. Thus, methods to increase the space-time-yield, and therefore reduce costs, while maintaining the product quality are key for the successful transfer of any recipe from the lab to the production line. In this section, the focus is on reducing the necessary process time to induce and complete the phase transformation in the time- and heat-intensive aging step. First, the impact and applicability of approaches described in the literature is evaluated. Then, on this basis, two promising approaches are further developed and investigated regarding their impact on space-time-yield and product quality.

5.1 State of the art and research hypotheses

The space-time-yield Y_{ST} of co-precipitation and aging is defined according to Eq. (5.1) as the ratio of the dry mass of newly formed aged intermediate $m_{\mathrm{age,dry}}$ per process time t_{process} needed to complete co-precipitation and aging and per reactor volume V_{reactor}. If seeding crystals with the mass m_{seeds} are added to the process, see below, the total mass of solids $m_{\mathrm{solids,total}}$ has to be corrected accordingly.

$$Y_{\mathrm{ST}} = \frac{\Delta m_{\mathrm{age,dry}}}{t_{\mathrm{process}} \cdot V_{\mathrm{reactor}}} = \frac{m_{\mathrm{solids,total}} - m_{\mathrm{seeds}}}{t_{\mathrm{process}} \cdot V_{\mathrm{reactor}}} \tag{5.1}$$

In principle, the most direct approach to increase the space-time-yield of the aging step would be to further increase the solids concentration, i.e. the ratio of $\Delta m_{\mathrm{age,dry}}$ to V_{reactor}. However, it is limited by the maximum solubility of the reactants which are, generally, already near the respective maximum[31,117,216]. Additionally, higher concentrations promote the formation of unwanted byproducts, cf. Section 4.5. Thus, several approaches on how to decrease the necessary aging time to complete the phase transformation for a defined solids concentration were investigated in the literature instead. Güldenpfennig et al. and others demonstrated with their experimental in-situ studies at milliliter scale that the transformation kinetics are accelerated for increased temperatures[75,78,79] and reduced Zn fractions[72,75]. Similarly, pH also affects aging kinetics[36,100]. However, these parameters cannot be chosen freely since they also strongly correlate with the catalyst performance, cf. Section 4.1, and are thus unsuitable to maximize yield.

The results from Section 3 indicate that morphology and composition of the co-precipitate may also impact the necessary aging time. Samples, that showed a variation in size and composition in between individual particles, remained inhomogeneous after aging was conducted for a limited time, cf. Figure 3.12. While some particles already transformed into crystalline zincian malachite, other particles were still amorphous. In theory, a phase transformation via the liquid phase should benefit from smaller particles with a larger specific surface area and thus enhanced dissolution kinetics[217,218]. A study by Jiang et al. showed a

variance of 25 to 33 % in the required aging time for varying mixing intensities, but without any trend regarding the mixing intensity[35].

According to Güldenpfennig et al., seeding may be another potential approach to reduce the necessary aging time without affecting the product properties. The authors halved the necessary induction time for a binary Cu/Zn based system by adding a small volume of previously aged suspension containing zincian malachite to the reaction vessel before adding the reactant solutions[75]. In general, the amounts of seeds added to a system is described with the seed mass fraction x_{Seeds} according to Eq. (5.2) with the mass of seeds m_{Seeds} and the total mass of solids in the suspension $m_{\mathrm{solids,total}}$:

$$x_{\mathrm{Seeds}} = \frac{m_{\mathrm{Seeds}}}{m_{\mathrm{solids,total}}} \tag{5.2}$$

A further increase of x_{Seeds} further decreased the induction time. However, these findings are limited to small volumes on the milliliter scale and low total metal concentrations in the suspension of $\tilde{c}_{\mathrm{M,susp}} = 0.1\ \mathrm{M}$. Furthermore, the impact of seeding, and the thus reduced aging times, on the intermediate properties and on the product qualities were not evaluated[75].

In general, seeding is applied in industrial crystallization to improve process control and avoid statistical fluctuations, particularly when particles smaller than 10 µm are involved or when the process is carried out within the metastable zone limit of primary nucleation[120,219,220]. This way, secondary nucleation instead of uncontrolled primary nucleation is achieved. Additionally, polymorphism can often be controlled by using seeds of the targeted polymorph[221–224]. Depending on the substance and process design, seed weight fractions x_{Seeds} between 0.1 to 1.0 wt.% according to Eq. (2.1) are required to allow secondary nucleation below the metastable zone limit[225]. Since the composition of the solution is not altered when adding solids to a supersaturated solution regarding this solid, the solid-liquid equilibrium is, in general, not altered when adding seeds. Finally, seeding is used to obtain defined particle shapes and size distributions, which affect the filterability and flow properties of the particles in downstream processes. The morphology is, in general, also crucial for the contemplated application, e.g., the dissolution properties of proteins[221] or the surface and microstructure properties of catalysts[84,85,101,120]. Since the effect of seeding is based on surface processes, not only the quantity of seed crystals but also the available surface area of the seed material is decisive for its function[226,227].

Based on these results, the target of this section is to validate if the reduction of aging time by seeding can be confirmed for industrially relevant solids concentrations of more than 5 wt.% and if seeding is the preferrable approach to optimize the space-time yield of aging. This is summarized as the following working hypothesis:

Seeding with an aged intermediate accelerates the aging kinetics without altering the properties of the thus resulting aged intermediate. Therefore, seeding is the most sensible method for space-time-yield optimization.

Accordingly, if an increase of the space-time-yield by seeding is possible, it is key to determine if the catalyst performance is affected negatively by the modified process and if other approaches result in similar space-time-yield improvements, i.e. an optimization of the co-

precipitate morphology. The findings are ultimately used to develop a workflow to recommend a process route for technical application.

5.2 The influence of co-precipitation on aging kinetics

According to the definition of the space-time-yield in Eq. (2.1), the two possibilities to increase Y_{ST} for a fixed reactant concentration and plant are to decrease the necessary process time $t_{process}$ or to increase the volume flow of feeds $\dot{V}_{feed\,i}$ during co-precipitation which correlates with the ratio of $\Delta m_{age,dry}$ to $V_{reactor}$. A further increase of $\dot{V}_{feed\,i}$ for the state-of-the-art semi-batch co-precipitation is generally difficult as stable pH control becomes increasingly challenging and the further increase of local inhomogeneities in the reactor results in a presumably more inhomogeneous material on the nano- and micrometer scale and, thus, worse-performing catalyst. However, by switching to a continuous co-precipitation, $\dot{V}_{feed\,i}$ can be increased arbitrary due to its steady-state nature as long as the integrated pumps allow a stable, pulsation-free supply of feeds. As the results in Section 3 confirm, the change of method also improves the properties of the resulting (pre)catalyst. For the current setup, the switch from semi-batch to continuous co-precipitation reduced the co-precipitation time from over 1 h to less than 4 min, i.e. by more than 90 %. A further increase of the volume flows for the continuous co-precipitation has a negligible effect on the total process time $t_{process}$ since, in general, an aging time of at least 20 min to, more frequently, 90 min and more is necessary to complete phase transformation[31,36,101] and aging becomes the dominating factor with $t_{process} \approx t_{age}$.

Therefore, an approach to reduce the necessary aging time is required to further increase the space-time-yield of co-precipitation and aging. In general, larger mass-specific surface areas increase dissolution kinetics[217,218] and are beneficial for contact-mediated (re)crystallization processes since the same solid mass then equals more particles which, in turn, result in larger collision frequencies[228,229]. Thus, a larger surface of the co-precipitate should result in faster aging kinetics regardless of whether aging proceeds via the liquid phase[75] or is the result of a solid-state transformation[70,78,95]. The previous results confirm that $S_{BET,prec}$ of a CZ co-precipitate is nearly quadrupled when increasing the energy dissipation rates during the mixing of the two reactant solutions, cf. Section 3.3. Accordingly, the influence of $S_{BET,prec}$ on the aging kinetics is investigated in Figure 5.1 by taking samples at defined aging times and analyzing them with PXRD.

For the coarse co-precipitate in Figure 5.1(a) that was precipitated in the laminar and mixing-influenced regime ($Re_{mix} = 176$), no reflexes are visible for $t_{age} = 0\,\text{min}$, which indicates the sole presence of the amorphous co-precipitate rich in (zincian) georgeite directly after co-precipitation is completed[71,72]. Only after aging for 90 min, the first, weakly pronounced reflexes are evident, that are allocated to the known intermediate $Na_2Zn_3(CO_3)_4{\cdot}3H_2O$ and the target phase zincian malachite[73]. Finally, the scattering pattern for $t_{age} = 300\,\text{min}$ matches zincian malachite and less than 1 % aurichalcite which corresponds to the phase composition predicted by the thermodynamic model, cf. Section 4.3. Further aging no longer changes the

crystalline phase composition of the solids confirming that the state of thermodynamic equilibrium is reached.[101]

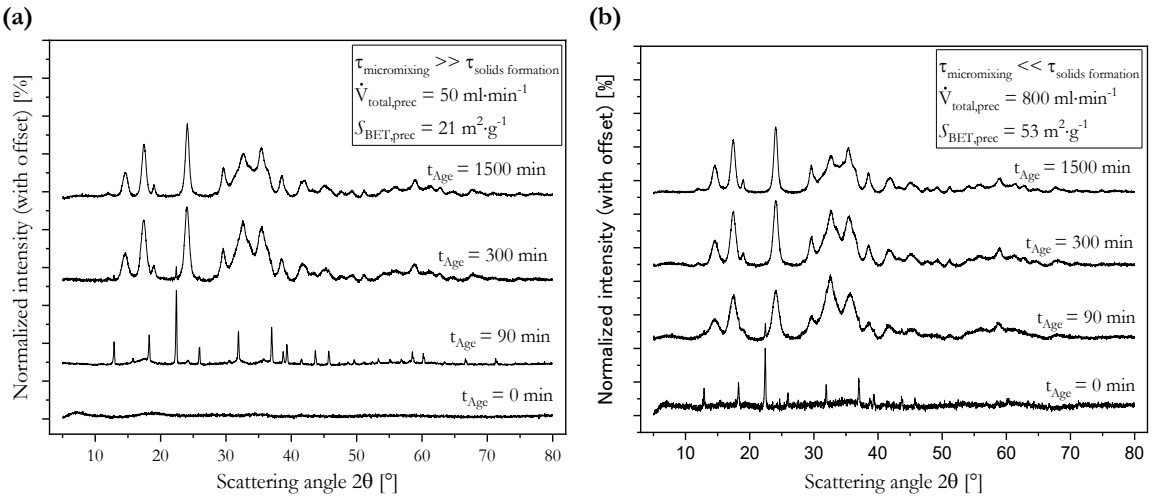

Figure 5.1: Development of the solids phase composition during aging analyzed by PXRD for two samples with, respectively, (a) slow and (b) fast mixing in the preceding co-precipitation. Based on Guse et al.[101]

The corresponding data in Figure 5.1 (b) for the fine co-precipitate with a specific surface area more than twice as large, that was precipitated in the turbulent regime ($Re_{mix} = 2812$) in the absence of mixing influences, shows that the metastable intermediate $Na_2Zn_3(CO_3)_4{\cdot}3H_2O$ is already present directly after co-precipitation is finished. Furthermore, the virtually identical final phase composition is already present after only 90 min of aging. Afterwards, the diffractogram, again, does not change noticeably meaning that the thermodynamic equilibrium is reached. The necessary aging times to complete phase transformation $t_{age,min}$ were confirmed by the occurrence of the aforementioned pH minimum[101] which resulted in 76 min, respectively, in 94 min. The resulting correlation between $t_{age,min}$ and $S_{BET,prec}$ is summarized in Figure 5.2 for both a simplified CZ catalyst precursor and the industrially relevant CZZ variant. Both catalyst compositions behave similarly: when the surface are of the co-precipitate is increased, the required aging time decreases significantly. The large uncertainties regarding $t_{age,min}$ are a result of increasingly long process times for precipitation. In these cases, co-precipitation and aging overlap and the aging time is not constant for all particles.

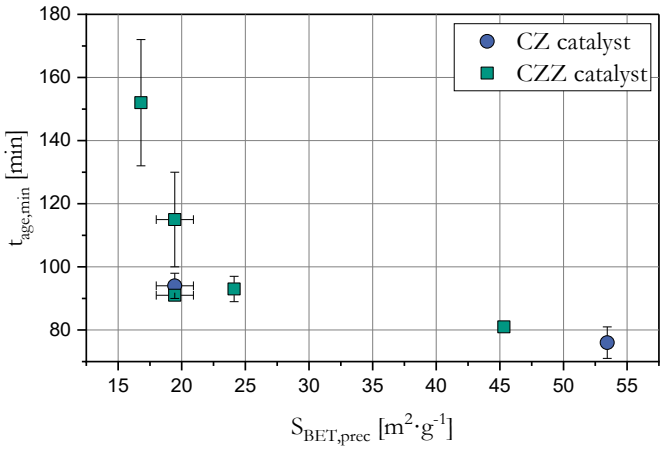

Figure 5.2: Correlation between the mass-specific surface area of the co-precipitate and the necessary aging time to complete phase transformation to zincian malachite.

Altogether, while the final phase composition after aging is controlled by the thermodynamic equilibrium, the aging kinetics do depend on the morphology, in particular S_{BET}, of the co-precipitate. The formation of particles as small as possible in the co-precipitation by mixing in the non-mixing influenced regime reduces the necessary aging time to complete phase transformation in the present setup by up to 50 %. This is equivalent to increasing the space-time yield by 50% if $t_{prec} \ll t_{age}$ applies.

5.3 Seeding as a decisive tool to accelerate aging

Seeding is a widely used method in technical crystallization processes for better control of the process and the resulting crystal morphology[219,220]. A study by Güldenpfennig et al. showed that the method can, in principle, also be applied to accelerate the aging step in the production of Cu/Zn based catalysts[75]. The aim of this chapter is, first, to verify the results for the more complex and industrially relevant CZZ variant and then to quantify the influence on aging kinetics and space-time-yield on the liter scale, cf. Section 5.3.1 and 5.3.2. Finally, it is evaluated in Section 5.3.3 if seeding and the thus possibly shortened aging time have a negative effect on the precatalyst properties and the catalyst performance as seen in studies with a reduced aging time[77,90]. A final assessment will tell whether seeding should be implemented on a technical scale.

5.3.1 Influence of seed mass fraction on the space-time-yield

First, the influence of the seed crystal amount on the necessary aging time to complete the phase transformation from (zincian) georgeite to zincian malachite $t_{age,min}$ is investigated. For this purpose, the pH profiles over the progressing aging time are plotted for an unseeded aging process and seeded aging experiments with varying amounts of seeds in Figure 5.3 (a), respectively, in Figure 5.3 (b).

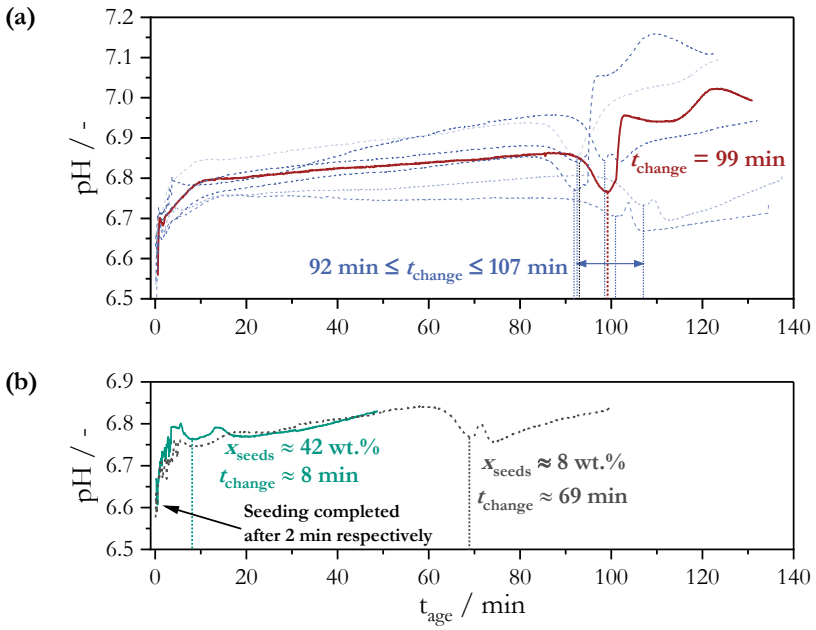

Figure 5.3: Evolution of pH over the progressing aging time t_{age} for **(a)** seven independent unseeded reference experiments and **(b)** two seeded experiments with $x_{Seeds} = 8$ wt. % and $x_{Seeds} = 42$ wt. %, respectively. CZZ catalyst precursor with $b_{M,susp} = 0.14\ mol \cdot kg_{H_2O}^{-1}$ ($x_{solids} \approx 2$ wt. %) and $n_{Cu}/n_{Zn}/n_{Zr} = 6/3/1$ at $T = 55$ °C. Adapted from Guse et al.[115,120]

As discussed previously, the effect of seed crystals is heavily influenced by their mass-specific surface $S_{\mathrm{BET,seeds}}$. Thus, for quantifying the correlation between the more accessible seeding mass and the aging time, $S_{\mathrm{BET,seeds}}$ or both the morphology and the PSD of the seeds have to be constant. This is confirmed by BET and PSD measurements discussed in Figure 5.7 and Figure 5.8 in the next section, where the influence of $S_{\mathrm{BET,seeds}}$ on the aging time is investigated separately. All curves in Figure 5.3 (a) from seven independent, unseeded CZZ aging experiments show the same characteristic progression. First, during initial wetting of the pH electrode when co-precipitation starts, pH rises sharply up to the target value of $pH(t_{\mathrm{age}} = 0\ \mathrm{min}) = 6.7$. During aging, pH is almost stable and rises, if at all, only slightly by approx. $\Delta pH \leq 0.25$ over 90 min. Then, after a total aging time of 92 to 107 min, a pH minimum is passed that coincides with a change in color and indicates that the phase transformation to zincian malachite is completed[31,88,230]. The XRD evaluation in Figure 5.4 (a) and FT-IR evaluation[120] both confirm this.

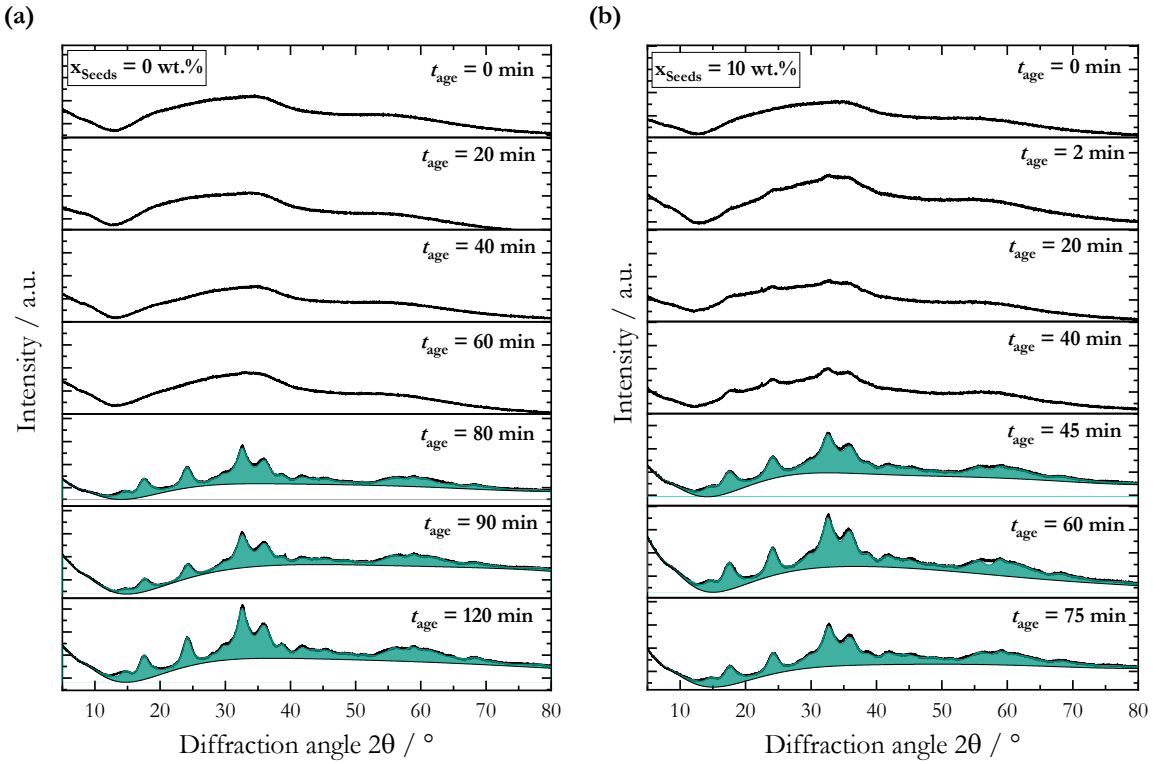

Figure 5.4: X-ray diffractograms of washed and dried samples as a function of aging time for: **(a)** the standard aging process without seeding ($x_{\mathrm{Seeds}} = 0\ \mathrm{wt.\%}$) and **(b)** a preparation where seeds were added after co-precipitation was completed at $t_{\mathrm{age}} = 0\ \mathrm{min}$ ($x_{\mathrm{Seeds}} = 10\ \mathrm{wt.\%}$). The phase composition in green (zincian malachite) was evaluated by Rietveld refinement. Adapted from Guse et al.[120]

After the respective pH minimum is reached, aging is continued for an additional 30 min, to make sure that the phase change is completed for each individual particle. In a few instances, a second pH minimum occurred 5–10 min after the first. However, it could not be correlated to any events by FT-IR or PXRD[120] and is unknown in the literature. Temporary deposits on the pH probe during the phase transformation might be a possible cause. Overall, the preparation with a necessary aging time of $t_{\mathrm{age,min}} = 93 \pm 8\ \mathrm{min}$ is deemed reproducible when the same process conditions are applied[120]. The same pH development is evident for both seeded experiments in Figure 5.3 (b). However, the pH minimum that corresponds to the phase

change already occurs after $t_{\mathrm{age,min}} = 69\ \mathrm{min}$ for $x_{\mathrm{Seeds}} = 8\ \mathrm{wt.\%}$ and, respectively, after only 8 min of aging for $x_{\mathrm{Seeds}} = 42\ \mathrm{wt.\%}$. Once more, an exemplary Rietveld refinement for 10 wt.% seeds in Figure 5.4 (b) and the FT-IR evaluation[120] validate the required time for phase transformation.

The development of the X-ray diffractogram over the aging time is depicted in Figure 5.4 for both an unseeded aging process ($x_{\mathrm{Seeds}} = 0\ \mathrm{wt.\%}$) and for $x_{\mathrm{Seeds}} = 10\ \mathrm{wt.\%}$. Without seeding, all four samples for $t_{\mathrm{age}} \leq 60\ \mathrm{min}$ are amorphous. The corresponding XRF evaluation, cf. Figure A.12 in the appendix, shows a quasi-consistent Zn fraction in the solids throughout aging. This implies that Cu and Zn co-precipitate directly and completely at the beginning ($t_{\mathrm{age}} \to 0$ min) as one or multiple amorphous solids as reported in literature[70,78,127] and that no subsequent incorporation of Zn ions from the solution occurs. First crystalline diffraction patterns corresponding to zincian malachite appear in the 80-minute sample. However, the evaluation of the Zn fraction $\tilde{x}_{\mathrm{Zn,zm}}$ by Rietveld refinement, cf. Figure A.12, shows large uncertainties for up to $t_{\mathrm{age}} = 100\ \mathrm{min}$ indicating that a transformation in the crystal structure is still proceeding and that areas of amorphous solids still exist until then. Only when the phase transformation is completed, as indicated by the pH minimum and the change in color, consistently high Zn fractions in the predicted range of $\tilde{x}_{\mathrm{Zn,zm}} \approx 0.27$ prevail. All additional Zn is present as minor amounts of aurichalcite or hydrozincite ($0.3\ \mathrm{wt.\%} < x_{\mathrm{aur}} < 6.4\ \mathrm{wt.\%}$) as confirmed by Rietveld refinement, cf. Figure 5.9 (a)[120].

For $x_{\mathrm{Seeds}} = 10\ \mathrm{wt.\%}$, a defined amount of dried seed crystals is added to the suspension directly after co-precipitation is completed at $t_{\mathrm{age}} = 0\ \mathrm{min}$. Accordingly, minimal hints of weakly pronounced diffraction pattern are evident for $t_{\mathrm{age}} \geq 2\ \mathrm{min}$ in Figure 5.4 (b). Yet, since 90 wt.% of the solids is freshly co-precipitated material, the diffractogram is still amorphous. Here too, $x_{\mathrm{Zn,total}}$ in the solid phase is constant over the progression of aging, cf. Figure A.12, which implies that the phase change proceeds by the restructuring of an amorphous Cu/Zn-based solid phase. Based on FT-IR analysis[120] and references from literature[72,95], zincian georgeite is the most probable phase. For $x_{\mathrm{Seeds}} = 10\ \mathrm{wt.\%}$, the phase transformation into zincian malachite already occurs for $t_{\mathrm{age}} = 45 \pm 2\ \mathrm{min}$ as implied by pH, color change and the X-ray diffractogram. All samples afterwards show $x_{\mathrm{zm}} \geq 95\ \%$ and $\tilde{x}_{\mathrm{Zn,zm}} \approx 0.27$. This verifies the results by Güldenpfennig et al.[75] and affirms that seeding does accelerate the induction time until the phase change to zincian malachite takes place ($t_{\mathrm{age,min}}$). Consequently, the use of seeds composed of zincian malachite accelerates the whole aging process significantly.[120]

In Figure 5.5 (a) and (b), the correlation between the seeding mass fraction x_{Seeds} and the necessary aging time, until a phase transformation to zincian malachite is evident, is plotted for two solids concentrations.

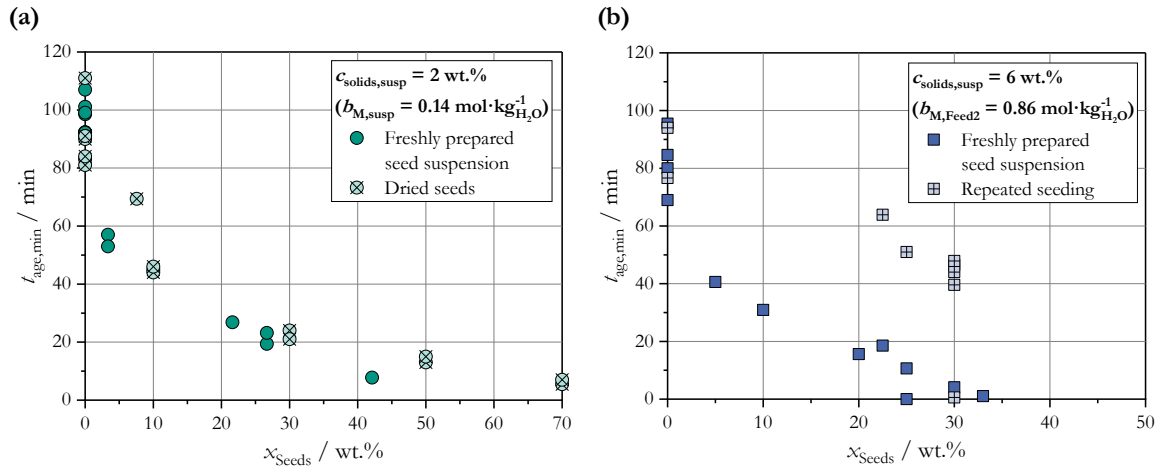

Figure 5.5: Necessary aging time until the phase change is completed ($t_{\mathrm{age,min}}$) for a CZZ catalyst precursor at $T = 55$ °C as a function of the seed mass fraction x_{Seeds} for **(a)** a low solids concentration ($x_{\mathrm{solids,susp}} = 2$ wt. %) and two different seeding methods and **(b)** an increased solids concentration ($x_{\mathrm{solids,susp}} = 6$ wt. %) showing the difference between one-time and repeated seeding. Adapted from Guse et al.[120]

For the lower solids concentration of $x_{\mathrm{solids,susp}} = 2$ wt. % ($b_{\mathrm{M,susp}} = 0.14$ mol · $\mathrm{kg}^{-1}_{\mathrm{H_2O}}$) the two seeding methods described in Section 2.3.2 are compared: using a (concentrated) seed suspension that has been aged directly before and stored for less than 15 min and the use of dried seed crystal that were kept for up to one month. In the absence of seeds, the phase transition requires a mean aging time of $t_{\mathrm{age,min}} = 94 \pm 9$ min. The necessary aging time decreases for both seeding techniques as x_{Seeds} increases. The most significant drop-off is evident between no seeding and $x_{\mathrm{Seeds}} = 3$ wt. %, where $t_{\mathrm{age,min}}$ is already lowered by 41 %. When seeds that have been dried and then resuspended are used, the impact is less pronounced. Still, the required aging time is minimized to only 6 min when $x_{\mathrm{Seeds}} = 70$ wt. % are applied. A similar aging time ($t_{\mathrm{age,min}} = 8$ min) is achieved for the seed suspension with $x_{\mathrm{seeds}} = 42$ wt. %. The higher mean particle size and smaller mass-specific surface area of the dried seeds in comparison to the fresh seed suspension, which are covered in Section 5.3.2, provide an explanation for the disparity in efficacy between both techniques. Güldenpfennig et al. claim that the phase change proceeds via the solution[75]. Therefore, a greater surface area, for example, when there are more seeds of the same diameter present, could account for the increased aging kinetics.

The experiments were repeated with an increased solids concentration of $x_{\mathrm{solids,susp}} = 6$ wt. % in Figure 5.5 (b) to validate if seeding is transferable to industrially more relevant concentrations. Compared to the low-concentration studies, the impact of seeding is even more pronounced as the required aging time decreases from $t_{\mathrm{age,min}} = 83 \pm 9$ min to 46 min for $x_{\mathrm{Seeds}} = 5$ wt. %. For $x_{\mathrm{seeds}} \geq 30$ wt. %, an instantaneous phase transformation when the co-precipitate suspension and seed suspension meet, is achieved. The improved efficacy on the aging time reduction may result from an increased number density of particles in the suspension and, thus, a larger absolute surface area[120]. Alternatively, the increased number of particles could increase the collision frequency between non-aged and aged particles, similar to the mechanism behind contact-mediated nucleation processes[231,232].

Additionally, repeated seeding is investigated for $x_{\mathrm{solids,susp}} = 6\ \mathrm{wt.\%}$ with the goal to operate the aging tank reactor continuously in the future. For this purpose, when aging is finished, a defined volume of the aged suspension is kept in the reactor and utilized as the seed suspension for a second aging process. This procedure is then repeated up to five times. Compared to a one-time seeding, the aging time rises to 36 to 53 minutes except one outlier at 4 min when seeding with $x_{\mathrm{Seeds}} = 30\ \mathrm{wt.\%}$ is conducted repeatedly. This anomaly is not explainable by an incomplete phase transformation of the thus generated seed suspensions as PXRD, cf. Figure 5.9 (a), and FT-IR analyses of the respective particles indicate zincian malachite as the sole phase[120]. The morphology and composition of the aged intermediate also show no differences between an unseeded, one-time and repeatedly seeded preparation, cf. Figure 5.10 and the available literature[120]. Accordingly, a more detailed analysis is required to understand the renewed increase in necessary aging time and to possibly mitigate this effect. Yet, repeated seeding still proves to be a viable option in its current form compared to the state-of-the-art process as the average aging time is 54% shorter than for the unseeded approach.

Next, the impact of the various seeding methods on the space-time-yield Y_{ST} as defined in Eq. (5.1) for the two solids concentrations investigated is summarized in Figure 5.6. This way, the scalability of the approaches can be discussed. In each case, Y_{ST} rises with increasing seed mass fractions, independent from the chosen seeding approach. No upper limit is evident, even though the reactor volume is effectively lowered when adding increasing amounts of seed suspension. As anticipated, the findings also show that the solid-liquid equilibrium is not altered by the addition of seeds as the yield increases according to the mass of seeds added and the elemental composition of the solid is constant, cf. Figure 5.9 and Table 5.1. Remarkably, the impact of seeding on Y_{ST} exceeds the impact of increasing the reactant concentration from $b_{\mathrm{M,Feed2}} = 0.27\ \mathrm{mol \cdot kg_{H_2O}^{-1}}$ to $b_{\mathrm{M,Feed2}} = 0.86\ \mathrm{mol \cdot kg_{H_2O}^{-1}}$. For $x_{\mathrm{seeds}} \approx 30\ \mathrm{wt.\%}$ and $b_{\mathrm{M,susp}} = 0.43\ \mathrm{mol \cdot kg_{H_2O}^{-1}}$, the biggest improvement is achieved with an increase of the space-time-yield by a factor of up to 60.

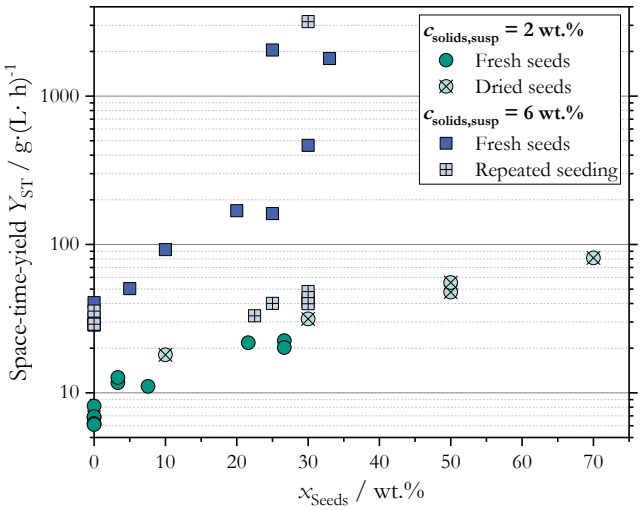

Figure 5.6: Space-time-yield of the aging process as a function of the seed mass fraction x_{Seeds} for the various seeding methods investigated for $x_{\mathrm{solids,susp}} = 2\ \mathrm{wt.\%}$ ($b_{\mathrm{M,susp}} = 0.14\ \mathrm{mol \cdot kg_{H_2O}^{-1}}$) and $x_{\mathrm{solids,susp}} = 6\ \mathrm{wt.\%}$ ($b_{\mathrm{M,susp}} = 0.43\ \mathrm{mol \cdot kg_{H_2O}^{-1}}$). Adapted from Guse et al.[120]

More than two kilograms of aged intermediate per hour and liter of reactor capacity can be prepared with this approach. When seeding is conducted repeatedly, Y_{ST} decreases in accordance with the results discussed above but remains 5% larger than it is without seeding. The space-time-yield was reproducibly increased by a factor of 12 for the highest seed mass fraction of dried seeds tested. This makes dried seeding crystals a dependable and storable substitute for the fresh seed suspension, e.g. to starting up the process.[120]

In summary, seeding the co-precipitate suspension with zincian malachite crystals was confirmed to accelerate aging by reducing the induction time until zincian malachite is detectable, also at liter scale and increased solids concentrations of approx. 6 wt.%. Increasing the amount of seeds increases the aging kinetics until for $b_{M,Feed2} = 0.86\ \mathrm{mol \cdot kg_{H_2O}^{-1}}$ and $x_{Seeds} = 30\ \mathrm{wt.\%}$ a quasi-instantaneous aging was reproducibly achieved. Accordingly, the space-time yield of aging was increased up by a factor of 60. However, repeated seeding reduced its impact on the aging time for unknown reasons in most of the cases making additional studies in the future necessary. The use of dried seeds instead of a seed suspension also showed an attenuated effect, probably due to a reduced specific surface area, but can be used as an alternative if seeds have to be stored for a prolonged time. In the next two sections, the role of the seed surface area for accelerating aging and the impact of seeding on the resulting catalyst properties are investigated. Then, a final evaluation of the question whether seeding should be applied in future catalyst preparations can be performed.

5.3.2 Relevance of the seed surface area

As discussed previously, the overall accessible surface area of the seeds is generally responsible for the effect of seeding[226,227]. The effective surface area of the seeds dispersed in the suspension can only be estimated, for example, based on static light scattering (SLS) measurements of the size using Eq. (5.3) or by BET analysis of the dried material. However, drying significantly changes the surface properties of the seeds compared to their suspended state[97] and is there not considered for analysis here.

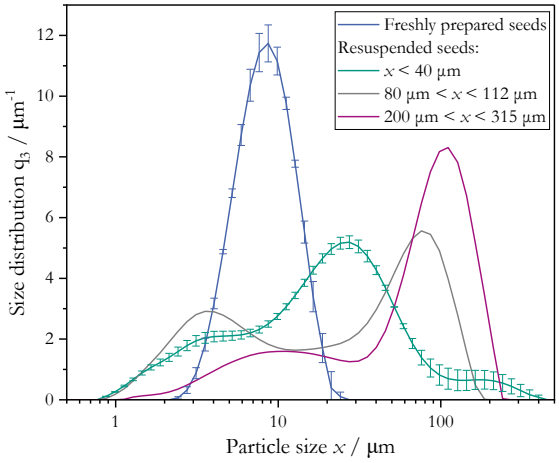

Figure 5.7: Mean particle size distribution of freshly prepared seed suspensions and of resuspended dried seeds with three different sieving fractions. Adapted from Guse et al.[120]

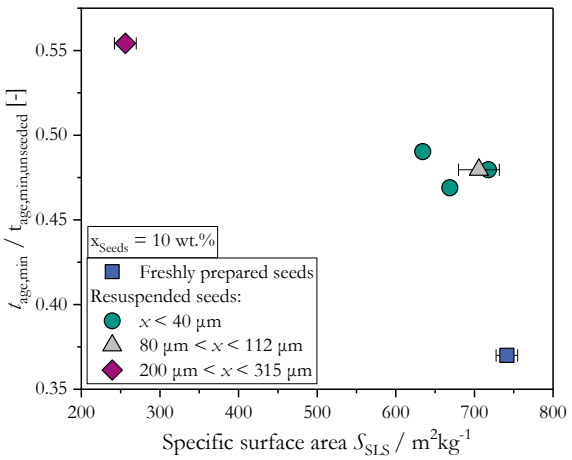

Figure 5.8: Influence of the specific surface area of seeds on the necessary aging time in relation to the aging time without seeding. Adapted from Guse et al.[120]

Instead, the directly measurable seed mass fraction x_{seeds} is mainly used for quantification. SLS analysis is used to validate that the PSD of the used seed particles are identical in each study. In Figure 5.7, the PSD and standard deviations of the two seed variants used in the studies in Section 5.3.1 are plotted: freshly prepared seed suspensions ("freshly prepared seeds") and dried, fractionated and then resuspended seed crystals ("x < 40 µm").[120]

Additionally, the PSD of two larger-sized fractions of dried and resuspended seeds are plotted, the influence of which on aging kinetics is discussed further below. Deviations across all independent samples examined ($N > 10$) are negligibly small. This confirms that x_{seeds} is a valid parameter to quantify the influence of seeding as long as the preparation of seeds and their composition remain the same. However, while the PSD of the freshly prepared seed suspension is monomodal, the PSD of the previously dried seeds is multimodal and shifted toward larger particle sizes compared to the sieve fraction of $x < 40\ \mu\mathrm{m}$. Both the small particle fractions of $x < 2\ \mu\mathrm{m}$ and the large fractions of $x \gg 20\ \mu\mathrm{m}$ probably result from resuspending the particles with a disperser and the subsequent agglomeration of not thoroughly wetted particles[233]. This shift in the PSD also explains why the required aging time is slightly larger when using dried seeds than for freshly prepared seeds as discussed previously in Figure 5.5.[120]

Next, the sieve fraction is varied in order to investigate if, for $x_{\mathrm{Seeds}} = \mathrm{const.}$, the variation of the PSD and, thus, the reduction of the mass-specific surface area negatively affects the impact of seeding on the necessary aging time $t_{\mathrm{age,min}}$. Figure 5.7 confirms that larger sieve fractions do shift the PSD of the resuspended particles to even larger particle sizes, with modal values of $x \approx 80\ \mu\mathrm{m}$ and $x \approx 110\ \mu\mathrm{m}$. The mass-specific surface area of the seeds in the suspension S_{SLS} is determined from the mass density distribution $q_{3,i}$ determined by SLS using the density of malachite $\rho_{\mathrm{zm}} = 4.0\ \mathrm{g \cdot cm^{-3}}$ [234] as an approximation:

$$S_{\mathrm{SLS}} = \frac{6}{\rho_{\mathrm{zm}}} \frac{\sum V_i}{x_i} \frac{}{V_{\mathrm{total}}} = \frac{6}{\rho_{\mathrm{zm}}} \sum \left(\frac{q_{3,i} \Delta x_i}{x_i} \right) \tag{5.3}$$

In Figure 5.8, the correlation between S_{SLS} and the reduction in aging time is plotted. The reduction is expressed as the ratio between the required aging time with seeding $t_{\mathrm{age,min}}$ and without seeding $t_{\mathrm{age,min,unseeded}}$ under otherwise identical conditions. For $x_{\mathrm{Seeds}} = \mathrm{const.}$, higher surface areas lead to an increased reduction of the required aging time confirming the hypothesis, that the total surface area of seeds is an essential parameter for describing seeding. Therefore, S_{SLS} must be considered complementary to the mass fraction of seeds, especially if the PSD changes.[120]

5.3.3 Impact on the precatalyst properties and catalyst performance

The two preceding sections confirmed that seeding does accelerate aging. Equally important for technical application, however, is the question of whether seeding negatively affects the product quality due to the thereby reduced aging times. In Figure 5.9 (a) and Figure 5.9 (b), the influence of x_{Seeds} and thus increasingly shorter aging times, cf. Figure 5.5, on the phase composition of the aged intermediate and the precatalyst is depicted.

Zincian malachite is the primary crystalline phase upon aging with $x_{zm} > 90\ wt\,\%$, regardless of x_{Seeds}. The three outliers are a result of inadequate temperature control leading to $T > 65\ °C$. Because of the large Zn fractions of $\tilde{x}_{Zn,metals} > 0.27$ in the reactant solution, aurichalcite is present as a second crystalline Cu/Zn phase with $x_{aur} \approx 5\ wt.\,\%$ in each case excluding the outliers. As anticipated[93], Zr precipitates separately as ZrO_2 with mass fractions of only $x_{ZrO_2} < 2\ wt.\,\%$ due its lower molar mass. The independence of the phase composition from the amounts of added seeds proves that seeding has no effect on the phase composition after aging and that the target phase zincian malachite is obtained in each scenario, even though the aging time was reduced to less than 5 min in the most extreme case. The evaluation of the phase composition after calcination in Figure 5.9 (b) confirms this conclusion as no dependency from x_{Seeds} is evident. The increased fluctuation of the mass fractions determined by Rietveld refinement result from the overlap of the phase-specific diffraction patterns of CuO and ZnO[120].

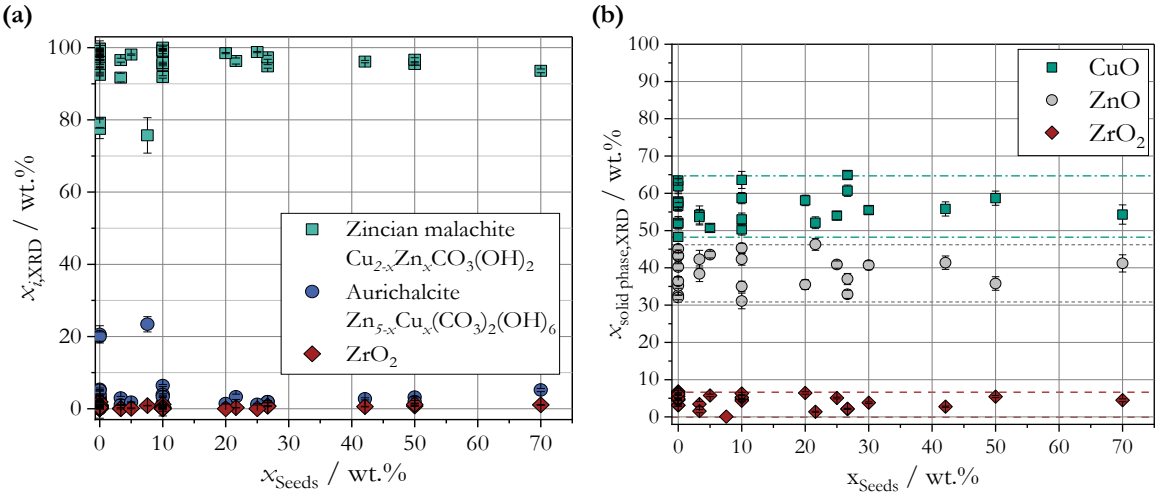

Figure 5.9: Solid phase composition as a function of the seeding mass fraction x_{Seeds}, as determined by PXRD and Rietveld refinement, of **(a)** the aged precursor and **(b)** the precatalyst. Adapted from Guse et al.[120]

The reason why zincian malachite is the preferred phase after aging is that it promotes the homogeneous distribution of Cu and Zn crystallites on the one- to two-digit nanometer scale as well as the formation of a particle morphology that increases the surface area of the precatalyst compared to material prepared without aging[31,37,38,41,64]. To verify that these improvements are also found when seeding is applied, TEM and TEM-EDXS images of an unseeded ($x_{Seeds} = 0\ wt.\,\%,\ t_{age} = 122\ min$) and a seeded preparation ($x_{seeds} = 30\ wt.\,\%,\ t_{age} = 55\ min$) are compared in Figure 5.10. Furthermore, a sample from a preparation without seeding, but a similarly short aging time ($x_{Seeds} = 0\ wt.\,\%$, $t_{age} = 60\ min$) is investigated as a benchmark to determine if the reduction of aging time without seeding would lead to the same product quality and increase of space-time-yield[120].

All samples exhibit a comparable PSD and shape in the TEM pictures in the upper row: a mesh-like structure is formed by the aggregation of single spherical particles. The mesh seems denser in the unseeded preparation with $t_{age} = 122\ min$. Since there is no discernible difference between the unseeded sample with $t_{age} = 122\ min$ and the seeded sample in the S_{BET} or S_{Cu} data displayed in Table 5.1, this is presumably a result of sample preparation for TEM imaging.

However, only in the unseeded sample with a shorter age time ($t_{age} = 60$ min) large spherical particles are found additionally to the fines. These spheres consist entirely of ZnO with very small CuO traces according to the TEM-EDXS analysis in the lower row. Furthermore, several CuO clusters with $x > 100$ nm exist. These inhomogeneities suggest that the transformation into zincian malachite as a prerequisite for a homogeneous Cu/Zn distribution on the one- to two-digit nanometer scale[72], was not completed at the time of sampling.

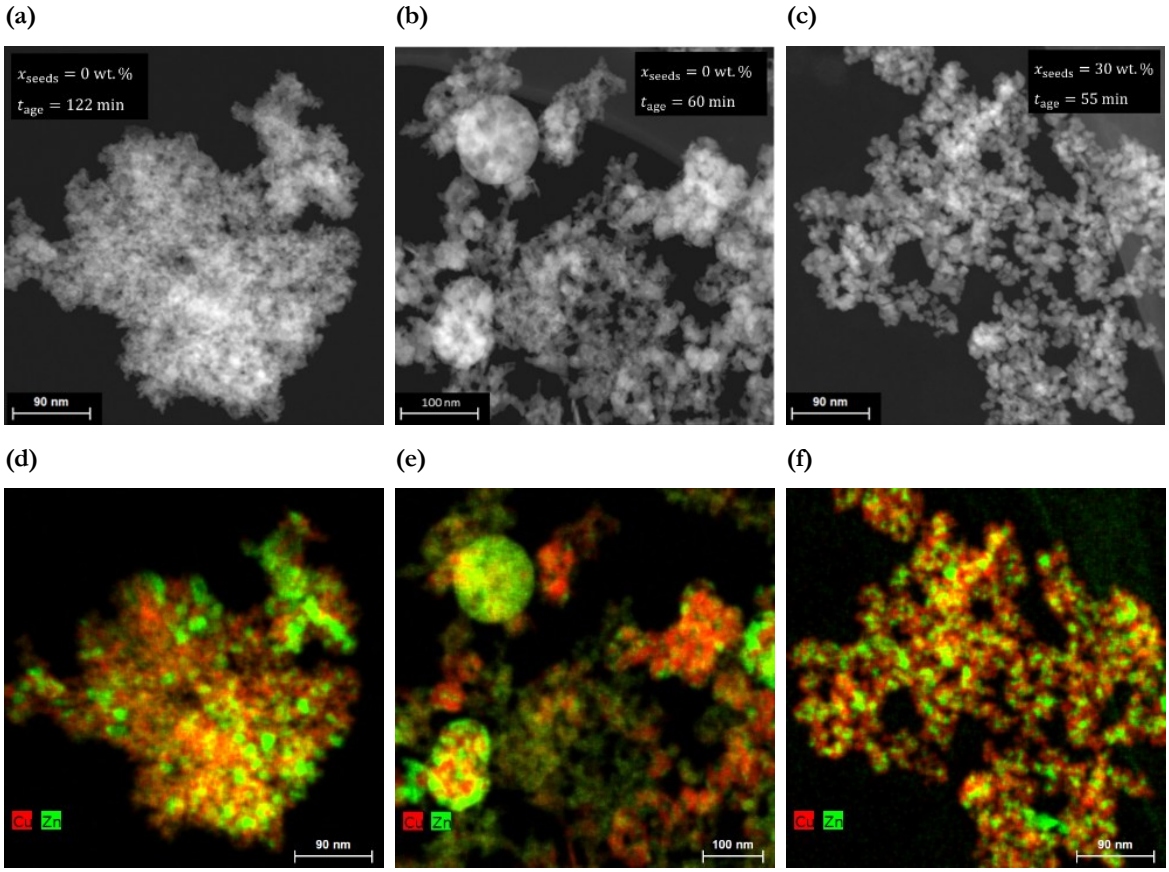

Figure 5.10: TEM and TEM-EDXS images of the calcined precatalysts. **(a)** and **(d)**: unseeded preparation (x_{Seeds} = 0 wt.%, t_{age} = 122 min); **(c)** and **(d):** unseeded preparation with a shortened aging (x_{Seeds} = 0 wt.%, t_{age} = 60 min); **(e)** and **(f):** seeded preparation (x_{Seeds} = 30 wt.%, t_{age} = 55 min). Cu is marked in red and Zn is marked in green. Adapted from Guse et al.[120]

This is confirmed by the PXRD evaluation in Figure 5.4 discussed previously. Conversely, the TEM-EDXS images for the other two samples exhibit a uniform distribution of Cu and Zn on the one- to two-digit nanometer scale. This confirms that by seeding, the aging time required to obtain a homogeneous material in the form of zincian malachite is reduced. The Zr distribution in the materials is depicted elsewhere[120]. As it shows no deviating tendency, it is not discussed further here. In addition to the visual findings, Table 5.1 gives a quantitative summary of how seeding affects the main characteristics of the precatalyst. Here too, a sample from a preparation without seeding, yet with a shortened aging ($t_{age} = 60$ min), is included as a benchmark for a low-performance material and a sample from a standard approach (x_{Seeds} = 0 wt.%, $t_{age} = 122$ min) as a high-performance benchmark.

Table 5.1: Selected physicochemical properties of the precatalysts from unseeded and seeded preparations for $b_{\mathrm{M,Feed2}} = 0.27\ \mathrm{mol \cdot kg_{H_2O}^{-1}}$, aged for the specified total process time t_{age}. Data from Guse et al.[120]

x_{Seeds} (wt.%)	t_{age} (min)	$\tilde{x}_{\mathrm{Cu,metals}}$ (mol%)	$\tilde{x}_{\mathrm{Zn,metals}}$ (mol%)	$\tilde{x}_{\mathrm{Zr,metals}}$ (mol%)	$\bar{x}_{\mathrm{CuO,XRD}}$ (nm)	$x_{\mathrm{Pore,BET}}$ (mol%)	S_{BET} ($m^2 \cdot g^{-1}$)	S_{Cu} ($m^2 \cdot g^{-1}$)
0	122 ± 6	63.2 ± 0.8	28.4 ± 0.9	8.4 ± 0.4	3 ± 1	10 ± 1	122 ± 4	68
0	60	65.7	24.0	9.1	9 ± 0	31	69	46
3	85 ± 2	59.1	32.1	8.7	3 ± 0	9 ± 0	123 ± 1	-*
10	78 ± 1	65.3	26.8	7.9	4 ± 0	-*	-*	-*
27	51 ± 2	64.3	28.4	7.2	2 ± 0	11	120	-*
30	55 ± 2	64.4	27.1	8.5	3 ± 0	9	148	66
50	14 ± 1	64.1	26.8	9.0	4 ± 0	-*	-*	-*
70	7 ± 1	64.3	26.8	7.9	4 ± 0	11	126	-*

*No data available due to limited resources.

The preparation method has little impact on the metal composition. The accuracy of the measurement itself causes small discrepancies within the range of ± 1 wt.%. However, the mean CuO crystallite size $\bar{x}_{\mathrm{CuO,XRD}}$, as calculated by Rietveld refinement and the mean pore size determined by physisorption, increase by a factor of three if aging is shortened without seeding. The spherical particles evident in the TEM images are the likely reason for this. Additionally, S_{BET} and S_{Cu} are reduced by a factor of approx. two due to the enlarged and inhomogeneous particles on the nanoscale. The adverse impact of reduced aging time on the sample characteristics aligns with the relationships outlined in the literature[18,31,43,68,74].

Conversely, although the aging time for the seeded samples is substantially reduced, in certain instances to under 7 minutes, no adverse effects on any of the physicochemical properties investigated are apparent. A TPR study supports this pattern, revealing a maximum reduction temperature of $T_{\mathrm{red,max}} = 175\ °\mathrm{C}$ for both the unseeded preparation with $t_{\mathrm{age}} = 122\ \mathrm{min}$ and the seeded preparation ($x_{\mathrm{seeds}} = 30\ \mathrm{wt.\%}$)[120]. This maximum is typically ascribed to the conversion of bulk Cu(II)O to Cu(0) [5]. In the unseeded experiment with $t_{\mathrm{age}} = 60\ \mathrm{min}$, the reduction is displaced towards elevated temperatures ($T_{\mathrm{red,max}} = 184\ °\mathrm{C}$). This shift typically arises from bigger crystallites[44] and is hence consistent with the previously stated evidence.

According to these results for the precatalysts and established correlations between physicochemical parameters and catalyst performance in the literature[31,44], seeding should not affect the catalyst efficacy in methanol synthesis accordingly. This hypothesis is examined based on an initial functional test of the differently prepared catalysts, also in comparison to a readily available $Cu/ZnO/Al_2O_3$ catalyst[44] . For this purpose, the average methanol productivity P_{MeOH} as defined in Eq. (2.11) throughout a 50-hour operating timeframe in the experimental configuration outlined in Section 2.5,. is displayed in Figure 5.11 for two distinct feed gas mixtures. Using a feed gas which consists of equal volumes of CO and CO_2 ($\dot{V}_{\mathrm{CO_2}}/(\dot{V}_{\mathrm{CO_2}} + \dot{V}_{\mathrm{CO}}) = 0.5$), methanol productivity is consistent for both the catalyst from an unseeded preparation ($x_{\mathrm{seeds}} = 0\ \mathrm{wt.\%}$) and the one from a preparation that included seeding ($x_{\mathrm{seeds}} = 30\ \mathrm{wt.\%}$) if the aging time surpasses the required time for phase transition: $t_{\mathrm{age}} = 122\ \mathrm{min}$ and $t_{\mathrm{age}} = 55\ \mathrm{min}$, respectively. The catalytic activity of both materials is comparable to the state-

of-the-art commercial catalyst. These values indicate that seeding facilitates the preparation of catalytic material with comparable product quality, but at a more than ten times higher space-time yield than previously documented in the open literature[31,36,101,115,120]. As presumed from the previous analytical results, methanol productivity in the functional test declines to only 77 % when the aging time is decreased to $t_{age} = 60$ min without using seed crystals in the aging step. This correlation is consistent with the findings reported in the literature[77,90].

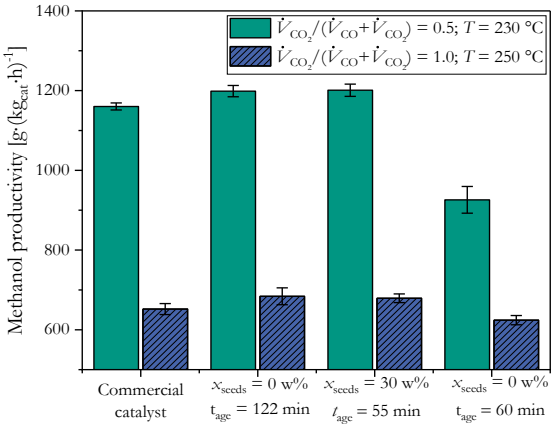

Figure 5.11: Functional test of catalysts prepared with and without seeding, also in comparison to a commercially available catalyst Mean methanol productivity over 50 h on stream for $p = 30$ bar and $GHSV = 4.4\ s^{-1}$. Error bars depict variation over 50 hours on stream. Adapted from Guse et al.[120]

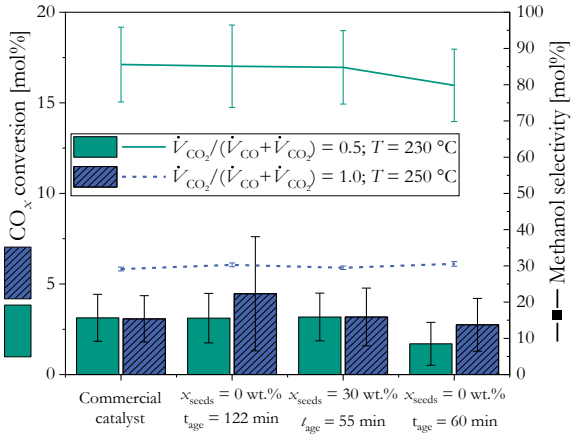

Figure 5.12: Influence of seeding and reduced aging time on CO_x conversion and methanol selectivity in a functional catalyst test, also in comparison with a commercially available catalyst. Methanol synthesis at $p = 30$ bar and $GHSV = 4.4\ s^{-1}$. Error bars depict variation over 50 hours on stream. Adapted from Guse et al.[120]

For a feed gas consisting of H_2 and pure CO_2 ($\dot{V}_{CO_2}/(\dot{V}_{CO_2} + \dot{V}_{CO}) = 1.0$), the productivity decreases to around 60% compared to $\dot{V}_{CO_2}/(\dot{V}_{CO_2} + \dot{V}_{CO}) = 0.5$. In this case, all catalysts considered show a comparable activity. None of the catalysts exhibit substantial deactivation over the examined timeframe for either feed gas composition.

Furthermore, the influence of the preparation on the CO_x conversion X_{CO_x}, cf. Eq. (5.4), and the methanol selectivity S_{MeOH} as defined in Eq. (5.5) in the functional test is analyzed in Figure 5.12.

$$X_{COx} = \frac{\dot{n}_{CO,in} - \dot{n}_{CO,out} + \dot{n}_{CO_2,in} - \dot{n}_{CO_2,out}}{\dot{n}_{CO,in} + \dot{n}_{CO_2,in}} \tag{5.4}$$

$$S_{MeOH} = \frac{\dot{n}_{MeOH,out}}{\sum \nu_x \dot{n}_{C_xO_yH_z,out}} \tag{5.5}$$

All four examined catalysts exhibit identical methanol selectivities and CO_x conversion in the scope of the functional test. For $\dot{V}_{CO_2}/(\dot{V}_{CO_2} + \dot{V}_{CO}) = 0.5$, a mean selectivity of 78% to 85% is achieved throughout a 50-hour operation. These quantities are similar to previous investigations employing comparable process parameters and result from the simultaneous formation of H_2O from CO_2 and H_2 in the reverse water-gas shift reaction[20]. For a pure CO_2 feed, which was subsequently set, the selectivity diminishes to around 30% for each catalyst. This arises from a modification in the water-gas shift reaction due to substantial CO_2 levels and

the concurrent lack of CO in the gas phase, which leads to heightened H_2O formation. Additional potential impact on the selectivity can be expected from the elevated temperature and the continuous degradation of the catalyst[20,235]. Fluctuations in the conversion of CO, and especially CO_2, over time on stream can be attributed to minor condensation in the reactor outlet[236]. Consequently, seeding appears to have little impact on methanol selectivity and CO_x conversion as far as the functional test can tell.

All in all, the hypothesis that seeding does not affect the characteristics of the precatalyst and, consequently, should not impact the performance of the catalyst in methanol synthesis when $t_{\mathrm{age}} > t_{\mathrm{age,min}}$ is satisfied, is validated. Furthermore, analysis of the phase composition after aging, as well as the metallic composition, mass-specific surface area, the mean pore size and the morphology of the precatalyst after calcination showed comparable values for seeded and unseeded preparations when the criterion $t_{\mathrm{age}} > t_{\mathrm{age,min}}$ holds true. This remains true even if the total aging time is lowered to merely 10% of the aging time of the unseeded preparation. In contrast, decreasing the aging time by a similar factor without implementing seeding will yield inferior properties, particularly regarding the homogeneity on nanoscale and the surface characteristics of the precatalyst. As expected, this also appears to reduce methanol productivity as demonstrated in a first functional test. Thus, seeding is essential for the increase of the space-time-yield while maintaining the catalyst quality.

5.4 Conclusions

In line with its title, the aim of this chapter was twofold: on the one hand, to find methods to enhance the space-time yield of co-precipitation and aging and on the other hand, to enable the transfer of all key findings of this work to technical application.

The focus of yield optimization in this work was on the aging step since the aging time is generally a multitude of the precipitation time and has, thus, the greater potential for improvement. Based on a literature review, seeding and a maximization of the surface area of particles after co-precipitation were deemed the two most promising approaches for this endeavor. Tripling the specific surface area of the co-precipitate from approx. 17 m^2g^{-1} to more than 50 m^2g^{-1} by more intense mixing during co-precipitation, halved the required aging time to complete phase transformation from (zincian) georgeite to zincian malachite to under 80 min.

An even bigger impact on aging time was achieved by seeding the co-precipitate suspension with aged intermediate either as dried crystals or as freshly prepared suspension. For seeds mass fractions as low as $x_{\mathrm{seeds}} = 3\ \mathrm{wt.\%}$, the required aging time for phase transformation had already decreased by more than 40 % compared to the mean values from 80 to 90 min without seeding. For the maximum seed mass fractions considered ($x_{\mathrm{seeds}} = 70\ \mathrm{wt.\%}$) with the same PSD, the aging time was reduced to less than 10 min. The approach was also transferred to higher concentrated suspensions where the effect was even more pronounced and instantaneous phase transformation after mixing the co-precipitate suspension with seeds was achieved for $x_{\mathrm{solids,susp}} = 6\ \mathrm{wt.\%}$ and $x_{\mathrm{seeds}} = 30\ \mathrm{wt.\%}$. The mass-specific surface area of the seeds proved to be equally decisive for the impact of seeding, which indicates that the total surface area of seeds and the number of seed crystals are decisive parameters. In contrast, the

method of adding seeds and whether they were dried or newly produced had no major effect. Applying seeding multiplied the space-time yield of aging and precipitation by up to a factor of 60.

The comparison of precatalysts from seeded and unseeded preparations with a similarly reduced aging ($t_{\mathrm{age}} \approx 60\ \mathrm{min}$) showed that seeding is required to complete the phase change to crystalline zincian malachite in this limited time frame. Without seeding, particles formed that were inhomogeneous on the nanoscale and had a reduced surface area. Accordingly, the resulting catalyst exhibited a diminished activity in methanol synthesis, which served as a first functional test. In contrast, if seeding was applied, methanol productivity was comparable to those of both a catalyst from an unseeded preparation with a longer aging time ($t_{\mathrm{age}} \approx 120\ \mathrm{min}$), but otherwise identical conditions, and those of a commercial CZA catalyst.

How seeding works on a fundamental level is not yet confirmed. One model concept for aging is a phase transformation via the liquid phase, as recently suggested by Güldenpfennig et al. and others[75,76]. First, preferably small co-precipitate particles dissolve, comparable to the well described Ostwald ripening, due to the metastable nature of the initially formed phases. Then, zincian malachite forms from the dissolved lattice ions. However, dissolution of the co-precipitate phases seems unplausible when the model calculations in Section 3.2 are considered, where zincian georgeite is supersaturated under typical aging conditions. Furthermore, no complete dissolution of solids[64,72,73,75,90] is reported in the literature during aging. Finally, a dissolution-based mechanism would not explain the effect that seeding showed on the aging kinetics.

Still, the seeding studies in this work do complement the general results by Güldenpfennig et al. regarding the acceleration of aging by seeding[75], i.e. the reduction of the necessary induction period until first crystalline zincian malachite particles are present. In contrast, the shortness of the transformation period seems unaffected: as soon as zincian malachite is first detectable, the further transformation is almost instantaneous. Based on the assumption that aging consists of these two periods and based on the quantified influences of the number, mass and mass-specific surface of seed crystals on aging time, it is plausible that phase transformation during aging predominantly happens by means of a contact-mediated recrystallization and only to a lesser share by spontaneous (re)crystallization of singular zincian georgeite particles. A corresponding reconceptualized model of what the underlying mechanisms of aging are and how seeding influences them is shown in Figure 5.13.

Generally, due to the formation of metastable zincian georgeite during initial, kinetically controlled co-precipitation, the supersaturation regarding zincian malachite is reduced to $S_{\mathrm{zm}} < 4$ compared to the hypothetical case where zincian malachite is formed directly after mixing the reactants ($S_{\mathrm{zm,init}} > 200$). This is illustrated in Figure A.30 and Figure A.33 in the appendix. Because of the reduced supersaturation and the saturated mother liquor regarding zincian georgeite, the recrystallization of zincian georgeite to zincian malachite is slow and maybe can be understood as a stochastic process, similar to primary nucleation[237,238]. This explains the prolonged induction period, where for several dozen minutes only (zincian) georgeite is present, as described in the literature[70,95,132] and confirmed in the experimental studies here, e.g. in Figure

5.3. However, as soon as a relevant number of zincian malachite particles were formed by spontaneous phase transformation, the second, much faster mechanism comes into play: the contact-mediated phase transformation when a zincian georgeite and a zincian malachite particle collide which would be a similar mechanism as described for emulsions[228,229] or the crystallization from solution[239], also known as the template effect[240]. This mechanism is self-amplifying. As the number of zincian malachite particles rises, the number of collisions between zincian malachite and zincian georgeite particle increases which would explain the fast transformation period described earlier[75].

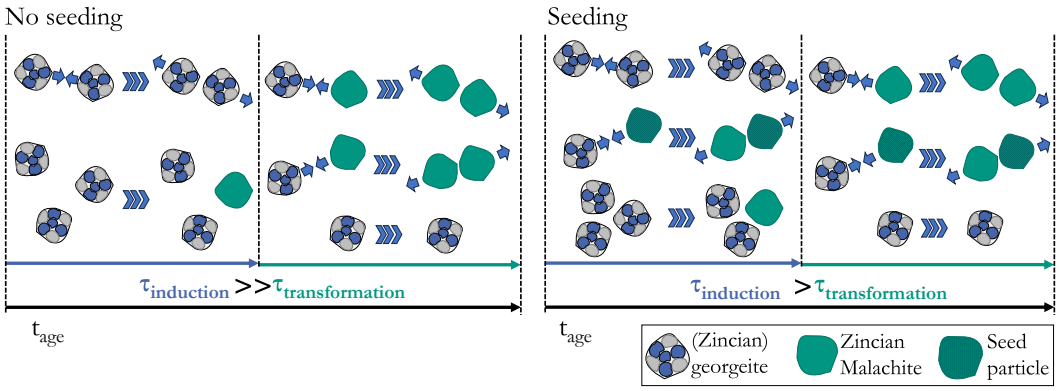

Figure 5.13: Model concept of the fundamental aging mechanisms with and without seeding.

If a small number of zincian malachite particles is added as seeds at the beginning of the aging process, the induction period is shortened as much less spontaneous phase transformations are required now to reach the state of self-amplifying contact transformations. This effect can be increased by increasing the number of seed particles, either by adding the same mass of seeds, but with a smaller PSD, or by increasing the seed mass and maintaining the PSD. If a sufficiently large number of seeds is added, as was the case for $x_{solids,susp} = 6\ \text{wt.}\%$ and $x_{seeds} = 30\ \text{wt.}\%$, the induction period is skipped entirely and the required aging time is equal to the transformation period and accordingly quasi-instantaneous. For now, this model is foremost based on derived measurands. To determine if contact-mediated phase transformation is indeed a key mechanism in the aging process, single-crystal experiments[232,241] or timed sample imagining, e.g. by cryo-quenching in liquid N_2 and subsequent high-definition SEM[156] should be applied in future studies. This way, the seeding procedure may be further optimized regarding space-time-yield. Additionally, more elaborate performance tests should be conducted to investigate if seeding is also unproblematic for the long-term performance of the resulting material.

In summary, the effect of seeding on the aging kinetics is significant and higher compared to other methods, such as temperature change[75,78,79] or increasing the surface area of the co-precipitate. Yet, it does not seem to negatively affect the resulting phase composition, surface characteristics or performance of the resulting material as other methods do as it only affects the kinetics and not the solid-liquid equilibrium.

Thus, the hypothesis that seeding is the most impactful and suitable method to increase the space-time-yield of the two process steps investigated without affecting the catalyst performance, is confirmed and seeding is recommended without restrictions.

In general, seeding should be transferable to similar catalyst precursors where an aging step is mandatory to increase product quality. How and if seeding works at a fundamental scale in these cases depends on the respective chemistry and has to be investigated separately.

6 Transfer to technical application

All results and discussions up to now focused on the preparation of Cu/Zn based catalysts at lab scale. However, the overarching approach of this work can also be applied to technical scale and any other substances produced by similar precipitation and/or aging steps. A generally applicable workflow for process design, which is derived from the results of this work, is given in Figure 6.1.

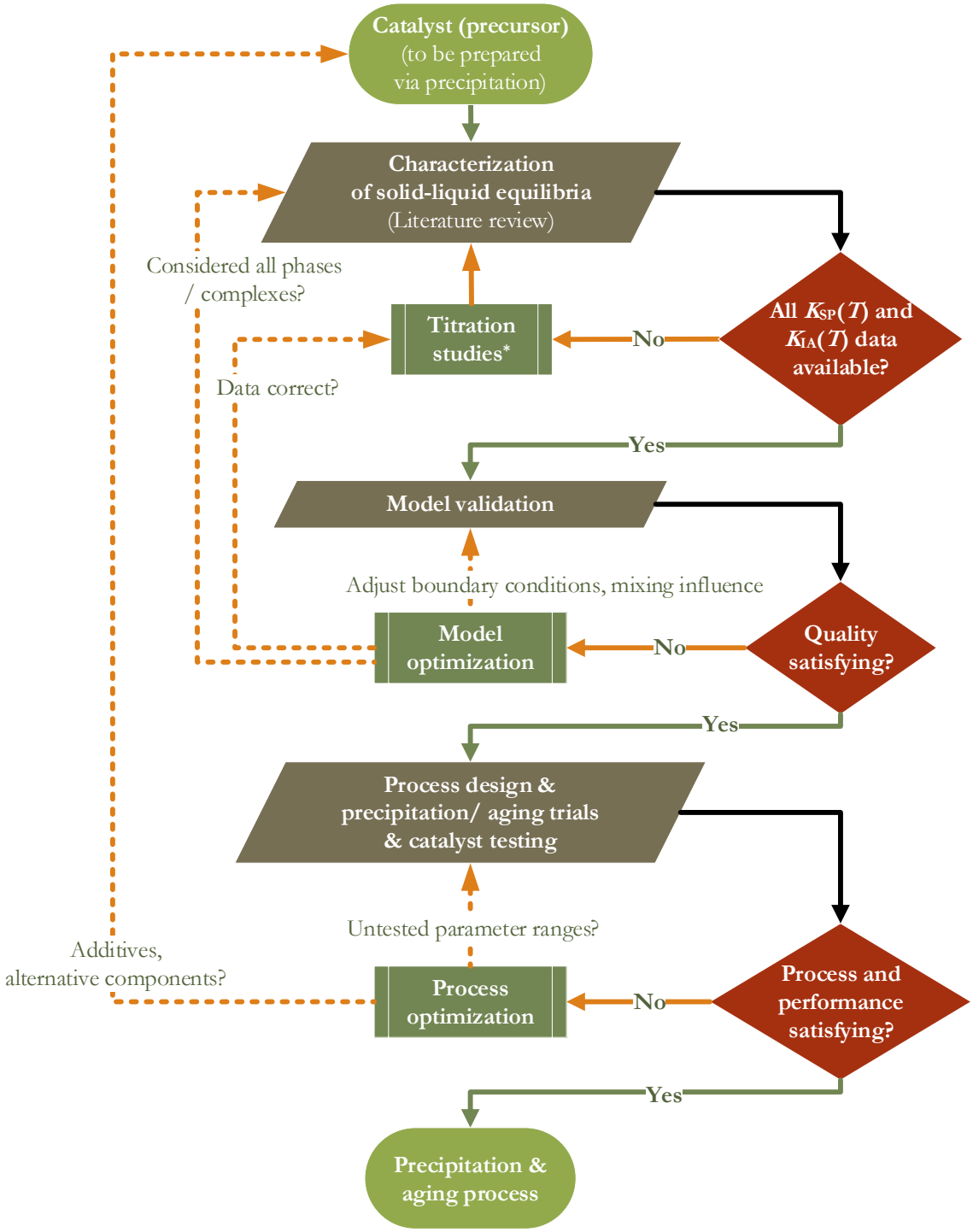

Figure 6.1: Workflow for process design of (co-)precipitation and aging. *Titration studies according to Guse et al.[105].

The first step for a given solid with a defined phase composition is a (literature) review of all available data regarding the temperature-dependent liquid-solid equilibria as well as the speciation of all relevant ions in the liquid phase. This also encompasses the data for all potential by-products as they are likely relevant to ruling out certain process conditions. Similarly relevant is information on the process function, i.e. the correlation between physicochemical properties, such as phase composition or PSD, and the resulting performance of the material. This knowledge enables seamless adjustment of the material composition in the subsequent workflow if a satisfactory process or sufficient performance could not be achieved. If necessary, titration studies as described in Section 4.2.3, are to be conducted if solubility data is missing for some phases.

When all necessary phase equilibria data is available, model calculations of the phase composition as a function of e.g. reactants, pH and temperature are to be conducted and complemented by corresponding experimental validation studies. If validation shows major deviations between model and experiment, it is to be resolved whether this is due to incompatible data, false assumptions or due to phases and species not yet included in the model. Then, suitable adjustments must be chosen accordingly and the experimental validation is to be repeated. For target compositions that do not correspond to the thermodynamic state of equilibrium, mixing influences during solids formation and kinetics might need to be considered.

Finally, the model is applied to identify ideal parameter areas resulting in the targeted phase composition. If necessary, the target data may be extended by PSD or process time specifications, depending on the requirements and model complexity. Based on the results, process design may be flexible or precisely defined.

Based on the results in Section 3.2, the usage of mixing nozzles in the non-mixing influenced regime for (co-)precipitation is to be favored compared to a state-of-the-art semi-batch approach. The respective material showed an increased homogeneity on nanoscale and in between individual particles, improved surface characteristics and increased productivity. The current gear pump setup at lab scale, cf. Section 2.3, allows volume flows of up to 800 ml·min^{-1} without any blockage tendency for 6 wt.% solids[101,120]. For the studies discussed here, the total runtime of the gear pumps was limited to less than 30 min per day. Still, a production capacity of more than 200 g aged and dried intermediate a day was achieved for the Cu/ZnO/ZrO_2 catalyst. The capacity was mainly limited by the time-consuming washing of the aged intermediate. A further production capacity increase in co-precipitation and aging is possible by either numbering-up or by adjusting the size of the mixing nozzle according to Rehage et al.[242,243]. In general, a numbering up approach is recommended for scale-up in order to maintain large energy dissipation rates and to simultaneously mitigate possible solids build-up in the mixing nozzle by using redundancy to rotate between in-situ cleaning and precipitation without downtime.

If the use of a tank reactor for (co-)precipitation is mandatory due to external requirements, high energy dissipation during intermixing, narrow residence time distributions and defined pH during aging must be ensured. In each case, seeding is strongly recommended for aging

processes as the required aging time is diminished while product quality is unaffected. Thus, applying seeding should allow to keep residence times below 10 min.

In summary, transferring the design workflow and the preparation approach to other substances or technical scale seem plausible in theory with no apparent downsides or necessary fallback positions beyond those specified in the graphical workflow in Figure 6.1. If mixing nozzles are to be used due to their positive impact on product quality, a cleaning concept is necessary to avoid outages due to blockage. A space-time yield optimization can then be carried out complementarily using seeding or by intensifying mixing during co-precipitation, cf. Section 5. This way, an easily scalable and quickly optimizable preparation of clearly defined high-performance material at technical scale becomes possible.

7 Summary and outlook

For the successful transition to a sustainable chemical industry in the next two to three decades, optimizing existing processes in terms of their energy footprint and resource utilization is crucial. The aim of this work was to understand the underlying mechanisms in the preparation of Cu/ZnO based catalysts in order to enable a systematic and scalable process design that also allows a methodical process optimization regarding the space-time yield and the resulting product qualities, e.g. the methanol productivity when switching from a CO feed to a CO_2 feed. This way, both the preparation process itself may be optimized economically and ecologically by reducing energy and reactant consumption as well as the methanol synthesis, where the catalysts are generally applied.

Catalyst preparation is a multi-step process with an interconnected web of process parameters, intermediates and their physicochemical properties that all possibly influence the performance of the resulting material. Due to this complexity, parameter studies are the most common approach for the optimization of preparation conditions[181]. They provided suitable parameter ranges for the three key steps co-precipitation, aging and calcination that result in a catalyst material with a high methanol productivity, selectivity and CO_x conversion for the synthesis from syngas, typically rich in CO[18,31,36]. However, they do not provide a solution when it comes to adapting the catalyst formulation to new challenges, i.e. the use of syngas rich in CO_2, or for a process scale-up, which is complicated by local effects, predominantly in the initial solids formation during co-precipitation.

Thus, this work instead focused on understanding the correlation between the various process parameters and the resulting physicochemical properties for the individual process steps. Here, co-precipitation and aging were investigated for these two process steps have the highest impact on the resulting catalyst quality if conditions are varied even slightly[31,37,38,41,64,80,84]. In the state-of-the-art semi-batch process, co-precipitation and aging overlap[31,36,87], making it challenging to differentiate between the respective influencing variables and intermediates.

Therefore, first, a new process was developed so that co-precipitation and aging were separated in time and space and could be investigated individually. The process consists of continuous co-precipitation in a mixing nozzle and a subsequent batch aging step in a stirred tank reactor. Based on previous studies, co-precipitation was believed to be a fast, kinetically dominated process that is largely influenced by mixing, completed in seconds and results in an amorphous, metastable co-precipitate which primarily contains georgeite or, if Zn ions are incorporated into the lattice, zincian georgeite[70,95,132]. In contrast, aging is a slow process that takes dozens of minutes to multiple hours and results in the targeted crystalline phase zincian malachite that is characterized by its large copper surface area and the defined ordering of Cu and Zn ions which proved to be beneficial for the performance of the resulting catalyst[36,37,41].

With the adapted experimental setup, the influence of mixing on the co-precipitate and, in turn, the impact of co-precipitation on the final catalyst quality were investigated. A comparison with the state-of-the-art semi-batch co-precipitation demonstrated that the mixing method of the two feeds influenced the pH pathway during solids formation, the speciation in the

surrounding liquid and, consequently, the composition and morphology of the resulting material. Even after the ensuing aging step, the crystallites from the continuous mixing in a mixing nozzle were approx. 40 % smaller, their specific surface area was increased by approx. 10 % and SEM images displayed that their pore distribution and size was more homogeneous compared to the semi-batch material. These differences were maintained throughout the subsequent calcination and evident in the respective precatalysts thereafter. S_{BET} and S_{Cu} increased up to three times and a more homogeneous Cu and Zn distribution on the one- to two-digit nanometer scale within the precatalyst was apparent according to TEM imagining. No more Cu or ZnO clusters were evident. Consequently, methanol productivity was increased for the mixing nozzle material by a factor of two to three.

Then, to quantify the impact of energy dissipation rate and mixing time on the morphology of the co-precipitate and their relevance for the catalyst performance, the volume flow in the continuous co-precipitation with a mixing nozzle was varied. For total volume flows of $\dot{V}_{\mathrm{total,prec}} \leq 400\ \mathrm{ml} \cdot \mathrm{min}^{-1}$, which corresponds to micromixing times of $\tau_{micro} \leq 1.2 \cdot 10^{-4}$ s, initial solids formation of Cu/Zn based catalysts was controlled by mixing as evident from increasing median particle sizes and the segregation of Cu and Zn within individual particles. This trend most probably resulted from the limited availability of solids forming ions (CO_3^{2-}) at reduced mixing intensity leading to the separate precipitation of Cu and Zn as georgeite and amorphous $Zn(OH)_2$ or aurichalcite. If the aforementioned critical volume flow was exceeded, mixing was completed before solids formation started and the morphology of the co-precipitate was no longer affected. The existence of these two regimes provides an explanation for the seemingly contradictory literature findings on the influence of mixing on the co-precipitate and catalyst properties. However, contrary to the comparison between semi-batch and continuous co-precipitation, the differences in morphology and composition due to mixing intensity during co-precipitation did not persist through aging, as aged intermediates showed no correlation with the total volume flow during co-precipitation. This was attributed to the homogeneity of individual particles in size, shape, and structure, ensuring similar behavior and the simultaneous completion of the phase transformation during aging. Consequently, similar catalytic activities in methanol synthesis were confirmed regardless of mixing intensity.

In conclusion, mixing does influence the co-precipitate morphology if it proceeds simultaneously to solids formation as it can then affect the availability of lattice ions or the pH trajectory. These morphological changes persist through the subsequent processes if particles are diverse in size, composition, and morphology or if aging time is insufficient. Standard methods to track the progress of aging (pH drop, color change, PXRD/FT-IR signal changes) were insufficient to observe impairments caused by insufficient mixing. To rule out any detrimental influence on the catalyst performance, an ideal process should include a co-precipitation step that is conducted in the non-mixing influenced regime, and ideally continuously, to obtain a co-precipitate that is homogeneous in particle size, morphology and composition, both on the nanometer scale and in between individual particles.

Secondly, the strict experimental separation of co-precipitation and aging also allowed to examine the fundamentals of aging independently. Given the established significance of zincian malachite as the target phase for high-performance catalysts[31,37,38,41,64], the primary aim was to

develop a model that predicts phase composition after aging as a function of key process parameters such as reactant composition, pH, and temperature. Ideally, this model would reduce the number of parameter studies required for future process developments and uncover previously unknown process optima. Considering the vastly different timescales of solid formation during co-precipitation and phase transformation during aging, it was hypothesized that aging leads to thermodynamic equilibrium. Consequently, the phase composition should be predictable using a thermodynamic model based on solid-liquid equilibria and hydrochemistry data alone with no kinetic considerations.

To validate this hypothesis, a thermodynamic equilibrium model was developed using readily available software solutions, focusing on Cu/Zn based intermediates. The model comprises an activity coefficient model that accounts for ion interactions, and a compilation of solubility products and ion association products to represent speciation in the liquid phase as well as the equilibria data of potential solid phases. Based on pH measurements, the Pitzer model was identified as the most suitable activity coefficient model, with deviations up to a maximum of 15 % at ionic strengths above 6 $mol \cdot L^{-1}$. Certain solubility data, such as the temperature dependency for synthetic zincian malachite and the solubility of the by-product $Na_2Zn_3(CO_3)_4 \cdot 3\,H_2O$, were unavailable. For these cases, an experimental method was developed and applied to determine the missing K_{SP} from titration studies. Additionally, titration studies confirmed that separate solubility products are necessary to describe the co-precipitate and the aged intermediate. For model validation, the calculated phase compositions at thermodynamic equilibrium were compared to experimentally determined solid compositions as a function of pH, temperature, and Cu/Zn ratio in the feed solution. In each case, the experimentally determined phase composition was quantitatively reproduced by the thermodynamic model, such as the presence of the by-products rouaite at pH ≤ 5 or aurichalcite for $T \geq 70\,°C$ and $n_{Cu}/n_{Zn} = 2$ as well as $T = 65\,°C$ and $\tilde{x}_{Zn,Feed1} \geq 27\,mol\%$. Deviations between model and measurements in the transition area between zincian malachite predominance and aurichalcite predominance likely result from uncertainties in the Rietveld refinement. As a separate, hypothetical boundary case, the initial state after complete and ideal mixing of the reactant solutions, but before solids formation, was considered for the calculation of supersaturations. The validated model was then applied to determine technically feasible process parameters (reactant ratio, pH, temperature, p_{CO_2}) that lead to a product as pure as possible in zincian malachite and that result in small particles, ergo large surface areas S_{BET}. A comparison of the determined parameter regimes with experimental S_{BET} optimization studies confirmed that the model approach yielded accurate results for parameter optimization. It also provided explanations for temperature and pH optima long promoted in the literature and a concept on how CO_2 could be used as a value-adding educt in future catalyst synthesis.

In conclusion, aging can be considered as a process towards thermodynamic equilibrium, and the composition of the aged intermediate can be described using the corresponding solid-liquid equilibrium. Thus, the hypothesis that (co-)precipitation as a kinetically dominated step and aging as a thermodynamically governed step are to be considered separately is affirmed. It is crucial to decouple both processes to better understand, predict, and optimize co-precipitation and aging, and consequently, the resulting catalyst.

Finally, the third goal was to develop a method to accelerate the phase transformation during aging without negatively affecting the resulting product quality in order to increase the space-time yield of the time-consuming and energy-intensive aging step. In addition, it was vital to ensure that the methods and key findings of this work could be transferred to the large-scale catalyst production. Based on a literature review, seeding and maximizing the surface area of particles after co-precipitation were identified as the most promising approaches. Increasing the specific surface area of the co-precipitate from approximately 17 $m^2 \cdot g^{-1}$ to over 50 $m^2 \cdot g^{-1}$ through more intense mixing during co-precipitation halved the required aging time for complete phase transformation from (zincian) georgeite to zincian malachite to under 80 minutes.

Seeding the co-precipitate suspension with aged intermediate, either as dried crystals or freshly prepared suspension, had an even greater impact on aging time. The required aging time was decreased between 40 % and 90 % compared to a preparation without seeding when 3 wt.% to 70 wt.% seeds were added. This approach was also applied to higher concentrated suspensions, where the effect was even more pronounced, achieving instantaneous phase transformation after mixing the co-precipitate suspension with seeds for $x_{\mathrm{solids,susp}} = 6\ \mathrm{wt.\,\%}$ and $x_{\mathrm{seeds}} = 30\ \mathrm{wt.\,\%}$. The mass-specific surface area of the seeds proved crucial for the impact of seeding, indicating that the total surface area of seeds and the number of seed crystals are decisive parameters. Seeding multiplied the space-time yield of aging and precipitation by up to a factor of 60. Comparing precatalysts from seeded and unseeded preparations with similarly reduced aging times ($t_{\mathrm{age}} \approx 60\ \mathrm{min}$) showed that seeding is required to complete the phase change to crystalline zincian malachite within this limited time frame. Without seeding, particles with a reduced surface area were formed, whose metal distribution was inhomogeneous on the nanometer scale as well as in between individual particles. Accordingly, the resulting catalyst exhibited a diminished methanol productivity in an initial functional test with syngas of varying composition. In contrast, seeding resulted in a catalytic activity comparable to those of both a catalyst from an unseeded preparation with a longer aging time ($t_{\mathrm{age}} \approx 120\ \mathrm{min}$) and a commercial CZA catalyst. Based on these results as well as the characteristic induction period and subsequent rapid phase transformation described in the literature[64,75,95,132], it was hypothesized that seeding promotes contact-mediated phase transformation by collision of (zincian) georgeite and zincian malachite particles. This way, the time-defining induction period during aging, that is most probably the result of stochastic, spontaneous phase transformations of individual particles at low supersaturations, is greatly reduced or even skipped for high seed mass fractions ($x_{\mathrm{solids,susp}} = 6\ \mathrm{wt.\,\%}$ and $x_{\mathrm{seeds}} \geq 30\ \mathrm{wt.\,\%}$.).

In summary, the effect of seeding on aging kinetics is significant and surpasses other methods, such as temperature change[75,78,79] or increasing the surface area of the co-precipitate. Importantly, seeding does not impact the resulting phase composition, surface characteristics, or performance of the material, as other methods do, since it affects only the kinetics and not the solid-liquid equilibrium. Thus, seeding is recommended without restrictions.

All results of this work are, in principle, transferable to similar catalyst compositions requiring an aging step and to larger scales for technical application, although the fundamental

mechanisms of seeding in these cases depend on the specific chemistry and may require separate research. To facilitate the transfer, a workflow was developed that is based on the findings regarding the impact of mixing during co-precipitation, the fundamentals of aging, and the effect of seeding. With this workflow, the main objective, to enable a structured process development by systematically identifying all influencing variables and providing optimal preparation parameters for the best possible catalyst performance, has been achieved. Space-time yield optimization can then be carried out complementarily using seeding or by intensifying mixing during co-precipitation. This approach makes catalyst preparation more controllable and efficient and hopefully contributes to the sustainable transition of the chemical industry.

Bibliography

1. IRENA AND METHANOL INSTITUTE, ed. *Innovation Outlook: Renewable Methanol*. International Renewable Energy Agency; 2021.
2. Production of methanol worldwide from 2017 to 2022. Published online May 2022. Accessed March 20, 2024. https://www.statista.com/statistics/1323406/methanol-production-worldwide/
3. Álvarez A, Bansode A, Urakawa A, et al. Challenges in the Greener Production of Formates/Formic Acid, Methanol, and DME by Heterogeneously Catalyzed CO2 Hydrogenation Processes. *Chem Rev*. 2017;117(14):9804-9838. doi:10.1021/acs.chemrev.6b00816
4. Olah GA, Goeppert A, Prakash GKS. Chemical recycling of carbon dioxide to methanol and dimethyl ether: From greenhouse gas to renewable, environmentally carbon neutral fuels and synthetic hydrocarbons. *J Org Chem*. 2009;74(2):487-498. doi:10.1021/jo801260f
5. Frusteri F, Cordaro M, Cannilla C, Bonura G. Multifunctionality of Cu–ZnO–ZrO 2 /H-ZSM5 catalysts for the one-step CO 2 -to-DME hydrogenation reaction. *Applied Catalysis B: Environmental*. 2015;162:57-65. doi:10.1016/j.apcatb.2014.06.035
6. Behrens M, Studt F, Kasatkin I, et al. The active site of methanol synthesis over Cu/ZnO/Al2O3 industrial catalysts. *Science*. 2012;336(6083):893-897. doi:10.1126/science.1219831
7. Olah GA. Beyond oil and gas: The methanol economy. *Angew Chem Int Ed Engl*. 2005;44(18):2636-2639. doi:10.1002/anie.200462121
8. Beck A, Newton MA, van de Water LGA, van Bokhoven JA. The Enigma of Methanol Synthesis by Cu/ZnO/Al2O3-Based Catalysts. *Chem Rev*. 2024;124(8):4543-4678. doi:10.1021/acs.chemrev.3c00148
9. Pacchioni G. From CO2 to Methanol on Cu/ZnO/Al2O3 Industrial Catalyst. What Do We Know about the Active Phase and the Reaction Mechanism? *ACS Catal*. 2024;14(4):2730-2745. doi:10.1021/acscatal.3c05669
10. Arena F, Barbera K, Italiano G, Bonura G, Spadaro L, Frusteri F. Synthesis, characterization and activity pattern of Cu–ZnO/ZrO2 catalysts in the hydrogenation of carbon dioxide to methanol. *Journal of Catalysis*. 2007;249(2):185-194. doi:10.1016/j.jcat.2007.04.003
11. Sternberg A, Bardow A. Life Cycle Assessment of Power-to-Gas: Syngas vs Methane. *ACS Sustainable Chem Eng*. 2016;4(8):4156-4165. doi:10.1021/acssuschemeng.6b00644
12. Bhardwaj R, Sharma T, Nguyen DD, et al. Integrated catalytic insights into methanol production: Sustainable framework for CO2 conversion. *Journal of Environmental Management*. 2021;289:112468. doi:10.1016/j.jenvman.2021.112468
13. Mondal U, Yadav GD. Methanol economy and net zero emissions: critical analysis of catalytic processes, reactors and technologies. *Green Chem*. 2021;23(21):8361-8405. doi:10.1039/D1GC02078A
14. Bampaou M, Haag S, Kyriakides AS, Panopoulos KD, Seferlis P. Optimizing methanol synthesis combining steelworks off-gases and renewable hydrogen. *Renewable and Sustainable Energy Reviews*. 2023;171:113035. doi:10.1016/j.rser.2022.113035
15. Chinchen GC, Denny PJ, Jennings JR, Spencer MS, Waugh KC. Synthesis of Methanol. Part 1. Catalysts and Kinetics. *Applied Catalysis*. 1988;36(C):1-65. doi:10.1016/S0166-9834(00)80103-7
16. Bart JCJ, Sneeden RPA. Copper-zinc oxide-alumina methanol catalysts revisited. *Catalysis Today*. 1987;2(1):1-124. doi:10.1016/0920-5861(87)80001-9
17. Marlin DS, Sarron E, Sigurbjörnsson Ó. Process Advantages of Direct CO2 to Methanol Synthesis. *Front Chem*. 2018;6. doi:10.3389/fchem.2018.00446
18. Guil-López R, Mota N, Llorente J, et al. Methanol Synthesis from CO2: A Review of the Latest Developments in Heterogeneous Catalysis. *Materials*. 2019;12(23):3902. doi:10.3390/ma12233902
19. Arena F, Italiano G, Barbera K, et al. Solid-state interactions, adsorption sites and functionality of Cu-ZnO/ZrO2 catalysts in the CO2 hydrogenation to CH3OH. *Applied Catalysis A: General*. 2008;350(1):16-23. doi:10.1016/j.apcata.2008.07.028
20. Wild S, Polierer S, Zevaco TA, et al. Direct DME synthesis on CZZ/H-FER from variable CO 2 /CO syngas feeds. *RSC Adv*. 2021;11(5):2556-2564. doi:10.1039/D0RA09754C

21. Słoczyński J, Grabowski R, Kozłowska A, et al. Effect of Mg and Mn oxide additions on structural and adsorptive properties of Cu/ZnO/ZrO2 catalysts for the methanol synthesis from CO2. *Applied Catalysis A: General*. 2003;249(1):129-138. doi:10.1016/S0926-860X(03)00191-1

22. Köppel RA, Stöcker C, Baiker A. Copper- and silver-zirconia aerogels: Preparation, structural properties and catalytic behavior in methanol synthesis from carbon dioxide. *Journal of Catalysis*. 1998;179(2):515-527. doi:10.1006/jcat.1998.2252

23. Raza A, Ikram M, Guo S, Baiker A, Li G. Green Synthesis of Dimethyl Carbonate from CO2 and Methanol: New Strategies and Industrial Perspective. *Advanced Sustainable Systems*. 2022;6(8):2200087. doi:10.1002/adsu.202200087

24. Larmier K, Liao WC, Tada S, et al. CO2 -to-Methanol Hydrogenation on Zirconia-Supported Copper Nanoparticles: Reaction Intermediates and the Role of the Metal-Support Interface. *Angew Chem Int Ed Engl*. 2017;56(9):2318-2323. doi:10.1002/anie.201610166

25. Jung KT, Bell AT. Effects of Zirconia Phase on the Synthesis of Methanol over Zirconia-Supported Copper. *Catalysis Letters*. 2002;80(1):63-68. doi:10.1023/A:1015326726898

26. Burch R, E. Golunski S, S. Spencer M. The role of copper and zinc oxide in methanol synthesis catalysts. *Journal of the Chemical Society, Faraday Transactions*. 1990;86(15):2683-2691. doi:10.1039/FT9908602683

27. Peláez R, Bryce E, Marín P, Ordóñez S. Catalyst deactivation in the direct synthesis of dimethyl ether from syngas over CuO/ZnO/Al2O3 and γ-Al2O3 mechanical mixtures. *Fuel Processing Technology*. 2018;179:378-386. doi:10.1016/j.fuproc.2018.07.029

28. Fichtl MB, Schlereth D, Jacobsen N, et al. Kinetics of deactivation on Cu/ZnO/Al2O3 methanol synthesis catalysts. *Applied Catalysis A: General*. 2015;502:262-270. doi:10.1016/j.apcata.2015.06.014

29. Sajnani S, Memon MA, Memon SA, et al. CO2 to Methanol Conversion: A Bibliometric Analysis with Insights into Reaction Mechanisms, and Recent Advances in Catalytic Conversion. *Processes*. 2025;13(2):314. doi:10.3390/pr13020314

30. Bukhtiyarova M, Lunkenbein T, Kähler K, Schlögl R. Methanol Synthesis from Industrial CO2 Sources: A Contribution to Chemical Energy Conversion. *Catal Lett*. 2017;147(2):416-427. doi:10.1007/s10562-016-1960-x

31. Behrens M, Schlögl R. How to Prepare a Good Cu/ZnO Catalyst or the Role of Solid State Chemistry for the Synthesis of Nanostructured Catalysts. *Z anorg allg Chem*. 2013;639(15):2683-2695. doi:10.1002/zaac.201300356

32. Shahsavar H, Taghizadeh M, Kiadehi AD. Effects of catalyst preparation route and promoters (Ce and Zr) on catalytic activity of CuZn/CNTs catalysts for hydrogen production from methanol steam reforming. *International Journal of Hydrogen Energy*. 2021;46(13):8906-8921. doi:10.1016/j.ijhydene.2021.01.010

33. Phongprueksathat N, Bansode A, Toyao T, Urakawa A. Greener and facile synthesis of Cu/ZnO catalysts for CO 2 hydrogenation to methanol by urea hydrolysis of acetates. *RSC Advances*. 2021;11(24):14323-14333. doi:10.1039/D1RA02103F

34. Fasanya OO, Atta AY, Myint MTZ, Dutta J, Jibril BY. Effects of synthesis methods on performance of CuZn/MCM-41 catalysts in methanol steam reforming. *International Journal of Hydrogen Energy*. 2021;46(5):3539-3553. doi:10.1016/j.ijhydene.2020.10.181

35. Jiang X, Chen S, Chen X, Ling C, Lu J. Effect of turbulence in micro-reactors on ultrafast competitive reactions in Cu-Zn co-precipitation. *AIChE J*. 2021;67(7). doi:10.1002/aic.17240

36. BALTES C, VUKOJEVIC S, SCHUTH F. Correlations between synthesis, precursor, and catalyst structure and activity of a large set of CuO/ZnO/Al2O3 catalysts for methanol synthesis. *Journal of Catalysis*. 2008;258(2):334-344. doi:10.1016/j.jcat.2008.07.004

37. Choi Y, Futagami K, Fujitani T, Nakamura J. The role of ZnO in Cu/ZnO methanol synthesis catalysts — morphology effect or active site model? *Applied Catalysis A: General*. 2001;208(1-2):163-167. doi:10.1016/S0926-860X(00)00712-2

38. Fujitani T, Nakamura J. The chemical modification seen in the Cu/ZnO methanol synthesis catalysts. *Applied Catalysis A: General*. 2000;191(1-2):111-129. doi:10.1016/S0926-860X(99)00313-0

39. Liao F, Huang Y, Ge J, et al. Morphology-dependent interactions of ZnO with Cu nanoparticles at the materials' interface in selective hydrogenation of CO2 to CH3OH. *Angew Chem Int Ed Engl*. 2011;50(9):2162-2165. doi:10.1002/anie.201007108

40. Palo DR, Dagle RA, Holladay JD. Methanol steam reforming for hydrogen production. *Chem Rev*. 2007;107(10):3992-4021. doi:10.1021/cr050198b

41. Kuld S, Thorhauge M, Falsig H, et al. Quantifying the promotion of Cu catalysts by ZnO for methanol synthesis. *Science*. 2016;352(6288):969-974. doi:10.1126/science.aaf0718

42. Kurtz M, Wilmer H, Genger T, Hinrichsen O, Muhler M. Deactivation of Supported Copper Catalysts for Methanol Synthesis. *Catalysis Letters*. 2003;86(1):77-80. doi:10.1023/A:1022663125977

43. Mota N, Guil-Lopez R, Pawelec BG, Fierro JLG, Navarro RM. Highly active Cu/ZnO–Al catalyst for methanol synthesis: effect of aging on its structure and activity. *RSC Adv*. 2018;8(37):20619-20629. doi:10.1039/C8RA03291B

44. Polierer S, Guse D, Wild S, et al. Enhanced Direct Dimethyl Ether Synthesis from CO2-Rich Syngas with Cu/ZnO/ZrO2 Catalysts Prepared by Continuous Co-Precipitation. *Catalysts*. 2020;10(8):816. doi:10.3390/catal10080816

45. Tsai SB, Ma H. A Research on Preparation and Application of the Monolithic Catalyst with Interconnecting Pore Structure. *Sci Rep*. 2018;8(1):16605. doi:10.1038/s41598-018-35021-2

46. Curry-Hyde HE, Sizgek GD, Wainwright MS, Young DJ. Improvements to Raney copper methanol synthesis catalysts through zinc impregnation: IV. Pore structure and the influence on activity. *Applied Catalysis A: General*. 1993;95(1):65-74. doi:10.1016/0926-860X(93)80197-X

47. Tikhov SF, Minyukova TP, Reshetnikov SI, et al. Particularities of low-temperature WGSR over ceramometal and oxide catalysts: Effect of catalyst particle size. *Chemical Engineering Journal*. 2019;374:405-411. doi:10.1016/j.cej.2019.05.089

48. Schulte ML, Catharina Sender V, Baumgarten L, et al. Tuning Flame Spray Pyrolysis for Variation of the Crystallite Size in Cu/ZnO/ZrO2 and its Influence on the Performance in CO2-to-Methanol Synthesis. *European Journal of Inorganic Chemistry*. 2025;28(4):e202400684. doi:10.1002/ejic.202400684

49. Tada S, Larmier K, Büchel R, Copéret C. Methanol synthesis via CO 2 hydrogenation over CuO–ZrO 2 prepared by two-nozzle flame spray pyrolysis. *Catal Sci Technol*. 2018;8(8):2056-2060. doi:10.1039/C8CY00250A

50. Ahmad R, Hellinger M, Buchholz M, et al. Flame-made Cu/ZnO/Al2O3 catalyst for dimethyl ether production. *Catalysis Communications*. 2014;43:52-56. doi:10.1016/j.catcom.2013.08.020

51. Baydir E, Aras Ö. The role of CO adsorption and CuO formation on the catalyst deactivation during the long-term performance evaluation of methanol steam reforming process for hydrogen production: Comparison of sono-coprecipitation and spray pyrolysis method. *International Journal of Hydrogen Energy*. 2022;47(91):38594-38608. doi:10.1016/j.ijhydene.2022.09.031

52. Polierer S, Pitter S, Grunwaldt JD, et al. Synthesis and characterization of copper-based catalysts applied in the one-step dimethyl ether synthesis (Poster). Presented at: 52. Jahrestreffen Deutscher Katalytiker (2019); March 13, 2019; Weimar, Germany.

53. Paris C, Karelovic A, Manrique R, et al. CO2 Hydrogenation to Methanol with Ga- and Zn-Doped Mesoporous Cu/SiO2 Catalysts Prepared by the Aerosol-Assisted Sol-Gel Process. *ChemSusChem*. 2020;13(23):6409-6417. doi:10.1002/cssc.202001951

54. Chen D, Mao D, Xiao J, Guo X, Yu J. CO2hydrogenation to methanol over CuO–ZnO–TiO2–ZrO2: a comparison of catalysts prepared by sol–gel, solid-state reaction and solution-combustion. *J Sol-Gel Sci Technol*. 2018;86(3):719-730. doi:10.1007/s10971-018-4680-4

55. Yang R, Yu X, Zhang Y, Li W, Tsubaki N. A new method of low-temperature methanol synthesis on Cu/ZnO/Al2O3 catalysts from CO/CO2/H2. *Fuel*. 2008;87(4):443-450. doi:10.1016/j.fuel.2007.06.020

56. Pospelova V, Aubrecht J, Kikhtyanin O, Kubička D. Towards efficient Cu/ZnO catalysts for ester hydrogenolysis: The role of synthesis method. *Applied Catalysis A: General*. 2021;624:118320. doi:10.1016/j.apcata.2021.118320

57. Sahibzada M, Chadwick D, Metcalfe IS. Hydrogenation of carbon dioxide to methanol over palladium-promoted Cu/ZnO/A12O3 catalysts. *Catalysis Today*. 1996;29(1):367-372. doi:10.1016/0920-5861(95)00306-1

58. Kaluza S, Behrens M, Schiefenhövel N, et al. A Novel Synthesis Route for Cu/ZnO/Al2O3 Catalysts used in Methanol Synthesis: Combining Continuous Consecutive Precipitation with Continuous Aging of the Precipitate. *ChemCatChem*. 2011;3(1):189-199. doi:10.1002/cctc.201000329

59. Simson G, Prasetyo E, Reiner S, Hinrichsen O. Continuous precipitation of Cu/ZnO/Al2O3 catalysts for methanol synthesis in microstructured reactors with alternative precipitating agents. *Applied Catalysis A: General*. 2013;450:1-12. doi:10.1016/j.apcata.2012.06.040

60. Hartig MAJ, Peukert W, Jacobsen N, Leuthold A. A model-based precipitation study of copper-based catalysts. *AIChE J*. 2015;61(7):2104-2116. doi:10.1002/aic.14810

61. Frei E, Schaadt A, Ludwig T, Hillebrecht H, Krossing I. The Influence of the Precipitation/Ageing Temperature on a Cu/ZnO/ZrO 2 Catalyst for Methanol Synthesis from H 2 and CO 2. *ChemCatChem*. 2014;6(6):1721-1730. doi:10.1002/cctc.201300665

62. Zhang F, Zhang Y, Yuan L, et al. Synthesis of Cu/Zn/Al/Mg catalysts on methanol production by different precipitation methods. *Molecular Catalysis*. 2017;441:190-198. doi:10.1016/j.mcat.2017.08.015

63. Sun M, Hu W, Cheng T, et al. A novel insight into the preparation method of Pd/Ce0.75Zr0.25O2-Al2O3 over high-stability close coupled catalysts. *Applied Surface Science*. 2019;467-468:723-739. doi:10.1016/j.apsusc.2018.10.190

64. Whittle DM, Mirzaei AA, Hargreaves JSJ, et al. Co-precipitated copper zinc oxide catalysts for ambient temperature carbon monoxide oxidation: Effect of precipitate ageing on catalyst activity. *Phys Chem Chem Phys*. 2002;4(23):5915-5920. doi:10.1039/b207691h

65. Spencer MS. The role of zinc oxide in Cu/ZnO catalysts for methanol synthesis and the water–gas shift reaction. *Topics in Catalysis*. 1999;8:259-266.

66. Behrens M, Girgsdies F. Structural Effects of Cu/Zn Substitution in the Malachite-Rosasite System. *Z anorg allg Chem*. 2010;636(6):919-927. doi:10.1002/zaac.201000028

67. Zwiener L, Girgsdies F, Brennecke D, et al. Evolution of zincian malachite synthesis by low temperature co-precipitation and its catalytic impact on the methanol synthesis. *Applied Catalysis B: Environmental*. 2019;249:218-226. doi:10.1016/j.apcatb.2019.02.023

68. Behrens M, Girgsdies F, Trunschke A, Schlögl R. Minerals as Model Compounds for Cu/ZnO Catalyst Precursors: Structural and Thermal Properties and IR Spectra of Mineral and Synthetic (Zincian) Malachite, Rosasite and Aurichalcite and a Catalyst Precursor Mixture. *Eur J Inorg Chem*. 2009;2009(10):1347-1357. doi:10.1002/ejic.200801216

69. Pollard AM, Thomas RG, Williams PA, Just J, Bridge PJ. The synthesis and composition of georgeite and its reactions to form other secondary copper(II) carbonates. *Mineral Mag*. 1991;55(379):163-166. doi:10.1180/minmag.1991.055.379.03

70. Pollard AM, Spencer MS, Thomas RG, Williams PA, Holt J, Jennings JR. Georgeite and azurite as precursors in the preparation of co-precipitated copper/zinc oxide catalysts. *Applied Catalysis A: General*. 1992;85(1):1-11. doi:10.1016/0926-860X(92)80125-V

71. Hartig MAJ, Jacobsen N, Peukert W. Multi-component and multi-phase population balance model: The case of Georgeite formation as methanol catalyst precursor phase. *Chemical Engineering Science*. 2014;109:158-170. doi:10.1016/j.ces.2014.01.026

72. Bems B, Schur M, Dassenoy A, Junkes H, Herein D, Schlögl R. Relations between synthesis and microstructural properties of copper/zinc hydroxycarbonates. *Chemistry*. 2003;9(9):2039-2052. doi:10.1002/chem.200204122

73. Zhang QC, Cheng KP, Wen LX, Guo K, Chen JF. A study on the precipitating and aging processes of CuO/ZnO/Al 2 O 3 catalysts synthesized in micro-impinging stream reactors. *RSC Adv*. 2016;6(40):33611-33621. doi:10.1039/C6RA02512A

74. Jeong Y, Kim I, Kang JY, et al. Effect of the aging time of the precipitate on the activity of Cu/ZnO catalysts for alcohol-assisted low temperature methanol synthesis. *Journal of Molecular Catalysis A: Chemical*. 2016;418-419:168-174. doi:10.1016/j.molcata.2016.03.044

75. Güldenpfennig A, Distaso M, Peukert W. In situ investigations on the amorphous to crystalline phase transformation of precursors for methanol synthesis catalysts. *Chemical Engineering Journal*. 2019;369:996-1004. doi:10.1016/j.cej.2019.03.088

76. Warmuth L, Zevaco TA, Pitter S. *In situ* FT-IR reveals ageing phenomena in the formation of a Cu/Zn/Zr methanol catalyst precursor. *Inorganic Chemistry Communications*. 2025;172:113753. doi:10.1016/j.inoche.2024.113753

77. Waller D, Stirling D, S. Stone F, S. Spencer M. Copper–zinc oxide catalysts. Activity in relation to precursor structure and morphology. *Faraday Discussions of the Chemical Society*. 1989;87(0):107-120. doi:10.1039/DC9898700107

78. Zander S, Seidlhofer B, Behrens M. In situ EDXRD study of the chemistry of aging of co-precipitated mixed Cu,Zn hydroxycarbonates--consequences for the preparation of Cu/ZnO catalysts. *Dalton Trans*. 2012;41(43):13413-13422. doi:10.1039/c2dt31236k

79. Farahani BV, Rajabi FH, Bahmani M, Ghelichkhani M, Sahebdelfar S. Influence of precipitation conditions on precursor particle size distribution and activity of Cu/ZnO methanol synthesis catalyst. *Applied Catalysis A: General*. 2014;482:237-244. doi:10.1016/j.apcata.2014.05.034

80. Jung H, Yang DR, Joo OS, Jung KD. The Importance of the Aging Time to Prepare Cu/ZnO/Al 2 O 3 Catalyst with High Surface Area in Methanol Synthesis. *Bulletin of the Korean Chemical Society*. 2010;31(5):1241-1246. doi:10.5012/bkcs.2010.31.5.1241

81. Muhamad EN, Irmawati R, Taufiq-Yap YH, et al. Comparative study of Cu/ZnO catalysts derived from different precursors as a function of aging. *Catalysis Today*. 2008;131(1-4):118-124. doi:10.1016/j.cattod.2007.10.010

82. Behrens M, Brennecke D, Girgsdies F, et al. Understanding the complexity of a catalyst synthesis: Co-precipitation of mixed Cu,Zn,Al hydroxycarbonate precursors for Cu/ZnO/Al2O3 catalysts investigated by titration experiments. *Applied Catalysis A: General*. 2011;392(1-2):93-102. doi:10.1016/j.apcata.2010.10.031

83. Sanches SG, Huertas Flores J, da Silva MIP. Influence of aging time on the microstructural characteristics of a Cu/ZnO-based catalyst prepared by homogeneous precipitation for use in methanol steam reforming. *Reac Kinet Mech Cat*. 2017;121(2):473-485. doi:10.1007/s11144-017-1161-7

84. Jiang X, Zheng L, Wang Z, Lu J. Microstructure characters of Cu/ZnO catalyst precipitated inside microchannel reactor. *Journal of Molecular Catalysis A: Chemical*. 2016;423:457-462. doi:10.1016/j.molcata.2016.07.046

85. Jiang X, Qin X, Ling C, Wang Z, Lu J. The effect of mixing on Co-precipitation and evolution of microstructure of Cu-ZnO catalyst. *AIChE J*. 2018;124(2-3):123. doi:10.1002/aic.16168

86. Angelo L, Girleanu M, Ersen O, Serra C, Parkhomenko K, Roger AC. Catalyst synthesis by continuous coprecipitation under micro-fluidic conditions: Application to the preparation of catalysts for methanol synthesis from CO 2 /H 2. *Catalysis Today*. 2016;270:59-67.

87. Wolf A, Michele V, Schlüter OFK, Herbstritt F, Heck J, Mleczko L. Precipitation in a Micromixer - From Laboratory to Industrial Scale. *Chem Eng Technol*. 2015;38(11):2017-2024. doi:10.1002/ceat.201500040

88. Behrens M. Meso- and nano-structuring of industrial Cu/ZnO/(Al2O3) catalysts. *Journal of Catalysis*. 2009;267(1):24-29. doi:10.1016/j.jcat.2009.07.009

89. Schumann J, Lunkenbein T, Tarasov A, Thomas N, Schlögl R, Behrens M. Synthesis and Characterisation of a Highly Active Cu/ZnO: Al Catalyst. *ChemCatChem*. 2014;6(10):2889-2897. doi:10.1002/cctc.201402278

90. Kniep BL, Girgsdies F, Ressler T. Effect of precipitate aging on the microstructural characteristics of Cu/ZnO catalysts for methanol steam reforming. *Journal of Catalysis*. 2005;236(1):34-44. doi:10.1016/j.jcat.2005.09.001

91. Behrens M. Coprecipitation: An excellent tool for the synthesis of supported metal catalysts – From the understanding of the well known recipes to new materials. *Catalysis Today*. 2015;246:46-54. doi:10.1016/j.cattod.2014.07.050

92. Sanches SG, Flores JH, de Avillez RR, Pais da Silva MI. Influence of preparation methods and Zr and Y promoters on Cu/ZnO catalysts used for methanol steam reforming. *International Journal of Hydrogen Energy*. 2012;37(8):6572-6579. doi:10.1016/j.ijhydene.2012.01.033

93. Jeong C, Suh YW. Role of ZrO2 in Cu/ZnO/ZrO2 catalysts prepared from the precipitated Cu/Zn/Zr precursors. *Catalysis Today*. 2016;265:254-263. doi:10.1016/j.cattod.2015.07.053

94. Bisotti F, Moioli E, Manenti F. Screening kinetic models for CO2-to-methanol over CuO–ZnO–ZrO2–Al2O3 (CZZA) and CuO–ZnO–ZrO2 (CZZ): are they consistent with the experimental evidence? A critical review of the existing kinetic models and relevant literature on experimental characterization of copper-based catalysts for CO2-to-methanol process. *Chemical Engineering Journal*. 2025;503:158033. doi:10.1016/j.cej.2024.158033

95. Smith PJ, Kondrat SA, Chater PA, et al. A new class of Cu/ZnO catalysts derived from zincian georgeite precursors prepared by co-precipitation. *Chem Sci*. 2017;8(3):2436-2447. doi:10.1039/c6sc04130b

96. Sengupta G, Das DP, Kundu ML, et al. Study of copper—zinc oxide catalysts, characterisation of the coprecipitate and mixed oxide. *Applied Catalysis*. 1989;55(1):165-180. doi:10.1016/S0166-9834(00)82326-X

97. Kaluza S, Muhler M. On the Role of Aging, Washing, and Drying in the Synthesis of Polycrystalline Zinc Oxide by Precipitation: Combining Fast Continuous Mixing, Spray Drying and Freeze Drying to Unravel the Solid-State Transformations of the Precipitate. *Catal Lett*. 2009;129(3-4):287-292.

98. Kikhtyanin O, Pospelova V, Aubrecht J, Lhotka M, Kubička D. Effect of Calcination Atmosphere and Temperature on the Hydrogenolysis Activity and Selectivity of Copper-Zinc Catalysts. *Catalysts*. 2018;8(10):446. doi:10.3390/catal8100446

99. Schumann J, Tarasov A, Thomas N, Schlögl R, Behrens M. Cu,Zn-based catalysts for methanol synthesis: On the effect of calcination conditions and the part of residual carbonates. *Applied Catalysis A: General*. 2016;516:117-126. doi:10.1016/j.apcata.2016.01.037

100. Kiener C, Kurtz M, Wilmer H, et al. High-throughput screening under demanding conditions: Cu/ZnO catalysts in high pressure methanol synthesis as an example. *Journal of Catalysis*. 2003;216(1-2):110-119. doi:10.1016/S0021-9517(02)00134-3

101. Guse D, Polierer S, Wild S, Pitter S, Kind M. Improved Preparation of Cu/Zn-Based Catalysts by Well-Defined Conditions of Co-Precipitation and Aging. *Chemie Ingenieur Technik*. 2022;94(3):314-327. doi:10.1002/cite.202100197

102. Etim UJ, Song Y, Zhong Z. Improving the Cu/ZnO-Based Catalysts for Carbon Dioxide Hydrogenation to Methanol, and the Use of Methanol As a Renewable Energy Storage Media. *Front Energy Res*. 2020;8. doi:10.3389/fenrg.2020.545431

103. Morozov IV, Znamenkov KO, Korenev YuM, Shlyakhtin OA. Thermal decomposition of Cu(NO3)2·3H2O at reduced pressures. *Thermochimica Acta*. 2003;403(2):173-179. doi:10.1016/S0040-6031(03)00057-1

104. Sumich AI, Yeshchanka LS. Study of the composition and properties of products formed in interaction of Na2CO3 with proton-containing reagents. *Russ J Appl Chem*. 2015;88(12):1923-1927. doi:10.1134/S10704272150120034

105. Guse D, Metzger L, Kriesten M, Eiche E, Kind M. Fast Method to Determine Solubility Products of Sparingly Soluble Salts by Combining Titration Experiments and Thermodynamic Modeling: A Case Study on the Example of Cu/Zn Based Catalyst Precursors and Ni/Mn Based Precursors for Cathode Active Material. *Ind Eng Chem Res*. 2024;63(32):14333-14351. doi:10.1021/acs.iecr.4c01616

106. Parkhurst DL, Appelo C a. J. *Description of Input and Examples for PHREEQC Version 3: A Computer Program for Speciation, Batch-Reaction, One-Dimensional Transport, and Inverse Geochemical Calculations*. U.S. Geological Survey; 2013. doi:10.3133/tm6A43

107. Alwan AK, Thomas JH, Williams PA. Mineral formation from aqueous solution. Part III. The stability of aurichalcite, (Zn,Cu)5(CO3)2(OH)6, and rosasite (Cu,Zn)2(CO3)(OH)2. *Transition Met Chem*. 1980;5(1):3-5. doi:10.1007/BF01396855

108. Martell AE, Smith RM. NIST Standard Reference Database 46 Version 8.0. NIST. January 1, 2004. Accessed June 28, 2024. https://www.nist.gov/srd/nist46

109. Giffaut E, Grivé M, Blanc Ph, et al. Andra thermodynamic database for performance assessment: ThermoChimie. *Applied Geochemistry*. 2014;49:225-236. doi:10.1016/j.apgeochem.2014.05.007

110. Guse D, Kind M. PHREEQC database for the thermodynamic modelling of Cu/Zn based catalyst precursors. Published online 2025:265,8 kB. doi:10.35097/38Q7C227W1ZJTK1D

111. Kügler RT, Kind M. Experimental study about plugging in confined impinging jet mixers during the precipitation of strontium sulfate. *Chemical Engineering and Processing: Process Intensification*. 2016;101:25-32. doi:10.1016/j.cep.2015.12.007

112. Metzger L, Kind M. On the transient flow characteristics in Confined Impinging Jet Mixers - CFD simulation and experimental validation. *Chemical Engineering Science*. 2015;133:91-105. doi:10.1016/j.ces.2014.12.056

113. Rehage H, Orthey J, Kind M. On the complete similitude of technical precipitation. Part I: Impinging mixers. *Chemical Engineering Journal*. 2021;415:129047.

114. Kügler RT, Doyle S, Kind M. Fundamental insights into barium sulfate precipitation by time-resolved in situ synchrotron radiation wide-angle X-ray scattering (WAXS). *Chemical Engineering Science*. 2015;133:140-147. doi:10.1016/j.ces.2014.12.024

115. Guse D, Warmuth L, Kreißig F, Pitter S, Kind M. Preparation of Cu/Zn Based Catalyst Precursors – Importance of Thermodynamics and Seeding. In: *Proceedings of the DGMK-Conference "The Role of Catalysis for the Energy Transition", October 5 -7 2022 in Ludwigshafen*. Vol 2022-3. Deutsche Wissenschaftliche Gesellschaft für Erdöl, Erdgas und Kohle e.V. (DGMK); 2022:19-39. doi:10.5445/IR/1000151320

116. Allahyari S, Haghighi M, Ebadi A, Hosseinzadeh S. Effect of irradiation power and time on ultrasound assisted co-precipitation of nanostructured CuO–ZnO–Al2O3 over HZSM-5 used for direct conversion of syngas to DME as a green fuel. *Energy Conversion and Management*. 2014;83:212-222. doi:10.1016/j.enconman.2014.03.071

117. D'Ans, D'Ans J, Lax, Lax E. *Taschenbuch Für Chemiker Und Physiker: Band III: Elemente, Anorganische Verbindungen Und Materialien, Minerale*. Vierte, neubearbeitete und revidierte Auflage. (Blachnik R, ed.). Springer; 1998. doi:10.1007/978-3-642-58842-6

118. Malvern Panalytical. Selecting an appropriate particle absorption for laser diffraction particle size calculations. Accessed April 7, 2025. https://www.malvernpanalytical.com/en/learn/knowledge-center/technical-notes/tn101104selectingparticleabsorbtionlaserdiffractio

119. Mastersizer User Guide. Published online February 5, 2024. Accessed June 12, 2024. https://www.malvernpanalytical.com/de/learn/knowledge-center/user-manuals/man0474en

120. Guse D, Warmuth L, Herfet M, et al. Seeding as a Decisive Tool for Increasing Space-Time-Yields in the Preparation of High-Quality Cu/ZnO/ZrO2 Catalysts. *Catalysts*. 2024;14(8):517. doi:10.3390/catal14080517

121. Doebelin N, Kleeberg R. Profex: a graphical user interface for the Rietveld refinement program BGMN. *J Appl Crystallogr*. 2015;48(Pt 5):1573-1580. doi:10.1107/S1600576715014685

122. Wild S, Lacerda de Oliveira Campos B, Zevaco TA, et al. Experimental investigations and model-based optimization of CZZ/H-FER 20 bed composition for the direct synthesis of DME from CO 2 -rich syngas. *React Chem Eng*. Published online January 1, 2022. doi:10.1039/D1RE00470K

123. Stone FS, Waller D. Cu–ZnO and Cu–ZnO/Al2O3 Catalysts for the Reverse Water-Gas Shift Reaction. The Effect of the Cu/Zn Ratio on Precursor Characteristics and on the Activity of the Derived Catalysts. *Topics in Catalysis*. 2003;22(3):305-318. doi:10.1023/A:1023592407825

124. Zander S, Kunkes EL, Schuster ME, et al. The role of the oxide component in the development of copper composite catalysts for methanol synthesis. *Angew Chem Int Ed Engl*. 2013;52(25):6536-6540. doi:10.1002/anie.201301419

125. Gao W, Qu G, Xu M, Chang S, Na W. Effect of pH on Co-precipitated Cu-ZnO-ZrO 2 Catalysts Used in CO 2 Hydrogenation: the Role of Zn-malachite in the Precursors ▲. *Fuel Cells*. 2021;21(1):31-38. doi:10.1002/fuce.202000032

126. L'hospital V, Heyte S, Paul S, Parkhomenko K, Roger AC. Optimization of the continuous coprecipitation in a microfluidic reactor: Cu-based catalysts for CO2 hydrogenation into methanol. *Fuel*. 2022;319:123689. doi:10.1016/j.fuel.2022.123689

127. Kondrat SA, Smith PJ, Wells PP, et al. Stable amorphous georgeite as a precursor to a high-activity catalyst. *Nature*. 2016;531(7592):83-87. doi:10.1038/nature16935

128. Haderlein M, Güldenpfennig A, Segets D, Peukert W. A widely applicable tool for modeling precipitation processes. *Computers & Chemical Engineering*. 2017;98:197-208. doi:10.1016/j.compchemeng.2016.12.007

129. Powell KJ, Brown PL, Byrne RH, et al. Chemical speciation of environmentally significant metals with inorganic ligands Part 2: The Cu2+-OH-, Cl-, CO32-, SO42-, and PO43- systems (IUPAC Technical Report). *Pure and Applied Chemistry*. 2007;79(5):895-950. doi:10.1351/pac200779050895

130. Shah N, Sandhu H, Choi DS, Chokshi H, Malick AW, eds. *Amorphous Solid Dispersions: Theory and Practice*. Springer; 2014. doi:10.1007/978-1-4939-1598-9

131. Davila LP, Risbud SH, Shackelford JF. Quartz and Silicas. In: Shackelford JF, Doremus RH, eds. *Ceramic and Glass Materials: Structure, Properties and Processing*. Springer US; 2008:71-86. doi:10.1007/978-0-387-73362-3_5

132. Kondrat SA, Smith PJ, Carter JH, et al. The effect of sodium species on methanol synthesis and water-gas shift Cu/ZnO catalysts: utilising high purity zincian georgeite. *Faraday Discuss*. 2017;197:287-307. doi:10.1039/c6fd00202a

133. Rua Gonzalez D. *Synthèse de Matériaux Catalytiques de Type Oxydes Mixtes Pour La Production de Méthanol Par La Précipitation En Flux Continu En Système Microfluidique = Synthesis of Catalytic Materials of Mixed Oxides Type for the Production of Methanol by Precipitation in Continuous Flow in Microfluidic Systems*. Strasbourg; 2024. Accessed March 25, 2025. https://ecrin.app.unistra.fr/search/notice/view/2024STRAF001

134. Behrens M, Kasatkin I, Kühl S, Weinberg G. Phase-Pure Cu,Zn,Al Hydrotalcite-like Materials as Precursors for Copper rich Cu/ZnO/Al2O3 Catalysts. *Chem Mater*. 2010;22(2):386-397. doi:10.1021/cm9029165

135. Schur M, Bems B, Dassenoy A, et al. Continuous coprecipitation of catalysts in a micromixer: Nanostructured Cu/ZnO composite for the synthesis of methanol. *Angew Chem Int Ed Engl*. 2003;42(32):3815-3817. doi:10.1002/anie.200250709

136. Lim AMH, Yeo JW, Zeng HC. Preparation of CuZn-Doped MgAl-Layered Double Hydroxide Catalysts through the Memory Effect of Hydrotalcite for Effective Hydrogenation of CO2 to Methanol. *ACS Appl Energy Mater*. 2023;6(2):782-794. doi:10.1021/acsaem.2c03045

137. Santos RJ, Sultan MA. State of the Art of Mini/Micro Jet Reactors. *Chemical Engineering & Technology*. 2013;36(6):937-949. doi:10.1002/ceat.201200678

138. Tofighi G, Lichtenberg H, Gaur A, et al. Continuous synthesis of Cu/ZnO/Al2O3 nanoparticles in a co-precipitation reaction using a silicon based microfluidic reactor. *React Chem Eng*. 2022;7(3):730-740. doi:10.1039/D1RE00499A

139. Kucher M, Babic D, Kind M. Precipitation of barium sulfate: Experimental investigation about the influence of supersaturation and free lattice ion ratio on particle formation. *Chemical Engineering and Processing: Process Intensification*. 2006;45(10):900-907. doi:10.1016/j.cep.2005.12.006

140. Schwarzer HC, Schwertfirm F, Manhart M, Schmid HJ, Peukert W. Predictive simulation of nanoparticle precipitation based on the population balance equation. *Chemical Engineering Science*. 2006;61(1):167-181. doi:10.1016/j.ces.2004.11.064

141. Johnson BK, Prud'homme RK. Chemical processing and micromixing in confined impinging jets. *AIChE J*. 2003;49(9):2264-2282. doi:10.1002/aic.690490905

142. Metzger L, Kind M. On the mixing in confined impinging jet mixers – Time scale analysis and scale-up using CFD coarse-graining methods. *Chemical Engineering Research and Design*. 2016;109:464-476. doi:10.1016/j.cherd.2016.02.019

143. Baldyga J, Bourne JR. Simplification of micromixing calculations. I. Derivation and application of new model. *The Chemical Engineering Journal*. 1989;42(2):83-92.

144. Siddiqui SW, Zhao Y, Kukukova A, Kresta SM. Characteristics of a Confined Impinging Jet Reactor: Energy Dissipation, Homogeneous and Heterogeneous Reaction Products, and Effect of Unequal Flow. *Ind Eng Chem Res*. 2009;48(17):7945-7958. doi:10.1021/ie801562y

145. Vicum L, Mazzotti M, Baldyga J. Applying a Thermodynamic Model to the Non-Stoichiometric Precipitation of Barium Sulfate. *Chem Eng Technol*. 2003;26(3):325-333. doi:10.1002/ceat.200390050

146. Prigiobbe V, Mazzotti M. Precipitation of Mg-carbonates at elevated temperature and partial pressure of CO2. *Chemical Engineering Journal*. 2013;223:755-763. doi:10.1016/j.cej.2013.03.033

147. Nemčovičová I, Smatanová IK, Nemčovičová I, Smatanová IK. Alternative Protein Crystallization Technique: Cross-Influence Procedure (CIP). In: *Crystallization and Materials Science of Modern Artificial and Natural Crystals*. IntechOpen; 2012. doi:10.5772/30461

148. Bonvillani P, Ferrari M, Ducros E, Orejas J. Theoretical and experimental study of the effects of scale-up on mixing time for a stirred-tank bioreactor. *Brazilian Journal of Chemical Engineering - BRAZ J CHEM ENG*. 2006;23. doi:10.1590/S0104-66322006000100001

149. Mersmann A, ed. *Crystallization Technology Handbook*. 2. ed., rev.expanded. Dekker; 2001.

150. Kügler RT, Kind M. On Precipitation of Sparingly Soluble Fluoride Salts. *Crystal Growth & Design*. 2018;18(2):728-733. doi:10.1021/acs.cgd.7b01115

151. Güldenpfennig A, Pflug L, Peukert W. How to Estimate Material Parameters for Multiphase, Multicomponent Precipitation Modeling. *Crystal Growth & Design*. 2019;19(5):2785-2793. doi:10.1021/acs.cgd.9b00027

152. Baḱldyga J, Podgórska W, Pohorecki R. Mixing-precipitation model with application to double feed semibatch precipitation. *Chemical Engineering Science*. 1995;50(8):1281-1300. doi:10.1016/0009-2509(95)98841-2

153. L'hospital V, Angelo L, Zimmermann Y, Parkhomenko K, Roger AC. Influence of the Zn/Zr ratio in the support of a copper-based catalyst for the synthesis of methanol from CO2. *Catalysis Today*. 2021;369:95-104. doi:10.1016/j.cattod.2020.05.018

154. Söhnel O, Garside J. *Precipitation: Basic Principles and Industrial Applications*. Butterworth-Heinemann; 1992. http://www.loc.gov/catdir/enhancements/fy1117/92022007-d.html

155. Stoilova D, Koleva V, Vassileva V. Infrared study of some synthetic phases of malachite (Cu2(OH)2CO3)–hydrozincite (Zn5(OH)6(CO3)2) series. *Spectrochimica Acta Part A: Molecular and Biomolecular Spectroscopy*. 2002;58(9):2051-2059. doi:10.1016/S1386-1425(01)00677-1

156. Judat B, Kind M. Morphology and internal structure of barium sulfate—derivation of a new growth mechanism. *J Colloid Interface Sci*. 2004;269(2):341-353. doi:10.1016/j.jcis.2003.07.047

157. N. Perchiazzi. Crystal structure determination and Rietveld refinement of rosasite and mcguinnessite. *Z Kristallogr Suppl 23*. Published online January 1, 2006:505-510. doi:10.1524/9783486992526-084

158. Perchiazzi N, Demitri N, Fehér B, Vignola P. On the Crystal-Chemistry of Rosasite and Parádsasvárite. *Can Mineral*. 2017;55(6):1027-1040. doi:10.3749/canmin.1700041

159. Fehér B, Szakáll S, Zajzon N, Mihály J. Parádsasvárite, a new member of the malachite-rosasite group from Parádsasvár, Mátra Mountains, Hungary. *Miner Petrol*. 2015;109(4):405-411. doi:10.1007/s00710-015-0370-x

160. Fehér B, Szakáll S, Bigi S. Minerals of the rosasite-zincrosasite series from the Andrássy-I. mine, Rudabánya, Hungary: The zincrosasite problem. Published online January 1, 2008.

161. Dasireddy VDBC, Likozar B. The role of copper oxidation state in Cu/ZnO/Al2O3 catalysts in CO2 hydrogenation and methanol productivity. *Renewable Energy*. 2019;140:452-460. doi:10.1016/j.renene.2019.03.073

162. Palomino RM, Ramírez PJ, Liu Z, et al. Hydrogenation of CO2 on ZnO/Cu(100) and ZnO/Cu(111) Catalysts: Role of Copper Structure and Metal–Oxide Interface in Methanol Synthesis. *J Phys Chem B*. 2018;122(2):794-800. doi:10.1021/acs.jpcb.7b06901

163. Kattel S, Ramírez PJ, Chen JG, Rodriguez JA, Liu P. Active sites for CO2 hydrogenation to methanol on Cu/ZnO catalysts. *Science*. 2017;355(6331):1296-1299. doi:10.1126/science.aal3573

164. Shi YF, Kang PL, Shang C, Liu ZP. Methanol Synthesis from CO2/CO Mixture on Cu–Zn Catalysts from Microkinetics-Guided Machine Learning Pathway Search. *J Am Chem Soc*. 2022;144(29):13401-13414. doi:10.1021/jacs.2c06044

165. Lunkenbein T, Schumann J, Behrens M, Schlögl R, Willinger MG. Formation of a ZnO overlayer in industrial Cu/ZnO/Al2 O3 catalysts induced by strong metal-support interactions. *Angew Chem Int Ed Engl*. 2015;54(15):4544-4548. doi:10.1002/anie.201411581

166. Tauster SJ. Strong metal-support interactions. *Acc Chem Res*. 1987;20(11):389-394. doi:10.1021/ar00143a001

167. Tusche C, Meyerheim HL, Kirschner J. Observation of Depolarized ZnO(0001) Monolayers: Formation of Unreconstructed Planar Sheets. *Phys Rev Lett*. 2007;99(2):026102. doi:10.1103/PhysRevLett.99.026102

168. Yoder CH, Bushong E, Liu X, et al. The synthesis and solubility of the copper hydroxyl nitrates: gerhardtite, rouaite and likasite. *Mineral Mag*. 2010;74(3):433-440. doi:10.1180/minmag.2010.074.3.433

169. TANAKA H, TERADA S. Preparation and thermal decomposition of synthetic gerhardtite Cu2(OH)2NO3. *J therm anal*. 1993;39(8-9):1011-1018.

170. Wells HL, Penfield SL. Gerhardtite and artificial basic cupric nitrates. *American Journal of Science*. 1885;3(175):50-57.

171. Fujita S ichiro, Satriyo AM, Shen GC, Takezawa N. Mechanism of the formation of precursors for the Cu/ZnO methanol synthesis catalysts by a coprecipitation method. *Catal Lett*. 1995;34(1-2):85-92. doi:10.1007/BF00808325

172. Shen GC, Fujita S ichiro, Matsumoto S, Takezawa N. Steam reforming of methanol on binary CuZnO catalysts: Effects of preparation condition upon precursors, surface structure and catalytic activity. *Journal of Molecular Catalysis A: Chemical*. 1997;124(2-3):123-136. doi:10.1016/S1381-1169(97)00078-2

173. Dang S, Yang H, Gao P, et al. A review of research progress on heterogeneous catalysts for methanol synthesis from carbon dioxide hydrogenation. *Catalysis Today*. 2019;330:61-75. doi:10.1016/j.cattod.2018.04.021

174. Dong X, Li F, Zhao N, Xiao F, Wang J, Tan Y. CO2 hydrogenation to methanol over Cu/ZnO/ZrO2 catalysts prepared by precipitation-reduction method. *Applied Catalysis B: Environmental*. 2016;191:8-17. doi:10.1016/j.apcatb.2016.03.014

175. Pitter S, De Campos L, Guse D, et al. Scalable synthesis of Cu-based catalysts as a tool for accelerated process development. Presented at: 19th Nordic Symposium on Catalysis (NSC 2022); June 7, 2022; Espoo, Finland. Accessed April 8, 2025. https://publikationen.bibliothek.kit.edu/1000150749

176. Pitter S, Warmuth L, Guse D, et al. Scalable laboratory synthesis of Cu-based methanol catalysts. Presented at: 15th European Congress on Catalysis; August 27, 2023; Prague, Czech Republic. Accessed April 8, 2025. https://www.europacat2023.cz/Amca-Europacat2021/media/content/Docs/Book_of_abstracts-EuropaCat2023.pdf

177. Behrendt G, Mockenhaupt B, Prinz N, Zobel M, Ras EJ, Behrens M. CO Hydrogenation to Methanol over Cu/MgO Catalysts and Their Synthesis from Amorphous Magnesian Georgeite Precursors. *ChemCatChem*. 2022;14(17):e202200299. doi:10.1002/cctc.202200299

178. Zhang W, Lassen K, Descorme C, Valverde JL, Giroir-Fendler A. Effect of the precipitation pH on the characteristics and performance of Co3O4 catalysts in the total oxidation of toluene and propane. *Applied Catalysis B: Environmental*. 2021;282:119566. doi:10.1016/j.apcatb.2020.119566

179. Choudhary VR, Dumbre DK. Magnesium oxide supported nano-gold: A highly active catalyst for solvent-free oxidation of benzyl alcohol to benzaldehyde by TBHP. *Catalysis Communications*. 2009;10(13):1738-1742. doi:10.1016/j.catcom.2009.05.020

180. Kim KJ, Hong GR, Ahn SY, Kim BJ, Lee YL, Roh HS. Effect of precipitation variables on the performance of CeO2-based catalysts for waste-to-hydrogen. *Catalysis Today*. 2024;425:114336. doi:10.1016/j.cattod.2023.114336

181. Bonura G, Cordaro M, Cannilla C, Arena F, Frusteri F. The changing nature of the active site of Cu-Zn-Zr catalysts for the CO2 hydrogenation reaction to methanol. *Applied Catalysis B: Environmental*. 2014;152-153:152-161. doi:10.1016/j.apcatb.2014.01.035

182. Ma Y, Sun Q, Wu D, Fan WH, Zhang YL, Deng JF. A practical approach for the preparation of high activity Cu/ZnO/ZrO2 catalyst for methanol synthesis from CO2 hydrogenation. *Applied Catalysis A: General*. 1998;171(1):45-55. doi:10.1016/S0926-860X(98)00079-9

183. SLOCZYNSKI J, Grabowski R, OLSZEWSKI P, et al. Effect of metal oxide additives on the activity and stability of Cu/ZnO/ZrO2 catalysts in the synthesis of methanol from CO2 and H2. *Applied Catalysis A: General*. 2006;310:127-137. doi:10.1016/j.apcata.2006.05.035

184. Behrendt G, Prinz N, Wolf A, et al. Substitution of Copper by Magnesium in Malachite: Insights into the Synthesis and Structural Effects. *Inorg Chem*. 2022;61(49):19678-19694. doi:10.1021/acs.inorgchem.2c01976

185. Huang CK, Kerr PF. null: Infrared Study of the Carbonate Minerals. *The American Mineralogist*. 1960;45(MARCH-APRIL).

186. Braithwaite RSW, Ryback G. Rosasite, aurichalcite, and associated minerals from Heights of Abraham, Matlock Bath, Derbyshire, with a note on infra-red spectra. *Mineral mag j Mineral Soc*. 1963;33(261):441-449. doi:10.1180/minmag.1963.033.261.01

187. Cardew PT, Davey RJ, Birchall JD. The kinetics of solvent-mediated phase transformations. *Proceedings of the Royal Society of London A Mathematical and Physical Sciences*. 1997;398(1815):415-428. doi:10.1098/rspa.1985.0043

188. Davey RJ, Cardew PT, McEwan D, Sadler DE. Rate controlling processes in solvent-mediated phase transformations. *Journal of Crystal Growth*. 1986;79(1, Part 2):648-653. doi:10.1016/0022-0248(86)90532-4

189. Jakubiak P, Wagner B, Grimm HP, Petrig-Schaffland J, Schuler F, Alvarez-Sánchez R. Development of a Unified Dissolution and Precipitation Model and Its Use for the Prediction of Oral Drug Absorption. *Mol Pharmaceutics*. 2016;13(2):586-598. doi:10.1021/acs.molpharmaceut.5b00808

190. Song Y, Hahn HH, Hoffmann E. Effects of solution conditions on the precipitation of phosphate for recovery: A thermodynamic evaluation. *Chemosphere*. 2002;48(10):1029-1034. doi:10.1016/S0045-6535(02)00183-2

191. Halim CE, Short SA, Scott JA, Amal R, Low G. Modelling the leaching of Pb, Cd, As, and Cr from cementitious waste using PHREEQC. *Journal of Hazardous Materials*. 2005;125(1):45-61. doi:10.1016/j.jhazmat.2005.05.046

192. Deng S, Chen Y, Kolliopoulos G, Papangelakis VG, Li Y. Thermodynamic and experimental analysis of Ni-Co-Mn carbonate precursor synthesis for Li-rich cathode materials. *Ionics*. 2020;26(6):2747-2755. doi:10.1007/s11581-020-03439-2

193. *User's Guide to PHREEQC (Version 2): A Computer Program for Speciation, Batch-Reaction, One-Dimensional Transport, and Inverse Geochemical Calculations*.; 1999. doi:10.3133/wri994259

194. Clever HL, Johnston FJ. The solubility of some sparingly soluble lead salts: An evaluation of the solubility in water and aqueous electrolyte solution. *Journal of Physical and Chemical Reference Data*. 1980;9(3):751-784. doi:10.1063/1.555628

195. Bénézeth P, Berninger UN, Bovet N, Schott J, Oelkers EH. Experimental determination of the solubility product of dolomite at 50–253 °C. *Geochimica et Cosmochimica Acta*. 2018;224:262-275. doi:10.1016/j.gca.2018.01.016

196. Preis W, Gamsjäger H. (Solid + solute) phase equilibria in aqueous solution. XIII. Thermodynamic properties of hydrozincite and predominance diagrams for (Zn2++ H2O+ CO2). *The Journal of Chemical Thermodynamics*. 2001;33(7):803-819. doi:10.1006/jcht.2000.0794

197. Puigdomènech I, Colàs E, Grivé M, Campos I, García D. A tool to draw chemical equilibrium diagrams using SIT: Applications to geochemical systems and radionuclide solubility. *MRS Proc*. 2014;1665:111-116. doi:10.1557/opl.2014.635

198. Taylor P. *Solubility and Stability of Inorganic Carbonates*.; 1987. Accessed June 28, 2024. https://inis.iaea.org/search/search.aspx?orig_q=rn:20062977

199. Cornu D, Coustel R, Durand P, Carteret C, Ruby C. How can pH drop while adding NaOH? Formation and transformation of Mn4(OH)6SO4. *Journal of Solid State Chemistry*. 2022;305:122631. doi:10.1016/j.jssc.2021.122631

200. Charlton SR, Parkhurst DL. Modules based on the geochemical model PHREEQC for use in scripting and programming languages. *Computers & Geosciences*. 2011;37(10):1653-1663. doi:10.1016/j.cageo.2011.02.005

201. Kim HT, Frederick WJ. Evaluation of Pitzer ion interaction parameters of aqueous electrolytes at 25.degree.C. 1. Single salt parameters. *J Chem Eng Data*. 1988;33(2):177-184. doi:10.1021/je00052a035

202. Kim HT, Frederick WJ. Evaluation of Pitzer ion interaction parameters of aqueous mixed electrolyte solutions at 25.degree.C. 2. Ternary mixing parameters. *J Chem Eng Data*. 1988;33(3):278-283. doi:10.1021/je00053a017

203. Pitzer KS, Mayorga G. Thermodynamics of electrolytes. II. Activity and osmotic coefficients for strong electrolytes with one or both ions univalent. *J Phys Chem*. 1973;77(19):2300-2308. doi:10.1021/j100638a009

204. Pitzer KS. Thermodynamics of electrolytes. I. Theoretical basis and general equations. *J Phys Chem*. 1973;77(2):268-277. doi:10.1021/j100621a026

205. Harvie CE, Møller N, Weare JH. The prediction of mineral solubilities in natural waters: The Na-K-Mg-Ca-H-Cl-SO4-OH-HCO3-CO3-CO2-H2O system to high ionic strengths at 25°C. *Geochimica et Cosmochimica Acta*. 1984;48(4):723-751. doi:10.1016/0016-7037(84)90098-X

206. Blanc Ph, Lassin A, Piantone P, et al. Thermoddem: A geochemical database focused on low temperature water/rock interactions and waste materials. *Applied Geochemistry*. 2012;27(10):2107-2116. doi:10.1016/j.apgeochem.2012.06.002

207. Brown DS, Allison JD. MINTEQA1. An Equilibrium Metal Speciation Model. US Environmental protection agency, ed. Published online January 1, 1987.

208. Knuutila H, Hessen ET, Kim I, Haug-Warberg T, Svendsen HF. Vapor–liquid equilibrium in the sodium carbonate–sodium bicarbonate–water–CO2-system. *Chemical Engineering Science*. 2010;65(6):2218-2226. doi:10.1016/j.ces.2009.12.024

209. Morel FMM, Hering JG. *Principles and Applications of Aquatic Chemistry*. Wiley; 1993.

210. Truesdell AH, Jones BF. WATEQ, a computer program for calculating chemical equilibria of natural waters. *Journal of Research of the US Geological Survey*. 1974;2(2):233-248.

211. Pitzer KS, Mayorga G. Thermodynamics of electrolytes. III. Activity and osmotic coefficients for 2?2 electrolytes. *J Solution Chem*. 1974;3(7):539-546. doi:10.1007/BF00648138

212. Lassin A, Christov C, Andre L, Azaroual M. A thermodynamic model of aqueous electrolyte solution behavior and solid-liquid equilibrium in the Li-H-Na-K-Cl-OH-H2O system to very high concentrations (40 molal) and from 0 to 250 C. *American Journal of Science*. 2015;315(3):204-256. doi:10.2475/03.2015.02

213. Kiseleva IA, Ogorodova LP, Melchakova LV, Bisengalieva MR, Becturganov NS. Thermodynamic properties of copper carbonates ? malachite Cu2(OH)2CO3 and azurite Cu3(OH)2(CO3)2. *Phys Chem Minerals*. 1992;19(5). doi:10.1007/BF00204009

214. Taylor SH, Hutchings GJ, Mirzaei AA. Copper zinc oxide catalysts for ambient temperature carbon monoxide oxidation. *Chem Commun*. 1999;(15):1373-1374. doi:10.1039/A903426I

215. Wang D, Tao F, Zhao H, Song H, Chou L. Preparation of Cu/ZnO/Al2O3 Catalyst for CO2 Hydrogenation to Methanol by CO2 Assisted Aging. *Chinese Journal of Catalysis*. 2011;32(9):1452-1456. doi:10.1016/S1872-2067(10)60256-2

216. Solubilities of Sodium Carbonate and Sodium Bicarbonate in Acetone-Water and Methanol-Water Mixtures. | Journal of Chemical & Engineering Data. Accessed April 4, 2025. https://pubs.acs.org/doi/10.1021/je60030a009

217. Sandri G, Bonferoni MC, Rossi S, Caramella CM, Ferrari F. Effects of Particle Size, Surface Nature and Crystal Type on Dissolution Rate. In: Merkus HG, Meesters GMH, Oostra W, eds. *Particles and Nanoparticles in Pharmaceutical Products: Design, Manufacturing, Behavior and Performance*. Springer International Publishing; 2018:303-328. doi:10.1007/978-3-319-94174-5_8

218. Diedrich T, Dybowska A, Schott J, Valsami-Jones E, Oelkers EH. The Dissolution Rates of SiO2 Nanoparticles As a Function of Particle Size. *Environ Sci Technol*. 2012;46(9):4909-4915. doi:10.1021/es2045053

219. Mullin JW. *Crystallization*. 4. ed. Butterworth-Heinemann; 2001.

220. Manuel García-Ruiz J. Nucleation of protein crystals. *J Struct Biol*. 2003;142(1):22-31. doi:10.1016/S1047-8477(03)00035-2

221. Myerson AS. *Handbook of Industrial Crystallization*. 2nd ed. Butterworth-Heinemann; 2002. https://ebookcentral.proquest.com/lib/kxp/detail.action?docID=317222

222. Beckmann W. *Crystallization: Basic Concepts and Industrial Applications*.; 2013. http://onlinelibrary.wiley.com/book/10.1002/9783527650323

223. Threlfall TL, De'Ath RW, Coles SJ. Metastable Zone Widths, Conformational Multiplicity, and Seeding. *Org Process Res Dev*. 2013;17(3):578-584. doi:10.1021/op3003486

224. Threlfall TL, Coles SJ. A perspective on the growth-only zone, the secondary nucleation threshold and crystal size distribution in solution crystallisation. *CrystEngComm*. 2016;18(3):369-378. doi:10.1039/C5CE01608H

225. Barros Groß M, Kind M. Comparative Study on Seeded and Unseeded Bulk Evaporative Batch Crystallization of Tetragonal Lysozyme. *Crystal Growth & Design*. 2017;17(6):3491-3501. doi:10.1021/acs.cgd.7b00456

226. Loï Mi Lung-Somarriba B, Moscosa-Santillan M, Porte C, Delacroix A. Effect of seeded surface area on crystal size distribution in glycine batch cooling crystallization: a seeding methodology. *Journal of Crystal Growth*. 2004;270(3):624-632. doi:10.1016/j.jcrysgro.2004.07.015

227. Choi JY, Lee T, Cheng Y, Cohen Y. Observed Crystallization Induction Time in Seeded Gypsum Crystallization. *Ind Eng Chem Res*. 2019;58(51):23359-23365. doi:10.1021/acs.iecr.9b06050

228. Chesters AK. The modelling of coalescence processes in fluid-liquid dispersions : a review of current understanding. *Chemical Engineering Research and Design*. 1991;69(A4):259-270.

229. Kaysan G, Elmlinger L, Kind M. Increasing the Efficiency of Emulsion Crystallization in Stirred Vessels by Targeted Application of Shear and Surfactant. *Colloids and Interfaces*. 2023;7(4):68. doi:10.3390/colloids7040068

230. Klokishner S, Behrens M, Reu O, et al. Cation ordering in natural and synthetic (Cu(1-x)Zn(x))(2)CO(3)(OH)(2) and (Cu(1-x)Zn(x))(5)(CO(3))(2)(OH)(6). *J Phys Chem A*. 2011;115(35):9954-9968. doi:10.1021/jp205848s

231. Evans TW, Sarofim AF, Margolis G. Models of secondary nucleation attributable to crystal-crystallizer and crystal-crystal collisions. *AIChE Journal*. 1974;20(5):959-966. doi:10.1002/aic.690200517

232. Kaysan G, Rica A, Guthausen G, Kind M. Contact-Mediated Nucleation of Subcooled Droplets in Melt Emulsions: A Microfluidic Approach. *Crystals*. 2021;11(12):1471. doi:10.3390/cryst11121471

233. Zhang K, Chanpura RA, Mondal S, et al. Particle Size Distribution Measurement Techniques and Their Relevance or Irrelevance to Sand Control Design. In: OnePetro; 2014. doi:10.2118/168152-MS

234. D'Ans J, Lax E. *Taschenbuch Für Chemiker Und Physiker.: Band I: Makroskopische Physikalisch-Chemische Eigenschaften*. 3rd ed. Springer-Verlag; 1967.

235. Warmuth L, Steurer M, Schild D, Zimina A, Grunwaldt JD, Pitter S. Reversible and Irreversible Structural Changes in Cu/ZnO/ZrO2 Catalysts during Methanol Synthesis. *ACS Applied Materials & Interfaces*. Published online February 9, 2024. doi:10.1021/acsami.3c17383

236. Stangeland K, Li H, Yu Z. Thermodynamic Analysis of Chemical and Phase Equilibria in CO2 Hydrogenation to Methanol, Dimethyl Ether, and Higher Alcohols. *Ind Eng Chem Res*. 2018;57(11):4081-4094. doi:10.1021/acs.iecr.7b04866

237. Selzer D, Frank C, Kind M. On the effect of the continuous phase on primary crystal nucleation of aqueous KNO3 solution droplets. *Journal of Crystal Growth*. 2019;517:39-47. doi:10.1016/j.jcrysgro.2019.04.004

238. Ramos Ojeda NA, Kind M. Evaluation of Crystallization Kinetics to Achieve Equant-Shaped Crystals from an Acicular Active Pharmaceutical Ingredient. *Crystal Growth & Design*. 2024;24(19):7961-7980. doi:10.1021/acs.cgd.4c00881

239. Zheng D, Zou W, Yan J, et al. Coupling of Contact Nucleation Kinetics with Breakage Model for Crystallization of Sodium Chloride Crystal in Fluidized Bed Crystallizer. *Journal of Chemistry*. 2019;2019(1):2150560. doi:10.1155/2019/2150560

240. Urbanus J, Roelands CPM, ter Horst JH, Verdoes D, Jansens PJ. Screening for templates that promote crystallization. *Food and Bioproducts Processing*. 2008;86(2):116-121. doi:10.1016/j.fbp.2008.03.002

241. Selzer D, Spiegel B, Kind M. A Generic Polycarbonate Based Microfluidic Tool to Study Crystal Nucleation in Microdroplets. *JCPT*. 2018;08(01):1-17. doi:10.4236/jcpt.2018.81001

242. Rehage H, Bartsch M, Kind M. A New Scale-up Method for Competitive Chemical Model Reactions Based on Complete Similarity. *Chemical Engineering Journal*. Published online January 1, 2020:125763. doi:10.1016/j.cej.2020.125763

243. Rehage H, Kind M. The first Damköhler number and its importance for characterizing the influence of mixing on competitive chemical reactions. *Chemical Engineering Science*. 2021;229:116007. doi:10.1016/j.ces.2020.116007

244. Nirschl H. L1.1 Druckverlust in einphasigen Strömungen. In: Stephan P, Kabelac S, Kind M, eds. *VDI-Wärmeatlas: Fachlicher Träger VDI-Gesellschaft Verfahrenstechnik Und Chemieingenieurwesen*. 12th ed. 2019. VDI Springer Reference. Springer Berlin Heidelberg; 2019:1353-1354. doi:10.1007/978-3-662-52989-8_74

245. Nirschl H. L1.2 Druckverlust in durchströmten Rohren. In: Stephan P, Kabelac S, Kind M, eds. *VDI-Wärmeatlas: Fachlicher Träger VDI-Gesellschaft Verfahrenstechnik Und Chemieingenieurwesen*. 12th ed. 2019. VDI Springer Reference. Springer Berlin Heidelberg; 2019:1355-1361. doi:10.1007/978-3-662-52989-8_75

246. Nirschl H. L1.3 Druckverlust in durchströmten Leitungen mit Querschnittsänderungen. In: Stephan P, Kabelac S, Kind M, eds. *VDI-Wärmeatlas: Fachlicher Träger VDI-Gesellschaft Verfahrenstechnik Und Chemieingenieurwesen*. 12th ed. 2019. VDI Springer Reference. Springer Berlin Heidelberg; 2019:1363-1373. doi:10.1007/978-3-662-52989-8_76

List of publications

Articles

D. Guse, L. Warmuth, M. Herfet, K. Adolf, T. A. Zevaco, S. Pitter, M. Kind. *Seeding as a Decisive Tool for Increasing Space-Time-Yields in the Preparation of High-Quality Cu/ZnO/ZrO2 Catalysts.* Catalysts, 2024. DOI: 10.3390/catal14080517.

D. Guse, L. Metzger, M. Kriesten, E. Eiche, M. Kind. F*ast Method to Determine Solubility Products of Sparingly Soluble Salts by Combining Titration Experiments and Thermodynamic Modeling: A Case Study on the Example of Cu/Zn Based Catalyst Precursors and Ni/Mn Based Precursors for Cathode Active Material.* Ind. Eng. Chem. Res., 2024. DOI: 10.1021/acs.iecr.4c01616.

D. Guse, L. Warmuth, F. Kreißig, S. Pitter, M. Kind. *Preparation of Cu/Zn Based Catalyst Precursors – Importance of Thermodynamics and Seeding.* DGMK. 2022-3 Tagungsbericht. Conference Proceedings: The Role of Catalysis for the Energy Transition, ISSN 1433-9013, ISBN 978-3-947716-45-6, 19-39. DOI: 10.5445/IR/1000151320.

D. Guse, S. Polierer, S. Wild, S. Pitter, M. Kind. *Improved Preparation of Cu/Zn-Based Catalysts by Well-Defined Conditions of Co-Precipitation and Aging.* Chem. Ing. Tech., 2022. DOI: 10.1002/cite.202100197.

S. Wild, B. Lacerda de Oliveira Campos, T. A. Zevaco, **D. Guse**, M. Kind, S. Pitter, K. Herrera Delgado, J. Sauer. *Experimental investigations and model-based optimization of CZZ/H-FER 20 bed composition for the direct synthesis of DME from CO2-rich syngas.* React. Chem. Eng., 2022. DOI: 10.1039/D1RE00470K.

S. Wild, S. Polierer, T. A. Zevaco, **D. Guse**, M. Kind, S. Pitter, K. Herrera Delgado, J. Sauer. *Direct DME synthesis on CZZ/H-FER from variable CO2/CO syngas feeds.* RSC Advances 2021, 11, 2556. DOI: 10.1039/D0RA09754C.

S. Polierer, **D. Guse**, S. Wild, K. Delgado, T. Otto, T. Zevaco, M. Kind, J. Sauer, F. Studt, S. Pitter. *Enhanced Direct Dimethyl Ether Synthesis from CO2-Rich Syngas with Cu/ZnO/ZrO2 Catalysts Prepared by Continuous Co-Precipitation.* Catalysts 2020, 10(8), 816. DOI: 10.3390/catal10080816.

Conference contributions as first author

D. Guse, L. Metzger, L. Warmuth, F. Kreißig, S. Pitter, M. Kind. *Using pH and XRD to understand solids phase formation and Cu/Zn distribution in the preparation of Cu/Zn based catalyst precursors* (Poster). EuroPACT2023, 07.05.-10.05.2023, Copenhagen, Denmark.

D. Guse, L. Warmuth, F. Kreißig, S. Pitter, M. Kind. *Preparation of Cu/Zn Based Catalyst Precursors - How Aging can be Accelerated by Seeding* (Poster). 56. Jahrestreffen Deutscher Katalytiker, 15.03.-17.03.2023, Weimar, Germany.

D. Guse, L. Warmuth, F. Kreißig, S. Pitter, M. Kind. *Improved Cu/Zn Based Catalyst Precursors - Controlled Aging by Understanding the Underlying Thermodynamics* (Talk). ProcessNet Jahrestreffen der Fachgruppe Kristallisation, 09.03.-10.03.2023, Frankfurt, Germany.

D. Guse, L. Warmuth, F. Kreißig, S. Pitter, M. Kind. *Preparation of Cu/Zn Based Catalyst Precursors – Importance of Thermodynamics and Seeding* (Talk). DGMK: The Role of Catalysis for the Energy Transition, 05.10.-07.10.2022, Ludwigshafen, Germany.

D. Guse, L. Metzger, M. Kind. *Description of solids formation in co-precipitation processes on the basis of a thermodynamic model* (Talk). ProcessNet Jahrestreffen der Fachgruppe Kristallisation, 16.03.-18.03.2022, Dortmund, Germany.

D. Guse, S. Polierer, S. Wild, K. Herrera Delgado, S. Pitter, M. Kind. *Experimental determination of solids formation times in the co-precipitation of Cu/Zn based catalyst precursors and their significance for catalyst preparation* (Talk). 21st International Symposium on Industrial Crystallization (ISIC 21), 30.08.-02.09.2021, online conference.

D. Guse, S. Polierer, S. Wild, K. Herrera Delgado, S. Pitter, M. Kind. *Experimental determination of solids formation times in the co-precipitation of Cu/Zn based catalyst precursors and their significance for catalyst preparation* (Poster). ProcessNet Jahrestreffen der Fachgruppe Kristallisation, 18.03. - 19.03.2021, online conference.

D. Guse, S. Polierer, S. Wild, S. Pitter, M. Kind. *Fundamental Description of Ageing in the Manufacturing of Copper-Zinc based Catalysts by using a Thermodynamic Equilibrium Model* (Poster). 10. ProcessNet-Jahrestagung, 21.09. - 24.09.2020, online conference. DOI: 10.1002/cite.202055240.

D. Guse, S. Polierer, S. Wild, S. Pitter, M. Kind. *Continuous Co-Precipitation of Copper-Based Catalysts Using Impinging Jet Mixers* (Poster). PARTEC. International Congress on Particle Technology, 09.04. - 11.04.2019, Nürnberg, Germany.

D. Guse, S. Polierer, S. Wild, S. Pitter, M. Kind. *Kontinuierliche Co-Fällung Cu-basierter Katalysatoren* (Poster). ProcessNet Jahrestreffen der Fachgruppen ZER & KRI & GFSP 2019, 12.03. - 13.03.2019, Bamberg, Germany.

D. Guse, M. Kind. *Morphologiebildung bei der Fällungskristallisation* (Poster). ProcessNet Jahrestreffen der Fachgruppen MPH & WSUE & CFD, HTT & AuW, KRI, PMT, 06.03. - 09.03.2018, Bremen, Germany.

Student theses conducted in conjunction with this thesis

R. Samman. *Technologietransfer der Co-Fällung von Cu/Zn basierten Katalysatoren in Mikromischern auf industrielle Rezepturen*. Master's thesis 01/2024.

K. Adolf. *Einfluss von Fällungsprodukt und Seeding auf die Alterungskinetik und das Alterungsprodukt bei Kupfer-Zink basierten Katalysator-Vorstufen*. Master's thesis 05/2023.

A. Karel. *Influence of Gas Phase Composition and Process Control on the Aging of Copper-Zinc Based Catalyst Precursors.* Bachelor's thesis 10/2022.

J. He. *Experimentelle Charakterisierung von Mischdüsen hinsichtlich des Druckverlusts und Anwendung auf die Bestimmung von Feststoffbildungszeiten bei der Fällung.* Bachelor's thesis 05/2022.

M. Lemke. *Quantitative Charakterisierung der Phasenzusammensetzung von Co-Fällungsprodukten mittels FTIR-Spektroskopie.* Master's thesis 12/2021.

C. Staudt. *Aufbau eines Kristallisationsmodells aus Populations- und Stoffmengenbilanzen für die Co-Fällung von Kupfer-Katalysatoren.* Master's thesis 11/2021.

X. Zhou. *Experimentelle Bestimmung von Feststoffbildungszeiten bei der kontinuierlichen Co-Fällung von Kupfer-Zink basierten Katalysator-Vorstufen.* Bachelor's thesis 07/2021.

F. Kreißig. *Inbetriebnahme einer Kristallisationsanlage zur Untersuchung von Co-Fällung und Alterung bei der Herstellung kupferbasierter Katalysator-Vorstufen.* 09/2020.

S. Fernández. *Charakterisierung des Vermischungseinflusses bei der kontinuierlichen Co-Fällung von Cu/ZnO/ZrO2 Katalysator-Vorstufen in einem Mikromischer.* Bachelor's thesis 09/2020.

K. Armbruster. *Bestimmung geeigneter Partikeleigenschaften von Zwischenprodukten zur Vorabbewertung der Produktqualität von Kupfer-basierten Katalysatoren.* Bachelor's thesis 03/2020.

F. Speier. *Untersuchung zum Einfluss der Fest-Flüssig-Trennung bei der Synthese Kupfer-basierter Katalysatoren auf deren Produkteigenschaften bei der Methanol-Synthese.* Bachelor's thesis 02/2020.

L. Jeck. *Modellierung der Co-Fällungskristallisation bei der Synthese Kupfer-basierter Katalysatoren für die Methanol-Katalyse.* Bachelor's thesis 12/2019.

A. Celik. *Studie zum Reaktions- und Dissoziationsverhalten von Kupfer-basierten Mehrstoffsystemen.* Bachelor's thesis 08/2019.

P. Ruppik. *Untersuchung zum Einfluss von Fällung und Alterung bei der Synthese Kupfer-basierter Katalysatoren.* Master's thesis 06/2019.

Appendix

A.1 Further information on the experimental setup

The complete geometric data of the two mixing nozzles used in this work are depicted in Figure A.1. The main difference between both variants is the positioning of the inlets which affect the energy dissipation and mixing times as quantified in Figure A.15 to Figure A.18.

The configuration of the syringe pump setup based on the adapted material testing machine, cf. Section 2.3.1, is shown in Figure A.2.

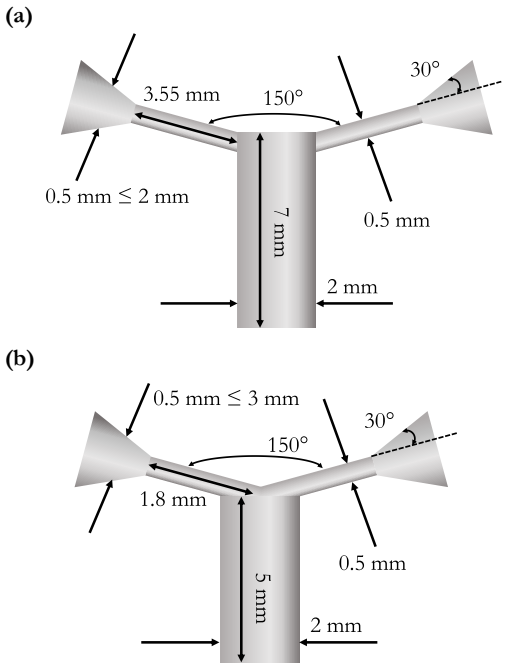

Figure A.1: Geometries of the two mixing nozzles applied in this work for **(a)** the studies in the continuous set-up depicted in Figure 2.2 (a) and **(b)** the studies in the syringe pump setup depicted in Figure A.2.

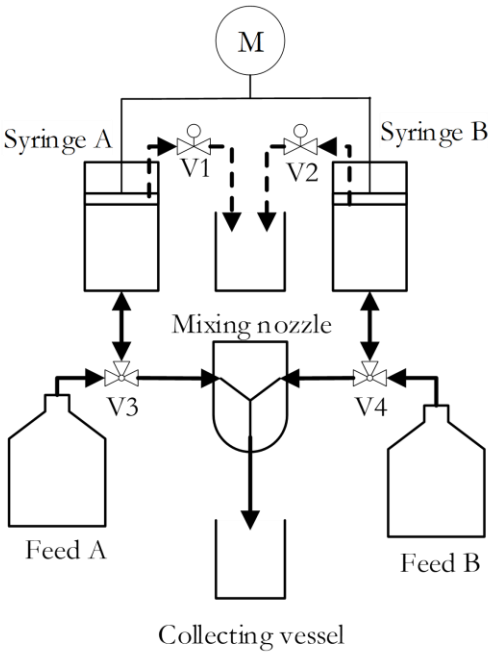

Figure A.2: Syringe pump setup used for the mixing studies in Section 3.3. Feed vessels, syringes and mixing nozzle are temperature-controlled (± 1 K).

First, the traverse of the testing machine is moved upwards to fill the metal syringes A and B via ventil V3, respectively V4, from the two temperature-controlled feed vessel A and B. Then, the valves are set to enable the supply of reactants from the syringes towards the mixing nozzle with a precisely defined volume flow ($\Delta\dot{V}_{\text{total,error}} < 1\,\%$). The valves V1 and V2 are used for degassing the system after cleaning and change of reactants. Further details on the syringe pump setup are available in the literature[111].

A.2 Influence of washing and drying

Since the focus of this work is on the two process steps co-precipitation and aging, possible influences of all further downstream processes on the product properties have to be ruled out. Particular attention was paid to washing and drying since various methods were available and utilized for both processes: solid-liquid separation and washing by centrifugation, vacuum filtration with resuspension or flow through washing or without any washing, spray drying, vacuum drying at low temperatures or drying at high temperatures and ambient pressure. The

respective quantitative parameters as well as the influence on the X-ray diffractogram of the dried and aged intermediate is plotted in Figure A.3.

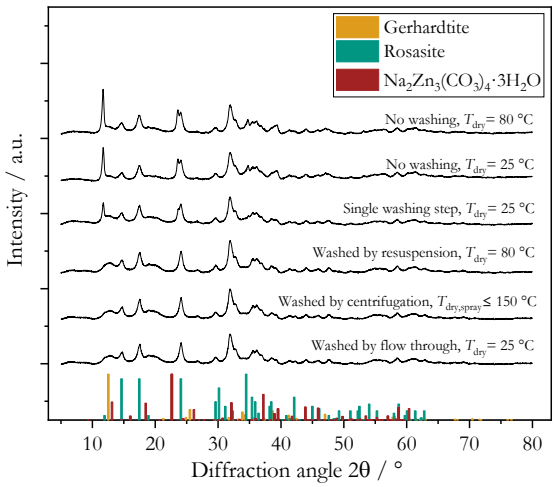

Figure A.3: Influence of washing and drying method on the phase composition.

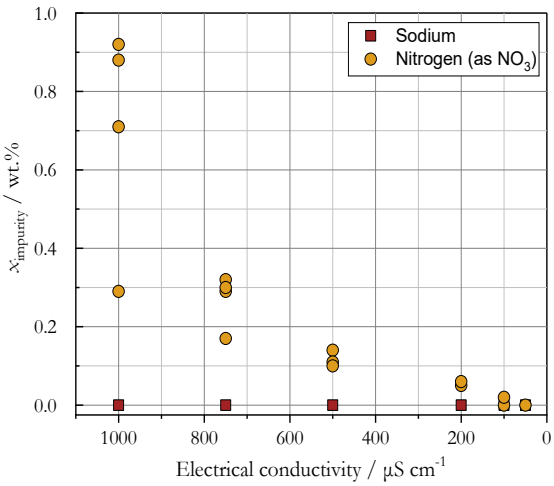

Figure A.4: Influence of residual electrical conductivity in the filtrate after washing on the weight fraction of impurities in the aged and dried intermediate.

All experiments were conducted with $b_{Cu(NO_3)_2,Feed1} = 0.16\ mol \cdot (kg\ H_2O)^{-1}$, $b_{Zn(NO_3)_2,Feed1} = 0.08\ mol \cdot (kg\ H_2O)^{-1}$, $b_{ZrO(NO_3)_2,Feed1} = 0.03\ mol \cdot (kg\ H_2O)^{-1}$ and $b_{NaHCO_3,Feed2} = 1.018\ mol \cdot (kg\ H_2O)^{-1}$ at 40 °C resulting in a pH = 6.9 after co-precipitation and a solids fraction in the suspension of approx. 2 wt.%. There are no apparent differences between the drying methods considered. However, washing does impact the phase composition in the dried material: if no washing is conducted, gerhardtite, respectively the structurally similar rouaite, are present afterwards indicating that some nitrate ions are adsorbed at the surface and react with the solid copper phases during drying. Similar effect were reported in the literature[72]. The same applies for $Na_2Zn_3(CO_3)_4 \cdot 3\ H_2O$ [97]. Thus, a washing study based on the electrical conductivity of the filtrate was conducted to determine how much washing is needed to rule out this effect, cf. Figure A.4. Based on these results, each sample was washed until a conductivity of $\sigma \leq 100\ \mu S \cdot cm^{-1}$ was achieved. For sodium, no accumulation in the solids was apparent, independent from washing.

A.3 Further analysis information and results

A.3.1 SEM and TEM imaging

Prolonged focusing of the TEM beam to acquire EDXS is an energy-intensive procedure. Thus, its influence on the aged intermediate is investigated in Figure A.5 since hydroxycarbonates are known to decompose at relatively low temperatures of approx. 250 °C [72]. Indeed, a comparison of the same particles before and after EDXS acquisition confirm that a partial decomposition occurs that is connected with a reduction of size. Most probably, the zincian malachite is partially oxidized to CuO and ZnO under release of H_2O and CO_2. However, the goal of the EDXS imagining here was to evaluate the Cu/Zn distribution within the particles on the nanometer scale. The decomposition of zincian malachite during image generation should have a neglectable influence on the position and ordering of Cu and Zn ions.

Therefore, the validity of the images for evaluating the Cu/Zn distribution is not considered diminished.

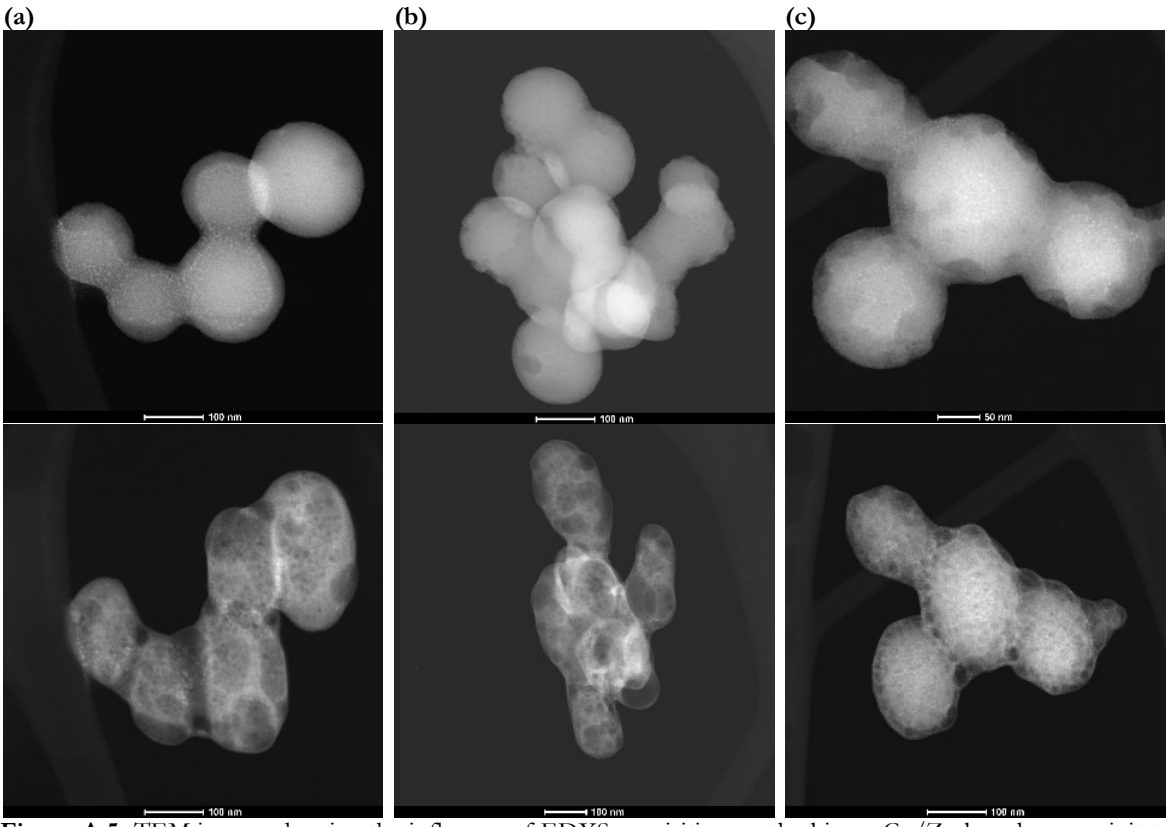

Figure A.5: TEM images showing the influence of EDXS acquisition on the binary Cu/Zn based co-precipitate particles on three examples (a), (b) and (c). The upper row shows the initial state of the particles, the lower row the state after 90 s.

In Figure A.7, exemplary TEM images for the binary Cu/Zn based co-precipitate show the difference in particle size for two volume flows, cf. Section 3.3. Additionally, TEM-EDXS images for $\dot{V}_{\mathrm{Feed1,total}} = 50\ \mathrm{ml} \cdot \mathrm{min}^{-1}$ are depicted in Figure A.6. In both cases, some agglomeration is apparent for $\dot{V}_{\mathrm{Feed1,total}} = 50\ \mathrm{ml} \cdot \mathrm{min}^{-1}$. The TEM(-EDXS) images in Figure A.8 imply that the formation of separate, small ZrO_2 particles further promote agglomeration. Additional TEM-EDXS images of precatalysts prepared by semi-batch respectively continuous co-precipitation are shown in Figure A.9. Figure A.10 displays the correlation between mixing intensity during co-precipitation and the inner pore structure of the particles.

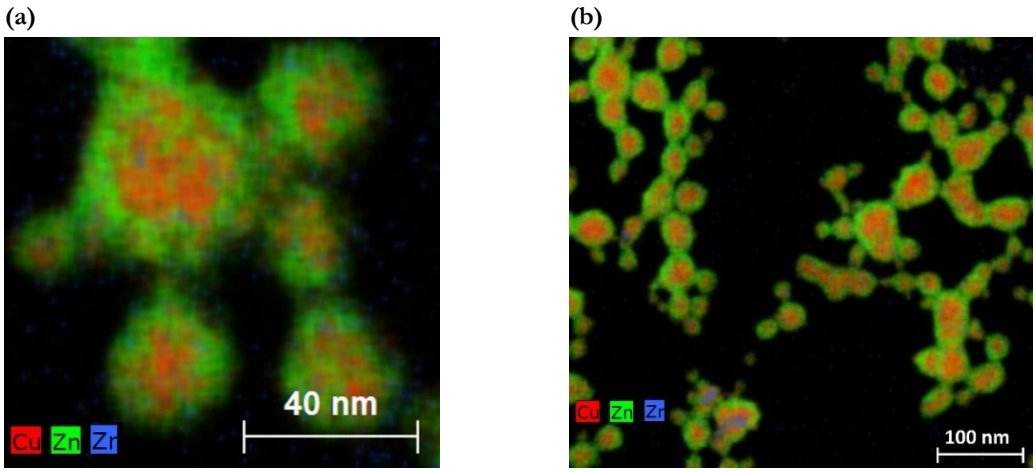

Figure A.6: TEM-EDXS images of a Cu/Zn/Zr based co-precipitate for $\dot{V}_{\text{total}} = 50\ \text{mL} \cdot \text{min}^{-1}$ without stabilizer showing two different sample areas (a) and (b). All metals present are highlighted: Cu in red, Zn in green and Zr in blue. From Guse et al.[101]

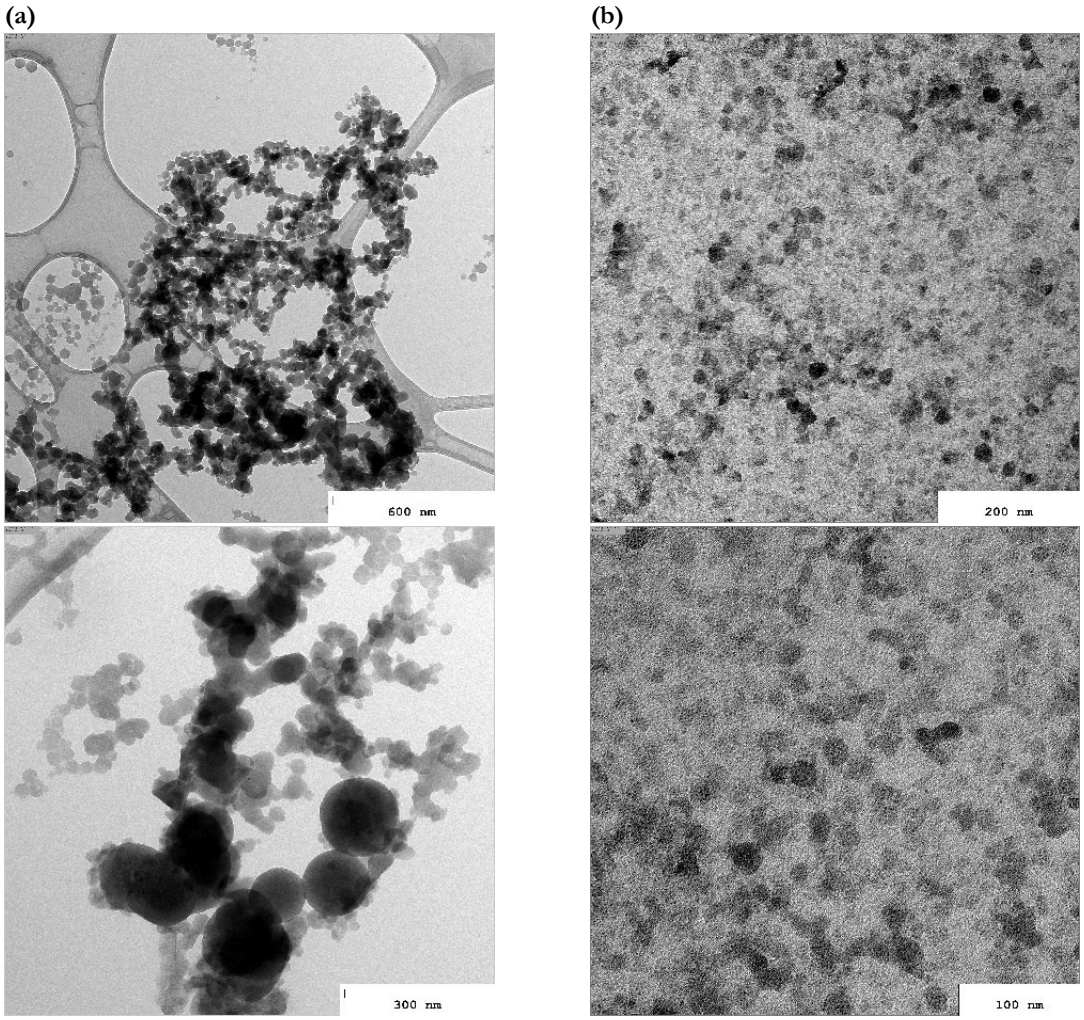

Figure A.7: TEM images showing the influence of volume flow on the morphology and aggregation tendency of Cu/Zn based co-precipitate particles for (a) $\dot{V}_{\text{Feed1,total}} = 50\ \text{ml} \cdot \text{min}^{-1}$ and (b) $\dot{V}_{\text{Feed1,total}} = 600\ \text{ml} \cdot \text{min}^{-1}$.

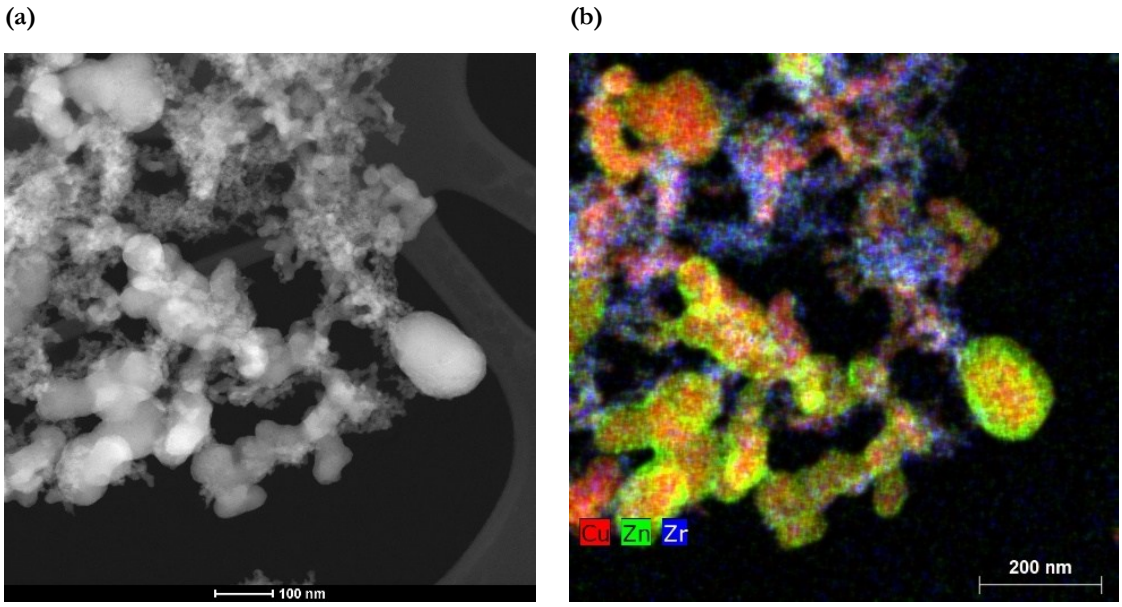

Figure A.8: TEM (a) and TEM-EDXS (b) image of a Cu/Zn/Zr based co-precipitate for $\dot{V}_{\text{total}} = 50\ \text{mL} \cdot \text{min}^{-1}$ without stabilizer showing the same sample area. All metals present are highlighted: Cu in red, Zn in green and Zr in blue.

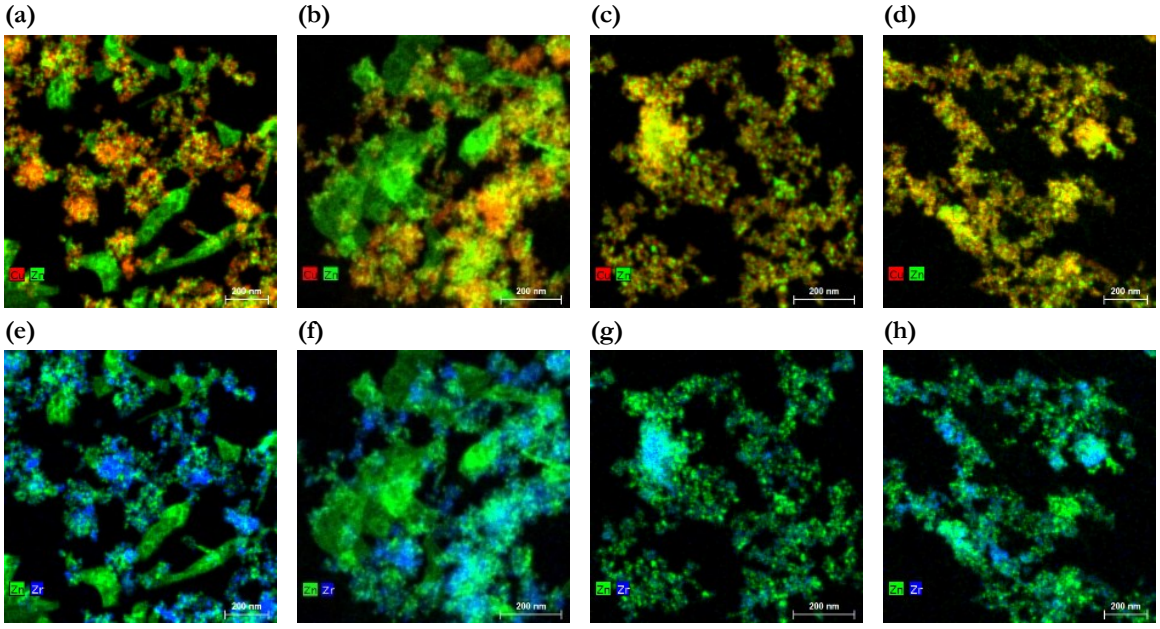

Figure A.9: TEM-EDXS images of the precatalysts prepared by semi-batch (a), (b), (e), (f) and by continuous co-precipitation with $\dot{V}_{\text{total}} = 300\ \text{mL} \cdot \text{min}^{-1}$ (c), (d), (g), (h). Red: Cu, green: Zn, blue: Zr.

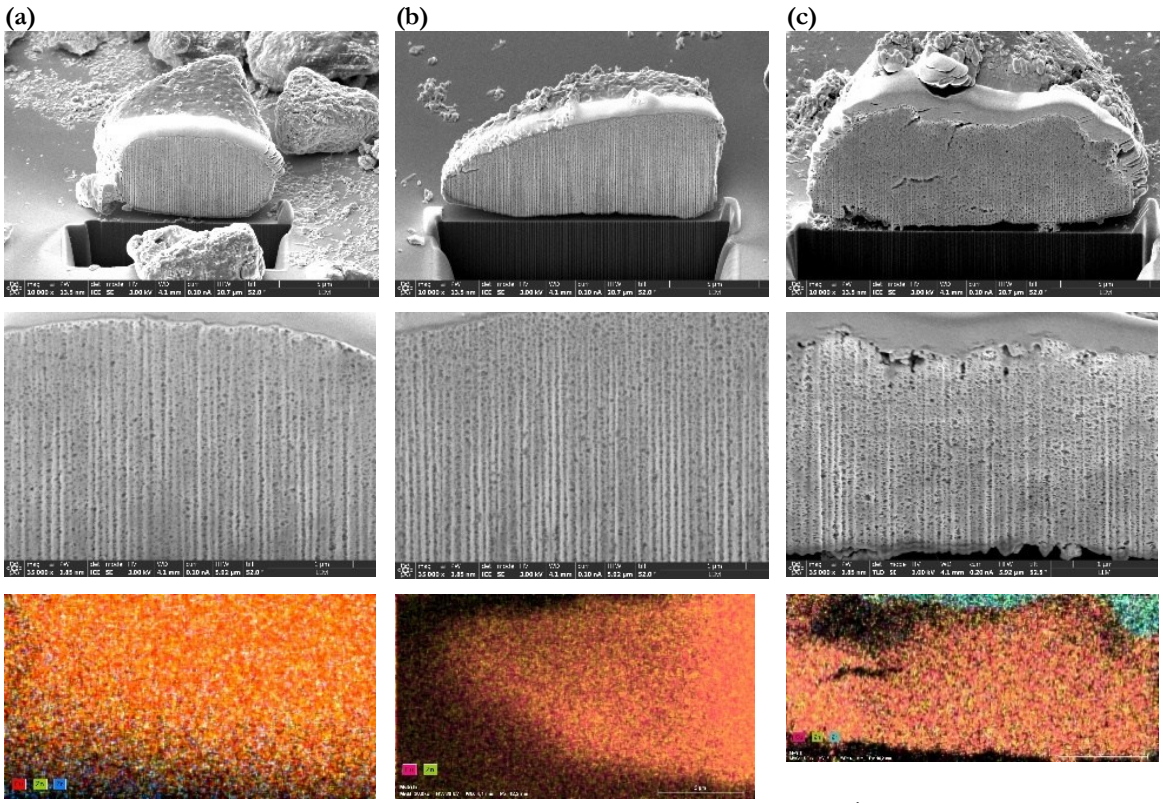

Figure A.10: SEM images of the CZZ aged intermediate prepared with (a) $\dot{V}_{\mathrm{Feed1,total}} = 25\ \mathrm{ml \cdot min^{-1}}$, (b) $\dot{V}_{\mathrm{Feed1,total}} = 50\ \mathrm{ml \cdot min^{-1}}$ and (c) $\dot{V}_{\mathrm{Feed1,total}} = 600\ \mathrm{ml \cdot min^{-1}}$ during co-precipitation (upper row), SEM images of the cross-sections of the respective samples prepared by FIB (middle row) and SEM-EDX images of the respective cross-sections with Cu in red, Zn in green and Zr in blue.

A.3.2 XRD and Rietveld refinement

For the evaluation of X-ray diffractograms with Rietveld refinement the following reference phases, cf. Table A.1, were applied. The lattice parameters of aurichalcite and zincian malachite were adjusted based on the respective fit functions that correlate the foreign ion share with a change of these parameters. The correlation for zincian malachite is discussed in the literature[66] and documented in Eq. (2.4) ff.

Table A.1: Overview of the reference phases used for Rietveld refinement.

Reference phase	Molecular formula	Reference Code (Profex 5.2.8)
Aurichalcite	$\left(Zn_{1-\tilde{x}_{Cu,aur}}Cu_{\tilde{x}_{Cu,aur}}\right)_5(CO_3)_2(OH)_6$	R060426-1 adapted according to Figure A.11
Cuprite	Cu_2O	BGMN Cuprite
Hydrozincite	$Zn_5(CO_3)_2(OH)_6$	ICSD_16583
Gerhardtite	$Cu_2(NO_3)(OH)_3$	amcsd_0013022
Likasite	$Cu_3(NO_3)(OH)_5 \cdot 2(H_2O)$	R090009-9
Malachite	$Cu_2(CO_3)(OH)_2$	BGMN Malachite
Nahcolite	$NaHCO_3$	BGMN Nahcolite
Rosasite	$(Cu_{1.24}Zn_{0.76})(CO_3)(OH)_2$	R050294-1
Rouaite	$Cu_2(NO_3)(OH)_3$	R080086-9
Smithsonite	$ZnCO_3$	ICSD_100679
Soda	Na_2CO_3	BGMN Natron(Soda)
Zincian malachite	$\left(Cu_{1-\tilde{x}_{Zn,zm}}Zn_{\tilde{x}_{Zn,zm}}\right)_2CO_3(OH)_2$	BGMN Malachite; adapted[66]
Zincite	ZnO	04-003-2106
-	CuO	04-007-1375
-	$Na_2Zn_3(CO_3)_4 \cdot 3(H_2O)$	ICSD_81305
-	NaOH	cod_2310820

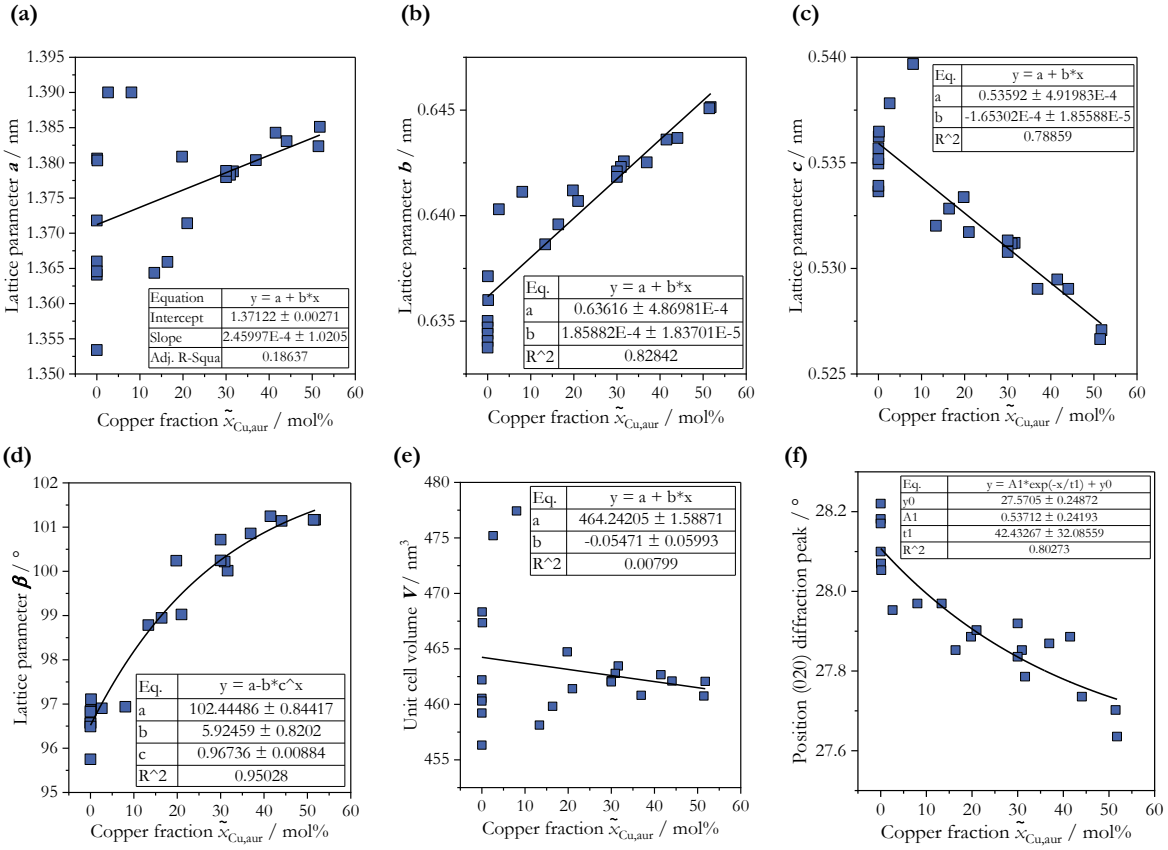

Figure A.11: Correlation between the molar Cu fraction in aurichalcite $\tilde{x}_{Cu,aur}$ and the lattice parameters *a*, *b*, *c*, β and *V* and the position of the diffraction peak corresponding to the (020) plane.

The correlations for aurichalcite are visualized in Figure A.12. In general, the fit quality between $\tilde{x}_{Cu,aur}$, cf. Eq. (A.1), and the lattice parameters is worse compared to the correlations for $\tilde{x}_{Zn,zm}$ and zincian malachite and mostly below a coefficient of determination of $R^2 \leq 0.9$. Yet, for the lattice constant β_{aur} a coefficient of $R^2 = 0.95$ was found. Thus, in contrast to

zincian malachite, the correlation for β_{aur} is used as the sole correlation to determine $\tilde{x}_{\mathrm{Cu,aur}}$ from Rietveld refinement.

$$\tilde{x}_{\mathrm{Cu,aur}} = \frac{n_{\mathrm{Cu,aur}}}{n_{\mathrm{Cu,aur}} + n_{\mathrm{Zn,aur}}} \tag{A.1}$$

In Figure A.12, the development of the total Zn fraction in the solids $\tilde{x}_{\mathrm{Zn,metals}}$ and the Zn fraction in zincian malachite $\tilde{x}_{\mathrm{Zn,zm}}$ over the aging time t_{age} is plotted for two seeding mass fractions x_{seeds}. In both cases, $\tilde{x}_{\mathrm{Zn,metals}}$ and $\tilde{x}_{\mathrm{Zn,zm}}$ approach for increasing aging time and are identical if the aging times exceeds the minimum aging time required for the phase transformation from zincian georgeite to zincian malachite. This confirms that alle available Zn ions are incorporated into the zincian malachite lattice as intended.

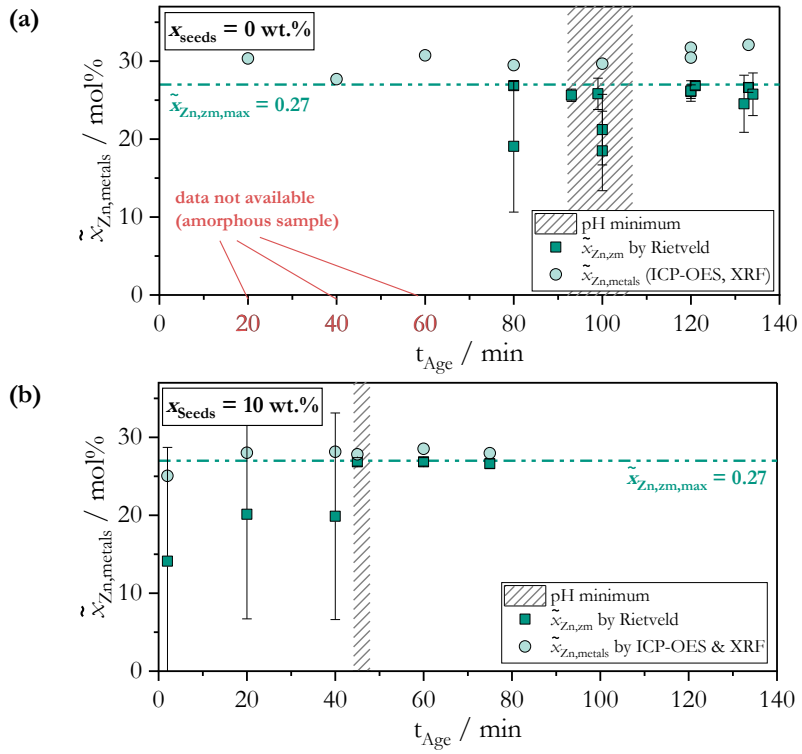

Figure A.12: Development of the molar fraction of Zn in the metals of the solids samples (○) and in zincian malachite (□) as a function of the aging time t_{age}: **(a)** a standard aging process without seeding ($x_{\mathrm{Seeds}} = 0$ wt.%) and **(b)** a seeded aging where seed crystals were added directly after co-precipitation was completed at $t_{\mathrm{age}} = 0$ min ($x_{\mathrm{Seeds}} = 10$ wt.%). Adapted from Guse et al.[115,120]

In Figure A.13, the X-ray diffractograms of two aged intermediates which were prepared by means of (a) a semi-batch co-precipitation respectively (b) a continuous co-precipitation are compared. The composition of the semi-batch material is more inhomogeneous as it shows a bigger aurichalcite fraction.

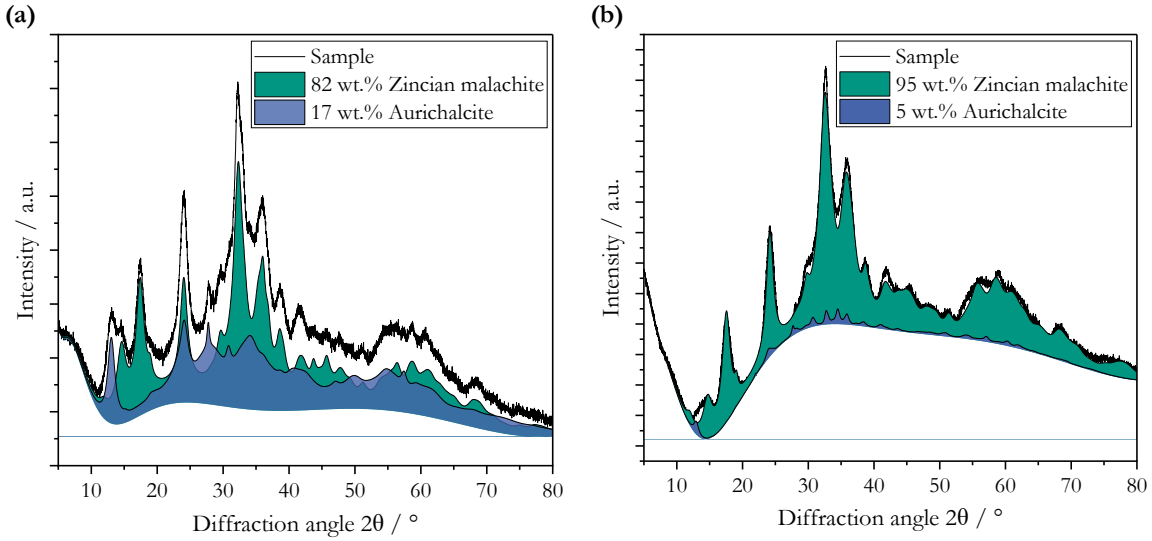

Figure A.13: Influence of co-precipitation mode on the phase composition of the aged intermediate. Comparison of the X-ray diffractograms for (a) a semi-batch and (b) a continuous co-precipitation.

The influence of mixing intensity on the phase composition of the co-precipitate is represented in Figure A.14. Independent of the volume flow set, the co-precipitate is amorphous in each case which agrees with the general consensus in the literature[64,70,75].

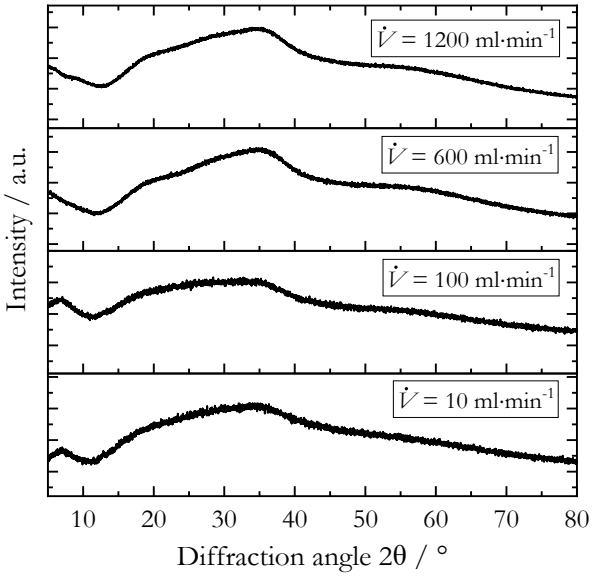

Figure A.14: Influence of volume flow on the X-ray diffractogram of the Cu/Zn/Zr based co-precipitate.

A.3.3 Pressure drop, energy dissipation rate and micro mixing times

Using the experimental setup described in Section 2.3 and A.1 Further information on the experimental setup, the mixing-induced pressure drop Δp_{mix} was measured with two methods: via a differential pressure transmitter and with the force sensor of the testing machine. Additional pressure drops due to pipe flow, bends and cross-sectional changes were calculated and subtracted accordingly[244–246]. The pressure drops of the two mixing nozzles applied, cf. Figure A.1, are plotted in Figure A.15 as a function of the total volume flow and the Reynolds number. As to be expected, Δp_{mix} increases with increasing Re_{mix}. The quantitative differences between both mixing nozzles result from the different positioning of the inlets.

The pressure drops are converted into the pressure loss coefficient ξ_{mix} according to Eq. (A.2) with the mean velocity in the inlet jets $\bar{u}_{\mathrm{inlet}}$ [245]. This way, flow regimes as a function of Re_{mix} can be distinguished in the mixing nozzles, cf. Figure A.16. For $Re_{\mathrm{mix}} \leq 2000$, ξ_{mix} decreases with increasing Re_{mix} which is characteristic for the laminar or transition regime also observed in tubes. For $Re_{\mathrm{mix}} > 2000$, the pressure loss coefficient remains constant for both mixing nozzles. This fits Reynolds ranges and ξ_{mix} from similar studies with similarly shaped and T-shape mixing nozzles[112,137]. In accordance with the pressure drops, the pressure loss coefficient of mixing nozzle (b) ξ_{mix2} is approx. 50 % larger than ξ_{mix1}. Furthermore, Eq. (A.2) was applied in Figure A.15 for validation.

$$\xi_{\mathrm{mix}} = \frac{\Delta p_{\mathrm{mix}}}{\frac{\rho_{\mathrm{fl}}}{2}\,\bar{u}_{\mathrm{inlet}}^{2}} \tag{A.2}$$

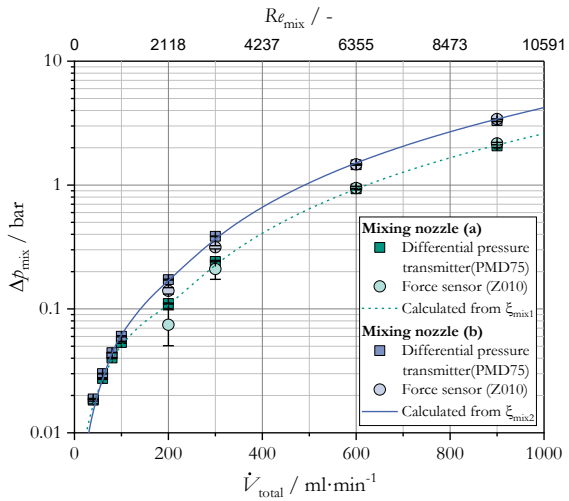

Figure A.15: Correlation between volume flow (Reynolds number) and mixing-induced pressure drop Δp_{mix} for the two mixing nozzles applied in this work. Determined experimentally with water at 25 °C.

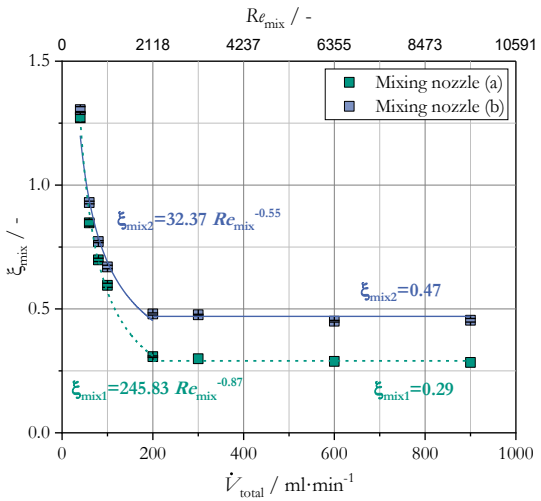

Figure A.16: Correlation between volume flow (Reynolds number) and pressure loss coefficient ξ for the two mixing nozzles applied in this work. Determined experimentally with water at 25 °C.

Using Eq. (3.1) and (3.2), the mean energy dissipation rates $\bar{\varepsilon}$ and micro mixing times τ_{micro} in the mixing nozzles were calculated for the co-precipitation of Cu/Zn based catalysts The results are summarized in Figure A.17 and Figure A.18. They may be applied for the transfer of the results to similar mixing setups and are used in Section 3 to understand to what extent solids formation during co-precipitation of the catalyst precursors is influenced by mixing and how mixing has to be implemented to ensure the formation of homogeneous solids under defined conditions. Table A.2 gives an overview of the physicochemical properties used for these calculations. The viscosities were measured with a Haake Mars II (Flügelgeometrie FLklein, Z20 DIN vial, Thermo Scientific), the densities with a DMA 4101 (Anton Paar).

Table A.2: Overview of physicochemical properties of the reactants and suspension.

Substance	$\rho(20\,°C)$ /kg·m^{-3}	$\rho(50\,°C)$ /kg·m^{-3}	$\mu(20\,°C)$ /mPa·s	$\mu(50\,°C)$ /mPa·s
Water	998.21	988.04	1.0	0.55
$Cu(NO_3)_2$/ $Zn(NO_3)_2$ solution	1037.6	1017.9	1.07	0.75
$NaHCO_3$ solution	1043.2	1013.5	1.38	0.91
Suspension (2 wt.% solids)	1036.5	1017.1	4.24*	3.07*

* The suspension showed characteristics of a Bingham plastic with a yield stress of approx. 0.5 Pa.

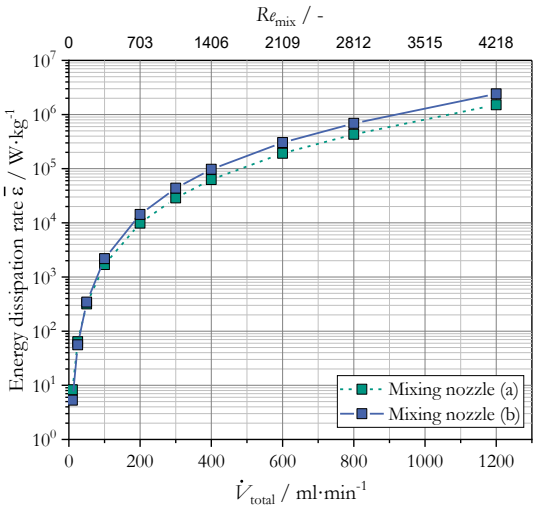

Figure A.17: Correlation between volume flow (Reynolds number) and the mean energy dissipation rate $\bar{\varepsilon}$ for the two mixing nozzles applied for co-precipitation of the binary Cu/Zn catalyst precursor for 50 °C.

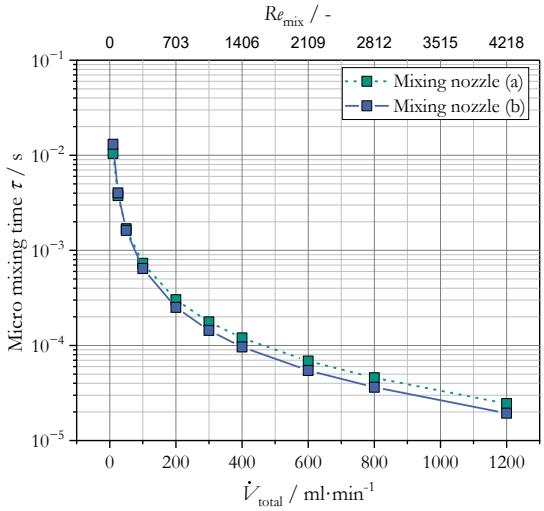

Figure A.18: Correlation between volume flow (Reynolds number) and the micro mixing time τ_{micro} for the two mixing nozzles applied for co-precipitation of the binary Cu/Zn catalyst precursor for 50 °C.

A.4 Solubility product of $Na_2Zn_3(CO_3)_4 \cdot 3\ H_2O$

In Section 4.2.3, an approach was introduced to determine missing solubility products by fitting experimental titration curves with a thermodynamic model. This approach was also applied for $Na_2Zn_3(CO_3)_4 \cdot 3\ H_2O$, a metastable phase repeatedly observed in the preparation of Cu/Zn based catalyst precursors[43,78,97]. However, despite its significance as a major by-product associated with deteriorated catalytic performance, no solubilities are documented. The fitting routine was conducted for three temperatures, cf. Figure A.19.

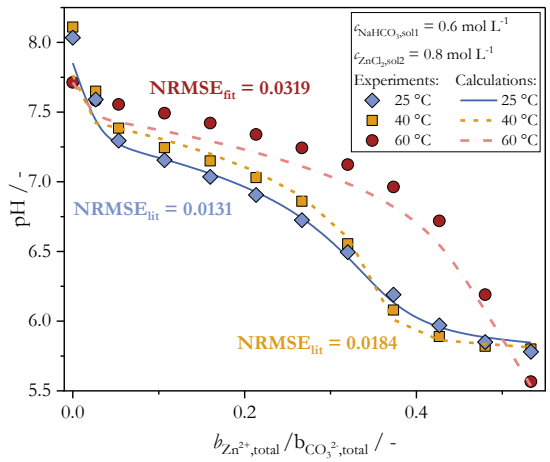

Figure A.19: Influence of temperature on the titration curve for the precipitation of ($Na_2Zn_3(CO_3)_4 \cdot 3\ H_2O$) with hydrozincite as a by-product.

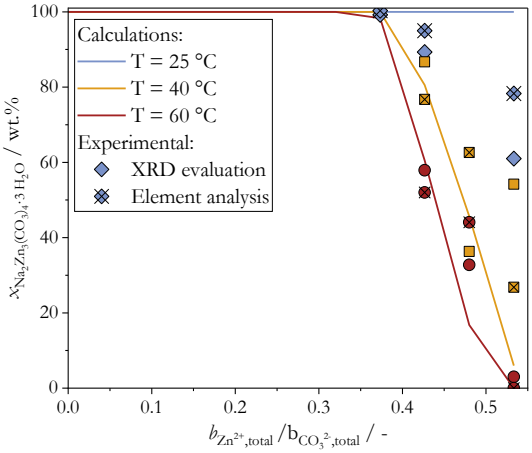

Figure A.20: Solid phase composition as a function of total lattice ion ratio for the precipitation of ($Na_2Zn_3(CO_3)_4 \cdot 3\ H_2O$) with hydrozincite as the single by-product.

In each case, the fit was successful resulting in the temperature-dependent solubility product recorded in Table 2.2. Furthermore, the validity of the thus extended database was evaluated in Figure A.20 by comparing the mass fraction of $Na_2Zn_3(CO_3)_4 \cdot 3\ H_2O$ as determined experimentally by Rietveld refinement and element analysis, cf. Eq. (A.3), and as calculated with the thermodynamic model. At low lattice ion ratios $b_{Zn^{2+},total} / b_{CO_3^{2-},total} < 0.4$, $Na_2Zn_3(CO_3)_4 \cdot 3\ H_2O$ is present exclusively according to both the experimental evaluation and calculations independent from temperature. For larger ion ratios, hydrozincite forms and $x_{Na_2Zn_3(CO_3)_4 \cdot 3\ H_2O}$ decreases accordingly. This effect is more pronounced at higher temperatures. Here, deviations between thermodynamic model and the experiments are evident. Yet, the general trend is represented correctly for $T \geq 40\ °C$ which is the temperature range typically applied for technical application[31,36].

$$x_{Na_2Zn_3(CO_3)_4 \cdot 3\ H_2O,solids} = \frac{x_{Na,total}}{x_{Na,Na_2Zn_3(CO_3)_4 \cdot 3\ H_2O}} \tag{A.3}$$

A.5 Simulation results

In the following some additional results of the thermodynamic model are visualized, which are mainly referenced in Section 3.2 (Figure A.21 and Figure A.22) and Section 4.5.

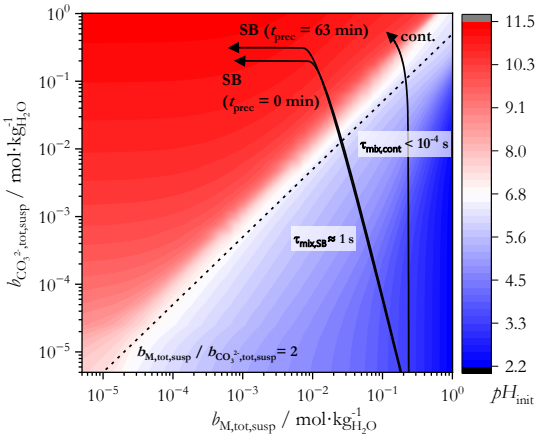

Figure A.21: Initial pH assuming complete mixing without solids formation as a function of the two total reactant molalities of Na_2CO_3 and $Cu(NO_3)_2$/ $Zn(NO_3)_2$ in the mixed suspension for T = 40 °C.

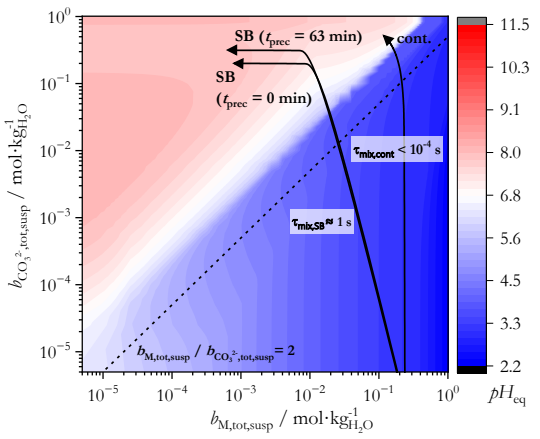

Figure A.22: pH for the metastable state after initial co-precipitation as a function of the two total reactant molalities of Na_2CO_3 and $Cu(NO_3)_2$/$Zn(NO_3)_2$ in the mixed suspension for T = 40 °C.

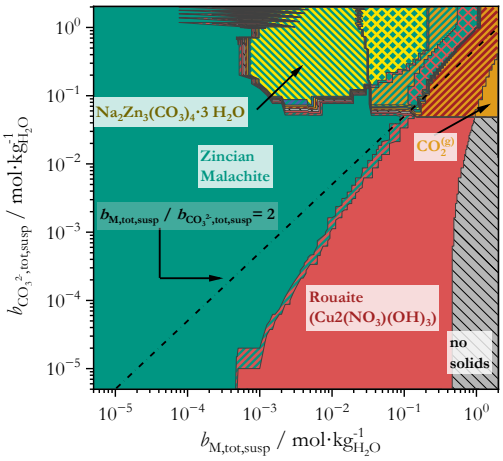

Figure A.23: Prevailing phases at thermodynamic equilibrium as a function of the two total reactant molalities of $NaHCO_3$ and $Cu(NO_3)_2$/$Zn(NO_3)_2$ in the mixed suspension for T = 55 °C.

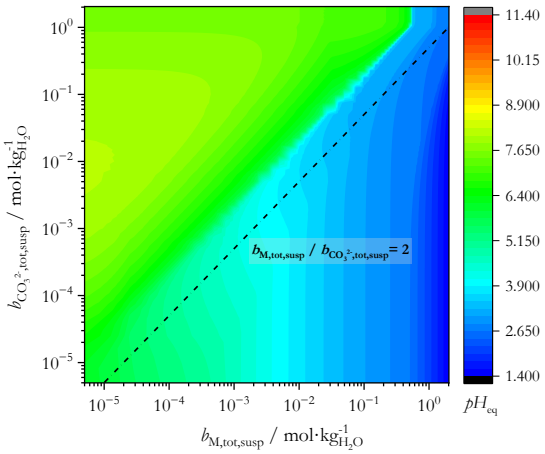

Figure A.24: pH at thermodynamic equilibrium as a function of the two total reactant molalities of $NaHCO_3$ and $Cu(NO_3)_2$/$Zn(NO_3)_2$ in the mixed suspension for T = 55 °C.

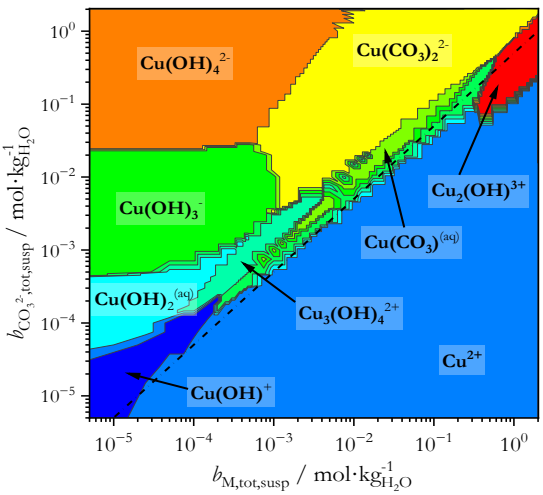

Figure A.25: Prevailing Cu^{2+} species assuming complete mixing without solids formation as a function of the two total reactant molalities of Na_2CO_3 and $Cu(NO_3)_2/Zn(NO_3)_2$ in the mixed suspension for T = 55 °C.

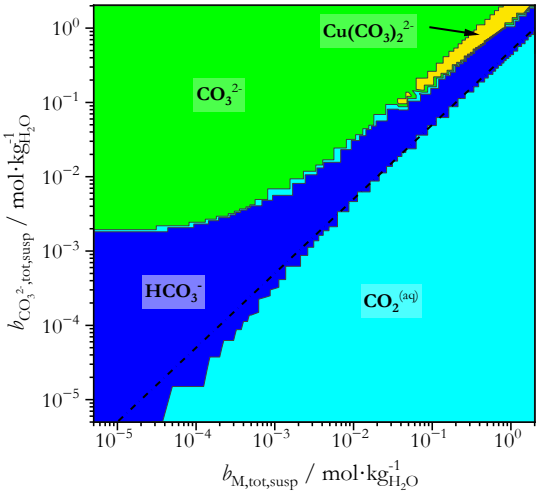

Figure A.26: Prevailing CO_3^{2-} species assuming complete mixing without solids formation as a function of the two total reactant molalities of Na_2CO_3 and $Cu(NO_3)_2/Zn(NO_3)_2$ in the mixed suspension for T = 55 °C.

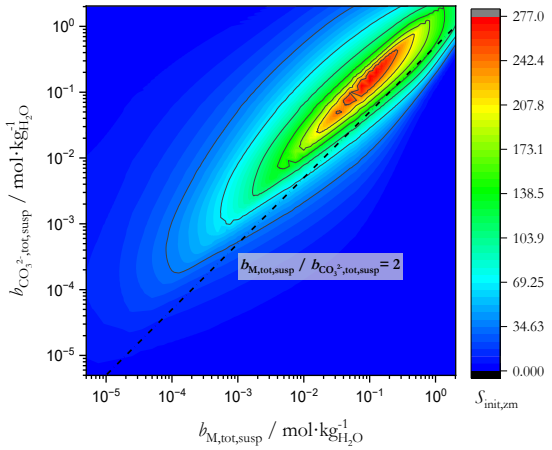

Figure A.27: Initial supersaturation of zincian malachite assuming complete mixing without solids formation as a function of the two total reactant molalities of Na_2CO_3 and $Cu(NO_3)_2/Zn(NO_3)_2$ in the mixed suspension for T = 55 °C.

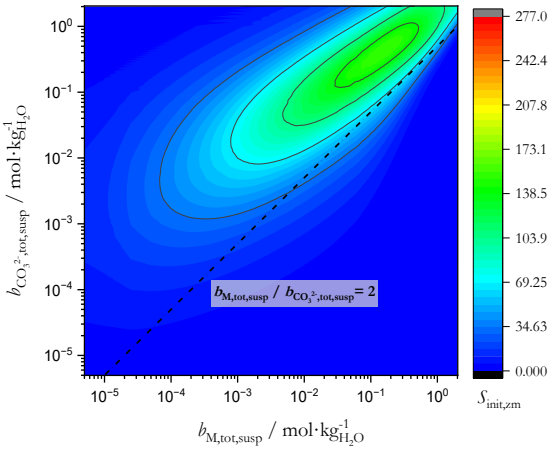

Figure A.28: Initial supersaturation of zincian malachite assuming complete mixing without solids formation as a function of the two total reactant molalities of $NaHCO_3$ and $Cu(NO_3)_2/Zn(NO_3)_2$ in the mixed suspension for T = 55 °C.

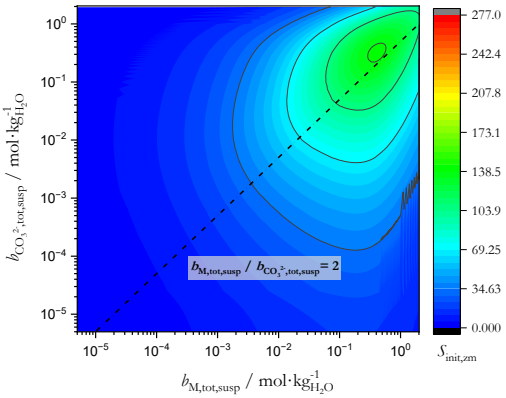

Figure A.29: Initial supersaturation of zincian malachite assuming complete mixing without solids formation as a function of the two total reactant molalities of Na_2CO_3 and $Cu(NO_3)_2/Zn(NO_3)_2$ in the mixed suspension for $T = 55$ °C and $pH_{eq} = 6.0$.

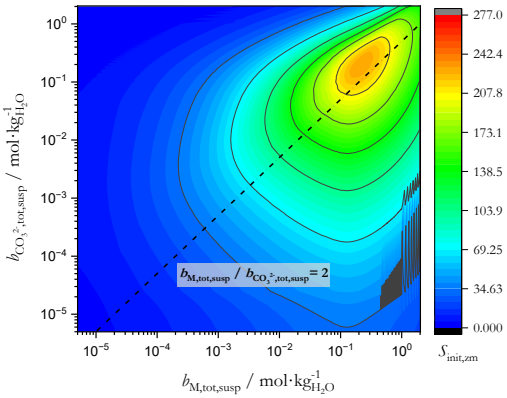

Figure A.30: Initial supersaturation of zincian malachite assuming complete mixing without solids formation as a function of the two total reactant molalities of $NaHCO_3$ and $Cu(NO_3)_2/Zn(NO_3)_2$ in the mixed suspension for $T = 55$ °C and $pH_{eq} = 6.9$.

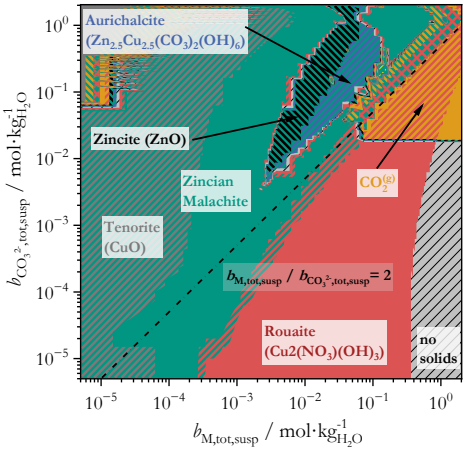

Figure A.31: Prevailing phases at thermodynamic equilibrium as a function of the two total reactant molalities of $NaHCO_3$ and $Cu(NO_3)_2/Zn(NO_3)_2$ in the mixed suspension for $T = 40$ °C.

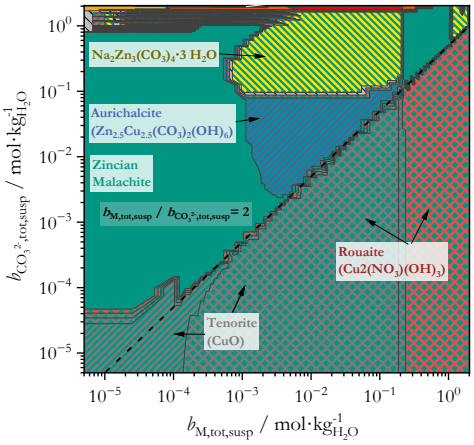

Figure A.32: Prevailing phases at thermodynamic equilibrium as a function of the two total reactant molalities of $NaHCO_3$ and $Cu(NO_3)_2/Zn(NO_3)_2$ in the mixed suspension for $T = 55$ °C and $pH_{eq} = 8.0$.

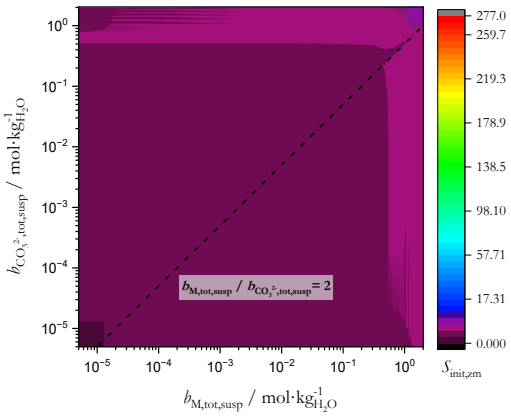

Figure A.33: Supersaturation of zincian malachite after complete mixing of reactants and co-precipitation of zincian georgeite as a function of the two total reactant molalities of $NaHCO_3$ and $Cu(NO_3)_2/Zn(NO_3)_2$ in the mixed suspension for $T = 55$ °C and $pH_{eq} = 6.9$.